The influence of environment on the star formation properties of galaxies

Bruno Rodríguez del Pino

Thesis submitted to the University of Nottingham
for the degree of Doctor of Philosophy, February 2015

"Imagination will often carry us to worlds that never were, but without it we go nowhere."

– Carl Sagan

"Caminante, son tus huellas
el camino, y nada más;
caminante, no hay camino:
se hace camino al andar."

– Antonio Machado

Supervisors:	Prof. Alfonso Aragón-Salamanca Dr. Steven P. Bamford
External supervisor:	Dr. Marc Balcells Comas
Examiners:	Dr. Bianca Maria Poggianti Prof. Frazer Pearce

Abstract

This thesis explores the properties of galaxies that reside in regions of high density and the influence of the environment in their evolution. In particular, it aims to shed more light on the understanding of how galaxies stop forming stars, becoming passive objects, and the role played by environment in this process. The work presented here includes the study of the properties of galaxies in clusters at two different stages of their evolution: we first look at cluster galaxies that have recently stopped forming stars, and then we investigate the influence of environment on galaxies while they are still forming stars.

The first study is based on Integral Field Spectroscopic (IFS) observations of a sample of disk 'k+a' galaxies in a cluster at $z \sim 0.3$. The 'k+a' spectral feature imply a recent suppression of star formation in the galaxies, and therefore the study of their properties is crucial to understanding how the suppression happened. We study the kinematics and spatial distributions of the different stellar populations inhabiting these galaxies. We found that the last stars that were formed (i.e., younger stars) are rotationally-supported and behave similar to the older stars. Moreover, the spatial distribution of the young stars also resembles that of the older stellar populations, although the young stars tend to be more concentrated towards the central regions of the galaxies. These findings indicate that the process responsible for the suppression of the star formation in the cluster disk galaxies had to be gentle, withouth perturbing significantly the old stellar disks. However, a significant number of galaxies with centrally-concentrated young populations were found to have close companions, therefore implying that galaxy-galaxy interactions might also contribute to the cessation of the star formation. These results provide very valuable information on the putative transformation of star-forming galaxies into passive S0s.

We then move to the study of the star formation properties and nuclear activity in galaxies in a multi-cluster system at $z \sim 0.165$. We employ Tuneable Filter observations to map the Hα and [NII] emission lines. We show the feasibility and advantages of using these type of observations to map emission lines in a large number of objects at a single redshift, and developed a procedure for the reduction and analysis of the data. We find a large number of optical AGN that were not previously detected as X-ray point sources. The probability that a galaxy hosts an AGN is not found to correlate with environment. From the analysis of the integrated star formation properties of the galaxies in the multi-cluster system we observe a significant number of galaxies with suppressed star formation with respect to the field. Although stellar mass is the main driver of the suppression of star formation, once its effect is removed, we find that galaxies in the core regions have reduced specific star formation rates (SSFRs) with respect to the infall regions. Moreover, the environment influences galaxies differently depending on their stellar mass. Galaxies with low masses experience a change in morphology (from irregulars and spirals to early-types) and colour (blue to red) as they fall into regions of higher density. However, many massive spiral galaxies retain their disk morphologies and the visibility of their spiral arms all the way to the core regions. Before becoming passive, these galaxies experience a phase exhibiting red colours and relatively high SSFRs. A significant fraction of the spiral galaxies with relatively high masses go through this phase, which could represent the transition towards becoming S0s.

We finish by presenting some interesting results on the spatial distribution of the emission-line regions in the cluster galaxies. We develop a method to create emission-line images, which successfully preserves the flux within the emission lines. Our analysis on the concentrations and sizes of the star-forming regions shows that the star-forming regions of cluster galaxies are generally more concentrated than the underlying stellar populations. However, we find no differences in the spatial distribution of the star formation between galaxies in the infall and in the core regions, but the star formation is more concentrated than in the field galaxies studied in previous works. These results imply that the process responsible for the concentration or truncation of the star formation in the galaxies took place before entering the multi-cluster system of our study.

Acknowledgements

The realization of this thesis has been possible thanks to the moral support and help of a large number of people, including my family, friends and colleagues. Without them, it would have been impossible to walk this path, and I am immensely grateful to them. Some people have directly contributed to the production of the thesis whereas others have been the best support I could have from outside. All of them have been essential.

I would like to express my deepest gratitude to Alfonso and Steven, for their constant support and guidance during these four years, especially in the more difficult moments. It has been a privilege. Thank you for your patience and sacrifice. Thanks to Alfonso for telling me 'don't despair!' when nothing was working, for always being positive and never let me leave the room with doubts. Thanks to Steven for the long discussions, despite that they started with a question and finished with five answers, and for his great help in my conversion to Python. Thanks to Marc for the useful discussions and supporting me throughout the progress of my thesis. To Meghan for all her great help with the STAGES data and to Tim for his last-minute contributions.

Many, many thanks to Aninha for appearing and together see the birth of OMEGA. With you I have discovered how much fun working in collaboration can be. Thanks for having so much energy and infecting it. It is indeed a pleasure to be next to you in the spectra of our galaxies.

During these four years, (almost) every day I have been willing to arrive to the office, even if it was only for the 11ish coffee, and that is because of the great friends and colleagues I have shared it with. I have to start with Fernando: thanks for making me feel at home from the very first day and for being such a great person. Thanks to Ismael, for the never-ending sessions of jokes and laughter that gave us a break in our thesis

writing, for your help from the beginning until the last day, and for the biscuits. To Evelyn for sharing so many moments and suffer together our friend ‘pepe’, to Dimitri for the great conversations and to Daniele for the good basketball and coffee times. Thanks to Mattia for his help understanding Bayes, to Berta for constantly coming to ‘disturb’ (don’t you ever stop doing that!), to Lyndsay for never being stressed and Ranga for working too hard and staying with us over the weekend at the office. I would also like to thank Will for being the master of the office and for his help during the first months. Thanks to Carlos, Ana Avilez, Ari, Ruth, Kevin, Cristina, Boris, Migue and the rest of staff and colleagues for creating such a good environment in the department, which has definitely been the best place to carry out my PhD. Finally, I would like to thank the Instituto de Astrofísica de Canarias, the Royal Astronomical Society and the University of Nottingham HPC facility “Minerva”.

Thanks a lot to all the people in Nottingham who has made these four years an unforgettable time of my life. Especially to Jole for being such a good friend and crazy person, to the amazing people from the Postgraduate New Theatre and the University’s basketball teams. Thanks to all the friends that came to visit and to those that could not come but have been with me in the distance these years.

I leave for last the people who, no matter when and where, have always been with me: my family. Thanks to all of you for always being such a happy thought in my mind and for all your support. Without you I could not have made it. Among many other reasons, thanks to Carlos for giving the most important step with me, to Javier for suddenly showing up with Anita, and to my parents, Jose Antonio y Mercedes for always being so helpful, even from the other side of the screen, and for sending us food! Thanks also to Ángeles’s family for being so supportive and understanding.

My deepest thanks go to Ángeles, for always encouraging me and never let me give up. Thank you for your laughter, happiness and your tireless support.

Declaration and published work

I declare the work contained in this thesis is mine unless explicitly stated otherwise.

Part of the material that appears in this thesis has been presented in a series of published manuscripts and conference proceedings. The remaining work will soon be written in the form of two more papers that will be submitted for publication.

The results presented in Chapter 2 have been published in:
Rodríguez Del Pino, B.; Bamford, S. P.; Aragón-Salamanca, A.; Milvang-Jensen, B.; Merrifield, M. R.; Balcells, M. '*Caught in the act: Cluster 'k+a' galaxies as a link between Spiral and S0s*', 2014, MNRAS, 438,1038.

The work presented in Chapter 3 and Chapter 4 have been done in collaboration with Ana Chies-Santos. I have been involved in most of the data analysis, with the exception of the steps of the data reduction performed using the software OOPs. These chapters are an extension of the work presented in:

Chies-Santos, A. L.; **Rodríguez Del Pino, B.**; Aragón-Salamanca, A.; Bamford, S. P.; Gray, M. E.; Wolf, C.; Böhm, A.; Maltby, D. T., Pintos-Castro, I.; Sánchez-Portal, M.; Weinzirl, T. '*OMEGA: OSIRIS Mapping of Emission-line Galaxies in A901/2. I: Introduction, data analysis and AGN/SF census in the highest density regions*', 2015, Accepted for publication in MNRAS.
Rodríguez Del Pino, B.; Chies-Santos, A. L.; Aragón-Salamanca, A.; Bamford, S. P.; Gray, M. E. '*OMEGA: OSIRIS Mapping of Emission-line Galaxies in A901/2*', 'Galaxies in 3D across the Universe, Proceedings of the International Astronomical Union, IAU Symposium, Volume 309'.
Chies-Santos, A. L.; **Rodríguez Del Pino, B.**; Aragón-Salamanca, A.; Bamford, S. P.; Gray, M. E. '*Emission line imaging survey of the Abell 901/902 supercluster*', 'XIV

Latin American Regional IAU Meeting', Revista Mexicana de Astronomí y Astrofísica (Serie de Conferencias), Vol.44

The results on the integrated properties of galaxies in the OMEGA survey presented in Chapter 4 will be contained in

Rodríguez Del Pino, B.; Chies-Santos, A. L.; Aragón-Salamanca, A.; Bamford, S. P.; Gray, M. E.; et al. *OMEGA: OSIRIS Mapping of Emission-line Galaxies in A901/2. II: Integrated AGN and SF properties across the multi-cluster system A901/2*', 2015, in preparation.

Chapter 5 is still work in progress and the results will be presented in

Rodríguez Del Pino, B.; Chies-Santos, A. L.; Aragón-Salamanca, A.; Bamford, S. P.; Gray, M. E.; et al. *OMEGA: OSIRIS Mapping of Emission-line Galaxies in A901/2. III: Spatially-resolved star formation in the multi-cluster system A901/2*', 2015, in preparation.

Contents

List of Figures

List of Tables

The influence of environment on the star formation properties of galaxies

Chapter 1

Introduction

Many of us, probably all, have once raised our heads and looked at the sky, and wondered about what is hidden behind the dark canopy of blinking points that covers us at night. The inherent human curiosity has driven us to go beyond any established ideas and contemplate the understanding of the Universe as a whole.

The sky has always been a matter of interest for human beings. Records of the earliest observations can be seen in architectonic monuments such as Stonehenge or the Egyptian Pyramids, which were very likely related to the position of the Sun and other stars in the sky. Ancient civilizations such as the Babylonians, Chinese, Egyptians, and many others, left written records of their observations of the cycles of the Sun, the Moon, stars and planets. However, far from being scientific, it was believed that the astronomical events were related to the gods and the heavens, although the observations also allowed people to make accurate predictions on the seasons by identifying the positions of the objects in the sky.

This divine vision of the sky was first defied by the Greeks, namely by Aristotle who, contrary to his master Plato's mystical view of the Universe, thought of the Universe as something that could be understood. The first Greek philosopher and scientist considered as such was Thales of Miletus, who used the astronomical records left by the Babylonians for the first time with a scientific purpose. The Greeks were therefore the first ones to consider the possibility of understanding the world surrounding them and the first ones to produce theories to explain the observations. Many years later, a

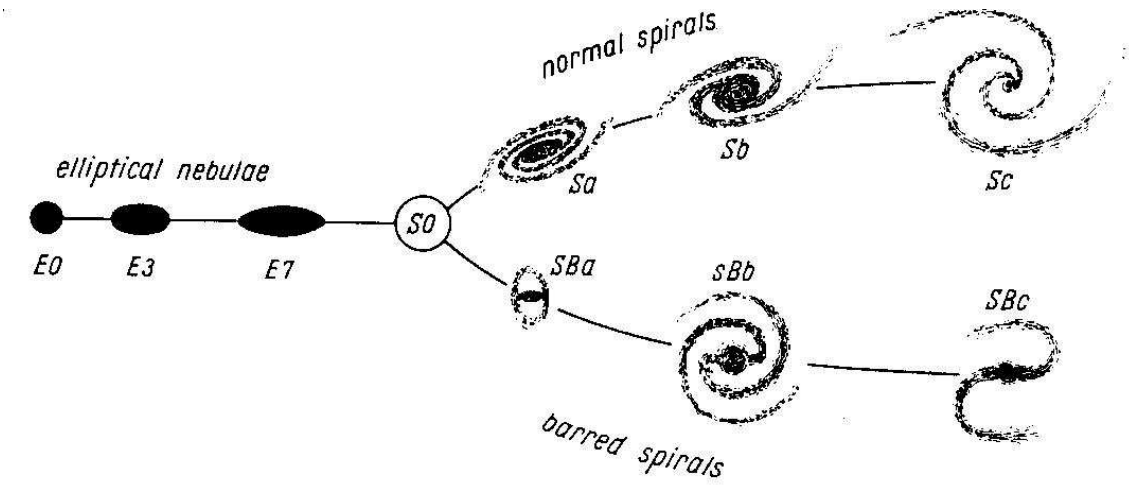

Figure 1.1: Morphological classification of galaxies by Hubble, (1936)

crucial benchmark in the development of Astronomy was the advent of the telescope and its first use to look at the sky by Galileo Galilei in 1609. His observations dismantled the long-established geocentric vision of the Universe in favour of an heliocentric one which placed the Sun at the center. On the other hand, a century earlier, Giordano Bruno already suggested the idea that some of the objects in the sky were not rotating around the Sun, and were actually stars which probably also had planets rotating around them. The idea of the existence of other systems was expanded with the observation of extended objects in the sky that were called 'nebulae' because of their smooth and 'fuzzy' appearance, although they were thought to be non-resolved stellar systems residing in our galaxy. It was not until 1926 when Edwin Hubble, using the 100-inch telescope at Mount Wilson, measured the distances to those nebulae and found out that they were much further than the Milky Way and therefore they had to be extragalactic objects. He performed these measurements by looking at Cepheid stars, a type of variable star with a tight relation between their luminosity and their variability, as found by Henrietta Leavitt in 1912.

Besides probing the extra-galactic origin of the nebulae, the unprecedented detail of the observations allowed Hubble to establish the first classification of galaxies based on their morphologies. This classification scheme, known as the Hubble Tuning Fork, is shown in figure 1.1. Galaxies were split into ellipticals, with ellipsoidal shape and little inner structure, and spirals, further divided into two parallel sequences according to the presence of a bar, which were characterized by a disk with outstanding spiral

arms. Elliptical galaxies were sorted by ellipticity, from high (E7) to low (E0), whereas spirals were sorted by the significance of the inner component or bulge and the opening up of their arms. Another morphological type are the lenticulars or S0 galaxies, which in the Hubble diagram are found between ellipticals and spirals because they have a prominent bulge and still retain a disk.

Initially, this diagram was not thought as an evolutionary sequence but a morphological one, in which galaxies were sorted from low to high complexity. In this way, Hubble referred to ellipticals and lenticulars as 'early-type' objects, due to their low complexity structure, and to spirals as 'late-type' objects, with much more complex appearance. Although the terms early and late have anything but a temporal meaning, due to the relevance of the study carried out by Hubble, the terms 'early' and 'late' type are still widely used.

Another crucial discovery made at the beginning of the 20th century was that galaxies have radial velocities with respect to us. These velocities were estimated by Vesto Slipher in 1914 by measuring the shift of the spectral lines or redshift, produced by the Doppler effect. A few years later, when Hubble measured the distances to those objects, they were combined to the velocities by Hubble and Humason in 1929 to find something that would revolutionize established ideas: the Universe was expanding! Recent work has shown that the expansion of the Universe is actually accelerating (Perlmutter *et al.*, 1999; Schmidt *et al.*, 1998; Riess *et al.*, 1998) which is explained by the presence of an still unknown component called Dark Energy or Λ.

1.1 Formation of the first structures

Our current view of the Universe is based on the Big Bang model. This model establishes that 13.8 Gyr ago the Universe was in a very hot and dense state, when its expansion began. After the Big Bang, the temperature was so high that all the matter was ionized. Eventually, the Universe cooled down enough to allow recombination of electrons into atoms. When recombination was complete, the photons ceased to scatter and they propagated freely through the Universe. It is only from that moment, 380,000 years after the Big Bang, when we are able to get information (radiation)

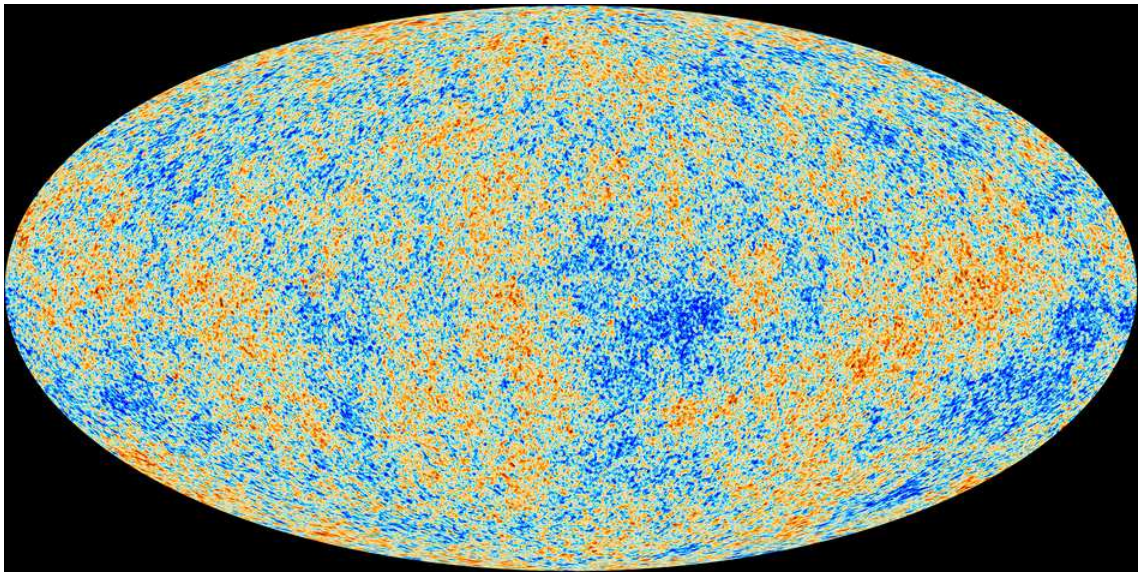

Figure 1.2: Cosmic Microwave Background as seen by Planck. It shows the fluctuations in the temperature between regions with different densities. Credits: ESA and the Planck Collaboration.

from the Universe, as these were the first photons that were not absorbed by atoms. This first radiation can be seen in the Cosmic Microwave Background (CMB), a relic of a sudden explosion of the Universe from its initial state, which was first observed by Penzias and Wilson in 1962 and is one of the greatest successes of the Big Bang model. From the CMB data we know that the Universe was very homogeneous at the beginning. However, the tiny fluctuations in temperature corresponding to regions of different density gave rise to the formation of the first structures in the Universe.

At this time, the growth of structure was dominated by dark matter, an invisible component of the Universe that seems to interact only gravitationally and therefore does not emit electromagnetic radiation. The existence of this invisible component was first introduced by Zwicky (1933), and it was used to explain the rotation curves of spiral galaxies by Rubin, Ford & Thonnard (1980), although it has also been used to explain many other astrophysical observations. The current model assumes a non-relativistic, Cold Dark Matter (CDM), that was introduced by Peebles (1982) to explain the observed large-scale structure of the Universe.

Structural growth then proceeded hierarchically: small clumps of dark matter gathered together assembling into larger ones. These big clumps or 'halos' also attracted baryonic matter (neutrons and protons), mainly in form of Hydrogen and Helium. Large clouds of this molecular gas started to cool down, eventually segregating in smaller

structures which would form the first stars. The radiation from these stars was the first produced after that of the CMB and, together with other sources such as nuclear activity in galaxies and decaying particles, was responsible for the reionization of the neutral gas (Fan, Carilli & Keating, 2006). The first galaxies were then formed from the stars and gas assembled by the haloes.

1.2 Evolution of galaxies

Following their formation, galaxies experience several internal and external processes that shape their evolution. As a consequence, the properties of galaxies change through cosmic time and therefore high-redshift galaxies are likely to be different from the ones found in the local Universe. Globally, galaxies at redshift between 1.5 and 2.5 have much higher star formation rates than local ones (Madau *et al.*, 1996; Bouwens *et al.*, 2007), due to the large availability of gas to form new stars which decreases with redshift (Papovich *et al.*, 2011). As a consequence of the higher accretion rates and the occurrence of mergers (Ownsworth *et al.*, 2014), galaxies also experience an increase in size, at least the most massive ones (Buitrago *et al.*, 2008; van Dokkum *et al.*, 2010).

1.2.1 Drivers of galaxy evolution

Besides the global dwindling of the star formation rate, there are two main agents that can quench star formation in galaxies: environment and galaxy mass. Galaxies are not randomly distributed in space, in fact the majority of them are part of groups and clusters, and a small fraction live in isolation. This variety of environments seems to shape the evolution of galaxies, affecting galaxy properties such as morphology, colour, size and mass.

The relation between galaxy morphology and environment has been known for decades, (Morgan, 1961; Abell, 1965; Dressler, 1980). As it can be seen in Figure 1.3, the morphological fractions change as a function of projected density: the spiral fraction, associated with rotationally-supported systems, dominates the low-density field but its presence decreases dramatically towards high-density regions, which are mostly

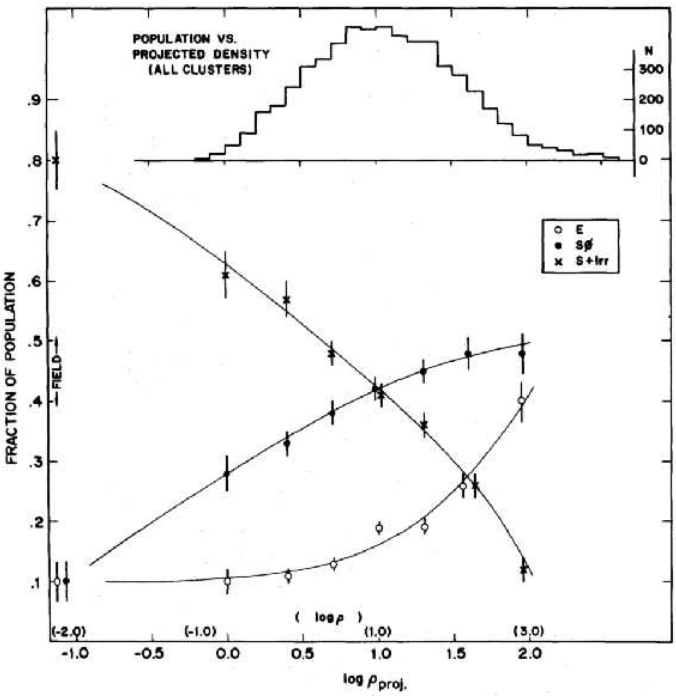

Figure 1.3: Morphology-density relation from Dressler (1980).

populated by pressure-supported ellipticals and S0s. However, a new version of the morphology-density relation has been recently proposed by Cappellari *et al.* (2011) as part of the ATLAS (3D) project, which is shown in Figure 1.4. Instead of only looking at the morphology of the galaxies, they also consider the stellar kinematics, splitting them into fast and slow rotators. They find that less than half of the galaxies morphologically classified as ellipticals are actual slow rotators, which is a population that only appears in the very dense regions. Although this relation is well established in the local Universe, the fraction of the different morphological types populating galaxy clusters has changed since redshift $z \sim 0.5$: while the fraction of ellipticals has remained roughly constant, the fraction of spirals has decreased towards redshift $z \sim 0$, and the S0 fraction has increased, being two to three times more abundant today than at $z \sim 0.5$ (Dressler *et al.*, 1997; Fasano *et al.*, 2000; Desai *et al.*, 2007).

These findings point to a possible transformation of spiral galaxies into S0s, which is supported by many studies (e.g., Larson, Tinsley & Caldwell, 1980; Bekki, Couch & Shioya, 2002; Shioya *et al.*, 2002; Aragón-Salamanca, Bedregal & Merrifield, 2006). On one hand, spiral galaxies are mainly characterized by the presence of a star-forming disk with prominent spiral arms and a central bulge. On the other hand, S0 galaxies also retain a disk, although hotter (Cortesi *et al.*, 2013), no or very little star formation and

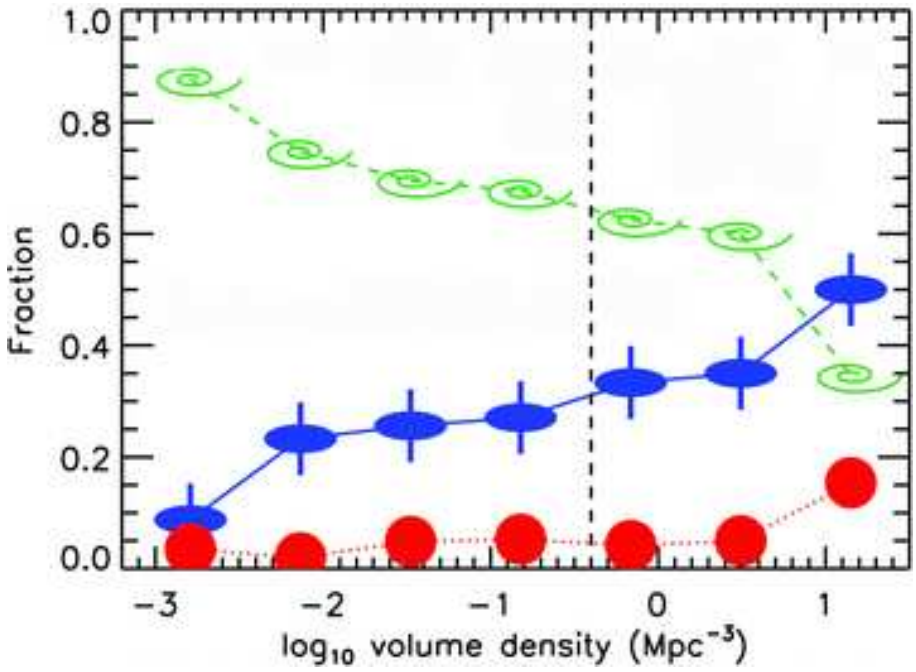

Figure 1.4: Morphology-density relation for fast rotators (blue ellipses), slow rotators (red circles) and spiral galaxies (green spirals) from Cappellari *et al.* (2011).

are more bulge dominated (Christlein & Zabludoff, 2004). Within this picture, blue, star-forming spiral galaxies at intermediate redshift $z \sim 0.5$ start falling into high-density regions such as groups and clusters, where they experience an environmental quenching of their star formation, which cannot strongly affect their structure since they retain their discs. Ultimately, they become the red, passive, S0 population that dominates the clusters at low redshift.

Environment also plays a role in the quenching of the star formation in galaxies. In the local Universe, star-formation activity is strongly related with environment: the fraction of star forming galaxies (Best, 2004; Balogh *et al.*, 2004a) and the star formation rates (Gómez *et al.*, 2003; Kauffmann *et al.*, 2004) decrease with local galaxy density. At higher redshifts ($z = 0.4 - 0.8$), Poggianti *et al.* (2008) found that the fraction of star-forming galaxies also decreases with density, whereas the current star formation activity in star-forming galaxies does not change continuously with environment. This change in the SFR-density relation might be connected with a possible reversal at higher redshift ($z \sim 1$), at least from field to groups (Sobral *et al.*, 2011). The fraction of star-forming, blue galaxies in clusters has also been shown to increase with redshift (Butcher & Oemler, 1978, 1984; Margoniner *et al.*, 2001), known as the

Butcher-Oemler effect, and these galaxies have been found to comprise mostly normal late-type spirals (Couch *et al.*, 1994; Dressler *et al.*, 1994). When galaxies stop forming stars they become redder as their stellar populations age, and therefore environment also correlates with galaxy colours (Blanton *et al.*, 2005; Bamford *et al.*, 2009).

Together with environment, the other main driver of galaxy evolution is galaxy mass. Galaxies with different stellar masses have different properties and also reside in different environments (Kauffmann *et al.*, 2004; Bamford *et al.*, 2009). The most massive ones are generally red and passive, with early-type morphologies (ellipticals and S0s), and tend to live in the highest-density regions; low-mass galaxies are generally blue, star-forming, late-type galaxies and reside in low-density environments. Galaxy mass seems to impose a threshold above which star formation is halted (Bundy *et al.*, 2006) and it also affects the rate at which galaxies form stars, producing what is known as *downsizing*: more massive galaxies stop forming stars first and therefore become passive earlier than low mass ones (Bell *et al.*, 2005; Bundy, Ellis & Conselice, 2005). At high halo masses, the star-formation quenching can also be produced by the establishment of a virialized hot halo (e.g., Rees & Ostriker 1977), implying long cooling times. Core cooling is further prevented by feedback from supernovae and active galactic nuclei (AGN; Booth & Schaye 2009, Newton & Kay 2013). In fact, the probability of a galaxy to host an AGN seems to be related with environment: while low-luminosity AGN do not show particular preference for any kind of environment (Martini *et al.* 2002, Miller *et al.* 2003, Martini *et al.* 2006), luminous AGN are preferentially found in the field (Kauffmann *et al.* 2004) and groups (Popesso & Biviano 2006) rather than in clusters.

There is ongoing debate about the relative role played by environment and galaxy mass in shaping galaxy evolution, the 'nature' versus 'nurture' paradigm, i.e., whether galaxies are more influenced by intrinsic properties such as their mass ('nature') or by the environment where they reside ('nurture'). However, it seems that both are important drivers of the quenching process, and their effects can be separated up to z $\sim$ 1 (Peng *et al.*, 2010). A summary of the effects of mass and environment in the quenching of star formation can be seen in Figure 1.5.

As a consequence of the mass and environmental quenching of the star formation,

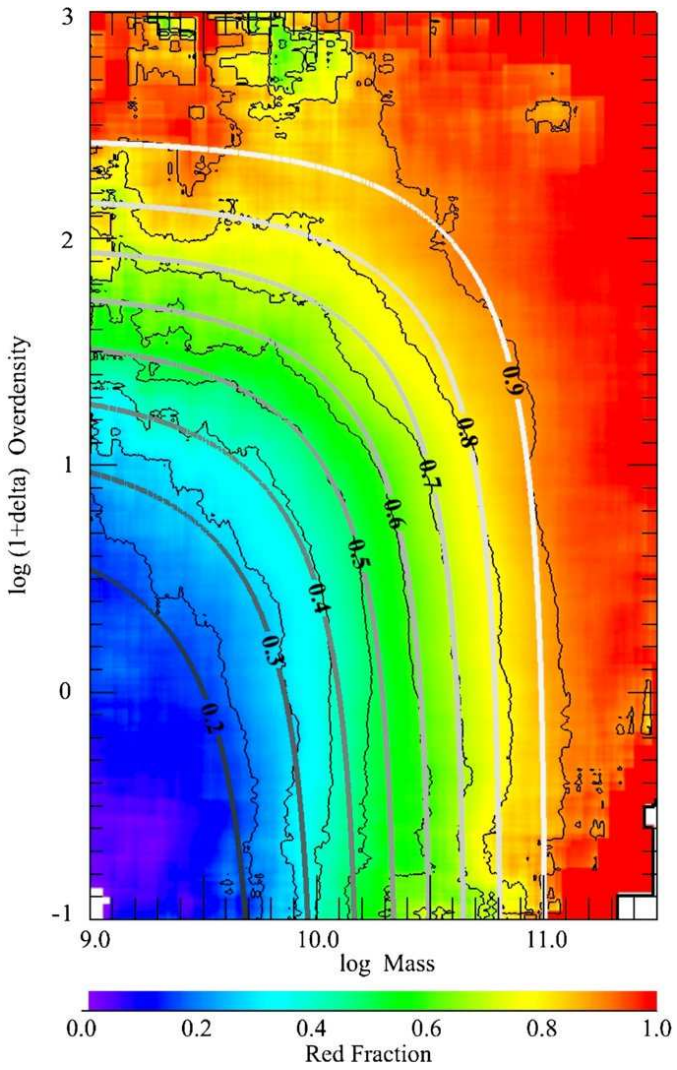

Figure 1.5: Separation of the effects of environment and stellar mass on the fraction of red galaxies from Peng *et al.* (2010). The grey lines show the fraction of red galaxies as a function of density and mass. The effects of environment are isolated at fixed stellar mass, and vice versa.

galaxies start to migrate from the blue cloud on to the red sequence of the colour-magnitude diagram (Strateva *et al.*, 2001). The red sequence, however, is not only populated by passive objects, but also by late-type galaxies with low star formation rates where the star-forming regions are enshrouded by dust and therefore have red colours (van den Bergh, 1976; Bamford *et al.*, 2009; Wolf *et al.*, 2009). The low number of galaxies found in the green valley (region in between the blue cloud and the red sequence) implies that the transition from blue to red has to be quite rapid. This idea is supported by the substantial change in the fractions of blue (star-forming) and red (passive) galaxies as a function of environment, whereas the colours and Hα equivalent widths of the star-forming fraction remain invariant (Balogh *et al.*, 2004a,b;

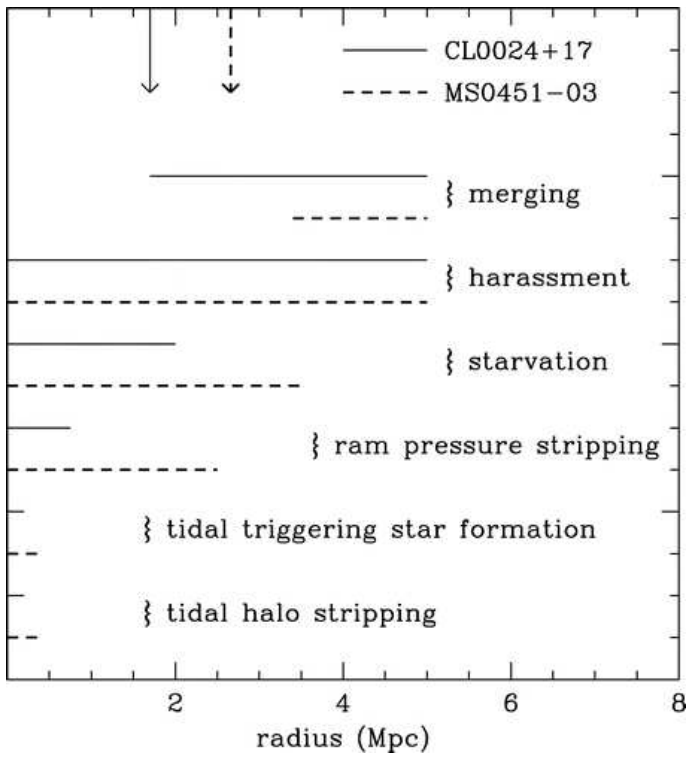

Figure 1.6: Schematic diagram showing the the radial range of action of the different environmental processes than can affect the star formation in galaxies. Solid and dashed lines correspond to the two clusters studied by Moran *et al.* (2007).

Bamford *et al.*, 2008). The morphological transition, on the other hand, requires longer timescales, as there are galaxies with late-type morphologies that show red colours (Kodama *et al.*, 2004; Lane *et al.*, 2007).

1.3 Environmental processes

The enviromental effects on galaxies causing the quenching of the star formation can be driven by a wide range of mechanisms, which have different ranges of action, act on different time-scales, and leave different imprints on the galaxies. A schematic view of the radial range of action of the different processes explained in this section can be seen in Figure 1.6. Their influence can affect both the stellar component and the gas in the galaxies. Regarding the gas, the process can either sweep it away preventing further star formation in the galaxy or compress it, triggering new episodes of star formation. Here I describe the main environmental processes that can play a significant role in the evolution of galaxies.

1.3.1 Gravitational interactions

Galaxies in the Universe are under the influence of the gravitational fields of other galaxies and larger structures such as groups and clusters. As a result, galaxies undergo gravitational interactions that can provoke dramatic disturbances in their stellar distributions (Toomre & Toomre, 1972; Hopkins *et al.*, 2009). These gravitational encounters can also produce perturbations that alter the distribution of the gas in galaxies, inducing changes in their star formation properties (Noguchi & Ishibashi, 1986; Casteels *et al.*, 2013). Here we summarize the gravitational interactions that galaxies may experience.

Tidal encounters: During slow encounters the gas from the galaxies can be stripped, which in the case of spirals would favour the formation of S0s especially for high surface brightness objects (Moore *et al.*, 1999). However these encounters are less likely to happen in the cluster environment where the relative speed between galaxies is large. If the encounters are close and at higher velocity the stellar disk can also be distorted (Icke, 1985).

Harassment: As a consequence of many fast and brief interactions with other galaxies, small ones can be seriously disrupted and star-forming disks truncated (Moore *et al.*, 1996; Moore, Lake & Katz, 1998). Galaxy harassment has also been considered as a candidate process to form S0s (Wilman *et al.*, 2009).

Mergers: These are strong interactions between galaxies with low relative speeds eventually becoming one single object. As they are more likely to happen at low velocities they are more frequently observed in low-density environments. Depending on the mass ratio between the merging galaxies they can be minor or major. On one hand, minor mergers take place between a large and a small galaxy, and they would not produce strong perturbations on the galaxy and therefore can explain the formation of S0s from spirals (Bekki, 1998; Eliche-Moral *et al.*, 2012, 2013). On the other hand, major mergers are strong encounters between galaxies with similar masses, which can end with the formation of an elliptical galaxy (Toomre, 1977; Naab, Burkert & Hernquist, 1999).

1.3.2 Gas-dynamical effects

When galaxies fall into clusters, they feel the gravitational field of the cluster and interact with the hot intra-cluster medium (ICM) which can affect the gas and therefore the star formation in the galaxies.

Ram pressure stripping: When galaxies orbit around clusters, their interstellar medium (ISM) can interact with the hot ICM, which can sweep out the cold gas of the galaxy, keeping the stars unaffected. This process, known as ram-pressure stripping (Gunn & Gott, 1972; Quilis, Moore & Bower, 2000; Bekki, Couch & Shioya, 2002) has been extensively studied to understand the removal of the gas in galaxies as they fall into denser regions and the transformation from spiral into S0s. The amount of gas affected depends on the pressure of the ICM and the relative velocity of the galaxy with respect to the ICM. Therefore, ram-pressure stripping will be stronger in the central parts of clusters and at higher densities, where the velocities and pressures are higher. Apart from the removal of the cold gas, it has been found that compression of the gas can also trigger new episodes of star formation (Kapferer *et al.*, 2009; Bekki, 2009).

Starvation: The gas reservoir in the halos of galaxies can be removed by the interaction with the ICM therefore preventing further replenishment of gas and therefore any future star formation (Larson, Tinsley & Caldwell, 1980). Spiral galaxies will stop the star formation in their disks and will turn into S0s.

Turbulent and viscous stripping: Viscosity between cold and hot gas in the intracluster medium can cause a drag that will remove the gas (Nulsen, 1982).

Tidal stretching: Tidal interactions with the ICM can also lead to perturbations on disk gas clouds, producing both removal of the gas and enhancement of the star formation (Byrd & Valtonen, 1990; Henriksen & Byrd, 1996)

Thermal evaporation: Massive galaxies can confine hot gas heated by supernovae which can evaporate the cold gas by a combination of thermal conduction and ablation (Nipoti & Binney, 2007).

1.4 Spectral signatures of galaxy evolution

Crucial information about the transformation of galaxies from actively star-forming to passive (and therefore from spiral to S0) can be obtained by looking at spectral features. In a galaxy with ongoing star formation, the gas surrounding the star-forming regions, mainly molecular hydrogen or H_2, is ionised by the radiation coming from young, massive stars, resulting in the formation of regions of ionised atomic hydrogen or H II regions. The recombination of this gas produces the emission of photons that are seen as emission lines in the spectrum of the galaxy. Emission lines due to star formation appear at different wavelengths, although of particular interest for this thesis are the hydrogen Balmer series lines, produced when an electron transitions to the energy level n = 2. The Balmer line that is generally used to trace star formation is $\mathrm{H}\alpha$ at λ = 6563Å which is one of the strongest emission lines in the optical, UV and IR. $\mathrm{H}\alpha$ emission traces star formation on time-scales of 6–8 Myr, coming from stars more massive than $\sim$ 20 $M_\odot$, although it is sensitive to uncertainties in the Initial Mass Function. The SFRs of galaxies can be estimated from the luminosity of $\mathrm{H}\alpha$, which is related to the ionising photon rate (Kennicutt, 1998). Due to its strength and availability in the optical range, the $\mathrm{H}\alpha$ emission has been one of the most widely used optical star formation indicators for decades.

1.4.1 'k+a' galaxies

In the same way as the presence of emission lines in the spectra of a galaxy implies ongoing star formation, their absence indicates that star formation is either absent or obscured, in which case the radiation is re-emitted in the IR by the absorbing dust. The spectra of galaxies without ongoing star formation are characterised by the presence of absorption lines coming from the different stellar populations hosted by the galaxies. Therefore, the transition from active to passive implies a significant change in the spectral properties that can be used to identify galaxies undergoing such transformation.

When galaxies stop forming stars, their light is dominated by young stellar type objects, mainly O and B stars. However the spectra of these stars lack strong absorption lines as they have a very powerful continuum, and therefore it is very difficult to detect

them. However, once the O and B stars die, after ~ 0.5 Gyr, A stars will dominate the light of the galaxy, and in this case, they show absorption in the Hydrogen Balmer lines, especially in Hδ at λ = 4101Å. This absorption line is not very strong if the quenching of the star formation is gradual. However, if there is an abrupt truncation or if this is preceded by a burst of star formation, the Hδ absorption feature becomes stronger, particularly 0.1 - 1 Gyr after the last episode of star formation, since the peak on the Hδ absorption occurs after ~ 0.5Gyr (Kauffmann *et al.*, 2003b; Poggianti, 2004). The spectrum of a galaxy in this phase is thus a combination of strong Balmer absorption lines, characteristic of the A stars, superimposed on to a spectrum of an older (several Gyr) stellar population with no emission lines (indicating no ongoing star formation). These galaxies are generally called 'k+a' (as they are dominated by old 'k' and young 'a' stellar types) or 'E+A' (indicating that their spectra is the typical of an early-type galaxy 'E' with additional 'A' stars).

This type of galaxy was found for the first time by Dressler & Gunn (1983), and due to their importance as observable instances of rapid evolution, they have been the subject of many studies (Dressler & Gunn, 1983; Zabludoff *et al.*, 1996; Norton *et al.*, 2001; Pracy *et al.*, 2009; Poggianti *et al.*, 2009; Pracy *et al.*, 2012, 2013). Although first discovered in the cluster environment (Dressler & Gunn, 1983), they have also been found in the field (Zabludoff *et al.*, 1996; Blake *et al.*, 2004) and in groups (Poggianti *et al.*, 2009). Relatively few 'k+a' galaxies are found in the local universe, but their prevalence increases significantly with redshift, such that in intermediate-redshift clusters they can represent up to 10 per cent of the total galaxy population (Poggianti *et al.*, 2009). In those intermediate-redshift clusters, 'k+a' galaxies tend to avoid the central regions, implying that the suppression of star formation does not require the extreme conditions of cluster cores, and may begin in less dense environments such as groups (Dressler *et al.*, 1999). While 'k+a' galaxies in general often show early-type morphologies (sometimes disturbed; Yang *et al.* 2008), in clusters they are generally associated with disk-like systems (Caldwell, Rose & Dendy, 1999; Tran *et al.*, 2003), and in many cases they also show spiral signatures, implying that the time-scale for the spectral evolution is shorter than that for any morphological transformation (Poggianti *et al.*, 1999).

1.5 Thesis outline

The motivation for the work carried out in this thesis is to achieve a better understanding of the transformation of galaxies from actively star-forming to passive as a function of environment. We look at the process of star formation quenching before and after it takes place and generate a general picture of the process of galaxy evolution in high-density environments.

In chapter 2 we look at galaxies that have quenched their star formation recently and investigate the processes that led to this suppression. We do this by studying a sample of 'k+a' galaxies in a cluster at $z \sim 0.31$ using Integral Field Spectroscopic (IFS) observations. From the spatial and spectral analysis we obtain estimates of the distribution of the young populations and their kinematic properties. From the results of the analysis we discuss the main processes acting on the transformation of galaxies in the cluster environment.

In chapter 3 we introduce the OSIRIS Mapping of Emission-line Galaxies in the A901/2 cluster survey (OMEGA), aimed at obtaining SFRs of a large number of galaxies in a cluster using Hα as a star formation indicator. In this chapter we explain its design, the procedure adopted for the reduction of the data and we explore the detection limits of our observations and the completeness of our sample. The results from the integrated analysis are presented in chapter 4, which include the study of the star formation and AGN activity as a function of mass, environment and SED type. Chapter 5 is devoted to the spatial analysis of the star-forming regions, where we present some of the first results. We conclude with a summary of the work presented in this thesis.

Throughout this thesis we adopt a cosmology of $H_0 = 70\ \mathrm{km\,s^{-1}\,Mpc^{-1}}$, $\Omega_\mathrm{m} = 0.3$ and $\Omega_\Lambda = 0.7$.

Chapter 2

Cluster 'k+a' galaxies as a link between spirals and S0s in clusters

2.1 Introduction

In this chapter we study the properties of a sample of cluster 'k+a' galaxies. From our analysis we evaluate the possibility that these objects are the link in the transformation of spirals into S0s in clusters. We also identify the candidate mechanisms that are responsible for such transformation and explore the influence they have on galaxies in high-density environments.

As explained in Section 1.4.1, 'k+a' galaxies host both young and old stellar populations as a consequence of a recent truncation of the star formation in the galaxy. Analysing the internal spatial distributions, and ideally kinematics, of these stellar populations is crucial to understanding the mechanisms responsible for the suppression of star formation. Galaxy-galaxy interactions such as tidal encounters and minor mergers will lead to the formation of stellar bars that drive gas into the central regions, (Mihos & Hernquist 1994; Bekki *et al.* 2005, and the discussion in Section 2.4 in this chapter), and therefore the young population must be found in the central regions, where the last episode of star formation took place. In contrast, a more extended young population could imply depletion of a galaxy's gas reservoir through interaction with the hot ICM (Rose *et al.*, 2001; Bekki *et al.*, 2005; Bekki, 2009).

To perform such an analysis, we have used Integral Field Spectroscopy (IFS), obtained with the FLAMES-GIRAFFE multi-object spectrograph at the VLT (Pasquini *et al.*, 2002), to analyse 13 galaxies with disk morphologies and strong $\mathrm{H}\delta$ absorption in the cluster AC114 (also known as Abell S1077; Abell, Corwin & Olowin 1989) at $z \sim 0.3$. AC114 has been shown to contain a significant population of blue star-forming galaxies by Couch & Sharples (1987, hereafter CS87), but also to have a substantial general suppression of the star formation (as inferred from $\mathrm{H}\alpha$ emission; Couch *et al.* 2001), which makes it an ideal laboratory for studying how cluster galaxies are transformed. A previous study of 'k+a' galaxies in this cluster has been carried out by Pracy *et al.* (2005, hereafter P05). They obtained observations using FLAMES with a very similar configuration, although they did not focus specifically on galaxies with disk morphology. We were not aware that their observations existed when ours were scheduled, but such repeated observations enable us to check the reproducibility of our measurements. Combining the P05 dataset with our own also adds some additional galaxies to the sample we consider in this work. In their study, P05 only consider the spatial distribution of the $\mathrm{H}\delta$ equivalent width. We expand on this, measuring the stellar populations in more detail and considering the resolved galaxy kinematics.

2.2 Data

2.2.1 Sample

The current sample consists of 13 galaxies, observed and identified by CS87 as members of the cluster AC114 at $z \sim 0.31$. The CS87 catalogue provides redshifts and spectral line measurements, as measured on 8 hour integrations with the 3.9 m AAT, using a spectrograph with a spectral resolution $R \sim 1400$ and fed by $2.6''$ diameter fibres. AC114 also has wide-field archive *HST* WFPC2 imaging, which is used to catalogue the morphological make-up of AC114 in Couch *et al.* (1998, hereafter C98). Based on the combined CS87/C98 catalogue, the sample galaxies were selected to have disk morphology, magnitude $R_{\mathrm{F}} \leq 20.5$ and $\mathrm{H}\delta$ rest-frame equivalent width $W_{\mathrm{H}\delta} > 3$Å (the sign convention here is that a positive $W_{\mathrm{H}\delta}$ means absorption), which is the common criterion to be considered 'k+a' (Poggianti *et al.*, 1999). Some further

sample limitations were imposed by the spectrograph's field-of-view and restrictions on the placement of each integral field unit (IFU) in order to avoid button collisions and crossed fibres.

Nine of the objects selected to be observed show no [OII]$\lambda 3727$ emission in the CS87 catalogue, and hence correspond to a true 'k+a' selection. The remaining four show some [OII]$\lambda 3727$ emission, indicating that they have ongoing star formation, though possibly declining given their $W_{\mathrm{H}\delta}$, or host an AGN.

In addition to these galaxies, we include in our analysis the objects observed by P05. This sample was selected from the same cluster in a similar manner to that described above, except that no restriction was placed on morphology and none of their galaxies had detected [OII]$\lambda 3727$ emission. Six galaxies from our selection were also observed by P05, as well as two additional disk galaxies, four ellipticals and one peculiar galaxy. The combined sample therefore comprises twenty galaxies, of which fifteen possess disk morphology.

Note that, for galaxy CN849, the flux present in our observations was very low. This was found to be due to an incorrect target position. Fortunately, this galaxy was also included in the P05 data sample and could be analysed using that data. Also, when comparing the redshifts measured for the galaxies observed by both P05 and ourselves we discovered an inconsistency for CN254. Inspecting the coordinates we discovered that the galaxy labelled CN254 in P05 is actually CN229, another disk galaxy at $z = 0.319$. The cross-comparison sub-sample with multiple observations therefore comprises four objects.

In Table 2.1 we list all of the objects considered in this work, with their coordinates, morphologies, colour ($B_J - R_F$, corrected for Galactic reddening) and projected distance to the cluster centre.

2.2.2 Observations

The observations were obtained at the VLT-UT2 using the Fibre Large Array Multi Element Spectrograph (FLAMES) in GIRAFFE mode at a resolution of R $\sim$ 9600. With this setup, 15 individual IFUs were deployed over the whole field of view, with

two of them being dedicated to the sky to ensure a reliable sky subtraction. Each IFU consists of 20 square microlenses of 0.52 arcsec on a side, making up a surface of 3×2 arcsec^2 per IFU, which corresponds to $\sim 14.0 \times 9.3$ kpc^2 at the distance of AC114 ($\sim 2.3 \times 2.3$ kpc^2 per spaxel).

The total exposure time was ~ 13 hours, distributed in 14 exposures in different nights of June, August and December of 2004. Observations were taken with seeing conditions within the requested service mode constraint (≤ 0.8 arcsec), and DIMM seeing ranged from 0.49 to 1.06 arcsec. The observed wavelength range was 5015–5831Å, which at a redshift of $z \sim 0.3$ corresponds to 3850–4394Å in the rest frame, covering the K and H calcium features (3934Å and 3969Å), the Balmer lines Hδ (4102Å) and Hγ (4341Å) and the G-band (4305Å). At that wavelength range, the instrumental resolution is 0.57Å sampled with 0.2Å pixels, yielding a velocity resolution of $\sigma = 10\,\mathrm{km s^{-1}}$ at $z \sim 0.3$. Since we expect $\sigma \geq 50\,\mathrm{km s^{-1}}$, this resolution is enough to comfortably resolve the lines.

In order to ensure an accurate calibration of the dataset, we obtained arc lamp and Nasmyth flatfield images immediately after each science exposure.

The observations by P05 were obtained with an identical setup, though with slightly lower integration times. The seeing values for these observations ranged from 0.54 to 0.84 arcsec. Their independent spectra for the four galaxies we have in common provide a useful check of the robustness of our results.

2.2.3 Data reduction

The data were reduced using the GIRAFFE pipeline provided by ESO (Izzo *et al.*, 2004). The pipeline first subtracts the bias and the overscan regions. Then, using the corresponding Nasmyth flatfield image, it determines the position and width of the spectra on the CCD and simultaneously produces a normalised flatfield to account for the variations in transmission from fibre to fibre. Because the observations were taken with the original CCD, which was only changed in May 2008, removal of the dark was necessary due to the presence of a prominent glow in the CCD. A dispersion solution was created using the corresponding ThAr arc lamp frame, and the spectra rebinned to

Target	α_{J2000} h m s	δ_{J2000} ° ′ ″	Morphology	$B_{\rm J} - R_{\rm F}$	$R_{\rm cl}$ (Mpc)
CN24	22 58 50.0	-34 47 57	Disk	2.4	0.10
CN74*	22 58 44.6	-34 49 11	Disk	1.26	0.34
CN119	22 58 42.3	-34 47 41	Disk	2.44	0.48
CN143^{P05}	22 58 42.8	-34 48 31	Disk	1.67	0.32
CN146*	22 58 49.7	-34 52 13	Disk	1.42	0.34
CN155*	22 58 43.4	-34 49 37	Disk	1.43	0.48
CN187^{P05}	22 58 50.5	-34 49 12	Disk	2.17	0.31
CN191^{P05}	22 58 52.9	-34 48 46	Disk	1.49	0.30
CN228^{P05}	22 58 46.5	-34 46 18	Disk	1.39	0.50
CN232	22 58 59.5	-34 51 46	Disk	2.34	0.50
CN243*	22 58 40.7	-34 46 44	Disk	1.58	0.56
CN254	22 58 39.8	-34 47 50	Disk	1.99	0.48
CN849^{P05}	22 58 37.3s	-34 48 20	Disk	1.8	0.61
CN4	22 58 40.7s	-34 47 53	Elliptical	2.48	0.42
CN22	22 58 50.0s	-34 48 13	Peculiar	1.48	0.09
CN89	22 58 48.9s	-34 46 57	Elliptical	2.24	0.32
CN229	22 58 45.3s	-34 46 21	Disk	2.3	0.51
CN247	22 58 39.6s	-34 47 15	Elliptical	2.46	0.53
CN667	22 58 41.0s	-34 46 21	Disk	1.6	0.62
CN858	22 58 48.0s	-34 47 26	Elliptical	2.35	0.19

Table 2.1: Identity number of the galaxy from Couch & Newell (1984), coordinates, morphologies, Galactic reddening corrected colours and distance to the cluster centre for the galaxies in our sample (top) and the P05 sample (bottom). At $z = 0.3$ one arc second corresponds to 4.454 kpc. Galaxies labeled with * have detected emission in [OII]λ3727. Galaxies labeled with "P05" are present in both samples.

a constant dispersion. No flux calibration was required for the analysis of the data.

The pipeline did not include a recipe for the subtraction of the sky. Therefore, the subtraction was done median-combining all fibres from the two IFUs dedicated to the sky, together with the single sky fibre associated with each IFU, giving a total of 52 fibres. We noticed that one of the sky IFUs was systematically too bright, perhaps due to contamination by a low surface brightness object, resulting in an oversubtraction of the sky in our object fibres. We decided to exclude this IFU and use the remaining 32 sky fibres for the sky subtraction.

For consistency, we obtained the raw data for the P05 observations from the ESO archive and reduced them in the same manner as our own observations.

2.2.4 Stellar population and kinematic analysis

To extract information about the kinematics and stellar populations of the galaxies, we used the penalized pixel fitting `pPXF` software described in Cappellari & Emsellem (2004). This algorithm uses a maximum-likelihood approach to fit the spectra in pixel space, simultaneously determining both the stellar kinematics and the optimal linear

combination of spectral templates required to match the input spectrum. We employed two separate collections of templates, one drawn from the ELODIE 3.1 stellar library (Prugniel *et al.*, 2007) and the other containing PEGASE-HR simple stellar population (SSP) models (Le Borgne *et al.*, 2004). The latter spectra are constructed using the ELODIE library, and hence both have the high resolution and wavelength coverage required to fit our spectra (0.5Å FWHM and 4000–6000Å, respectively). Internally, `pPXF` convolved the template spectra with a Gaussian in order to match the spectral resolution of our observations. We restricted the templates to two classes (II-III and V) for each stellar type OBAFGKM, and to SSPs with 12 different ages logarithmically distributed between 1Myr and 15 Gyr and 5 different metallicities [Fe/H] ranging from -1.7 to 0.4.

For each spectrum, the program outputs the velocity, V, and velocity dispersion, σ, together with a refined estimate of the redshift. The values obtained for the kinematics when using the stellar library templates and those obtained using the SSP models were, in general, very similar. However, for some of the galaxy spectra, occasional noise features present in the stellar library template spectra resulted in obviously discrepant fits and wrong values for the kinematics. In these cases, we only use the results obtained using the SSP models. Errors in the kinematic parameters obtained with `pPXF` were estimated in the recommended manner, by performing Monte Carlo simulations on the best-fit template with added noise.

In addition to the kinematics, `pPXF` also provides the weights of the templates which provide the best fit to the observed spectrum. These weights, after normalisation, represent the fractional contribution of each template to the total luminosity. Below we use the weights obtained using the stellar library and the SSP models separately, in order to study the distribution of different stellar types and stellar populations throughout our sample galaxies.

2.3 Analysis

We begin by studying the global properties of the sample, by integrating the fibres from each IFU to produce a single spectrum per galaxy. For most of the sample we

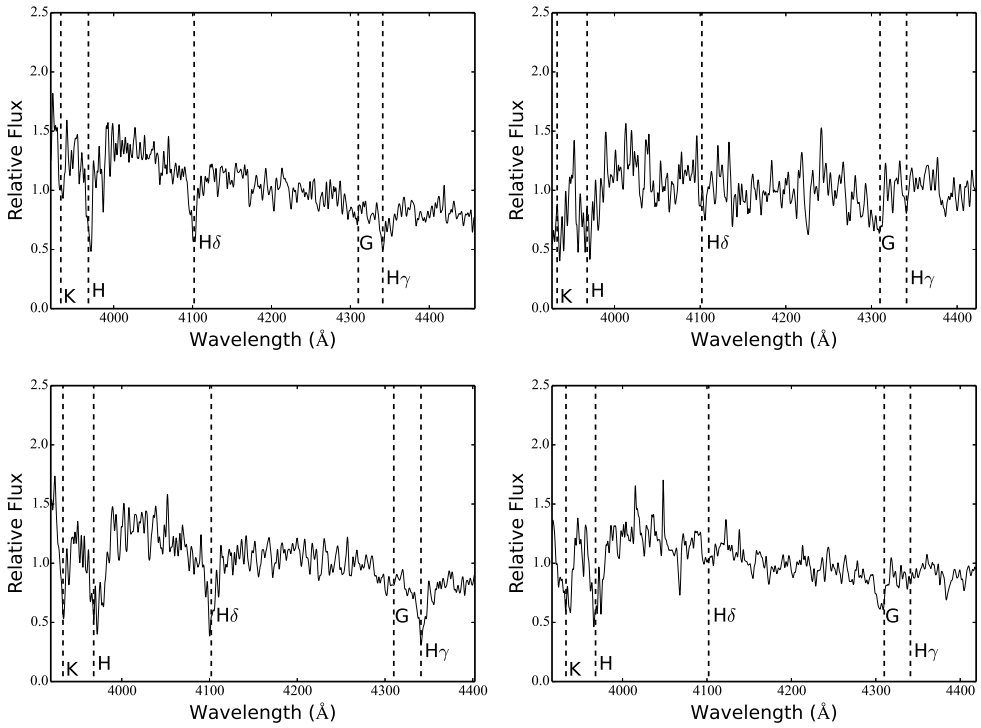

Figure 2.1: Integrated spectra for a representative sample of our galaxies, from left to right and top to bottom: CN191, CN232, CN143 and CN74. We provide two examples of targets with prominent Balmer absorption (left) and two targets without (right). The spectra have been smoothed with a Gaussian of FWHM 1Å to improve their presentation. Note that the spectra have not been flux calibrated.

combined all the fibres. However, in a few cases this resulted in an excessively-noisy spectrum, and therefore only fibres with signal-to-noise ratio (S/N) $\gtrsim 5\text{Å}^{-1}$ (defined in selected regions of the continuum) were then combined. The rejected fibres were always far from the brightest pixel, in the outskirts of the target galaxy.

In Figure 2.1 we plot the integrated spectra for a representative subsample of the galaxies: CN191, CN232, CN143 and CN74. The signal-to-noise ratios (S/N) of the integrated spectra were relatively high, reaching values of $\sim 22\text{Å}^{-1}$ (CN146). All of the spectra display the K and H Calcium lines and the G-band, which are characteristic of an old population. However, the $\mathrm{H}\delta$ and $\mathrm{H}\gamma$ absorption lines, produced by the young, A-star population are only strong in two of the spectra. The lack of strong Balmer absorption in the remainder contrasts with their selection as 'k+a' galaxies. Below we measure the $\mathrm{H}\delta$ index of the galaxies in order to quantify the strength of this feature.

We are also interested in considering spatially-resolved information from the different regions of the galaxies covered by the IFUs. In the majority of the galaxies at least

some of the central fibres had sufficient S/N (reaching values of $\sim 15\text{Å}^{-1}$) to be analysed individually, although the degree to which this is possible varies between galaxies. For this reason, in addition to performing the analysis for the individual fibres, in each galaxy we combined all the pixels immediately adjacent to the brightest one, which we refer to as the 'surroundings' (covering from $\sim$1.6 to 3.2 kpc), and those placed further away, which we define as the 'outskirts' ($\sim$3.2 to 4.8 kpc). In some cases, due to the low S/N in the pixels far away from the centre, we could not obtain reasonable quality spectra for the 'outskirts'.

To find the centre of each galaxy we built images of the light distribution in the continuum region between the $\mathrm{H}\delta$ feature and the sky line at λ5577 for each IFU. The centre of the galaxy was associated with the brightest (and hence usually highest S/N) pixel. Some large and inclined galaxies were purposefully offset to include their outer regions in the IFU. However, many of the other galaxies also display offsets from the IFU centre. These offsets, which are also present in the observations carried out by P05, are likely a result of inaccuracies in the astrometry and IFU positioning errors. They are, however, significantly smaller than the field of view so do not compromise the analysis.

2.3.1 Indicators of a young population in the 'k+a' galaxies

2.3.1.1 Line index measurements

As explained above, 'k+a' spectral features arise from the truncation of star formation in a galaxy, which may be preceded by a starburst, and reflect the composite of a young and an old stellar population. These galaxies are usually identified by the strong Balmer absorption lines in their spectra. Since the higher-order Balmer lines are less affected by emission from ionized gas (Osterbrock, 1989), the most commonly used indicator is the $\mathrm{H}\delta$ line at 4102Å, which is also conveniently located in the optical part of the spectrum at low and intermediate redshift. Although the selection criteria does vary depending on the study, 'k+a' galaxies are generally selected to have $W_{\mathrm{H}\alpha} > 3$Å and no detected emission lines.

The strength of the $\mathrm{H}\delta$ absorption line is related to the mechanism responsible for

the 'k+a' feature. Poggianti *et al.* (1999) showed that strong Hδ absorption lines ($W_{\mathrm{H}\delta}$ > 4–5Å) can only be caused by the abrupt truncation of star formation after a starburst. Lower values of $W_{\mathrm{H}\delta}$ can also be achieved by a simple truncation of a continuous and regular star formation in the galaxy. However, the strength of the Hδ line subsides with time, so it is difficult to distinguish between recent truncation and an older one that was preceded by a starburst.

Although we consider more sophisticated indicators of the stellar population later in this chapter, given the importance and simplicity of the Hδ absorption feature, we first measure the equivalent width of this line for the sample galaxies. We utilised the redshifts obtained from the template fits with `pPXF` (Section 2.2.4), as listed in Table 2.2. Equivalent widths were measured using the software `INDEXF` (Cardiel, 2010), which uses the Lick/IDS index definitions of Worthey & Ottaviani (1997) to measure the signal within the line with respect to the neighbouring continuum. To make our results comparable with those obtained by P05, we use the index Hδ_F, which takes the continuum intervals 4057.25–4088.5Å and 4114.75–4137.25Å around the central 4091.00–4112.25Å bandpass. Errors are estimated from the propagation of uncertainties in the spectra and the measured radial velocities.

Four of the galaxies in our sample display emission lines, which would affect the line index measurement due to the filling of the absorption lines. To avoid this, for these four galaxies instead of using the original spectrum we measured the line index on the best fit spectrum constructed by `pPXF`. This procedure has been shown to produce very good results by Johnston *et al.* (2013b).

The values of Hδ_F of all the galaxies in our sample are listed in Table 2.2. We also list the values obtained for the galaxies from the P05 sample. For galaxies that are present in both samples we obtained very similar values, consistent within the given uncertainties. Hereafter we used the values measured in our data, because they possess higher S/N ratios.

The first surprising finding is the number of galaxies for which we measure Hδ_F lower than 3Å. This was already suggested from the weak Balmer absorption lines apparent in some of the spectra upon visual inspection, see (Figure 2.1). These low values contrast with those expected from the spectroscopic study by CS87, in which all of

our sample showed $W_{\rm H\delta}$ higher than 3Å. This discrepancy was also found by P05. It appears that the uncertainties in the CS87 Hδ EWs are rather large, and hence their spectral classifications are only reliable for the most extreme 'k+a' cases.

From our analysis, only seven of the twenty galaxies display $W_{\rm H\delta} > 3$Å, with three of them also having detected [OII]λ3727 emission. If we consider also those with $W_{\rm H\delta} > 2$ Å, three more galaxies are included, giving a total of ten. The values obtained in our analysis of the P05 sample are in reasonable good agreement with what they found, considering that each study applied a different method. We only found one galaxy, CN849, where we measured a lower value of Hδ_F (2.3 ± 0.4) than what they obtained (3.6 ± 0.3), which in this case is significant because it changes the galaxy's 'k+a' classification.

As mentioned above, four of the galaxies we observed are listed as having [OII]λ3727 emission in CS87 and therefore do not meet the standard 'k+a' criteria. Their EW([OII]) values range from 7.6Å to 39.6Å. These are likely reliable emission line identifications. Three of them are found to have H$\delta_F > 3$ Å (CN146, CN155 and CN243) and they also show signs of emission in Hγ and Hδ in our data. However, it is not clear whether these emission lines result from residual star formation or AGN activity.

One would expect that if star formation has been recently truncated in those galaxies with strong Hδ absorption, they should have bluer colors due to the presence of the young population. To test this, in Fig. 2.2 we plot Hδ_F versus $B_J - R_F$ for all the sample galaxies. Objects with strong Hδ absorption are conspicuously bluer than those with weaker Hδ absorption. CS87 also present this plot, finding a consistent trend, though somewhat weaker, presumably due to the larger uncertainties on their $W_{\rm H\delta}$ estimates. This trend gives compelling support that the galaxies in our sample with stronger Hδ absorption, and particularly $W_{\rm H\delta} \gtrsim 2$, contain younger stellar populations.

In Fig. 2.2 we also indicate the galaxies which have observed [OII] emission. Recall that, for these galaxies, $W_{\rm H\delta}$ was measured on the template fits produced by `pPXF`, rather than the data itself, to avoid the effect of line-filling. It is possible that in the case of the bluest galaxy the line-filling has affected the `pPXF` fit itself, resulting in an underestimate of $W_{\rm H\delta}$. These four galaxies are not strictly 'k+a' systems, they

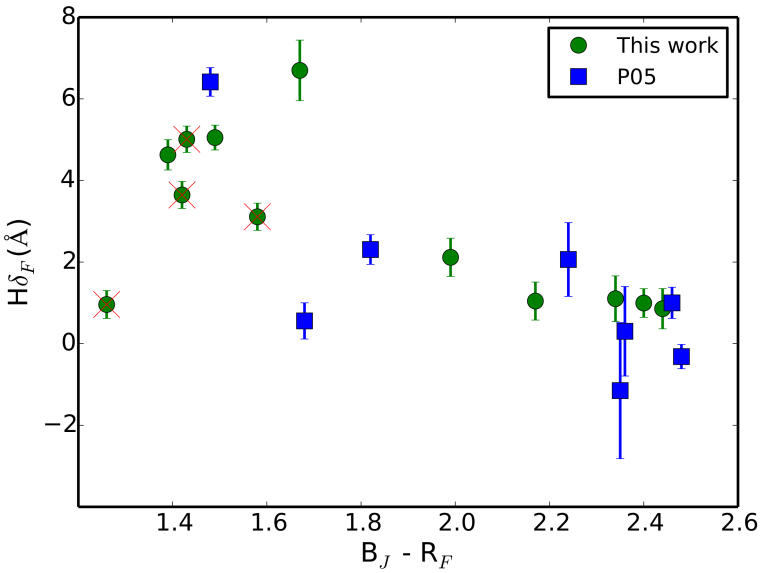

Figure 2.2: $\mathrm{H}\delta_F$ versus $B_J - R_F$ colour for our entire galaxy sample. In the case of objects that were observed by both P05 and ourselves, we only plot our values. Galaxies with detected emission in [OII] by CS87 are indicated by a red cross.

may simply be normal star-forming galaxies, although their high $W_{\mathrm{H}\delta}$ might indicate some recent suppression of their star formation. Nevertheless, we retain them in the analysis because they probably lie just outside the boundaries of the 'k+a' class, and may provide useful clues on the process by which galaxies become 'k+a' systems.

2.3.1.2 A/(AFGKM) and f_{young} measurement

Although strong $\mathrm{H}\delta$ absorption is the standard indicator of a young population in 'k+a' galaxies, this simply reflects the presence of a substantial stellar population with ages between 0.5 and 1.5 Gyr, whose light is dominated by A stars, but an absence of younger populations containing OB stars, powering nebular emission from HII regions. The presence of this intermediate-age stellar population may also be inferred using other, more quantitative, methods. One approach is template fitting, which uses the full wavelength range available and accounts for the fact that populations of all ages contribute to $W_{\mathrm{H}\delta}$ (and other spectral features). We use the results of template fits performed using `pPXF`, as described in Section 2.2.4.

To estimate the relative proportion of each stellar population, we use the normalized light-weighted proportions assigned to the various templates in the best-fitting model.

From the weights obtained using the stellar library templates we determine the frac-

tions of each stellar type (OBAFGKM) contributing to the galaxy spectrum. For the fits using the SSP models, we group the templates into four age bins: '$\mathrm{Age} < 0.5$ Gyr', '$0.5 < \mathrm{Age} < 1.5$ Gyr', '$1.5 < \mathrm{Age} < 7$ Gyr' and '$\mathrm{Age} > 7$ Gyr'. One expects an approximate correspondence between the stellar types and SSP ages: stars formed very recently (OB) will dominate the $\mathrm{Age} < 0.5$ Gyr bin, stars with lifetimes ~ 1 Gyr (main sequence A and F stars) will dominate the '$0.5 < \mathrm{Age} < 1.5$ Gyr' bin, and longer-lived stars (GKM) will correspond to the two older age bins. However, the stellar population templates contain contributions from stars of all types with lifetimes longer that the SSP age.

To evaluate the fraction of A-type stars we use the ratio A/(AFGKM). OB stars are excluded from this fraction because their presence is ill-constrained by our fits, due to their featureless spectra together with the uncertain flux calibration and limited wavelength range of our data. Also, OB stars do not contribute significantly to the stellar mass of a galaxy. For the stellar populations, our primary quantity is the fractional contribution of SSPs with $0.5 < \mathrm{Age} < 1.5$ Gyr over the total, hereafter f_{young}. The values of A/(AFGKM) and f_{young}, determined with the integrated spectra for each galaxy, are listed in Table 2.2.

Thus now we have three different indicators of the presence of a young populations in these galaxies, $\mathrm{H}\delta_F$, A/(AFGKM) and f_{young}. Comparing these parameters provides a useful indication of their robustness, and therefore the reliability of using only one of them in cases when the other ones cannot be obtained. This comparison is done in Fig. 2.3, where we plot A/(AFGKM) and f_{young} against $\mathrm{H}\delta_F$ for our entire galaxy sample. Uncertainties on the $\mathrm{H}\delta_F$ measurements are indicated, but `pPXF` does not provide error estimates for the template weights. We therefore estimate average uncertainties for A/(AFGKM) and f_{young} from the standard deviation of the scatter from a linear correlation with respect to $\mathrm{H}\delta_F$ after subtracting the contribution to their error by $\Delta\mathrm{H}\delta_F$. We obtain an uncertainty in both quantities of 0.2. which is also noted in Table 2.2.

As expected, there is a good correlation between these quantities. Galaxies with strong Balmer absorption lines also show high fractions of A/(AFGKM) and f_{young}, while those with weak $\mathrm{H}\delta_F$ show very low values of A/(AFGKM) and f_{young}. The fractions of A/(AFGKM) and f_{young} also present good correlation between them. More quan-

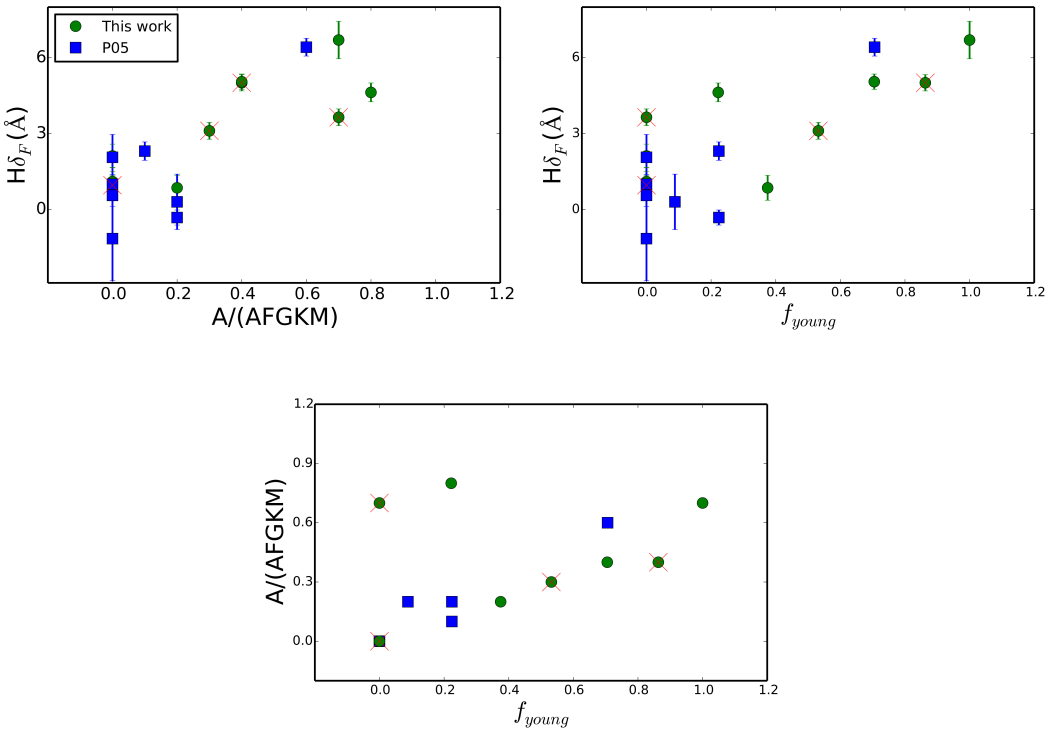

Figure 2.3: Values of A/(AFGKM), $f_{\rm young}$ and $\mathrm{H}\delta_F$ plotted against each other for our sample (green circles) and measured by us on spectra obtained by P05 (blue squares). For galaxies that are present in both samples we only plot values measured in our data because they have higher S/N. We only plot error bars in $\mathrm{H}\delta_F$, as `pPXF` does not provide uncertainties on the weights in the best-fitting combination of templates. Galaxies with detected emission in [OII] by CS87 are indicated by a red cross. In the plot of $f_{\rm young}$ vs A/(AFGKM) there are fewer visible points because they are superimposed onto each other.

titatively, for A/(AFGKM) and $\mathrm{H}\delta_F$ we obtain a Spearman's correlation coefficient $\rho = 0.65$, while for $f_{\rm young}$ and $\mathrm{H}\delta_F$, $\rho = 0.56$. In the case of A/(AFGKM) and $f_{\rm young}$, $\rho = 0.76$. The chance of any of these correlations being spurious is $\lesssim 1$ per cent.

2.3.2 Spatial distributions

As mentioned previously, in addition to providing global information about a galaxy, integral field spectroscopy allows us to study properties at smaller spatial scales and hence consider different regions within a galaxy. We exploit this possibility by performing the same analysis described above, but now applied both to the spectra from individual IFU elements and to combined spectra from the 'centre', 'surroundings' and 'outskirts' regions of each galaxy.

We have used these results to construct maps of the three different age indicators, $\mathrm{H}\delta_F$,

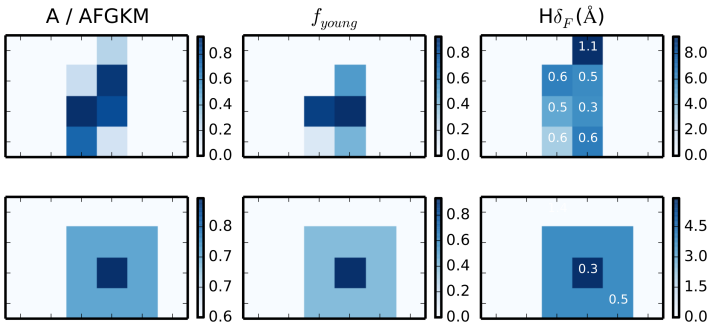

Figure 2.4: Maps of the individual fibre values of A/(AFGKM), $f_{\rm young}$ and Hδ_F index (top) and the corresponding values for the integrated regions 'centre' and 'surroundings' (bottom) in CN228. The bottom maps show the averaged values within the defined regions; therefore, contrary to the top maps, these do not have a one-to-one correspondence with regions in the galaxy. Errors of the Hδ_F index are printed over the regions. Each spatial pixel (or spaxel) has a size of 0.52 x 0.52 arcsec^2 which corresponds to $\sim$ 2.3 x 2.3 kpc^2 at the redshift of AC114.

A/(AFGKM) and $f_{\rm young}$, for each galaxy. In many galaxies, due to the S/N being too low in the 'outskirts', only the 'centre' and 'surroundings' could be analysed. Cases where the three integrated regions could be analysed (CN74 and CN849) can be found in the Appendix A. An example of this analysis is shown in Fig. 2.4 for the galaxy CN228, where the three indicators show a high concentration of the young population in the centre of the galaxy. This is particularly clear when considering the 'centre' versus 'surroundings' regions. The values of the individual fibres for A/(AFGKM) and $f_{\rm young}$ also show a high concentration towards the centre, while the individual Hδ_F are less conclusive.

To examine the stellar population in more detail, in Fig. 2.5 we show the normalized distributions of the different spectral types and SSP ages obtained for different regions of the same galaxy. The two approaches are broadly consistent: a prominent fraction of A-stars is associated with a significant young-age population.

The maps of Hδ_F, A/(AFGKM) and $f_{\rm young}$ for each galaxy are our primary source of information regarding the spatial distributions of the young and old stellar populations. However, the maps are difficult to deal with quantitatively, and there is some subjectivity in identifying the trends they reveal. We have examined these maps in detail, and in the Appendix A we present qualitative descriptions of each galaxy, in addition to the maps themselves.

In an attempt to quantify the differences in the spatial distributions of the young and old stellar populations we have used these maps to estimate the luminosity-weighted

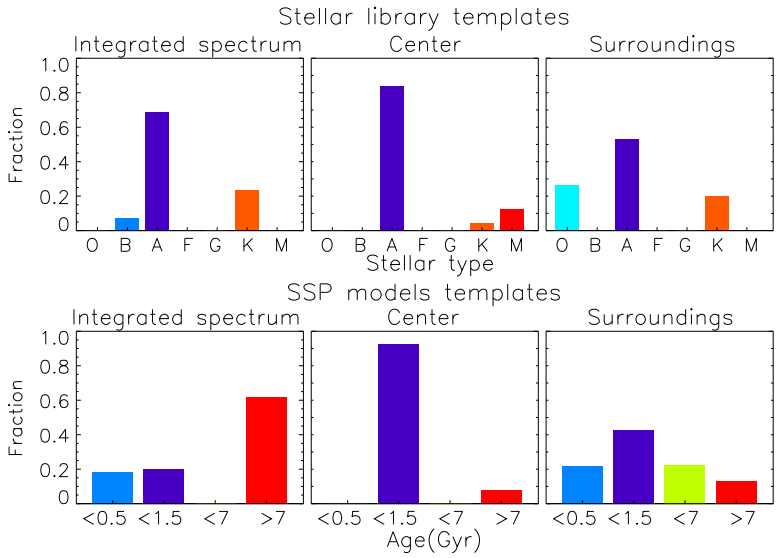

Figure 2.5: Histograms of stellar type and stellar population age obtained with pPXF for the integrated spectra, 'centre' and 'surroundings' of CN228.

fraction of the young stellar population contained within the half-light radius of the old population. We have assumed exponential intensity profiles for both populations. A value of this fraction larger than 0.5 indicates that the young population is more concentrated than the old one. Figure 2.6 shows this fraction plotted against the global $\mathrm{H}\delta_F$ values. There is a large scatter, indicating significant differences in the current properties and formation histories of the galaxies. Nevertheless, galaxies with the strongest $\mathrm{H}\delta_F$ seem to show some tendency to have more centrally-concentrated young populations. This suggests that the last episode of star formation often took place in the central regions of these galaxies. The sample size, spatial resolution and uncertainties of this study prevent us from reaching a very robust conclusion in this respect, but it is reassuring that our findings are consistent with independent evidence from recent studies of local S0 galaxies (Bedregal *et al.*, 2011; Johnston *et al.*, 2012, 2013a).

2.3.3 Kinematics

If spiral galaxies are being transformed into S0s by any of the processes discussed in the introduction, in addition to the changes in stellar populations considered above, their kinematics may also be affected. The kinematics of the 'k+a' galaxies in our sample can therefore indicate what mechanisms are responsible for the truncation of their star formation. If the process acts primarily to starve a spiral galaxy of its gas

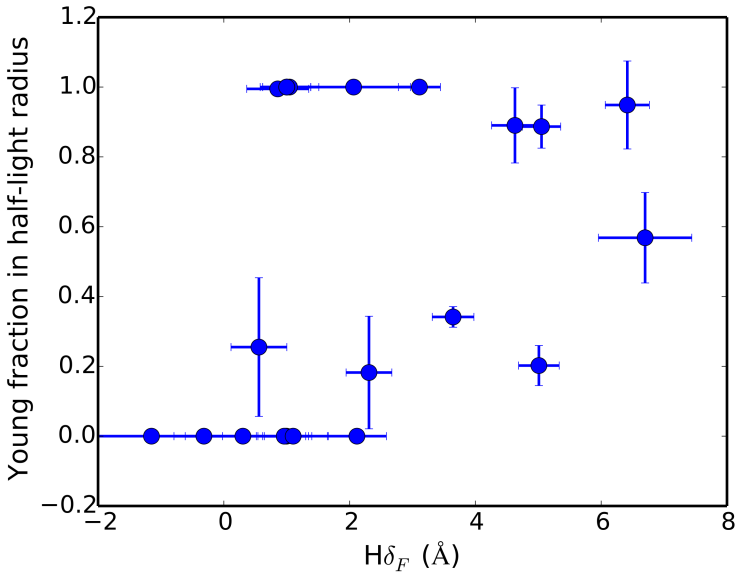

Figure 2.6: The luminosity-weighted fraction of the young stellar population contained within the half-light radius of the old population plotted against the global $H\delta_F$. A value of this fraction larger than 0.5 indicates that the young population is more concentrated than the old one (see text for details).

Target	z	$H\delta_F$ (Å)	A/(AFGKM) ($\pm$ 0.2)	f_{young} ($\pm$ 0.2)	$\sigma_{\rm int}$ (kms^{-1})	$V_{\rm rot}$ (kms^{-1})	$V_{\rm rot}/\sigma_{\rm int}$	Interacting
CN143	0.310	6.7 ± 0.7	0.7	1.0	107 ± 15	133 ± 18	1.2 ± 0.2	NO
CN191	0.305	5.1 ± 0.3	0.4	0.7	61 ± 8	137 ± 51	2.2 ± 0.9	NO
CN155*	0.320	5.0 ± 0.3	0.4	0.9	282 ± 72	-	-	YES
CN228	0.317	4.6 ± 0.4	0.8	0.2	210 ± 66	177 ± 38	0.8 ± 0.6	YES
CN146*	0.300	3.7 ± 0.3	0.7	0.0	184 ± 20	-	-	NO
CN243*	0.326	3.1 ± 0.3	0.3	0.5	232 ± 19	-	-	YES
CN254	0.309	2.1 ± 0.5	0.0	0.0	202 ± 26	166 ± 20	0.8 ± 0.2	NO
CN232	0.315	1.1 ± 0.6	0.0	0.0	185 ± 32	137 ± 55	0.7 ± 0.3	NO
CN24	0.322	1.0 ± 0.4	0.0	0.0	93 ± 12	-	-	NO
CN74*	0.316	1.0 ± 0.3	0.0	0.0	239 ± 88	152 ± 75	0.6 ± 1.6	NO
CN187	0.308	1.0 ± 0.5	0.0	0.0	202 ± 24	-	-	NO
CN119	0.308	0.9 ± 0.5	0.2	0.4	144 ± 134	-	-	NO
CN22	0.336	6.4 ± 0.4	0.6	0.7	83 ± 22	83 ± 21	1.0 ± 1.0	YES
CN849	0.324	2.3 ± 0.4	0.1	0.2	189 ± 7	86 ± 11	0.5 ± 0.3	YES
CN89	0.317	2.1 ± 0.9	0.0	0.0	94 ± 40	-	-	NO
CN247	0.319	1.0 ± 0.4	0.0	0.0	214 ± 10	-	-	YES
CN667	0.312	0.6 ± 0.4	0.0	0.0	128 ± 18	-	-	YES
CN229	0.320	0.3 ± 1.1	0.2	0.1	186 ± 97	-	-	NO
CN4	0.308	-0.3 ± 0.3	0.2	0.2	185 ± 20	-	-	NO
CN858	0.312	-1.2 ± 1.7	0.0	0.0	182 ± 52	-	-	NO

Table 2.2: Galaxy ID, redshifts, young population indicators, velocity dispersions, $V_{\rm rot}/\sigma$ and state of interaction for the galaxies in our sample (top) and the P05 sample (bottom). Note that morphology and colour are listed in Table 2.1. Galaxies labeled with * have [OII]λ3727 detected emission by CS87.

supply, the disk rotation should be preserved in the resulting galaxy. However, if a merger is involved, the remnant would be expected to show more random motions.

The kinematics of the galaxies analysed here were extracted using the software `pPXF`, as explained in Section 2.2.4. First of all, we obtained a value of the overall velocity dispersion $\sigma_{\rm int}$ for the integrated spectrum of each galaxy, which are listed in 2.2. It should be borne in mind that for the galaxies with detected emission by CS87, the measurement of $\sigma_{\rm int}$ might be affected by the filling of the absorption lines due to emission. A wide range of values of $\sigma_{\rm int}$ are found, from ~ 60 to $\sim 280\,{\rm kms}^{-1}$. These overall $\sigma_{\rm int}$ include contributions from both rotational and random motions, which we will attempt to separate below.

If the gas and the kinematics of the galaxies are being affected by the cluster environment, one would expect galaxies closer to the cluster centre to show different behaviour to those that are further out, as found by Jaffé *et al.* (2011). To test this, we consider $\sigma_{\rm int}$ as a function of the projected distance from the cluster centre (Table 2.1), which is plotted in Figure 2.7. For the full sample there does not appear to be any clear trend. However, if we separate galaxies with high ($\geq$ 3Å) and low ($<$ 3Å) Hδ_F, we see that those with high Hδ_F (blue squares) present a strong trend. High Hδ_F galaxies have higher $\sigma_{\rm int}$ the further they are from the cluster centre, while those with low Hδ_F (green circles) show little change with position. Some of the high-Hδ_F and high-$\sigma_{\rm int}$ galaxies display emission-lines (red crosses), which may make the estimation of $\sigma_{\rm int}$ unreliable. However, if we remove them from the plot, we see that the trend remains.

We now turn our attention to the kinematics of the galaxies on smaller scales, which can be studied using the outputs of fits performed to the individual IFU fibres. We construct line-of-sight velocity, $V_{\rm obs}$, and velocity dispersion, σ, maps of the galaxies, in a similar manner to those for the young population indicators. An example is shown in Figure 2.8 for the galaxy CN228.

We have studied these maps for signs of rotation and differences in velocity dispersion between the central and surrounding pixels. One problem we had to face here was that the 'good' fibres were not always distributed around the brightest pixel in the IFU, and it was sometimes difficult to identify patterns of rotation or velocity dispersion. Since the observed velocity is $V_{\rm obs} = V_{\rm rot}{\rm sin}i$, where $V_{\rm rot}$ is the rotational velocity and i the

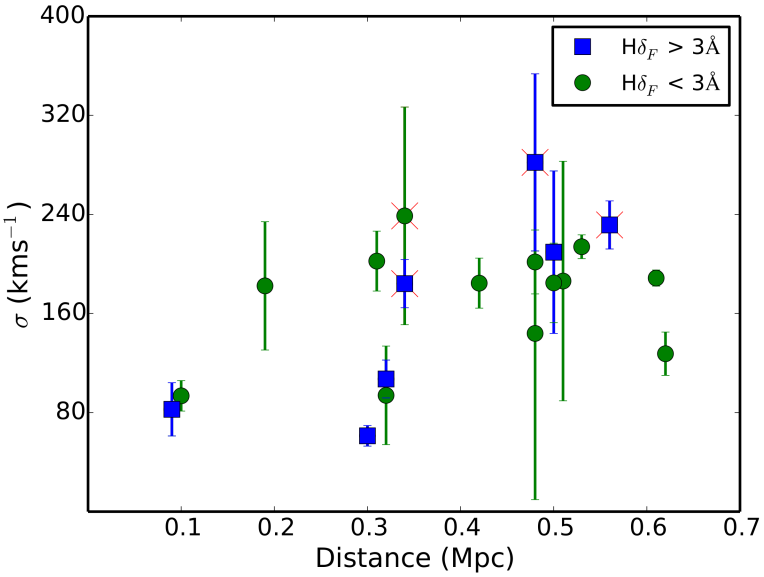

Figure 2.7: Velocity dispersion σ vs projected distance to the centre of the cluster for galaxies with H$\delta_F > 3$Å (blue squares) and H$\delta_F < 3$Å (green circles). For those galaxies that are observed by both P05 and ourselves we plot the mean value. Galaxies with detected emission in [OII] by CS87 have a red cross overplotted.

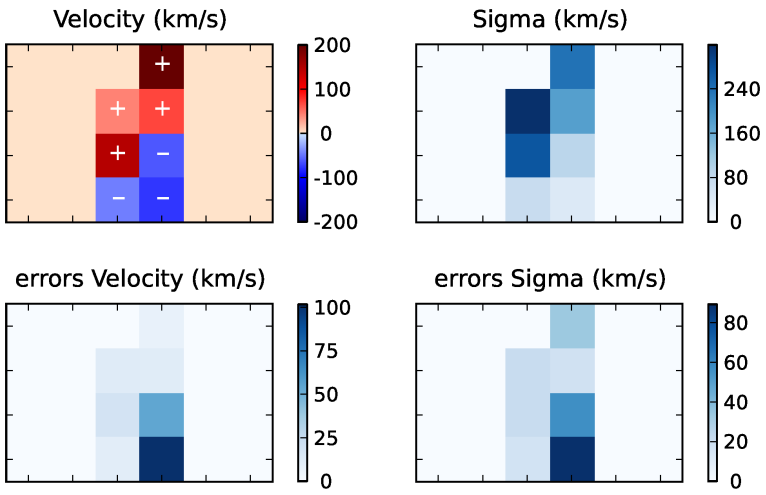

Figure 2.8: Example of the radial velocity and velocity dispersion maps, with errors plotted below. The plus ('+') and minus ('−') symbols indicate the direction of rotation. In this image we show the example of CN228, showing a clear pattern of rotation and with similar values of σ along the galaxy.

inclination of the galaxy, we need to know the galaxy inclination in order to obtain the actual rotational velocity. The inclination was therefore determined by the apparent ellipticity obtained by fitting an ellipse to the HST/WFPC2 images using the `IRAF` task `ELLIPSE`. In the case presented in Fig. 2.8, we can see a clear pattern typical of rotation, with $V_{\rm rot} = 177 \pm 38\,{\rm kms}^{-1}$. The distribution of σ is roughly flat.

Previous studies of the kinematics of 'k+a' galaxies have found significant rotation in many of them (Franx, 1993; Caldwell *et al.*, 1996; Pracy *et al.*, 2009; Swinbank *et al.*, 2012; Pracy *et al.*, 2013), although some are found to be mainly pressure-supported (Norton *et al.*, 2001). We attempted our kinematic analysis in all the galaxies, including the observations of P05, and found that at least 8 galaxies display rotation, with values of $V_{\rm rot} \sim 85$–$180\,{\rm kms}^{-1}$.

The measured values of $\sigma_{\rm int}$ and $V_{\rm rot}$ are listed in Table 2.2, along with their ratio ($V_{\rm rot}/\sigma_{\rm int}$), which indicates whether a galaxy is a rotationally (> 1) or pressure (< 1) supported system. Using this last parameter, we see that 2 of the systems displaying rotation are clearly rotationally supported, typical of disk-like systems, while 5 show $V_{\rm rot}/\sigma_{\rm int} < 1$ indicating they are dominated by random motions. Coming back to Figure 2.7, now we are able to establish if the high values of $\sigma_{\rm int}$ found for some galaxies are due to rotation or to random motions. From the 10 galaxies with $\mathrm{H}\delta_{\rm F} \geq 2$Å, rotation is detected in 6 of them and dominant in 2 of these. However, the amount of rotation in galaxies far from the centre, in particular CN254 and CN228 is conspicuously higher ($\geq 160\,{\rm kms}^{-1}$) than in those closer to the centre such as CN143 and CN191 ($< 140\,{\rm kms}^{-1}$). The observed trend to lower internal velocities with decreasing distance from the cluster core may therefore indicate a trend to less regular kinematics, and hence environmentally induced disturbances in the centre of the cluster.

2.3.4 Kinematic decomposition

The kinematics studied in the previous section are derived assuming that all stellar populations contributing to a spectrum have the same kinematics. However, our data affords the possibility of measuring the kinematics of the young and old populations in 'k+a' galaxies separately (e.g., Franx 1993; Norton *et al.* 2001). Separated kinematics offer a further method of distinguishing between the mechanisms responsible for the

'k+a' signature. Rotation in the young components implies it is in a disk and that the galaxy has not been subject to a violent process, particularly if the young population kinematics and distribution are consistent with the older population. On the other hand, a pressure-supported young population implies that a significant interaction has occurred. The degree of rotational support in the old population may then indicate the strength and nature of this interaction.

In order to study the kinematics of the two different populations, we modified the `pPXF` algorithm in such a way that it could fit two different stellar templates to one spectrum simultaneously, convolving each one with different radial velocities and velocity dispersions. The same modified algorithm has been used to study a galaxy with two counter-rotating disks by Johnston *et al.* (2013b), with good results. In our case, we used a set of templates containing only A-stars and K-stars with a range of different metallicities so that `pPXF` could clearly distinguish between the two populations.

Decomposing the kinematics is very challenging, and requires higher signal-to-noise than available in most of the individual IFU elements. The decomposition was therefore attempted on coadded spectra corresponding to three regions for each galaxy, the centre and both sides, where the orientation of each galaxy is judged from the kinematic maps from Section 2.3.3. We found that the algorithm was sometimes sensitive to the initial values of V and σ used. We therefore varied these input values and, in order to be considered robust, the outputs of the fits were required to remain constant for a wide range of initial values.

The results are presented in terms of V and σ maps in a similar manner to the previous section. As an example, the kinematic decomposition of CN228 is shown in Figure 2.9. In this case, the galaxy is a composite of two populations with similar patterns of rotation, while the young population displays higher values of σ than the old population throughout the galaxy (note the different colour scales). As shown previously in Figure 2.4, CN228 shows central concentration in the distribution of the three indicators $\mathrm{H}\delta_F$, A/(AFGKM) and f_{young}, implying a concentration of the young population in the centre of the galaxy. Now, adding the information provided by the kinematic decomposition, the fact that this galaxy and others show similar rotation between the young and old population seems to indicate that these were fairly normal disk galaxies

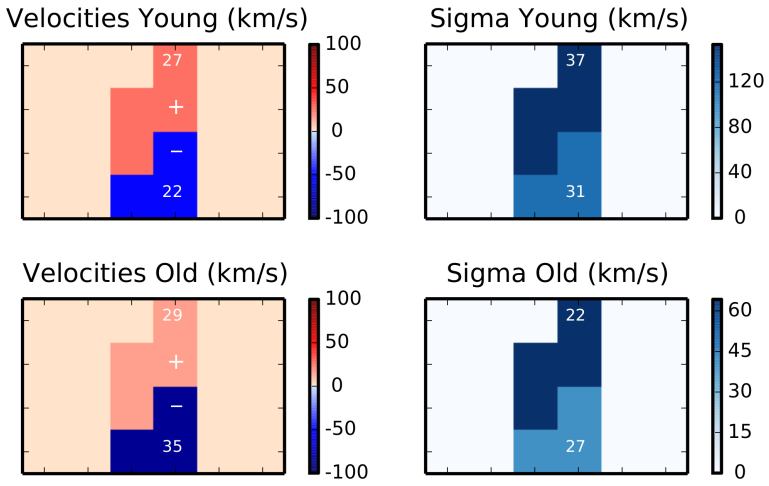

Figure 2.9: Kinematic decomposition of the young and old stellar populations in CN228, obtained using our two-component fitting method. Mean velocity and velocity dispersion values are presented in the IFU image. The plus ('+') and minus ('−') symbols indicate the direction of rotation. Errors in the fits are plotted over the corresponding regions.

which have not experienced a major merger or dominant central starburst. However, the higher σ does suggest that they have experienced an interaction which increased the random motions in the gas from which the last population of stars was formed.

In total, three disk galaxies with $\mathrm{H}\delta_F \geq 3$Å (CN228, CN146 and CN191) and two more with $\mathrm{H}\delta_F \geq 2$Å (CN254, CN849) could be kinematically decomposed into two populations. In four of these cases both the young and old populations were found to have similar patterns of rotation, whereas no clear pattern was found in the remaining one (CN146).

The σ values obtained for the two populations display a variety of behaviours, both in terms of their relative strength and their radial gradients. In the case of CN228 discussed above, the σ of the young stars is higher than that of the old population, which suggests that this disky 'k+a' galaxy may have experienced a recent interaction, which has increased the random motions of their cold gas, from which the latest generation of stars have formed, but had less effect on their previously existing stellar populations. Thus, the process cannot be purely gravitational, since the old population is not perturbed, and it must be affecting only the gas (Jaffé *et al.*, 2011). A more detailed analysis of the kinematic decomposition for each galaxy is presented in the Appendix A.

2.3.5 Influence of interactions

Dynamically interacting galaxies are often observed to be experiencing a starburst (e.g. Keel *et al.* 1985). Simulations have long suggested that mergers and interactions can cause gas in a galaxy disk to lose angular momentum and fall toward the centre of the galaxy, potentially fueling a central starburst (Barnes & Hernquist, 1991; Mihos & Hernquist, 1996; Bekki *et al.*, 2005). However, observations often find that interactions promote star formation throughout the galaxies involved (e.g. Kennicutt *et al.* 1987; Elmegreen *et al.* 2006), not just in the nuclear region. This can now be reproduced by models which pay closer attention to the role of shock-induced star formation (e.g. Chien & Barnes 2010; Teyssier, Chapon & Bournaud 2010).

Assuming that the starburst process occurs faster than the replenishment of the gas disk via infall, or alternatively that such infall is suppressed, then following the starburst the galaxy will cease star formation. The resulting galaxy will therefore display a k+a spectrum for a time.

The importance of mergers and interactions as the origin of the 'k+a' feature is supported by studies which find that 'k+a' galaxies (of all morphologies) are more likely to be found with a companion galaxy, when compared to normal galaxies (Goto, 2005; Yamauchi, Yagi & Goto, 2008; Pracy *et al.*, 2012). For example, in their catalogue of k+a and their companion galaxies, Yamauchi, Yagi & Goto (2008) found that k+a galaxies were 54 per cent more likely than normal galaxies to have a significant companion. Similarly, the two 'k+a' galaxies with late-type morphology and with a central concentration of the young population studied by Pracy *et al.* (2012) have nearby companions and could be experiencing tidal interactions. However, note that all of these results are based on the general 'k+a' population, and thus may differ from the disky, cluster 'k+a' population considered in this work. We have therefore looked for evidence of interactions in the sample.

In Table 2.2 we have included a column specifying whether each galaxy displays indications of interacting with other objects. This was evaluated by visual inspection of the HST/WFPC2 images of the AC114 cluster. Of the twenty galaxies in our sample, seven have a close companion and show clear signs of a merger or interaction. The remainder appear fairly isolated and undistorted. However, the fact that a galaxy does

not appear to be currently interacting does not rule out such a process as the cause of a 'k+a' feature. The spectral 'k+a' signature can last for up to 1.5 Gyr, which is enough time for an interacting galaxy to have moved to a completely different region of the cluster and any distortion feature might have faded.

To test if interactions have any influence in the properties of the galaxies, we looked for any kind of correlation with any of the results obtained so far in this study. Of the ten galaxies with $\mathrm{H}\delta > 2$Å, five show signs of interaction. But interestingly, of the seven $\mathrm{H}\delta > 2$Å galaxies with disky morphology and usable spatial information, three have centrally concentrated young populations (CN155, CN228 and 849) and *all* of these show evidence for interactions. In contrast, *none* of the four disk galaxies with their young population extended throughout the galaxy show any sign of mergers or interactions.

This finding strongly supports a link between dynamical interactions and a centrally concentrated starburst in disky, cluster k+a galaxies. The remainder, with an apparently less concentrated young stellar population may simply be the result of weaker or older interactions, or caused by an alternative mechanism. However, the strength of $\mathrm{H}\delta_F$ for the interacting and non-interacting galaxies does not differ significantly.

2.4 Discussion

Our analysis reveals that disky 'k+a' galaxies in intermediate-redshift clusters are a mixed population. However, despite the small sample size, we do see some consistent behaviour in a number of important respects. These results are robust to changes in the way we quantify the presence and kinematics of the young and old stellar populations.

The young stellar populations within our sample galaxies are always either distributed similarly to, or more compactly than, the older population. Importantly, however, they are rarely consistent with being purely confined to the galaxy nucleus. Furthermore, the young stars often display rotational kinematics corresponding to the rest of the galaxy, implying they are located in the disk. However, there are some indications that their velocity dispersions are somewhat greater than in normal spiral galaxies.

Together these results suggest that the young stellar component formed in an extended disk, in a manner similar to previous generations of stars in these galaxies. It is not associated with the aftermath of a nuclear starburst, nor star formation in tidally accreted material. However the gas from which the latest stars formed was typically more centrally concentrated than that from which their predecessors were born.

The scenario presented by our data can be brought together with many other pieces of observational evidence to support a consistent picture describing the evolution of the majority of disk galaxies in intermediate-redshift clusters and groups.

Firstly, we note that any satellite galaxy within a larger halo, particularly one massive enough to have developed a quasi-static hot atmosphere (Rees & Ostriker, 1977), is very likely to have its own gas halo rapidly removed by interactions with the host halo's intergalactic medium and tidal field, via the mechanisms discussed in the introduction. The environmental removal of HI gas reservoirs is observed both locally (e.g., Vogt *et al.* 2004a) and at intermediate redshift (e.g., Jaffé *et al.* 2012). Star-forming galaxies entering a dense environment (i.e. becoming satellites: low mass galaxies in groups and higher mass galaxies in clusters), would therefore be expected to gradually decrease their star formation rate as they consume their remaining supply of dense gas.

However, a gradual decline in the star formation rates of star-forming galaxies in dense environments is at odds with results from large surveys. The colours and Hα equivalent widths of star-forming galaxies are invariant with environment (e.g., Balogh *et al.* 2004a,b; Baldry *et al.* 2006; Bamford *et al.* 2008), although the relative proportions of blue versus red or star-forming versus passive galaxies vary substantially. This strongly implies that galaxies must rapidly transform from star-forming to passive, such that a transition population is not seen. The transformation mechanism cannot be particularly violent, as many galaxies become passive whilst maintaining their disk morphology, first as red spirals, and then as lenticulars (e.g., Lane *et al.* 2007; Bamford *et al.* 2009; Maltby *et al.* 2012). We must therefore reconcile the need for a rapid transformation in terms of observed colour and emission-line properties, with the requirement that the mechanism only act relatively gently on galaxy structure.

Star-forming galaxies are observed in environments of all densities, though they become much rarer in dense regions. However, it is not yet clear whether those star-

forming galaxies which appear to inhabit dense regions are simply the result of projection effects, or whether some galaxies are able to maintain their star formation, at least for a while, in such extreme environments. The former would imply that the transition from star-forming to passive is driven by a deterministic mechanism, specific to particular environments, whereas the latter would permit something more stochastic in nature, in which the effect of environment is simply to increase the likelihood of such a transition (Peng *et al.*, 2010).

A stochastic mechanism, which is not directly related to a galaxy's broad-scale environment, is supported by the observation that the proportions of red or passive galaxies show trends across a wide range of environmental density, and that galaxies with truncated star formation are often associated with groups (Moran *et al.*, 2007; Poggianti *et al.*, 2009; Wilman *et al.*, 2009; Lackner & Gunn, 2013), which also host normal star-forming galaxies.

The reality is probably a combination of the deterministic and stochastic pictures, for example a mechanism whose effectiveness depends sensitively on the detailed small-scale substructure of the environment and a galaxy's orbit through it (e.g., Font *et al.* 2008; Peng *et al.* 2012). In any case, the deterministic removal of a galaxy's gas halo soon after it becomes a satellite makes the galaxy more vulnerable, helping to reduce the timescale of any tranformation instigated by a subsequent mechanism.

An initial enhancement of star formation efficiency early in the star-forming-to-passive transformation process will effectively reduce the observability of the transition. The increased star formation efficiency would balance the effect of the declining fuel supply, maintaining the appearance of normality, until the fuel supply is entirely depleted. The galaxy would then immediately cease star formation and rapidly appear passive.

Our results support the occurrence of briefly enhanced or extended star formation episodes in the central regions of cluster spirals, as well as the prevalence of 'k+a' spectral types in the cluster environment (Poggianti *et al.*, 2009). We also find evidence for more centrally concentrated young populations in spirals (Caldwell *et al.*, 1996; Koopmann & Kenney, 2004a,b; Vogt *et al.*, 2004a,b; Crowl & Kenney, 2008; Rose *et al.*, 2010; Bamford, Milvang-Jensen & Aragón-Salamanca, 2007; Jaffé *et al.*, 2011; Bösch *et al.*, 2013a) and S0s (Bedregal *et al.* 2011; Johnston *et al.* 2012; con-

trary to earlier results, e.g., Fisher, Franx & Illingworth 1996), as well as hints of a brightened population in the Tully-Fisher relation (Bamford *et al.*, 2005; Bösch *et al.*, 2013b). The process responsible for a more centrally concentrated young population could be either a suppression of star formation in the outer parts (due to gas heating or stripping) or star formation enhancement in the central regions (perhaps due to inward movement or perturbation of gas within the galaxy).

Recent studies have found disturbed kinematics in the emission-line gas in cluster spirals, from which their final generation of stars would be expected to form (Jaffé *et al.*, 2011; Bösch *et al.*, 2013a). The increased central concentration of the young population in many of our galaxies is certainly consistent with a decrease in the degree of rotational support. Unfortunately, the quality of our data makes it hard to directly determine whether the relative velocity dispersion of the young stars in our cluster spirals is higher than that of the old stellar populations. However, together these results suggest that future studies of cluster S0s may expect to find that the most recent disk stellar population has a smaller scalelength (and possibly greater scaleheight) compared to previous generations, implying the presence of a young, small, thick disk. Such a feature may also be interpreted as a lens or additional exponential bulge (Erwin *et al.*, 2015).

Dust may also play a role in accelerating the progression of the observational signatures that would be associated with a transition. The concentration of star formation, as described above, to the dustier inner regions of galaxies (Driver *et al.*, 2007) results in a greater fraction of that star formation being obscured from optical indicators (Wolf *et al.*, 2009). The transition stage may thus be hidden from optical studies, but a population of dusty, red galaxies forming stars at a significant, though possibly suppressed, rate is revealed by observations at longer wavelengths (Gallazzi *et al.*, 2009; Geach *et al.*, 2009).

Our results indicate that galaxy–galaxy interactions may be associated with stronger or more recent truncated starbursts, and hence may be a significant transition mechanism. We therefore support the conclusions of Moran *et al.* (2007), that a combination of galaxy–galaxy interactions, ram-pressure stripping, and other more minor mechanisms are responsible for spiral to S0 transformation.

Galaxy–galaxy interactions have long been theoretically associated with strong bar formation and nuclear starbursts (e.g., Mihos & Hernquist 1996). However, due to the high relative velocities of galaxies in a dense environment, tidal interactions can also have a relatively gentle effect (Moore *et al.*, 1996). There is growing observational evidence that even pair interactions may not cause nuclear starbursts as readily as anticipated, enhancing star formation in spiral arms instead (e.g., Casteels *et al.* 2013). Furthermore, bars are found to be prevalent in gas-poor, red spirals (e.g., Masters *et al.* 2011, 2012), and so may be more associated with the suppression of star formation, rather than its enhancement.

The final argument for a spiral to lenticular tranformation is the properties of the final galaxies. Lenticulars are consistent with being formed from faded spirals in terms of their Tully-Fisher relation (Bedregal, Aragón-Salamanca & Merrifield, 2006), globular cluster specific frequencies (Aragón-Salamanca, Bedregal & Merrifield, 2006). However, they do tend to be more bulge dominated (Christlein & Zabludoff, 2004) and have hotter disks than spiral galaxies (Cortesi *et al.*, 2013). This can be achieved by an enhancement of central star formation prior to transformation, and a marginal increase in pressure support, perhaps through an accumulation of galaxy-galaxy interactions. Both of these processes are suggested by our results and many of the other studies discussed above. The clearing of dust in the central regions during the transition from spiral to S0 may also enhance the bulge-to-disk ratio (Driver *et al.*, 2007). Separately measuring the stellar population properties of bulges and disks for large samples of spiral and S0 galaxies, in both spectroscopic (e.g., Johnston *et al.* 2012) and multi-band photometric data (e.g., Simard *et al.* 2011; Lackner & Gunn 2012; Bamford *et al.* 2012; Häußler *et al.* 2013), will help to fill in many of the missing details.

2.5 Conclusions

The transformation from spiral galaxies into S0s must comprise a spectral transformation, resulting from the suppression of star formation in the disk of the galaxy; a morphological transformation, in terms of the removal of spiral features from the disk and growth of the bulge; and a modest dynamical transformation, with a relatively

small increase in the ratio of pressure versus rotational support.

We have studied the significance of disky 'k+a' galaxies, indicative of a spiral galaxy in which star formation was truncated ~ 0.5–1.5 Gyr ago, as the possible intermediate step in the transformation of star-forming spirals into passive S0s in the intermediate-redshift cluster environment.

These galaxies are typically identified by their strong Balmer absorption line equivalent widths, an expected signature of a dominant ~ 1 Gyr old stellar population. We have used spectral template fitting to show that galaxies selected via the $\mathrm{H}\delta_F$ index do, indeed, contain significant fractions of A-type stars and stellar populations with ages between 0.5 and 1.5 Gyr. We study the spatial distribution of the young population using these different indicators, finding generally consistent results. While the disky 'k+a' galaxies appear to be a rather mixed population, their final episode of star formation is always distributed over a region of size similar to, or somewhat smaller than, the older stars.

We have coarsely measured the velocity field of these galaxies, both in terms of the full stellar population and, in a limited number of cases, the separate young and old populations. The results support the picture that, in the majority of our sample, the last generation of stars formed in a disk, in a very similar manner to previous generations.

None of the disky 'k+a' galaxies in this intermediate redshift cluster appear to have experienced a violent event, such as a merger or significant nuclear starburst, prior to the truncation of their star formation. Instead, their regular disk star formation has simply ceased with only, in some cases, a small increase in central concentration beforehand.

A relatively gentle mechanism must thus be responsible for the cessation of star formation. Gas-related mechanisms, such as ram pressure stripping, are therefore favoured. However, there is also an indication that many of our galaxies with more centrally concentrated young populations have experienced recent galaxy-galaxy interactions. This raises the possibility that, thanks to prior removal of the gas halo and outer disk, stochastic gravitational interactions may provide the necessary impetus to halt star formation, perhaps via a brief period of central enhancement.

Chapter 3

OMEGA I.– Survey description and data analysis

3.1 Introduction

In this chapter we introduce the OMEGA survey (OSIRIS Mapping of Emission-line Galaxies in A901/2). This survey was designed to study star formation and AGN activity as a function of environment in the A901/2 multi-cluster system at z ~ 0.165. This structure encompasses a wide range of environments as it contains different substructural components, which implies that it is not a relaxed system. Besides that, it has been the subject of study of the STAGES project (Gray *et al.* 2009), where a wealth of data exists: an 80-orbit F606W *HST*/ACS mosaic covering the full $\sim 0.5 \times 0.5$ deg^2 ($\sim 5 \times 5$ Mpc^2) span of the system, complemented by extensive multi-wavelength observations with *XMM-Newton*, *GALEX*, *Spitzer*, 2dF, GMRT, Magellan, and the 17-band COMBO-17 photometric redshift survey (Wolf *et al.* 2003, Wolf *et al.* 2004). This structure is then the perfect laboratory to understand the full degree of galaxy transformation and to study both obscured and unobscured star formation, stellar masses, AGN activity, and galaxy morphologies.

Previous studies of the A901/2 have looked at the star formation and AGN activity. Regarding AGN activity, Gilmour *et al.* (2007) and Gallazzi *et al.* (2009) attempted to quantify the fraction of galaxies hosting an AGN using *XMM-Newton* X-ray and

Spitzer $24\,\mu$m data; however, the lack of emission-line diagnostics in the optical prevented them from sampling the whole AGN population. With respect to star formation, a significant number of red star-forming galaxies were first discovered by Wolf, Gray & Meisenheimer (2005) using the COMBO-17 SEDs and later on studied in detail in combination with the IR data by Wolf *et al.* (2009). These galaxies appear in high fractions in the multi-cluster system and seem to be the drivers of the SFR-density relation, therefore being interpreted as a possible stage in the transformation from active to passive in the cluster environment. From the study of the global star formation properties, Gallazzi *et al.* (2009) found a significant decrease in the fraction of star-forming galaxies with environment. In a more recent work, Bösch *et al.* (2013a) find that this suppression of star formation is partially driven by ram-pressure stripping, which could lead to the production of *dusty reds* and, ultimately, S0s.

Although the integrated star-forming properties have yielded important results, crucial information about the suppression of star formation can be obtained from the actual spatial scale of the star-forming regions, which is still unknown. Likewise, the current census of AGN activity is limited to the X-Ray and IR, as no emission-line diagnostic is available yet for this multi-cluster.

In order to obtain spatially-resolved optical emission-line diagnostics, we have used the Optical System for Imaging and low Resolution Spectroscopy (OSIRIS) tunable filter at the 10.4 m Gran Telescopio Canarias (GTC) to obtain very deep spatially-resolved emission-line images of the complete A901/2 STAGES field. We have targeted the Hα ($\lambda_0 = 6563$ Å) and [NII] ($\lambda_0 = 6583$ Å) lines. The former is the best optical measurement of the SFR (Kennicutt 1998), whereas the combination of the two lines provides one of the most reliable optical AGN diagnostics available (Cid Fernandes *et al.* 2010).

In this chapter we present the design of the OSIRIS Mapping of Emission-line Galaxies in A901/2 (OMEGA) survey, the data reduction and a description of the procedure employed for the analysis of the data.

3.1.1 Data from STAGES

Before going into the description of OMEGA, we briefly describe the data from the STAGES collaboration that is used in this work. These data are combined with the OMEGA observations to study the properties of the galaxies in our sample.

From the COMBO-17 SED fits, galaxies are classified by SED type (flag `sed_type` in Gray *et al.* 2009), dividing them into normal star-forming galaxies or *blue cloud*, dust-reddened star-forming galaxies or *dusty reds*, and passive ones or *old red*. The term *dusty red* was introduced by Wolf, Gray & Meisenheimer (2005) and Wolf *et al.* (2009). These galaxies show red colours but ongoing star formation that is typically ~ 4 times lower than that in blue spirals at fixed stellar mass. The term *dusty* is perhaps misleading because they do not have more dust than normal star-forming galaxies. However, because their star formation is suppressed, their amount of dust appears relatively high compared with their star formation. Perhaps, a better name would be *red star-forming*, but we will keep the term *dusty red* throughout this thesis for consistency with previous published works.

The stellar masses of the galaxies were also obtained from the SED fits (Borch *et al.*, 2006) following two approaches. The first uses the photometric redshift of each individual galaxy, and the second assumes the cluster redshift (z = 0.167) for all galaxies (flag `logmass_cl` in Gray *et al.* 2009). In this work we use the second method since all bona-fide Hα-detected galaxies are expected to be at the cluster redshift. This avoids the undesirable propagation of photometric redshift errors. We will omit from our analysis any spiral galaxy with $\log(M/\mathrm{M}_{\odot}) > 11$ as they suffer from aperture effects and their masses are overestimated (see section 2.2 in Wolf *et al.* 2009).

Visual morphologies based on the HST images are also available for all the galaxies with $m_R \leq 23.5$ and $z_{phot} < 0.4$ (Gray et al. in preparation). Star formation rates are also provided, determined by Gallazzi *et al.* 2009 using a combination of 24μm data (to probe the obscured star formation) and COMBO-17 derived rest-frame 2800Å extinction-corrected luminosities (to probe unobscured star formation).

3.2 Description of the programme and design of the observations

The OMEGA survey was designed to obtain very deep spatially-resolved emission-line images for the A901/2 multi-cluster system and, in turn, recover low-resolution spectra in a wavelength range that covers $\mathrm{H}\alpha$ and $[\mathrm{NII}]$ for the galaxies of the system. OMEGA samples the $16.0 \leq m_R \leq 23$ magnitude range, which roughly corresponds to stellar masses of $9.0 \leq \log(M_\star/M_\odot) \leq 11.5$ at the cluster redshift. The survey is based on a 90 h ESO/GTC Large Programme allocation (PI: A. Aragón-Salamanca, GTC 2002–12ESO).

In order to meet the objectives of OMEGA, we make use of the tunable filter capabilities of the OSIRIS instrument (Cepa *et al.* 2013a, Cepa *et al.* 2013b), located at the Nasmyth-B focus of the 10.4 m GTC, at the Roque de los Muchachos Observatory on La Palma.

Tunable filter imaging is a method that lies between classical narrow-band imaging and spectroscopy, in terms of observing time costs and the quality of the information obtained. Although the spectral resolution is relatively low, the wavelength sampling is quite sufficient for reliable star formation and AGN activity estimates for most of the cluster members. Using traditional spectroscopy to map the spectral region around $\mathrm{H}\alpha$, $[\mathrm{NII}]\,\lambda6548$ and $[\mathrm{NII}]\,\lambda6583$ for all the galaxies in the A901/2 would definitely be much more expensive.

A further advantage of tunable filter imaging, with respect to slit spectroscopy, is the spatial information that it provides. While long-slit spectroscopy normally only provides information along one of the axes of the galaxies (usually chosen to be the major axis), tunable filter imaging provides 2D maps. The tunable filter technique has been used very few times in this field, with only a few heroic attempts such as the the CADIS survey of emission line galaxies measuring SFRs between $z = 0.25$ and $z = 1.2$ (Hippelein *et al.* 2003).

Our higher spectral resolution compared to standard narrow-band $\mathrm{H}\alpha$ imaging surveys (see, e.g., Kennicutt 1992, Gallego *et al.* 1997) has the advantages of avoiding contamination from the $[\mathrm{NII}]$ line in the star formation estimates and providing reliable

identification of AGN (Cid Fernandes *et al.* 2010).

Finally, while IFS surveys such as CALIFA (Sánchez *et al.*, 2012), MaNGA (Bundy *et al.*, 2015) and those carried out with the recently installed MUSE (Bacon *et al.*, 2010) on the VLT also provide spatial information, their fields of view are much smaller than that of OSIRIS. The full unvignetted field-of-view (FOV) of OSIRIS is $7.8 \times 7.8\ \mathrm{arcmin}^2$, imaged using two 2048×4096 Marconi CCDs with a $9.4\ \mathrm{arcsec}$ gap between them. The plate scale, using 2×2 pixel binning, is $\sim 0.25\ \mathrm{arcsec\,pixel}^{-1}$. Therefore, with OSIRIS we have access to a larger number of galaxies than we would do using current IFSs.

The OSIRIS tunable filter system consists of two reflecting plates (a Fabry-Pérot etalon) working in a collimated beam. The wavelength of the light transmitted can be tuned by modifying the separation between the optical plates of the device, whereas standard narrow-band order-sorting filters (OSF) are used to isolate specific interference orders. Reliable observations are limited to a circular field of view of radius $4\ \mathrm{arcmin}$, within which they are assured to be free from contamination by other orders. OSIRIS has two different tunable filters, one for the blue and one for the red wavelength range. We use the latter, which is capable of tuning filters to wavelengths in the 6510–9350 Å range with a spectral resolution of 14Å FWHM.

A given radius from the optical centre in the image plane corresponds to a specific angle of an incident collimated beam on the Fabry-Perot etalon. As the transmission wavelength of the interferometer depends upon incidence angle, the wavelength of the transmitted light varies with the position in the image. The result is a circular pattern with rings of constant effective wavelength, λ, which depends on the radius, r, from the optical centre. The adopted procedure for the wavelength calibration is given in section 3.3.2

In Fig. 3.1 we show the OSIRIS observed fields as circles $8\ \mathrm{arcmin}$ in diameter, overlaid on top of the footprint of the 80-tile STAGES *HST*/ACS mosaic (Gray *et al.*, 2009) and ground-based COMBO-17 R-band image (Wolf *et al.*, 2004). Cluster galaxies with $m_R < 23$ are also plotted. Given the available observing time, the initial plan was to tile the field-of-view uniformly in a 4×5 grid. However, the North-East and North-West tiles contain bright stars that would have produced reflection ghosts, seri-

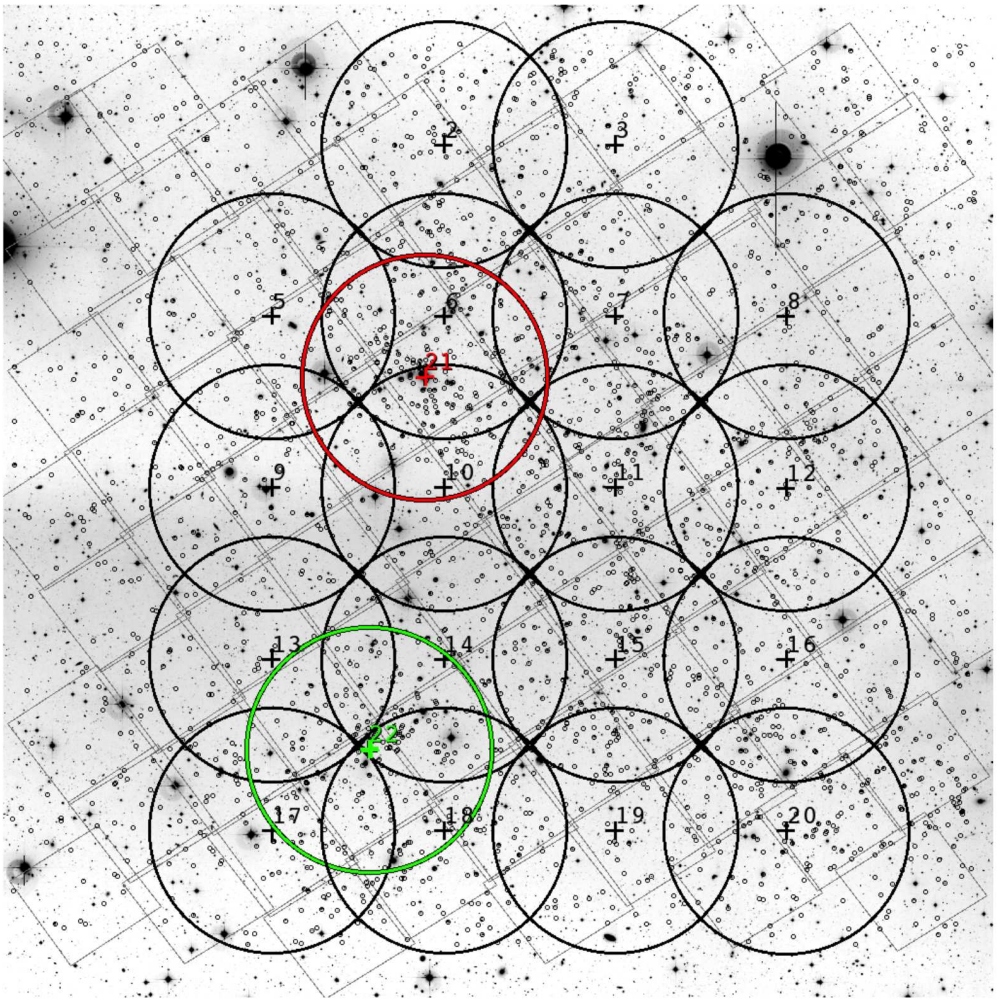

Figure 3.1: The OSIRIS observed fields (labeled 2–3, 5–22), represented as circles of radius 4 arcmin, overlaid on top of the footprint of the 80-tile STAGES HST/ACS mosaic and a COMBO-17 R-band image. The very small black circles mark the position of cluster galaxies with $m_R < 23$, where cluster membership is defined as in Gray *et al.* (2009) using the COMBO-17 photometric redshifts.

ously compromising the quality of the data for these tiles. For this reason, we decided to re-locate these two pointings to cover the regions with the highest galaxy densities, which correspond to Fields 21 (A901a) and 22 (A902).

Fig. 3.2 shows the spectroscopically determined redshift distribution of galaxies within 1.2 Mpc diameter apertures centred upon the three main cluster cores. The redshifts were drawn from a spectroscopic survey of the 300 brightest cluster galaxies in the region obtained with the AAT 2dF spectrograph (Gray et al., in prep.). The dashed lines indicate the redshift range probed by our observations which is chosen to target both Hα and [NII] $\lambda6583$ emission lines. The z ranges are slightly narrower for the two pointed observations of the A901a and A902 regions (F21 and F22).

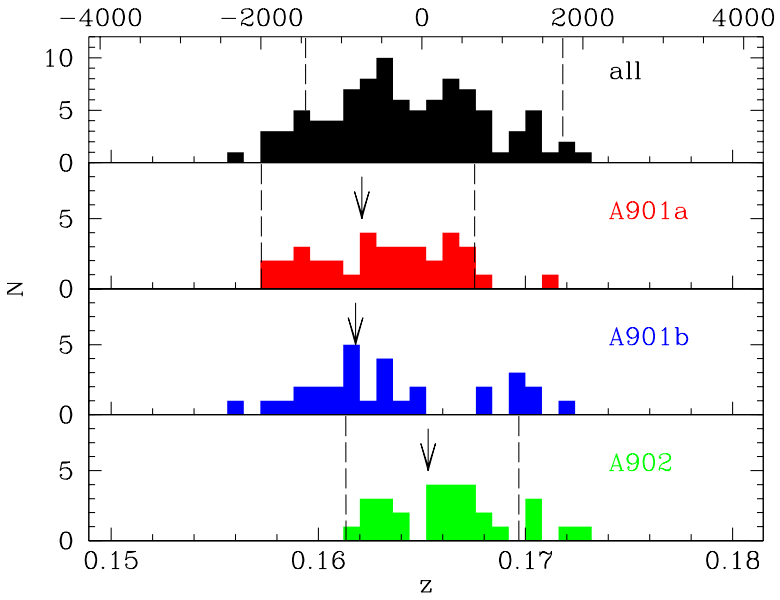

Figure 3.2: Redshift distribution of galaxies within 1.2 Mpc diameter apertures around the three main cluster cores, from a limited spectroscopic survey of the ∼300 brightest galaxies in the region, taken with the AAT 2dF instrument. Arrows mark the positions of the brightest cluster galaxies. Dashed lines indicate the velocity range probed by OMEGA: the top histogram indicates the limits of the survey proper (fields 2, 3 and 5–20), while the ranges for the two pointed observations of the A901a and A902 cluster cores (fields 21 and 22 respectively) are especially tuned (cf. Table 3.1).

For an optimal de-blending of Hα and [NII] λ6583, the tunable filter FWHM bandwidth is set to 14 Å, and the spacing between successive wavelengths to 7 Å. Therefore, in order to cover the desired wavelength range in F21 and F22 we require 14 and 12 wavelength settings, respectively, whereas for the rest of the fields we need 16 wavelength settings (see Figs. 3.2 and 3.3, and Table 3.1). Moreover, for each wavelength setting, 3 dithered images are taken typically with a $\sim$ 40 pix (10″) separation. The dithered images increase our number of images (and individual wavelengths sampled) by a factor of three and ensure that the inter-CCD gap is imaged. A total of 42 and 36 images have been obtained for Fields 21 and 22 respectively, and 48 for the remaining 18 fields.

Since the wavelength varies across the FOV, the central wavelength λ_c of each wavelength setting needs to be optimised in such a way that the desired wavelength range is covered for as many galaxies as possible. The average wavelength λ_{ave} of each setting was calculated as the mean λ within the central 5.6 arcmin diameter circle of each pointing (the approximate area uniquely covered by one tile). For fields F2 to F20, 7609 Å $\leq \lambda_{ave} \leq$ 7714 Å, ensuring that both Hα and [NII] are observed in the $0.1594 \leq z \leq 0.1718$ redshift ranges. This corresponds to rest-frame velocities in

Table 3.1: Summary of the Observations.

OBs (F2-20)	OBs (A901a/F21)	OBs (A902/F22)	λ_c (Å)	λ_{ave} (Å)	OSF	Exp. Time (s)
	1		7615	7595	f754/50	3×200
	1		7622	7602	f754/50	3×200
1	1		7629	7609	f754/50	3×200
1	1		7636	7616	f754/50	3×200
1	2	1	7643	7623	f754/50	3×200
1	2	1	7650	7630	f754/50	3×200
2	2	1	7657	7637	f754/50	3×200
2	3	1	7664	7644	f754/50	3×200
2	3	2	7671	7651	f754/50	3×200
2	3	2	7678	7658	f754/50	3×200
3	4	2	7685	7665	f770/50	3×200
3	4	2	7692	7672	f770/50	3×200
3	4	3	7699	7679	f770/50	3×200
3	4	3	7706	7686	f770/50	3×200
4		3	7713	7693	f770/50	3×200
4		3	7720	7700	f770/50	3×200
4			7727	7707	f770/50	3×200
4			7734	7714	f770/50	3×200

the range $-1447 \leq v \leq 1751$, where $v = 0$ corresponds to $z = 0.165$, the average redshift of the multi-cluster. For field F21, $7595\,\text{Å} \leq \lambda_{ave} \leq 7686\,\text{Å}$, and for F22, $7623\,\text{Å} \leq \lambda_{ave} \leq 7700\,\text{Å}$, thus covering a slightly narrower redshift/velocity range for these two fields (see Fig. 3.2 and Table 3.1 for details). Note that these are average values: the exact wavelength range covered for each galaxy depends on its position with respect to the centre of the pointing. Moreover, given the significant tile overlap, a sizeable fraction of the galaxies will be observed in more than one pointing, increasing the available wavelength range and the number of independent wavelength samples obtained.

A summary of the observational setup is given in Table 3.1. The observations were executed in 'Observing Blocks' (OBs), as shown in Table 3.1 and illustrated in Fig. 3.3. They were carried out during the first half of 2012 and 2013, and completed in February 2014.

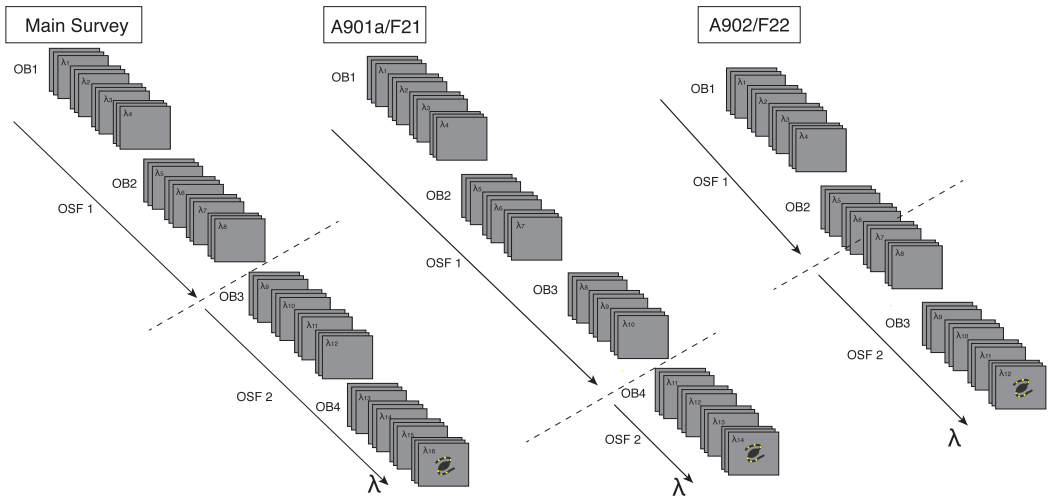

Figure 3.3: A cartoon illustrating the design of the observations for the main survey and the two cluster core fields (F21 and F22). Note that this illustration is valid in the case of a single galaxy, for which the wavelength is almost constant (for a given image there is wavelength variation across the field-of-view, see Eq. 3.3.2 and Fig. 3.5). A given galaxy is observed using a series of wavelength setups λ_i and a 3-position dithered pattern. In each dithered position the wavelength changes slightly because the distance to the centre of the field changes. The order-sorting filter (OSF) separates the different tuned wavelengths. The observations are executed in 'Observing Blocks' (OBs).

3.3 Data Reduction

In this section we describe the data reduction methods we have developed for the OMEGA data.

3.3.1 Imaging Data Reduction

The data reduction was carried out with the Osiris Offline Pipeline software OOPs. The OOPs reduction consists of two steps. In the first step the calibration files 'masterbias' and 'masterflat' are prepared combining the individual bias and flatfield frames taken at the telescope. Flatfields were obtained using dome flats with the filter tuned to the same wavelength as the science observations. Usually 3–5 flat frames were taken each night at each wavelength. In the second step the science frames are reduced, removing the overscan and subtracting the bias from the science frames, which are then divided by the masterflat. The vignetted regions of the images are also trimmed at this stage.

The final step carried out within OOPs is the sky subtraction. Due to the wavelength variation across the FOV, sky OH emission lines appear as rings (see left panel of

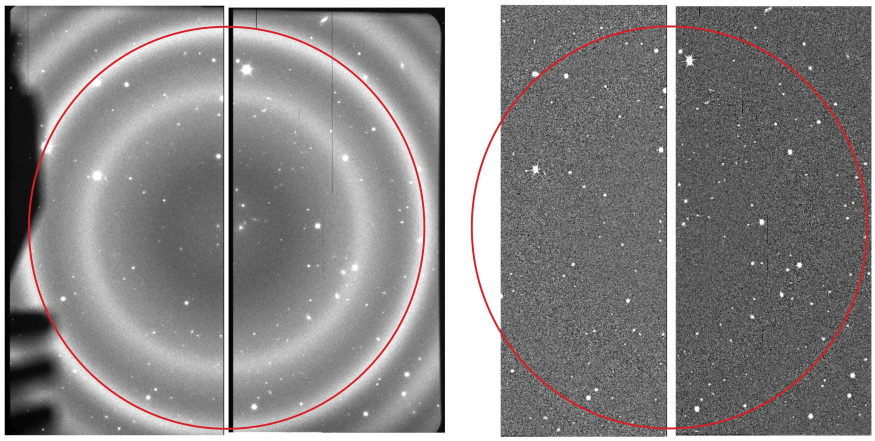

Figure 3.4: Example of the first image of F21 with $\lambda_c = 7615$ Å. *Left panel:* raw image. *Right panel:* after OOPs processing. The red circle has a radius of 4 arcmin, within which the observations are free from contamination by other interference orders.

Fig. 3.4). To correct for these features, each science exposure is artificially dithered on a 3 by 3 grid. The dither step size (a few arcseconds) is larger than the vast majority of the objects, but small compared to the ring features. Therefore, median-combining the dithered images leaves only the sky rings. These can then be subtracted from the original image. Fig. 3.4 presents the first image of Field 21, with $\lambda_c = 7615$ Å. The left panel shows the raw image while the left panel displays the final output from OOPs.

As mentioned in Section 3.2, we obtain three dithered exposures for each λ_c (see Fig. 3.3). This dithering introduces small shifts in the wavelength corresponding to each pixel. As we wish to retain this information, to improve our spectral sampling, we do not co-add the dithered images. To correct for cosmic rays, we therefore employ a similar routine to QZAP in IRAF applying a 3σ clipping with a flux-ratio of 0.1 (comparison value between the flux in the surrounding pixels and the flux in the candidate one to check whether the pixel has been hit by a cosmic ray).

Bad pixels are corrected using the IRAF task FIXPIX. Astrometry solutions are found using CCMAP and CCSETWCS in IRAF with the COMBO-17 R-band image as reference. In order to avoid unnecessary distortions, we work with the two separate CCDs of OSIRIS throughout the analysis, obtaining astrometric solutions with rms accuracies ≤ 0.1 arcsec.

3.3.2 Wavelength Calibration

The nature of the observations mean that the wavelength of a given object will depend on the central wavelength of each image as well as its distance to the optical centre, parameters that change for different exposures. The wavelength calibration of the OSIRIS Tunable filter has been a question of debate (Méndez-Abreu *et al.* 2011) because its accuracy is crucial for studies of extended sources, as well as for estimating redshifts of both point-like and extended sources. Fortunately, the sizes of our objects are small (the largest objects have a radius of ~ 7 arcsec), and hence the wavelength changes are negligible across individual objects in the OMEGA sample (at most ~ 2Å, i.e., much smaller than the spectral resolution).
In order to achieve the best accuracy in the estimation of the wavelength we use the following expression (González *et al.* 2014):

$$\lambda = \lambda_0 - 5.04\, r^2 \; + a_3(\lambda) r^3, \tag{3.1}$$

where

$$a_3(\lambda) = 6.0396 - 1.5698 \times 10^{-3}\lambda + 1.0024 \times 10^{-7}\lambda^2, \tag{3.2}$$

where λ is in Å and λ_0 is the effective wavelength at the optical centre. Since the usable FOV is limited to a radius of 4 arcmin, the maximum variation in the effective wavelength is ~ 80 Å. The variation of wavelength across the field-of-view for a given central wavelength is shown in Fig. 3.5.
The optical centre is located on pixel $X_0 = 1051$ and $Y_0 = 976$ (CCD1) and $X_0 = -10$ and $Y_0 = 976$ (CCD2) of the raw images, according to the OSIRIS website.[1] This corresponds to $X_0 = 772$, $Y_0 = 976$ (CCD1) and $X_0 = -35$ and $Y_0 = 976$ (CCD2) on the images output from OOPs. Although there are other optical centres listed in the literature (Méndez-Abreu *et al.* 2011 and the OSIRIS manual), the change they introduce is smaller than 0.2 per cent in wavelength.

[1] http://www.gtc.iac.es/instruments/osiris/

3.3.2.1 Additional refinements

Although it was not noticed in the analysis of the first two fields F21 and F22, when comparing the spectra of galaxies obtained in different overlapping fields, we found that in some cases there were significant wavelength offsets. The magnitude of the offsets varied from field to field, and in the case of the preliminary analysis of F21 and F22 it did not affect the flux estimates. However, for the general goals of the survey we do need much better accuracy in the estimation of the observed wavelength.

An improved wavelength calibration was developed by Tim Weinzirl and Alfonso Aragón-Salamanca (private communication). This new calibration was obtained by comparing the sky lines present in the OSIRIS raw spectra with the OSIRIS sky spectrum provided by GTC, which was convolved with a 14Å FWHM Gaussian kernel to simulate what the sky spectrum should look like given our chosen instrument settings. The sky spectrum from our data was generated in two steps: first, the final sky-subtracted frame (last data product of OOPs, section 3.3.1) was subtracted from an intermediate-step frame still containing the sky; second, the sky frames were converted from Cartesian x–y coordinates into polar r–θ. This coordinate change transforms circles in the image plane into straight lines in the r–θ plane, which are easier to manipulate. The transformed frames were collapsed by taking the median flux over all θ at a given radius. Then, the sky lines within a radius of 4 arcmin were identified and their peaks measured. Assuming that the wavelength dependence on radius provided by González *et al.* (2014, Equation 3.1) was correct (also tested and confirmed), the frame-by-frame wavelength offsets between the detected skylines and the simulated sky spectrum were calculated. The overall average offset was calculated for each wavelength setting in a given field, and that correction was applied to correct the central wavelength setting as calculated by (González *et al.*, 2014). Correcting the central wavelengths with the offsets calculated from the sky lines in this way yielded a wavelength calibration accurate to within $\pm$ 0.5 Å for most (75$\%$) of the individual image frames, and accurate to within $\pm$ 1Å for 95$\%$ of the frames. All the results presented in this thesis are based on the refined wavelength calibration.

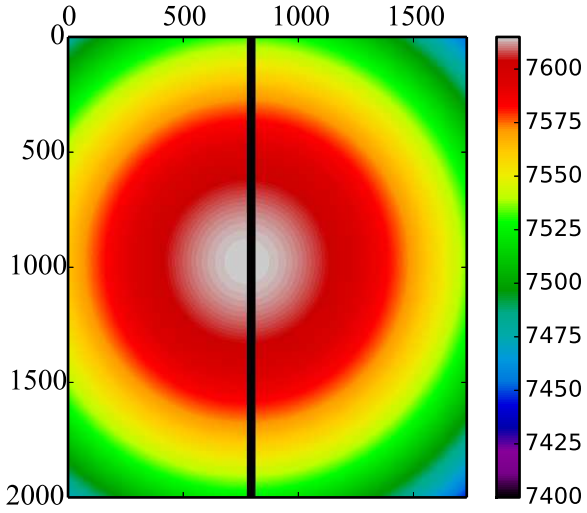

Figure 3.5: A mock reduced image with $\lambda_c = 7615$ Å, illustrating the radial dependence of wavelength according to the colour bar (labelled by wavelength in Å). The vertical line in the middle represents the 9.4 arcsec gap between CCD1 and CCD2.

3.3.3 Flux calibration and zero-point estimation

Different image sets (OBs) for a single field are not necessarily observed on the same night or with the same observing conditions. In order to perform consistent photometry, we therefore need to correct for differences in the seeing conditions, transparency and airmass.

To match the seeing conditions our procedure is as follows: we measure the PSF in all the images of all the fields using unsaturated stars with $m_{R,\mathrm{COMBO-17}} < 19$ (from the STAGES catalogue of Gray *et al.* 2009). We then convolve each image with a Gaussian function of the required width to produce images with a PSF equal to the worst seeing, which is 1.2 arcsec. These operations were performed using the IRAF tasks PSFMEASURE and GAUSSIAN.

We perform photometric measurements using PHOT within IRAF on the stars in each individual OSIRIS image (typically, 15–25 stars per field) using an aperture of 2 arcsec (8 pixels) radius, sufficient to measure the total flux for these point sources. Because the wavelength at which each star is observed varies for different images, we obtain a wavelength-dependent zero-point $zp(\lambda)$ function,

$$zp(\lambda) = m_{\star\,\mathrm{W753f}} - m_{\star\,\mathrm{OSIRIS}}\ , \tag{3.3}$$

where $m_{\star\,\mathrm{W753f}}$ is the standard magnitude of that star, defined below, and $m_{\star\,\mathrm{OSIRIS}}$ is the instrumental magnitude of the star measured in PHOT.

To calibrate our fluxes we use the Vega magnitudes, $m_{\star\,\mathrm{W753f}}$, of the same stars in the closest COMBO-17 filter, $\mathrm{W753f}$, as standard magnitudes. This filter samples the range 7440–7620 Å. Vega magnitudes were calculated from the photon fluxes tabulated in the COMBO-17 catalogue. Our zero-point functions are shown in Fig. 3.6. Because there is a strong absorption feature caused by a double telluric sky line at $\lambda = 7633$ Å, the zero-point function has a strong wavelength dependency.

In order to correct for the effect of the atmospheric telluric absorption in each field, we fit this feature with a series of Chebyshev polynomials. The shape of the absorption feature is constant, except for a scaling factor and offset that vary with the observing conditions. We therefore fit all the zero-point functions in one field simultaneously, to obtain a general set of polynomial coefficients, together with an offset and scaling factor for each image. As an example, in Fig. 3.6 we show the zero-points for F21, as well as the fits and residuals, as a function of wavelength. For clarity, we only show the zero-points for 4 of the 14 images.

The scatter in the zero-point introduces additional wavelength-dependent errors that must be incorporated in our photometric uncertainties. We estimate these by taking a 3σ–clipped standard deviation of the residuals in bins of 10 Å. These zero-point errors are found to be always $\lesssim 0.1$ mag.

3.3.4 Galaxy photometry

We perform aperture photometry on the galaxies with PHOT. We measure each galaxy using two apertures: a PSF-matched aperture of radius 1.2 arcsec (5 pixels, from now on referred to as R_{PSF}) and a total aperture (essentially the Kron radius; Bertin & Arnouts 1996), with $R_{\mathrm{tot}} = 2.5 \times SMA$. Here SMA is the second central moment of the light distribution, derived from ACS images with SEXTRACTOR and contained within the STAGES catalogue (Gray *et al.* 2009). R_{PSF} provides information about the nucleus of a given galaxy, while R_{tot} covers its full extent. Fig. 3.7 shows the spectra constructed for one of the galaxies in F21 using both R_{PSF} and R_{tot} apertures.

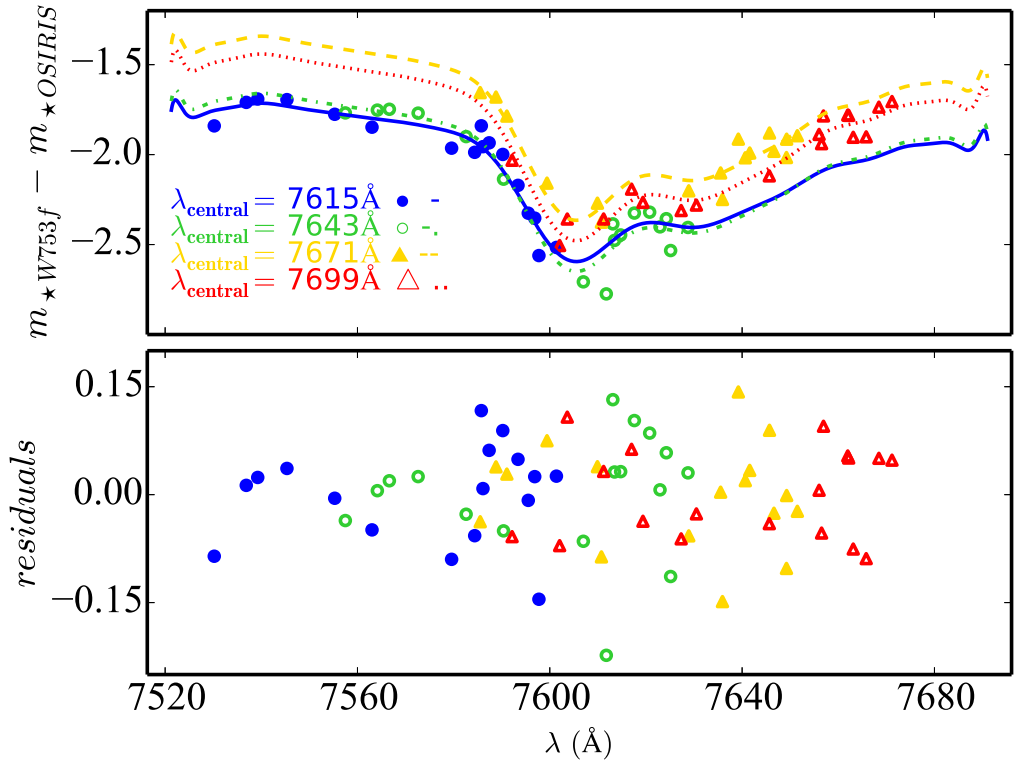

Figure 3.6: *Top panel:* The wavelength-dependent zero-point, $zp(\lambda) = m_{\star\,\mathrm{OSIRIS}} - m_{\star\,\mathrm{W753f}}$, for 4 different dithered images in Field 21. Each set of $\sim$20 stars is shown with a different colour and symbol. We only show 4 of the total 42 images for clarity. In order to model the effect of the telluric line, we fit a polynomial. The best solution for each image set is shown by the lines. *Bottom panel:* The residuals with respect to the polynomial fits.

Since at different wavelengths the galaxies' light distributions may change, we do not re-centre the aperture for each measurement, but instead fix the aperture position to the RA and DEC from the STAGES catalogue of Gray *et al.* (2009). The flux calibration is then applied to each individual field using the zero-point $zp(\lambda)$ previously obtained via Eq. 3.3:

$$m_{\mathrm{calib}}(\lambda) = m_{\mathrm{OSIRIS}}(\lambda) - zp(\lambda)\ . \tag{3.4}$$

When working in fluxes this becomes

$$F_{\mathrm{calib}}(\lambda) = F_{\mathrm{OSIRIS}}(\lambda) \times 10^{zp(\lambda)/2.5}\ , \tag{3.5}$$

where $F_{\mathrm{calib}}(\lambda)$ is our calibrated flux in $\mathrm{ergs\,cm^{-2}\,s^{-1}\,\AA^{-1}}$ and $F_{\mathrm{OSIRIS}}(\lambda)$ is the flux measured with PHOT.

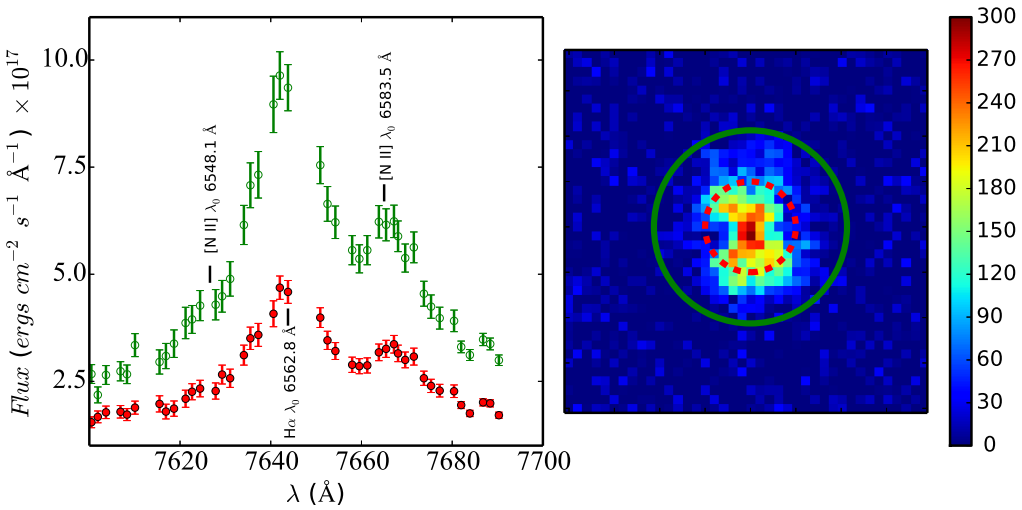

Figure 3.7: *Left panel:* The flux-calibrated spectra for the central (filled red circles) and total (open green circles) apertures of the bright ($m_R \sim 18.7$) galaxy with STAGES ID 42713. The locations of Hα ($\lambda_0 = 6562.8$ Å) and the two [NII] lines ($\lambda_0 = 6548.1$ Å and 6583.5 Å) are indicated. *Right panel:* Image of galaxy 42713 at $\lambda_c = 7664$ Å, with the $R_{\rm tot}$ and $R_{\rm PSF}$ apertures overlaid as solid green and dashed red lines, respectively. This image has not been convolved to the standard PSF although the fluxes are actually measured on the convolved images. The image is 40 pixels on a side, which corresponds to 10 arcsec or 28 kpc at $z = 0.165$. The colour bar indicates the flux in counts.

3.3.5 Building the spectra

After the flux and wavelength calibrations are performed, we are able to construct a spectrum for each of the galaxies in the observed fields. An example of such a spectrum can be found in the left panel of Fig. 3.7, where we indicate the location of Hα and the two [NII] lines with their respective rest-frame wavelengths. By design, the wavelength range of the spectra for cluster members should cover both Hα and [NII] λ6583, which will appear as emission lines in galaxies hosting star formation and/or AGN activity. In addition to finding spectra of galaxies with clear emission lines, we also expect to obtain spectra of galaxies with weak or absent emission (or absorption in Hα) lines.

3.4 Analysis

3.4.1 Spectral fitting

Our goal is to measure fluxes for Hα as well as the brightest [NII] line at 6583 Å. We also wish to obtain reliable constraints for the continuum, in order to measure the

equivalent widths ($W_{\mathrm{H}\alpha}$ and $W_{[\mathrm{NII}]}$) of these lines. Due to the limited wavelength coverage and the moderate spectral resolution and sampling of our spectra, this exercise becomes very challenging for weak emission-line galaxies.

To account for all the features present in our spectra, we fit them with a composite of three Gaussian functions and a linear continuum

$$f_{model}(\lambda) = c_0\lambda + c_1 + \mathcal{N}(\lambda_{H\alpha}(1+z)|F_{H\alpha}, \sigma_{H\alpha}) + \mathcal{N}(\lambda_{[N\mathrm{II}]\lambda6548}(1+z)|F_{[N\mathrm{II}]\lambda6548}, \sigma_{[N\mathrm{II}]}) + \mathcal{N}(\lambda_{[N\mathrm{II}]\lambda6583}(1+z)|F_{[N\mathrm{II}]\lambda6583}, \sigma_{[N\mathrm{II}]}) \tag{3.6}$$

where c_0 and c_1 are the continuum slope and intercept, z is the redshift of the galaxy and σ is the width of the emission lines in Å. The notation $\mathcal{N}(\lambda_0|F, \sigma)$ indicates a Gaussian distribution evaluated at λ_0 with total flux F and standard deviation σ .

In this model, the two $[\mathrm{NII}]$ emission lines have the same width, which is limited by the instrumental resolution (see below). The ratio between their fluxes is also fixed by atomic physics to a value of 3.06 (determined by the ratio between the transition probabilities of each line in Osterbrock 1989), thus only one parameter ($F_{[N\mathrm{II}]\lambda6583}$) is needed to fit both fluxes. Therefore, our model depends on six parameters: c_0, c_1, z, $\sigma_{H\alpha}$, $F_{\mathrm{H}\alpha}$ and $F_{[\mathrm{NII}]}$.

In order to exploit all the information contained in our data, the fitting procedure must evaluate all possible combinations of the parameters in a thorough yet efficient way. Conventional fitting techniques, such as Levenberg-Marquardt optimisation, can be sensitive to the initial values, and can become trapped in local maxima in the parameter likelihood space. These problems can be ameliorated by a Bayesian approach based on Markov Chain Monte Carlo (MCMC) techniques. From the Bayes theorem, the posterior probability density distribution $\mathcal{P}(\theta|x)$, which describes how likely each possible set of model parameters θ is given the data x, is proportional to the product of the prior distribution $\pi(\theta)$ and the likelihood function $\mathcal{L}$

$$\mathcal{P}(\theta|x) \propto \mathcal{L}(\theta|x) \cdot \pi(\theta), \tag{3.7}$$

The prior distribution can be thought of as pre-existing constraints on the parameter values whereas the likelihood function describes how closely the data correspond to the model, for a given set of parameters.

The MCMC technique generates a series of random walks or chains that explore the parameter space in such a way that it is sampled in proportion to the posterior probability density. Along a chain, at each step new values for the parameters are proposed. These are accepted or rejected, depending on the probability of the proposed values relative to that of the current parameter set. If the probability is higher, then the proposed parameters will be adopted, and the chain will move to a new point in the parameter space. However, if the probability is lower, the chain will remain in the same position, although the method still gives some chance of the new values being accepted. In this way, the parameter space is thoroughly explored and the posterior distribution efficiently sampled. The posterior distribution contains the probability density distributions of all the parameters, and therefore one can extract from it the expected values of any function of the parameters and its uncertainties.

For the analysis of our spectra we use the software EMCEE (Foreman-Mackey *et al.* 2013), which implements the Affine Invariant MCMC Ensemble sampler of González *et al.* (2010). The Affine Invariant MCMC Ensemble sampler uses multiple 'walkers' to produce a set of chains. These are started at different points of the parameter space. Each walker moves following a proposal distribution that depends on the current position of the rest of the walkers. We also make use of parallel tempering, which uses walkers at different temperatures (T) sampling flatter versions of the likelihood $\mathcal{L}_T = \mathcal{L}^{1/T}$. In this way, at higher temperatures the walkers can escape from local maxima. Walkers also exchange temperatures allowing different frequency of sampling for different regions. Parallel tempering eases the communication in the case of multimodal posterior distributions and generally speeds up convergence.

The performance of the MCMC depends on two issues: the 'initialization bias' and the 'autocorrelation in equilibrium' (Sokal 1996). The first one refers to the need of reaching the equilibrium distribution and therefore 'erasing' any dependence on the initial conditions. This check is done by estimating the autocorrelation time in an initial run of the MCMC or burn-in phase, which is an estimate of the number of steps needed before the samples drawn from the target density are independent. This burn-in phase is then discarded and not included in the posterior distribution. The second issue implies that once the chains have reached equilibrium, we need to take enough

samples to obtain a statistically-significant estimate of the errors. Therefore two of the key factors ensuring a good performance of the MCMC sampling are the length of the chains and the number of walkers.

To ensure a good performance for our analysis we use 300 walkers, a burn-in phase of 500 iterations ($\sim$10 times the autocorrelation time) which are discarded, 500 iterations after the burn-in phase and 10 different temperatures to sample the posterior distribution.

Assuming that the uncertainties follow a normal distribution, our likelihood function can be written as:

$$\ln\mathcal{L} = -\frac{1}{2}\sum_{i=1}^{n}\left(\frac{f_i - f_{\rm model}}{\sigma_i}\right)^2 = -\frac{1}{2}\chi^2, \tag{3.8}$$

where n is the number of points in each spectrum and χ^2 is the chi-square distribution.

Another factor that is instrumental for a good performance of the MCMC sampling method is the selection of the prior distributions of the parameters that appropriately constrain the regions of parameter space to be explored. The priors are flat with the shape of a step function, i.e., giving probability equal to 0 for the values outside a certain range. We use the following priors

1. $F_{[\rm NII]\,\lambda6583} > 0$;
2. z consistent with the $\rm H\alpha$ line being within the wavelength range probed by our spectrum, with an additional 20 Å window in each side; and
3. $F_{[\rm NII]\,\lambda6583} < 3\,(F_{\rm H\alpha} + \mathit{continuum})$.

The first prior forces the flux of $[\rm NII]\,\lambda6583$ (which, physically, can never be negative) to be positive; the second assumes that the $\rm H\alpha$ line lies within the spectral range; the third sets an upper limit for the $[\rm NII]\,\lambda6583$ flux such that it cannot be larger than 3 times the flux of $\rm H\alpha$ (which is the maximum value of $[\rm NII]\,/\,\rm H\alpha$ observed in the WHAN diagram (Cid Fernandes *et al.* 2010), including the possibility of up to 3 Å equivalent-width of absorption in $\rm H\alpha$.

As mentioned above, we define our model using six different parameters. This number can be reduced if we assume some properties of our spectra. First, one can assume that the slope of the continuum is roughly the same for all the galaxies, which is reasonable considering the short wavelength range covered by the OMEGA spectra ($\leq$ 200 Å). Secondly, the width of the emission lines will be limited by the instrumental resolution and only substantially broadened in cases of strong AGN (1000–25000 km s^{-1}). Due to the low spectral resolution and the faintness of some of the objects, adding these constraints will benefit the reliability of our estimates.

In order to find a fixed value for the slope of the continuum and for the instrumental width of the lines, we first perform six-parameter MCMC runs considering only those galaxies that show clear emission lines. We then select galaxies with less than 10 per cent uncertainty in the estimation of the flux in $\mathrm{H}\alpha$ and $[\mathrm{NII}]\,\lambda6583$, the width and equivalent width of the $\mathrm{H}\alpha$ line and the median value of z consistent with $\mathrm{H}\alpha$ and $[\mathrm{NII}]\,\lambda6583$ being within the wavelength range. In total we find 88 galaxies that fulfil these requirements. For these galaxies, Fig. 3.8 shows the distribution of the line-width and the slope of the continuum. The continuum slope is consistent with ~ 0 ergs cm^{-2} s^{-1} Å^{-2} $\times$ 10^{-19}, while the distribution of the width of the lines shows a clear peak at 7.5 Å. These findings allow us to confidently fix these two parameters to the mentioned values and use only a four-parameter model to fit the spectra: c_1, z, $F_{\mathrm{H}\alpha}$ and $F_{[\mathrm{NII}]}$.

In Figure 3.9 we show an example of the performance of the MCMC algorithm using a four-parameter model for the spectrum of one of our galaxies. Unless otherwise specified we summarise our fit results using the median value of the (marginalised) posterior distribution of each parameter, and estimate uncertainties from the 16th- and 84th-percentiles.

3.4.2 Defining the OMEGA sample of Emission-Line galaxies (ELGs)

After fitting the $\mathrm{H}\alpha$ and $[\mathrm{NII}]$ lines, we describe here the criteria we use to define the sample of emission-line galaxies. Our parent sample is drawn from the STAGES catalogue, where we select all the objects with $\leq m_R \leq 23$ that are detected in COMBO-17 and HST (`combo_flag` > 1 and `stages_flag` > 1 in Gray *et al.* (2009)) and lay within the 20 observed fields shown in Figure 3.1, adding up to 7600 objects.

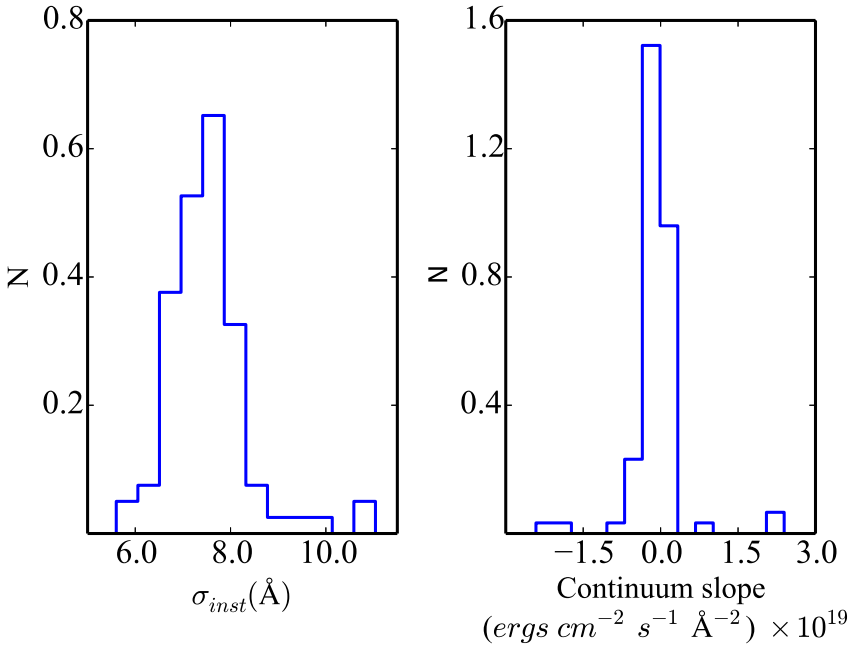

Figure 3.8: Distribution of the width (σ) of the spectral lines and the continuum slope for a sample of 88 galaxies with very clear emission lines.

3.4.2.1 Cuts based on the quality of the fits

To study the properties of the target galaxies we are interested in both the total flux of the galaxy within $R_{\rm tot}$, and the flux in the central region inside $R_{\rm PSF}$. These measurements can be quite different in galaxies with nuclear activity and in those with non-homogeneous distribution of the star formation. Therefore, the sample of galaxies in which we apply the AGN diagnostic is drawn using the measurements performed with $R_{\rm PSF}$, whereas the selection of galaxies for the study of their global properties is done using the fluxes measured within $R_{\rm tot}$.

As mentioned in section 3.2, there is a large number of galaxies observed in more than one field, especially in the regions covered by the fields 21 and 22. In these cases we only use the spectrum of the galaxy with the lowest error in the estimation of $W_{\rm H\alpha}$.

Our selection criteria are based on the probability density distributions obtained from the MCMC runs on the spectra. Aiming to include all the clear cases of spectra with emission lines, we consider those galaxies fulfilling the following selection criteria:

1. relative error$(W_{\rm H\alpha}) < 0.15$;

2. probability of detecting the Hα line in emission, $P(F_{\rm H\alpha} > 0) > 99.7$; and

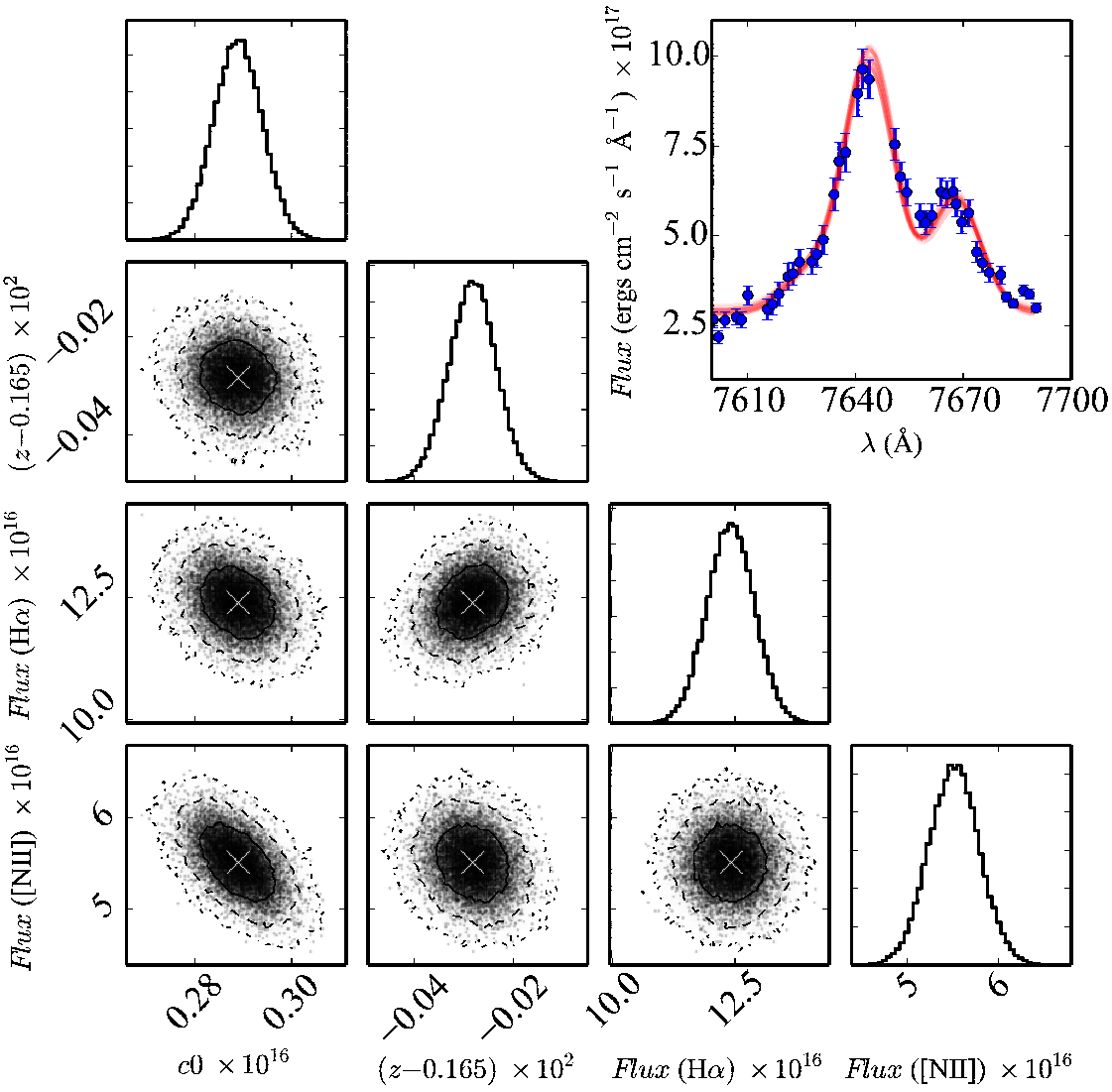

Figure 3.9: Parameter-parameter likelihood distributions with one- (solid), two- (dashed) and three- (dash-dotted) sigma contours obtained for the four-parameter model of the $R_{\rm tot}$ aperture spectrum of galaxy 42713 (the same galaxy shown in Fig. 3.7). We have fixed the continuum slope and the width of the lines as explained in the text. On the top right we show the observed spectrum (blue points) together with the model fits (red lines). We plot only 1/100 of all the individual MCMC fits for clarity, but they are all very similar. The median values of the parameters' probability distribution are plotted as a white cross on the two-dimensional distributions. The parameters shown are the continuum flux density, the redshift, and the integrated fluxes of the Hα and [NII] λ6583 emission lines. Fluxes are given in *c.g.s* units.

3. the $\mathrm{H}\alpha$ line falls within the wavelength range probed by our observations (for the R_{PSF} measurements we also require $[\mathrm{NII}]\,\lambda6583$ to fall within this wavelength range).

Applying these cuts, we include a total of 2076 galaxies. For the parts of our analysis that make use of both $\mathrm{H}\alpha$ and $[\mathrm{NII}]$ measurements within R_{PSF} (e.g., Sect. 4.2.1), we define a sub-sample requiring both $\mathrm{H}\alpha$ and $[\mathrm{NII}]\,\lambda6583$ to be within our wavelength range. This subsample contains 1725 ELGs.

3.4.2.2 Cuts based on photometric redshifts

Apart from selecting the galaxies with clear emission lines in their spectra, it is crucial to ensure that the lines we are detecting are indeed $\mathrm{H}\alpha$ and $[\mathrm{NII}]$. As explained above, our programme is designed to map these two lines in galaxies residing in the cluster system, in particular at redshifts between 0.151 and 0.176. Besides that, galaxies in front and behind the cluster are also imaged, although in these cases the rest-frame wavelength range covered is different. However it might happen that the spectrum of a non-cluster galaxy has an emission line that appears at the same observed wavelength as $\mathrm{H}\alpha$ at z ~ 0.165, and therefore would be a contaminant in our sample.

The analysis on the sources of contamination and completeness has been carried out by the OMEGA team and led by Tim Weinzirl. To understand the sources of contamination we compare our redshift estimates for the R_{tot} measurement with the COMBO-17 photometric redshifts, the spectroscopic redshifts from the AAT observations and 182 VIMOS/VLT spectroscopic redshifts of disk galaxies in A901/2 kindly provided by Asmus Böhm (Bösch *et al.*, 2013a,b). The two sets of spectroscopic redshifts were compared to detect any systematics between them that turned out not to be present, and therefore redshifts of galaxies included in both samples were averaged. A total of 186 $\mathrm{H}\alpha$ detected galaxies were matched with spectroscopic redshifts.

In Figure 3.10 we compare our redshifts with the COMBO-17 photometric redshifts only for those $\mathrm{H}\alpha$ detected galaxies with spectroscopic redshifts, and we divide them in low- and high-$W_{\mathrm{H}\alpha}$ (below and above 10Å, respectively). Galaxies with high $W_{\mathrm{H}\alpha}$ have smaller scatter than low-$W_{\mathrm{H}\alpha}$ ones, which seem to show a bimodal distribution.

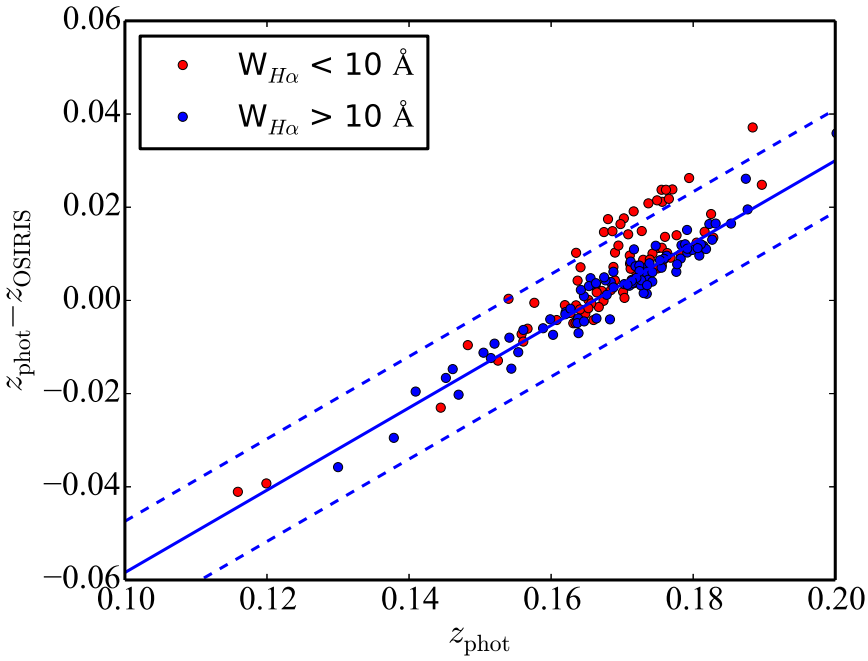

Figure 3.10: Comparison of the STAGES photometric redshifts and the ones obtained in OMEGA for the 186 Hα detected galaxies with available spectroscopic redshifts. We split the sample in low- and high-$W_{\rm H\alpha}$, shown in red and blue, respectively. The low-$W_{\rm H\alpha}$ points show larger scatter, partially due to contamination from lower-redshift galaxies where we are detecting [SII] instead of Hα. The thick and dotted blue lines show the fit to the high-$W_{\rm H\alpha}$ objects and three times the scatter between these points, respectively. The upper dotted line, with slope 0.88 and intercept 0.136, is used to remove the SII contaminants.

This bi-modality appears because in lower-redshift galaxies instead of detecting Hα we are detecting the [SII] line at $\lambda = 6724$, which generally has lower equivalent width than Hα. To discard those galaxies where [SII] is being detected instead of Hα, a line was fitted to the objects with high $W_{\rm H\alpha}$, which is shown in the plot as a blue line, together with two dotted lines indicating the 3σ scatter. All the sources above this 3σ boundary were removed. The linear fit has the following form

$$z_{\rm phot} - z_{\rm osiris} \leq 0.884 z_{\rm phot} - 0.1358. \tag{3.9}$$

To further restrict our selection to galaxies that are in the cluster system, we also perform a second cut based on the accuracy on the estimation of the photometric redshifts. We do it by using the standard deviation on the photometric redshifts from equation 5 in Gray *et al.* (2009). For a galaxy with $m_R = 19.1$ (the mean m_R among sources with spectroscopic redshifts), the standard deviation is of the order of ~ 0.006 at $z = 0.165$. We then allow a window of three times this value outside the minimum and maximum redshifts sampled by OSIRIS (0.151 and 0.176, respectively), constraining the sample

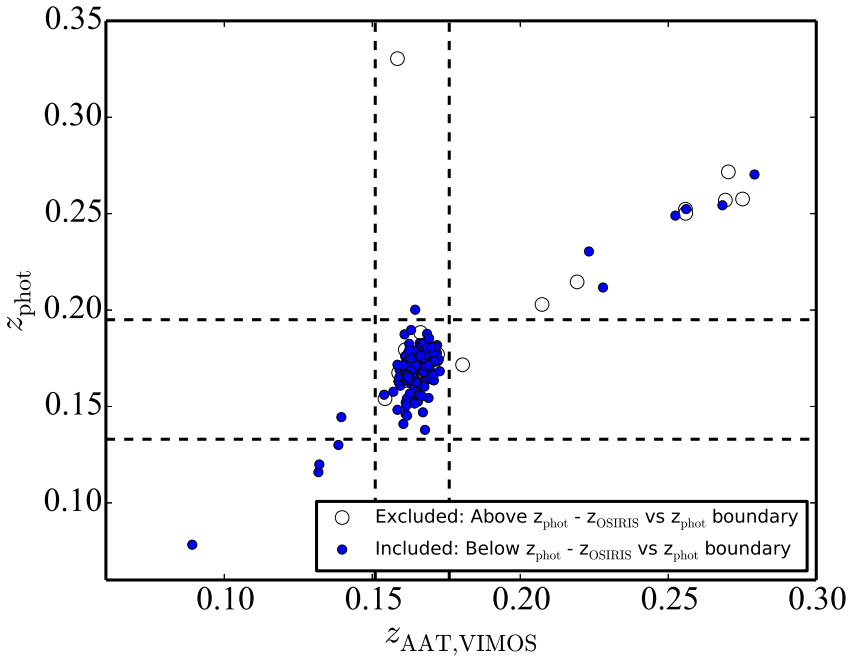

Figure 3.11: Comparison of photometric and spectroscopic redshifts for Hα detected objects with the lines delimiting our sample. Open circles are the 27 objects that were discarded as likely [SII] contaminants. The windows marking the range of values in photometric and spectroscopic redshifts are different because for the photometric redshifts we account for the uncertainty in their estimation (see text for details).

to galaxies with photometric redshifts in the range [0.133,0.195].

In Figure 3.11 we show the performance of these two cuts, comparing photometric and spectroscopic redshifts for the 186 matched galaxies. If we remove the objects above the 3σ scatter in $z_{\rm phot} - z_{\rm OSIRIS}$ vs $z_{\rm phot}$, which are in all probability [SII] contaminants, we keep a total of 159 objects. Applying the photometric redshift cut ($0.133 \leq z_{\rm phot} \leq 0.194$) we select 147 objects, of which only one object is outside the spectroscopic redshift cut (cf. figure 3.2), and therefore the contamination in our cluster definition is smaller than 1%. In the spectroscopic redshift cut, we coincidentally also select 147 objects, but of these one galaxy is not included in the photometric redshift cut. We therefore detect 146 out of the 147, which implies a redshift completeness level of $> 99\%$.

Applying all the selection criteria explained in this section, we detect Hα in a total of 622 cluster galaxies, whereas the sample requiring both Hα and [NII] to be detected contains 488 objects.

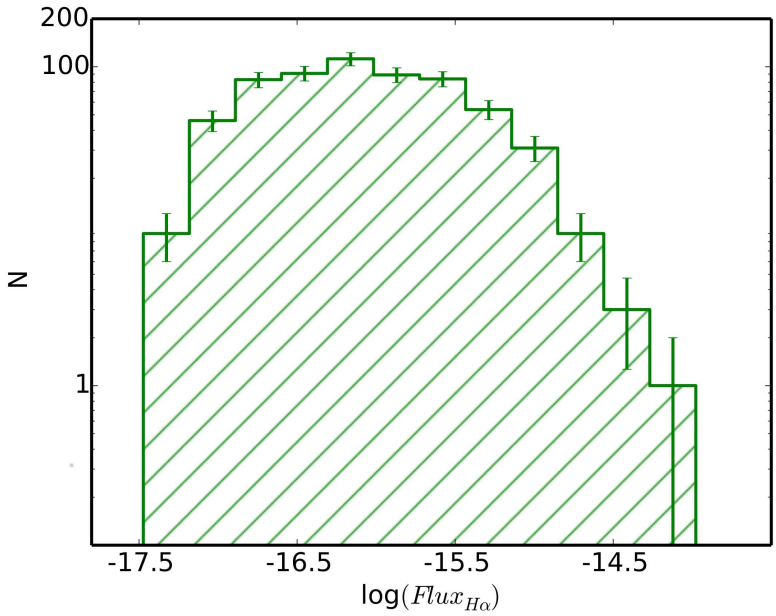

Figure 3.12: The distribution of the Hα flux for the 622 ELGs in our sample, where the error bars are $1/\sqrt{N}$.

3.4.3 Detection efficiency and limits

Our ability to detect Hα emission depends on a complex interplay between the brightness of a galaxy, its size, and its Hα flux and equivalent width. For instance, for a given Hα flux, galaxies with stronger continuum will be harder to detect. Figs. 3.12 and 3.13 show the distribution of the Hα fluxes and equivalent widths ($W_{\mathrm{H}\alpha}$) for the 622 ELGs in our sample. We are able to detect galaxies with Hα fluxes as low as $\sim 3.4 \times 10^{-18}\,\mathrm{erg\,cm^{-2}s^{-1}}$. The $W_{\mathrm{H}\alpha}$ distribution we obtain is broadly compatible with the one found by Balogh *et al.* (2004a). For equivalent widths larger than $\sim$ 20–30Å the distribution declines steeply, following roughly a power law. At lower equivalent widths the distribution flattens out until incompleteness probably kicks in below ~ 5Å. When interpreting our data it is important to bear in mind that the sensitivity of our survey declines for lower equivalent widths.

Due to the complex nature of the Hα detection process, it would be very difficult to model accurately the detection limits and the completeness of our sample from first principles. Instead, we follow an empirical approach that takes advantage of the wealth of data available from the STAGES database. Hα emission is expected to be present in blue, star-forming galaxies. Moreover, many *dusty reds* have been shown to have a

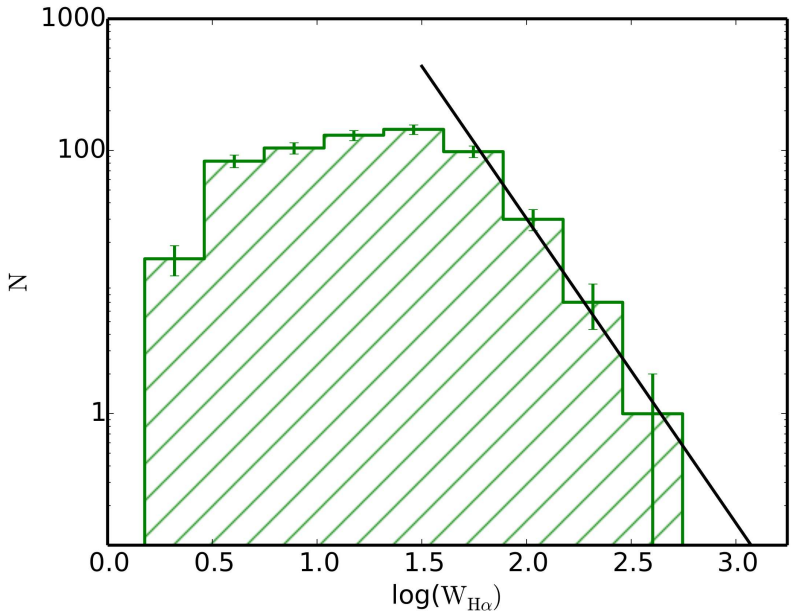

Figure 3.13: The distribution of $W_{\mathrm{H}\alpha}$ for the 622 ELGs in our sample, where the error bars are $1/\sqrt{N}$. For equivalent widths larger than $\sim$ 20–30Å the distribution declines steeply with incompleteness kicking in below $\sim$ 5Å. We have fitted a line with slope -2.3 and an intercept of 6.1.

certain degree of star formation (Wolf, Gray & Meisenheimer 2005). Here we compare our $\mathrm{H}\alpha$ detections with the numbers of blue-cloud and *dusty red* galaxies (star forming candidates) in the STAGES catalogue in order to evaluate how efficient the OMEGA survey is at detecting these two types of star-forming galaxies and to assess the sample completeness.

In the top panel of Fig. 3.14 we show the m_R distribution for the galaxies in our sample where $\mathrm{H}\alpha$ has been detected (green). For comparison, we over-plot in red and blue the distributions of *dusty reds* and *blue cloud* galaxies classified as cluster members by COMBO-17, both considered as star-forming types. The dashed histograms show the same COMBO-17 samples corrected for completeness and contamination (see below). One caveat here is that we do not separate the so-called "retired" galaxies (Cid Fernandes *et al.*, 2011; Yan & Blanton, 2012), which also have $\mathrm{H}\alpha$ emission, from the star-forming ones. More details are given in Sect. 4.2.1, when we discuss AGN activity.

As explained in section 3.4.2, the parent sample drawn from the STAGES catalogue contains $\sim$ 7600 objects, but we only consider in our study those objects with pho-

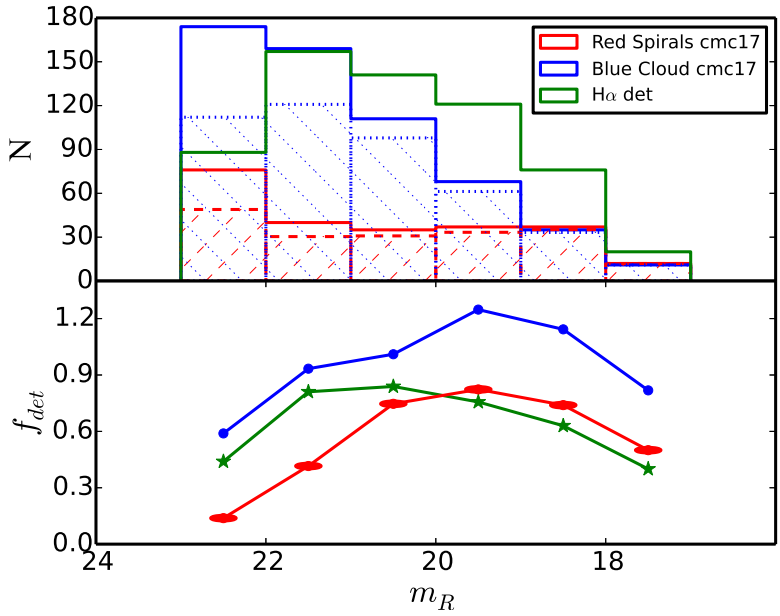

Figure 3.14: *Top panel*: the m_R distribution of *dusty reds* and *blue cloud* galaxies determined to be cluster members using the COMBO-17 photometric redshifts (sample denoted cmc17).The dashed histograms indicate the same cmc17 samples, but corrected for completeness and contamination as discussed in the text. The green square-filled histogram is the distribution of galaxies for which Hα has been detected in our OSIRIS spectra. *Bottom panel*: The Hα detection rate, expressed as a fraction of the full sample of cluster members ($f_{\mathrm{H}\alpha\,\mathrm{det}}$; green stars) and as the fraction of cluster *dusty reds* ($f_{\mathrm{RS,H}\alpha\,\mathrm{det}}$; red ellipses) and cluster *blue cloud* galaxies ($f_{\mathrm{BC,H}\alpha\,\mathrm{det}}$; blue circles), plotted as a function of m_R. See text and equations 3.13 and 3.14 for details.

tometric redshifts compatible with being cluster members (see section 3.4.2.2). This selection reduces the parent sample to 1262. Of these, 296 are *dusty reds* and 662 belong to the *blue cloud*, both thus considered to be star-forming galaxies, based on their COMBO-17 SEDs (see Sec. 3.1.1). We securely detect Hα in 107 *dusty reds* and in 435 *blue cloud* galaxies. From this we estimate that we are able to detect Hα in $\sim 36\%$ of the *dusty reds* and in $\sim 66\%$ of the *blue cloud* galaxies.

As described in Gray *et al.* (2009), the cluster membership was determined using COMBO-17 photometric redshifts. Despite the relatively high accuracy of these redshifts, the cluster sample suffers from a certain degree on incompleteness and contamination, particularly at faint magnitudes. Therefore, the "true" (corrected for incompleteness and contamination) number of cluster galaxies $N^{\mathrm{c}}_{\mathrm{cmc17}}$ can be estimated as

$$N^{\mathrm{c}}_{\mathrm{cmc17}} = \frac{N_{\mathrm{cmc17}}(1 - cont_{\mathrm{frac}})}{comp_{\mathrm{frac}}}, \tag{3.10}$$

where N_{cmc17} is the observed number of cluster members based on their photometric

redshifts. In this equation, $comp_{\rm frac}$ and $cont_{\rm frac}$ are the magnitude-dependent completeness and contamination fractions respectively (see Fig. 14 of Gray *et al.* 2009).

The "true" number of *blue cloud* (BC) cluster galaxies $N^{\rm c}_{\rm BC,cmc17}$ is

$$N^{\rm c}_{\rm BCcmc17} = \frac{N_{\rm BCcmc17}(1 - cont_{\rm frac})}{comp_{\rm frac}}, \tag{3.11}$$

where $N_{\rm BC,cmc17}$ is the observed number of *blue cloud* cluster galaxies.

Similarly, the "true" number of *dusty red* (RS) cluster galaxies $N^{\rm c}_{\rm RS,cmc17}$ is

$$N^{\rm c}_{\rm RScmc17} = \frac{N_{\rm RScmc17}(1 - cont_{\rm frac})}{comp_{\rm frac}}, \tag{3.12}$$

where $N_{\rm RS,cmc17}$ is the observed number of *dusty red* cluster galaxies.

The bottom panel of Fig. 3.14 shows as green stars the fraction of cluster galaxies detected in $\rm H\alpha$, defined as

$$f_{\rm H\alpha\,det} = \frac{N_{\rm H\alpha\,det}}{N^{\rm c}_{\rm cmc17}}, \tag{3.13}$$

as red ellipses the fraction of *dusty reds* cluster galaxies detected in $\rm H\alpha$

$$f_{\rm RS,H\alpha\,det} = \frac{N_{\rm H\alpha\,det}}{N^{\rm c}_{\rm RS,cmc17}}, \tag{3.14}$$

and as blue circles the fraction of *blue cloud* cluster galaxies detected in $\rm H\alpha$

$$f_{\rm BC,H\alpha\,det} = \frac{N_{\rm H\alpha\,det}}{N^{\rm c}_{\rm BC,cmc17}}. \tag{3.15}$$

Here we can see a clear difference in our efficiency of detecting star formation in *blue cloud* and *dusty reds*. Whereas we effectively detect $\rm H\alpha$ for all *blue cloud* cluster members brighter than $m_R \sim 20$, the fraction of *dusty reds* detected is always lower although following the same behaviour. In both cases, for fainter magnitudes, the completeness drops off, as expected – only galaxies that are bright in $\rm H\alpha$ are detected. Note that the apparent drop for galaxies brighter than $m_r \sim 19$ is due partially to low-number statistics in the brightest bins. However, massive galaxies tend to have lower specific star formation rates and thus low $W_{\rm H\alpha}$, making them harder to detect. Regarding the fraction of all cluster members, the completeness does not depend strongly on m_R since at lower masses a greater fraction of cluster galaxies are star forming. Note that $f_{\rm det} > 1$ means that we are detecting $\rm H\alpha$ in more galaxies than are expected to be star forming (based on the `sed_flag_cl` flag). This reflects both the uncertainty in the COMBO-17 SED classification and the high sensitivity of our survey.

The information on the detection efficiency and limits derived here will be used in the subsequent analysis of the properties of the galaxies presented in the following chapters.

Chapter 4

OMEGA II – Integrated properties of A901/2 galaxies.

In this chapter we present the results obtained from the analysis of the integrated properties of the galaxies in A901/2, as measured from the OSIRIS data. Here we focus on the dependence of star formation and AGN activity as a function of stellar mass, SED type, morphology and environment.

4.1 Definition of environment

We first need to define how we measure environment. Previous works using the STAGES data, such as Wolf *et al.* (2009) and Maltby *et al.* (2010), have defined their field and cluster samples using the photometric redshift distribution. In our case, OMEGA is designed to only target galaxies that are in the cluster and therefore we need a measure to account for the different environments where our cluster galaxies reside. It has been previously shown that in the A901/2 system, trends of galaxy properties with environment are more sensitive to local galaxy density than to cluster-centric distance (Lane *et al.*, 2007). Therefore, here we evaluate the environment using the stellar mass surface density which, unlike galaxy number surface density, does not depend strongly on the selection of the underlying sample (either by luminosity or by stellar mass). Following the procedure of Wolf *et al.* (2009) we use as our density

measure the parameter $\Sigma^{M}_{300kpc}(> 10^{9}\mathrm{M}_{\odot})$, in units of $\mathrm{M}_{\odot}/\mathrm{Mpc}^{2}$. This is the stellar mass surface density inside a fixed aperture with radius r = 300kpc at the redshift of the multi-cluster system (z = 0.167), using only those galaxies with log $M_{\star}/\mathrm{M}_{\odot}$ > 9. We also define a cluster core region containing those galaxies with $\Sigma^{M}_{300kpc}(> 10^{9}\mathrm{M}_{\odot})$ > 12.5 $\mathrm{M}_{\odot}\mathrm{Mpc}^{-2}$. The estimates of $\Sigma^{M}_{300kpc}(> 10^{9}\mathrm{M}_{\odot})$ have been kindly provided by David Maltby.

4.2 Results

4.2.1 AGN and star-forming galaxies in OMEGA

In this section we identify star-forming galaxies and AGN from our sample and investigate their properties by cross-matching our OMEGA observations with the STAGES catalogue (Gray *et al.* 2009). The identification of AGN using optical emission lines is based on the fact that the radiation coming from an accreting black hole produces a harder radiation field than star formation, and therefore produces a higher level of ionization in the gas. As a consequence, the intensities of the emission lines after recombination are different, something that can be identified in the spectrum of a galaxy. Historically, the most-widely used diagnostics are based on the BPT diagrams (Baldwin, Phillips & Terlevich 1981), of which the most common one uses four strong emission lines, [O III], Hβ, [NII] and Hα. However, in order to obtain reliable measurements of these four lines one needs access to different parts of the spectrum with relatively high signal to noise. With the motivation of establishing a more economical way of differentiating between the sources of ionization in a galaxy, Cid Fernandes *et al.* (2010) proposed a new alternative diagram that only makes use of two emission lines: Hα and [NII]. This diagram, known as WHAN, compares the equivalent width in Hα ($W_{\mathrm{H}\alpha}$) with the ratio between the fluxes in [NII] and in Hα ([NII] / Hα). Based on these parameters, four different populations can be identified in the diagram: *star-forming* galaxies, strong AGN (sAGN) or *Seyferts*, weak AGN (wAGN) or *LINERs*, and the so-called "retired" galaxy population (Cid Fernandes *et al.* 2011, Yan & Blanton 2012, Stasińska *et al.* 2015). The former two classes have been already described here, whereas the last two ones need to be introduced. LINERs are in fact galaxies with

'LINER-like spectra', given that LINER is the abbreviation of 'low ionization nuclear emission regions' (as introduced by Heckman 1980). LINERs are objects where the weak emission lines are apparently produced by low-level nuclear activity. Regarding the retired galaxies, they are also located in the bottom-right part of the diagram (figure 4.1). These retired galaxies have stopped forming stars, and their gas is believed to be ionized by hot low-mass stars in the post-AGB phase. Therefore, they do not have a detectable contribution from an AGN. Furthermore, their $\mathrm{H}\alpha$ emission is often extended (Belfiore *et al.*, 2014).

In Figure 4.1 we show this WHAN diagram for all the 488 sources where the redshift of each galaxy is consistent with both $\mathrm{H}\alpha$ and $[\mathrm{NII}]$ being within the wavelength range sampled (see Section 3.4.2.2). The values that appear in this plot come from the measurements performed using the R_{PSF} aperture, as this provides the cleanest measurement of the nuclear emission from the galaxy. The galaxies that appear with high values of $[\mathrm{NII}]\,/\,\mathrm{H}\alpha$ on the right-hand side of this plot are artifacts produced by the spectral fitting procedure hitting a constraint (see selection of priors in Section 3.4.1). They are not removed in this thesis but they will not be included in the papers presented for publication.

When using this kind of diagnostic diagrams one has to be aware that in reality there is no hard division between SF- and AGN-dominated systems. In fact, other works place the vertical boundary in slightly different values of $[\mathrm{NII}]\,/\,\mathrm{H}\alpha$ (Kewley *et al.*, 2001; Kauffmann *et al.*, 2003a; Stasińska *et al.*, 2006). Bearing that in mind, we still want to know which sources are more likely to be hosting an AGN or to be dominated by star formation. Therefore, besides showing the median values of the $W_{\mathrm{H}\alpha}$ and $[\mathrm{NII}]\,/\,\mathrm{H}\alpha$ probability density distributions in Fig. 4.1, we also use these distributions to evaluate the probability of each galaxy being at either region of the diagram, based on the positions of the horizontal and vertical boundaries. The sources with probabilities larger than 99.7% (3σ confidence) of being AGN or star forming are highlighted in red and blue, respectively. Based on this procedure we find 52 objects with high likelihood of hosting an AGN and 184 probably dominated by star formation. For the remaining 252 galaxies (plotted as green squares) the classification is more uncertain or intermediate.

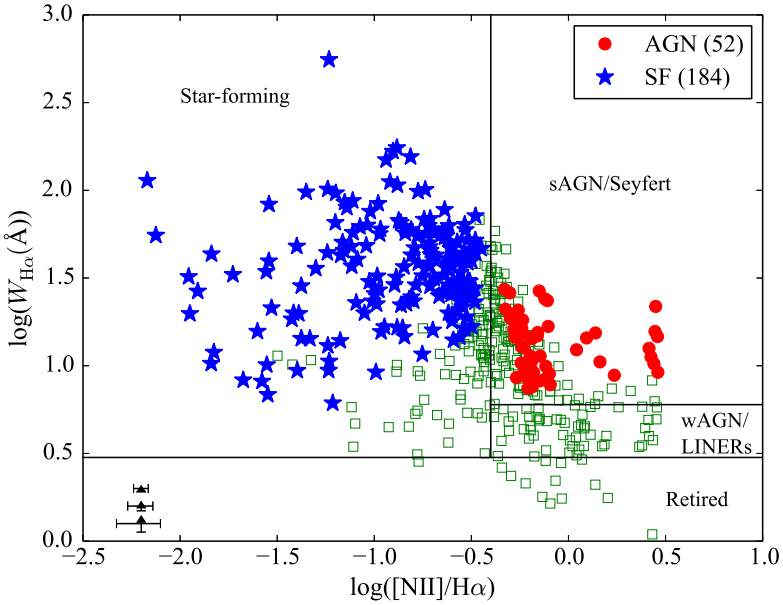

Figure 4.1: A diagnostic plot of $W_{\mathrm{H}\alpha}$ vs. [NII] / Hα, the so-called WHAN diagram (Cid Fernandes *et al.* 2011). The vertical and horizontal lines separate regions with different sources of ionisation. We only show detections using R_{PSF} aperture measurements where both Hα and [NII] fall in the OMEGA probed wavelength range: a total of 488 ELGs. From these we find 52 secure ($\geq 3\sigma$ confidence) AGN hosts (Seyferts; red circles) and 184 star-forming galaxies (SF; blue stars). The green squares represent galaxies that contain mixed sources of ionisation and/or the classification is more uncertain. In the bottom-left corner we show the 25, 50 and 75 percentiles of the errors for reference.

4.2.1.1 OMEGA and X-Ray AGN cross-matching

As a first test of our ability to detect AGN, in this section we make a comparison between the optical AGN detected in OMEGA with those X-ray AGN detected as *XMM* point sources in the A901/902 field by Gilmour *et al.* (2007, see their table 12). The 12 galaxies they detect in the X-ray are present in our parent sample and therefore we have OMEGA spectra available for all of them. From these 12 galaxies, two of them, 12593 and 41435, do not pass the photometric redshift cuts described in Section 3.4.2.2, although galaxy 41435 has a spectroscopic redshift from the AAT compatible with being in the cluster ($z = 0.1585$). These objects are the two most luminous sources in the X-ray. From their variability in the broad-band photometry Gilmour *et al.* (2007) interpreted them as probable optical type I AGN. However, the spectra we obtain in OMEGA show $W_{\mathrm{H}\alpha}$ values smaller than 3Å, probably due to high continuum emission, making it very challenging to detect them as emission-line objects.

Of the remaining ten objects, only four pass our cuts based on the quality of the fits

(section 3.4.2.1), either because they are poor detections ($\mathrm{relative\ error}(W_{\mathrm{H}\alpha}) > 0.15$) or because the redshift found in the fitting process is not compatible with $\mathrm{H}\alpha$ and [NII] being sampled. Interestingly, one of the six discarded objects, ID 15698, has 100% probability of being an AGN despite showing only $\mathrm{H}\alpha$ and the weak [NII] $\lambda 6548$ line in the spectrum. We show its spectrum on the right-hand side of figure 4.2 where we can see that in fact the [NII] $\lambda 6548$ line is quite strong, implying an even stronger [NII] $\lambda 6583$, and therefore a large value of [NII] / $\mathrm{H}\alpha$, placing it in the 'Seyfert' side of the WHAN diagram (figure 4.1). This galaxy has Sb morphology and has an SED corresponding to the *dusty red* class.

The four AGN that pass the two cuts have IDs 9020, 11827, 19305 and 39549, which have probabilities of being an AGN of 99.8%, 67.1%, 78.8% and 0%, respectively. Therefore, out of the 12 X-ray-detected AGN, only ID 9020 is classified as a bona-fide AGN following our selection and identification criteria (see figure 4.2). This galaxy presents Sa morphology and is classified as *old red* based on its SED. It is also the most luminous galaxy in the X-ray among the 10 objects classified as cluster members based on the photometric redshifts, having a X-ray luminosity of $L_x = 2.56 \times 10^{42}$ ergs s^{-1}. For the lower probability ones, both 11827 and 19305 are still likely AGN candidates and they inhabit the right-hand side of the WHAN diagram, although their low $W_{\mathrm{H}\alpha}$ values (~ 6Å) place them close the LINERs population. These two galaxies have disk morphologies (Sa–Sb) and they belong to the *blue cloud*. Finally, 39549 is a Sa *dusty red* with $W_{\mathrm{H}\alpha} \sim 3$Å and therefore belongs to the LINERs population.

We therefore securely classify as optical AGN 1 (or 2 if we include 15698) out of the 12 X-ray AGN detected by Gilmour *et al.* (2007), which is less than $\sim 10\%$. Martini *et al.* (2006) found that only 4 of at least 35 X-ray objects ($\sim 11\%$) would be classified as optical AGN from their emission-line signatures, which is in close agreement with what we found. The lack of optical signatures in X-ray AGN might be a consequence of these objects being heavily obscured Compton-thick AGN and therefore they would not be expected to show optical signatures of nuclear activity. On the other hand, the fact that only 1 (or probably 2) of the 52 highly likely optical AGN found in the OMEGA survey is associated with a Gilmour *et al.* (2007) X-ray source clearly shows that OMEGA is able to detect a large number of optical AGN with relatively weak or

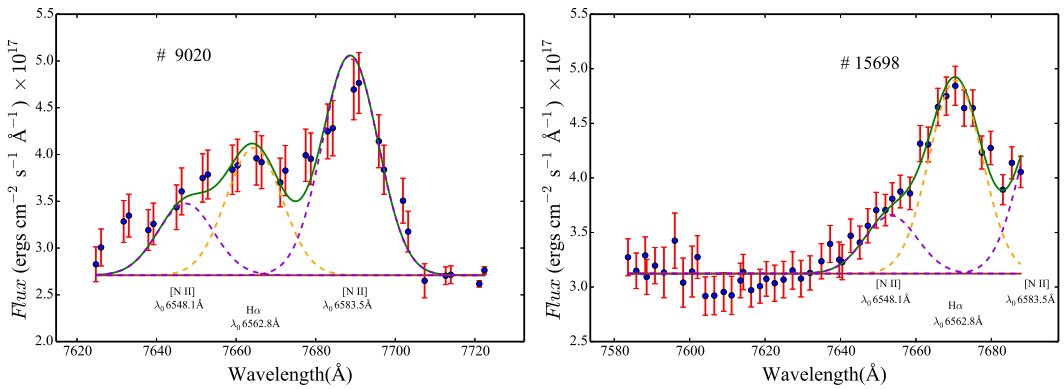

Figure 4.2: Spectra of two of the 12 X-ray AGN detected by Gilmour *et al.* (2007). In orange and purple we show the position of the Hα and [NII] lines, respectively. *Left:* The only X-ray AGN detected as bona-fide in OMEGA: ID 9020. *Right:* Although only Hα is present in the spectrum of ID 15698, this galaxy is assigned a 100% probability of being an AGN due to the strength of the weak [NII] λ6548 line.

no X-ray emission.

The four X-ray AGN with reasonably high probability ($> 66\%$) of being an optical AGN (9020, 11827, 19305 and 39549) present morphologies with significant bulges, as it would be expected in galaxies hosting a black hole. However, they have different SEDs, implying that the presence of an active nucleus is not strongly related to their stellar populations.

We can summarise the results found in this section as follows:

- None of the X-ray detected AGN expected to be type I optical AGN by Gilmour *et al.* (2007) is detected as such in our emission-line survey. The absence of strong optical emission lines might be due to very high continuum emission, yielding $W_{\mathrm{H}\alpha}$ values below our detection limits.

- We detect a large population of optical AGN with no X-ray counterparts. Only one (although probably two), of the 12 galaxies detected as X-ray point sources is detected as a bona-fide AGN in our spectral measurements, although some remain unclassified because we do not have the required wavelength coverage. We attribute this lack of optical counterparts to heavily obscured Compton-thick AGN with no or weak emission lines.

- X-ray AGN with optical counterparts are found in objects with a prominent bulge but still late-type morphologies. The presence of an AGN in these objects does

not seem to affect their colours.

4.2.1.2 Properties of OMEGA AGN

Once we have identified the candidate galaxies to be AGN hosts, we now explore their properties as a single population and compare them with the overall cluster population. We will also look at the properties of galaxies found to be dominated by star formation, although the integrated star formation properties of the emission-line galaxies will be more thoroughly analysed in section 4.3.

In the following analysis we study the properties of the AGN and star-forming populations with respect to the overall cluster population. We work with two different samples: one including only the bona-fide detections (3σ) and another one including also the objects that appear in either the *Seyfert* or the *star-forming* regions of the WHAN diagram, despite not having $> 3\sigma$ probability. This increases the sample size in a way that is statistically robust when analysing the properties of these two populations.

We start by looking at the WHAN diagram colour-coded by stellar mass in figure 4.3. Looking first at the star-forming galaxies we see that almost all have stellar masses below $10^{10}\mathrm{M}_{\odot}$, which might be a direct consequence of the mass quenching of star formation. Seyfert objects span a wider range in masses than star-forming ones, including some of the most massive galaxies. Interestingly, LINERs also tend to have high stellar masses, which might also be related to their past truncation of star formation. We also show the mass distribution of the AGN and star-forming populations, together with their fraction with respect to the cluster population (figure 4.4). In this plot, galaxies hosting an AGN become generally more common at higher masses compared with the cluster mass distribution (shown in black). Star-forming galaxies appear in larger fractions at low masses, decreasing towards higher masses. The lack of high-mass star-forming galaxies is also seen here.

We look now at the morphologies of these two populations. Here we only consider ellipticals, S0s, spirals and irregulars, which include 456 out of the 486 galaxies with detected $\mathrm{H}\alpha$ and $[\mathrm{NII}]\,\lambda6583$ (the remaining objects did not have a reliable visual classification). We show the WHAN diagram for different morphological types (Figure

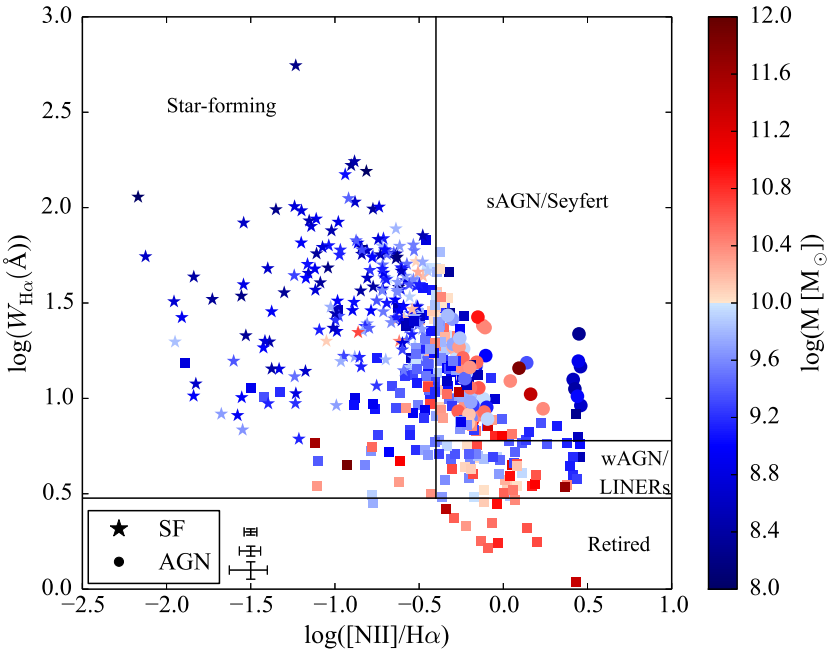

Figure 4.3: WHAN diagram colour-coded by the stellar mass of the galaxies. Squares represent galaxies that contain mixed sources of ionisation and/or the classification is more uncertain
. In the bottom-left corner we show the 25, 50 and 75 percentiles of the errors for reference.

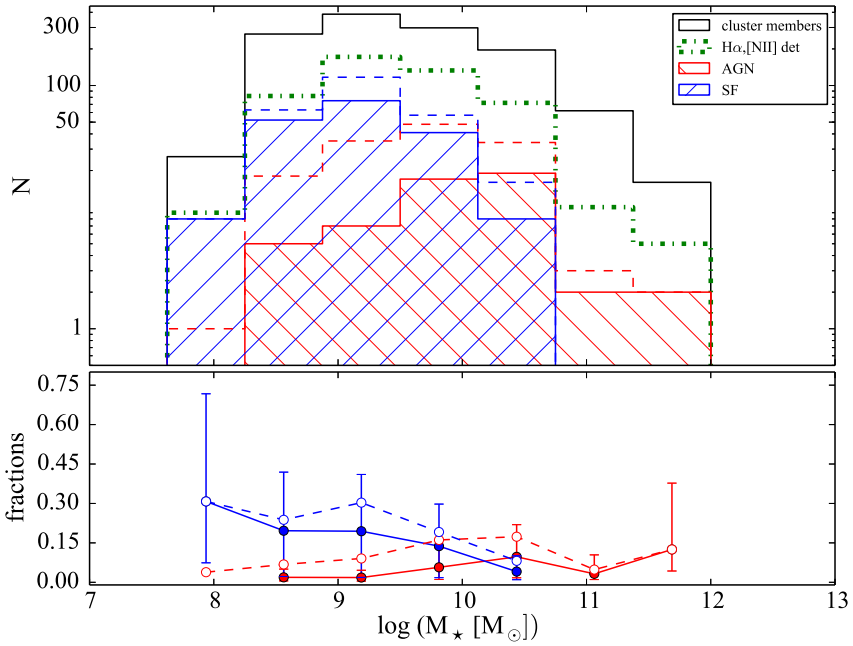

Figure 4.4: *Top panel:* Stellar mass distribution for the overall cluster population (black), ELGs with detected [NII] λ6583 and Hα (green), together with the AGN (red) and star-forming subsamples (blue). The dashed lines represent the AGN and SF distribution including all objects in each region of the WHAN diagram 4.1. *Bottom panel:* Fractions of each population compared with the global cluster sample. We only show errors for the bona-fide fractions for clarity.

4.5) and the morphology distributions for the AGN and star-forming galaxies (Figure 4.6). Galaxies hosting an AGN become more common in spirals with bulges (Sa-Sc),

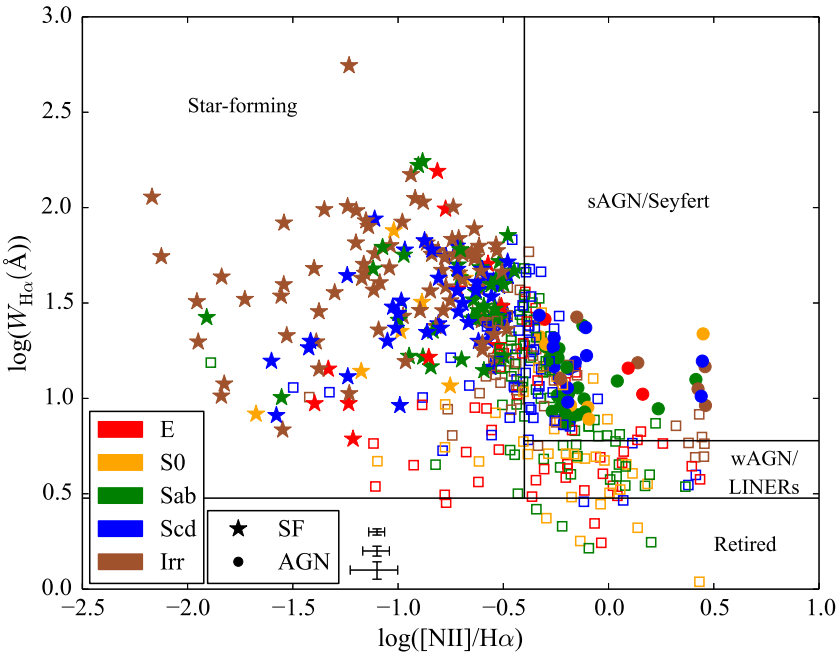

Figure 4.5: WHAN diagram colour-coded by galaxy morphology. Squares represent galaxies that contain mixed sources of ionisation and/or the classification is more uncertain
. In the bottom-left corner we show the 25, 50 and 75 percentiles of the errors for reference.

whereas very few have early-type morphologies. However, two of the most massive Seyferts shown in figure 4.3 have elliptical morphologies. Irregular galaxies dominate the regions of high $W_{H\alpha}$ and low $[NII]\,/\,H\alpha$, where Scd types are also common. Star-forming galaxies have generally late-type morphologies, with a large number of irregulars.

To shed more light into the properties of these two different populations we show again the WHAN diagram but in this case using their SED classifications from COMBO-17. This is shown in figure 4.7.

Interestingly, from the 52 bona-fide AGN only 3 are classified as *old red*. Two of them (39020 and 46643) are elliptical galaxies with very high mass ($> 10^{11} M_\odot$, see figures 4.5 and 4.3), and both of them reside in the core regions ($\Sigma^M_{300kpc}(> 10^9 M_\odot)$ > 12.5 $M_\odot Mpc^{-2}$). The third one is in fact the only X-ray detected galaxy that we securely classify as optical AGN, as shown in section 4.2.1.1. There is a large number of *dusty red*[1] AGN, comprising $\sim$ 36% of the total AGN population and in fact $\sim$ 24% of the *dusty red* galaxies are classified as bona-fide AGN. This implies that *dusty*

[1]As argued in chapter 3, a better term for these galaxies would be *red star-forming*

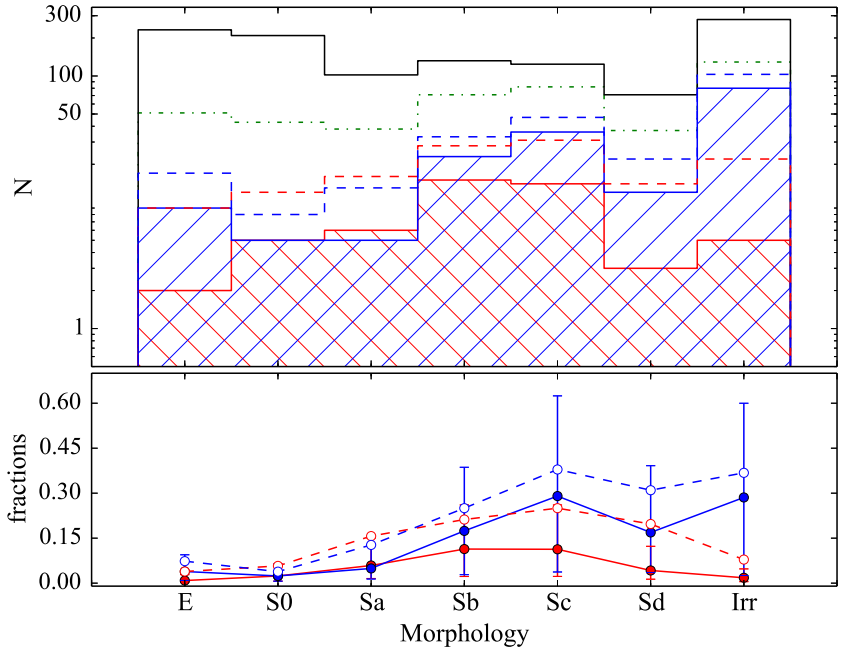

Figure 4.6: *Top* and *Bottom panels:* The distribution of morphologies from ellipticals to irregulars and the corresponding fractions of AGN and star-forming galaxies for each morphological type. We only show errors for the bona-fide fractions for clarity. Line and point styles have the same meaining as in Fig. 4.4

red galaxies are common hosts of an active nucleus. Perhaps, the suppression of star formation in *dusty red* galaxies is linked, at least in some cases, to AGN feedback.

We finally look at the two populations of low $W_{\mathrm{H}\alpha}$ emission, LINERs and "retired galaxies". Although we do not have any 3σ classification, we still find many objects located in these two regions of the WHAN diagram. They both tend to be *dusty red* or *old red*, as expected from their low $W_{\mathrm{H}\alpha}$ emission. Regarding the retired galaxies, as the emission lines are not produced by nuclear activity but by old low-mass stars in their post-AGB phase, we should expect them to have extended emission. Therefore, if we were to use the values of $[\mathrm{NII}]\,/\,\mathrm{H}\alpha$ obtained using R_{tot} they should occupy the same region in the diagram. Besides that, with the spatial information of the emission lines that we obtain in chapter 5 we will be able to identify the regions in the galaxy were the emission originated. There we will also learn whether the $\mathrm{H}\alpha$ emission is only nuclear, which will confirm the AGN nature of the galaxies classified as such in this diagram.

Environmental influence on AGN activity

We finish the comparison between galaxies hosting AGN or star formation by explor-

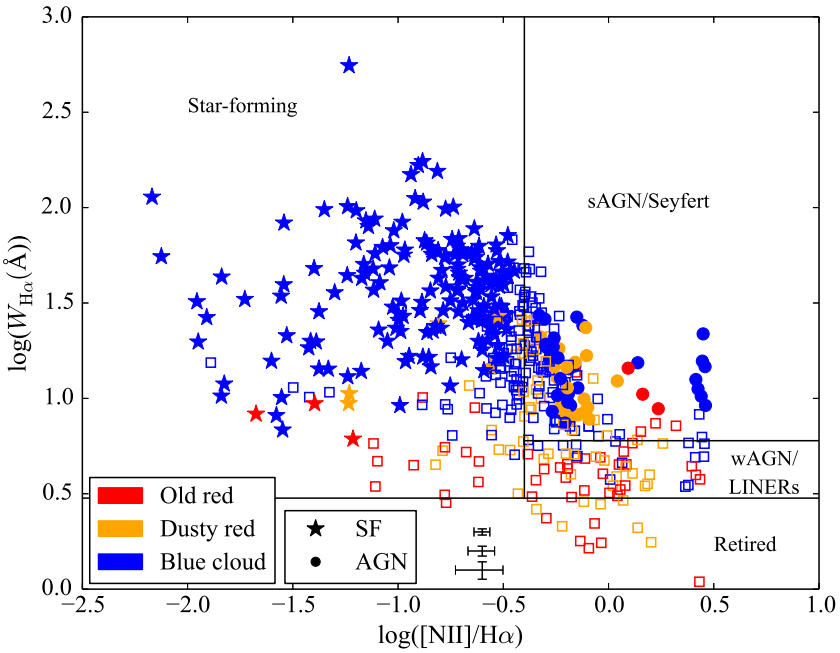

Figure 4.7: WHAN diagram colour-coded by SED type of the galaxies. Squares represent galaxies that contain mixed sources of ionisation and/or the classification is more uncertain
. In the bottom corner we show the 25, 50 and 75 percentiles of the errors for reference.

ing the influence of environment. In Figure 4.8 we show the distribution of AGN and star-forming galaxies as a function of stellar mass density in a similar way as in figures 4.4 and 4.6. The fraction of AGN galaxies shows little dependence on density. Regarding star-forming galaxies, the dependence is also weak, although they tend to show marginally larger fractions at low density. Comparing the distributions of the two populations, a K-S test gives a $\sim 1.3\%$ probability of the bona-fide AGN and star-forming galaxies being drawn from the same distribution, but this probability is much larger $\sim 98.5\%$ when considering all the sources in each side of the WHAN diagram. This difference might be produced because some of the non-3σ-detection objects are very similar to one another, since they probably present mixed sources of ionization and therefore by including them we are increasing the similarity between the AGN and star-forming distributions.

To further explore the dependence of AGN with environment, we show in figure 4.9 the distribution of the line ratio [NII] / Hα for the infall and the core regions. We have also plotted the whole line ratio probability density distributions of the galaxies with detected Hα and [NII], and $W_{H\alpha} > 6$ Å to account for all the information obtained

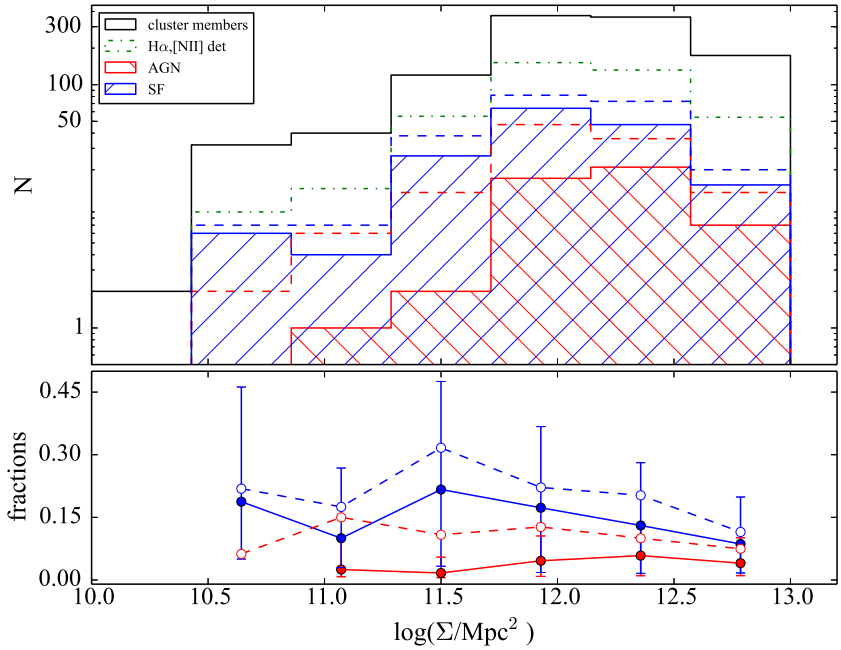

Figure 4.8: *Top* and *Bottom panels:* Stellar mass density distributions for the different samples considered in figure 4.4 and the corresponding fractions of AGN and star-forming galaxies in each stellar mass density bin. We only show errors for the bona-fide fractions for clarity. Line and point styles have the same meaining as in Fig. 4.4

from the spectra in the fitting process. Here we can see that the data for infall and core show quite similar distributions. A K-S test gives a probability $\sim 34\%$ of them being drawn from the same population, which is in complete agreement with the lack of the dependence of the AGN fraction with stellar mass density.

In a previous study of X-ray AGN by Gilmour *et al.* (2007), it was found that the X-ray AGN tend to avoid the highest and lowest density regions, being more dominant in regions of moderate density. However, with OMEGA we are able to probe lower luminosity AGN and therefore study the distribution with environment of a different AGN population. Our findings point towards very little dependence of the low luminosity AGN with environment, which is supported by previous studies (Martini *et al.* 2002, Miller *et al.* 2003, Martini *et al.* 2006).

The findings on this section can be summarized as follows:

- AGN galaxies appear with a wide range of stellar masses, slightly increasing their fractions with stellar mass and dominating the high mass end of the emission-line galaxies. The fraction of star-forming galaxies decreases with mass and they are absent at masses above $5 \times 10^{10} \mathrm{M}_{\odot}$.

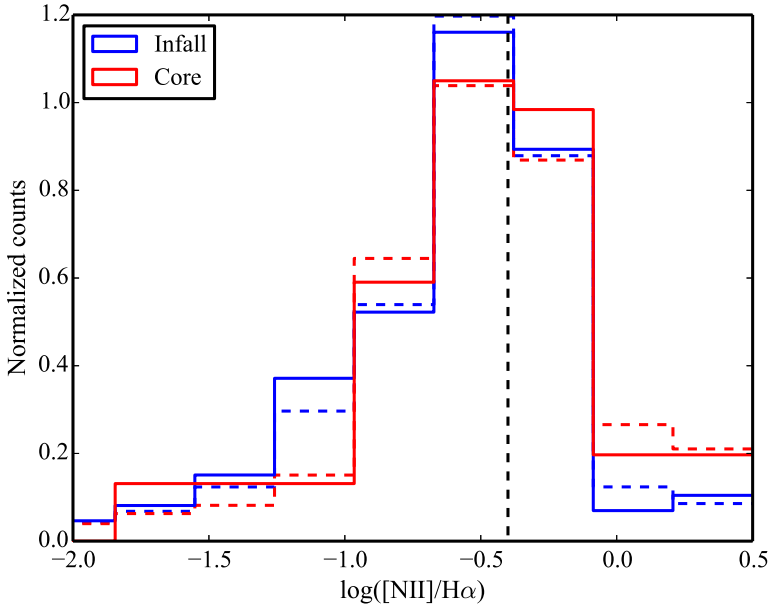

Figure 4.9: Dashed lines represent the [NII] / Hα probability density distributions for all the galaxies in the infall (blue) and core (red) regions of the cluster. Solid lines correspond to the median values of [NII] / Hα in each environment.

- AGN hosts are generally disk-dominated systems and only a few have early-type morphologies. Star-forming objects are dominated by irregulars and late-type disks.

- There is little dependence, if any, of the AGN fraction as a function of environment. Besides that, our results show hints of a possible difference between the distributions of the star-forming galaxies and the AGN in the cluster environment, particularly the most securely classified AGN, which may also be those in which the AGN is most dominant.

- A large fraction ($\sim 35\%$) of the bona-fide AGN are classified as *dusty reds* from their SEDs. Further analysis on the spatial distribution of the emission will help to confirm the classifications obtained using the measurements within R_{PSF}.

4.3 Integrated star formation

We now turn our attention to the study of the global star formation rates (SFRs) of the 622 objects where we detect Hα. To obtain the integrated SFRs we use the measure-

ments within $R_{\rm tot}$, which encompasses the whole extent of the galaxies.

4.3.1 Star Formation Rates

The rate at which galaxies are forming stars can be obtained by looking at different tracers. In OMEGA we obtain SFRs based on the $\mathrm{H}\alpha$ luminosity ($L_{\mathrm{H}\alpha}$) which, as explained in section 1.4, traces star formation on time-scales of a few million years, coming from stars more massive than $\sim$ 10–20 $\mathrm{M}_{\odot}$. These massive stars produce copious amounts of ionising photons which are responsible for the ionisation of the gas surrounding the star-forming regions and subsequent emission from recombination lines such as $\mathrm{H}\alpha$. Therefore, the luminosity we measure in $\mathrm{H}\alpha$ is directly proportional to the amount of new stars being formed. This relation is given by the expression

$$\mathrm{SFR}_{\mathrm{H}\alpha}\ \left[\mathrm{M}_{\odot}\,\mathrm{yr}^{-1}\right] = 2\times10^{-41} L_{\mathrm{H}\alpha}\ \left[\mathrm{erg\,s}^{-1}\right]\ , \tag{4.1}$$

where we have assumed 1 mag average extinction following Kennicutt (1998). $L_{\mathrm{H}\alpha}$ is obtained from the $\mathrm{H}\alpha$ fluxes using

$$L_{\mathrm{H}\alpha} = 4\pi\, D_{\mathrm{L}}^{2}\, F_{\mathrm{H}\alpha}\ , \tag{4.2}$$

where D_{L} is the luminosity distance (795 Mpc at $z = 0.167$).

SFRs for the galaxies in A901/2 have also been calculated by Gallazzi *et al.* (2009) using the extinction-corrected light from the UV (COMBO-17 derived rest-frame 2800Å luminosities) and the IR dust reprocessed light (as observed with Spitzer/MIPS at $24\mu m$). The rest-frame UV also comes from massive stars, although it traces slightly longer time-scales than $\mathrm{H}\alpha$; however, it is strongly attenuated by dust. In the presence of dust, the radiation coming from these stars is absorbed, heating up the dust. The energy is subsequently re-radiated in the far infrared, which therefore traces obscured star formation.

The SFRs from these indicators are also available in the STAGES master catalogue (Gray *et al.*, 2009). Due to the different coverage of the COMBO-17 and Spitzer/MIPS observations there is not IR data available for all the objects. In these cases only UV data is employed to estimate the SFRs, which are considered as lower limits since the amount of radiation re-emitted by the dust is unknown. When IR data is available

but is below the detection limit of $58\mu Jy$ (corresponding to an IR-only SFR of 0.14 $M_{\odot}yr^{-1}$), the IR luminosities are predicted from UV-optical luminosities (see Section 3.2 in Wolf *et al.*, 2009), and they represent upper limits. When IR is detected, the SFRs are calculated using equation (1) in Gallazzi *et al.* (2009).

In figure 4.10 we compare these SFRs with those estimated using $\mathrm{H}\alpha$. For this purpose, we use the UV and IR SFRs estimated assuming that the galaxies are at the redshift of the cluster, $z = 0.165$, as all our $\mathrm{H}\alpha$-detected galaxies are expected to be at the cluster redshift. In the figure, blue triangles show the SFRs as measured when only UV data was available (lower limits); red triangles are estimations for galaxies where UV and IR are available but there is a non-detection in the IR (upper limits); and green circles are SFRs for galaxies with UV and IR detections. These latter points, which account for both the obscured and unobscured star formation are, on average, ~ 0.3 dex above the one-to-one line. We associate this difference to the fact that the $\mathrm{H}\alpha$ SFR estimates might be missing heavily-obscured SF, but it could also be indicative of a declining SFR, since the IR traces stars with longer range of ages. In the case of the SFRs from the UV alone, the correlation with the $\mathrm{H}\alpha$ SFR is stronger, which is not surprising as the UV and $\mathrm{H}\alpha$ are sensitive to comparable SF timescales, with the UV tracing slightly longer ones than $\mathrm{H}\alpha$. However, there is also a clear ~ 0.3 dex offset since the effect of extinction is significantly stronger in the UV than in the optical.

4.3.2 The $\mathrm{H}\alpha$ Luminosity Function

The galaxy luminosity function (LF) is an estimate of the number of galaxies with different luminosities found in a given region of the Universe. The distribution of galaxy luminosities can provide relevant information about the evolutionary processes affecting galaxies. In this work we are interested in the distribution of $\mathrm{H}\alpha$ luminosities for our cluster members, and its comparison with other clusters and the low-density field. In figure 4.11 we show the $\mathrm{H}\alpha$ LF for different samples in OMEGA. The top axis shows the SFR, assuming 1 mag average extinction, according to Equation 4.1. To correct the OMEGA $\mathrm{H}\alpha$ LF for incompleteness we use the fraction of detected galaxies per bin of R-band magnitude (m_R) as obtained in section 3.4.3. We interpolate between the different bins of m_R shown in figure 3.14.

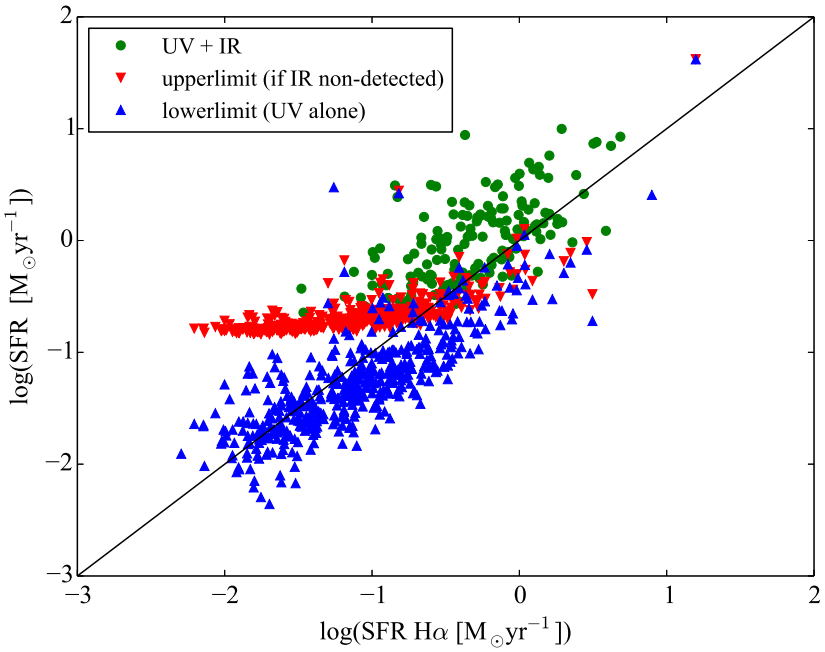

Figure 4.10: The $\log \mathrm{SFR}_{\mathrm{H}\alpha}$ determined from R_{tot} aperture measurements compared with other estimates of $\log \mathrm{SFR}$. See legend and text for details on the meaning of the different datapoints.

For comparison we show the A1689 luminosity function (at $z = 0.18$) from Balogh *et al.* (2002) as well as the field Hα LF from Gunawardhana *et al.* (2013). For the field Hα LF we use the best-fitting parameters of the Saunders function (Saunders *et al.* 1990) that Gunawardhana *et al.* (2013) obtain for the redshift bin $z = 0.1$–0.2 ($\log L^* = 34.55$, $\log C = -2.67$, $\alpha = -1.35$, $\sigma = 0.47$). For A1689 we use the Schechter (1976) function parameters: $\alpha = -0.1$ and $L^* = 10^{40}$ erg s^{-1} given by Balogh *et al.* (2002). We normalize all the Hα LFs to have the same value at $L_{\mathrm{H}\alpha} = 1 \times 10^{40}$ergs s^{-1}. These two H$\alpha$ LFs use the same cosmology as we do and therefore no corrections are needed.

On the left of figure 4.11 we plot the Hα-detected galaxies and the bona-fide star-forming objects. As we are normalizing at $L_{\mathrm{H}\alpha} = 1 \times 10^{40}$ergs s^{-1} we cannot evaluate differences at these luminosities, however we can study the faint and bright ends. At low Hα luminosities, both samples, but especially the bona-fide star-forming galaxies, show lower number densities at a given Hα luminosity when compared with the field, following a qualitatively similar trend to that seen in the very dense cluster A1689. On the bright end, bona-fide star-forming galaxies never have $L_{\mathrm{H}\alpha} < 1 \times 10^{41}$ergs s^{-1}, whereas the Hα-detected galaxies fall in between the field and A1689, disappearing above $L_{\mathrm{H}\alpha} > 1 \times 10^{42}$ergs s^{-1}. This is not a surprise, as A1689 is a more evolved and

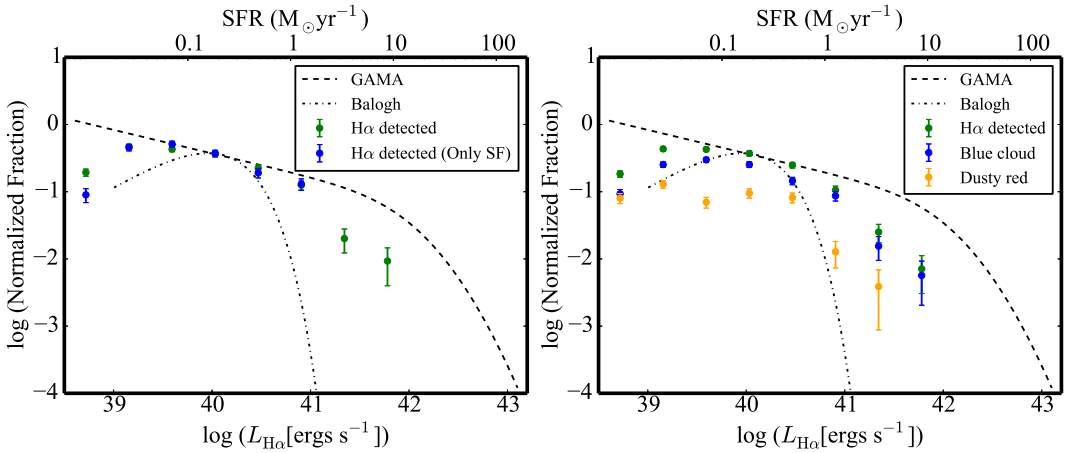

Figure 4.11: The Hα luminosity function for different subsamples of the Hα-detected galaxies. For comparison, we show the Hα LF from the cluster A1689 at $z = 0.18$ (black dash-dot line; Balogh *et al.* 2002) and the field from the GAMA survey at $z = 0.1$–0.2 (black dashed line; Gunawardhana *et al.* 2013). All the LF are corrected for contamination and completeness. Errors are always Poissonian. *Left:* The green points show the Hα-detected galaxies and the blue ones the bona-fide star-forming objects. *Right:* The LF for *dusty reds* and *blue cloud* independently, normalized to the total number Hα-detected sources.

denser cluster than A901/2 (Lemze *et al.* 2009, Alamo-Martínez *et al.* 2013). Thus, we find the bright and faint ends of our LF to be intermediate between a more evolved cluster, where galaxies have been processed by the environment for a longer period of time, and the field at a similar redshift, where environment has played no role.

In the right of the same figure we show the Hα luminosity for *dusty reds* and *blue cloud* samples. The *blue cloud* galaxies follow the Hα-detected sample, as they are the dominating population, whereas *dusty reds* appear in much lower numbers especially at the high-Hα luminosity end.

4.3.3 Effects of mass and environment

We turn now our attention to the study of the role that mass and environment play in shaping the evolution of the galaxies in A901/2 by looking at the integrated star formation properties. Again, we use the flux measurements within $R_{\rm tot}$ to estimate the global star formation in the galaxies. Here we will focus on the specific star formation rates (SSFRs), which measure the star formation rate per unit stellar mass. We start by looking at the effects of stellar mass and stellar mass density on the SSFRs of galaxies. First, we show a raw comparison of the change in SSFRs with respect to mass and

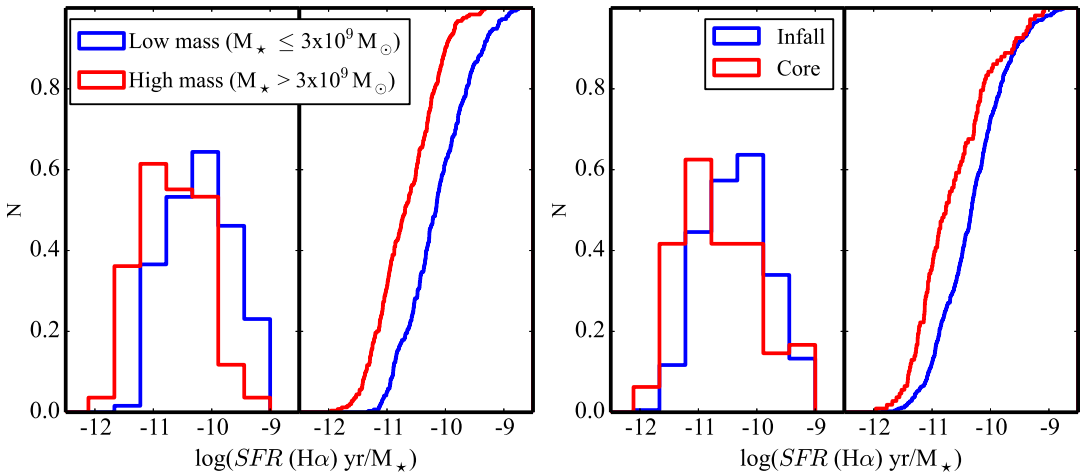

Figure 4.12: Non-cumulative and cumulative histograms showing the comparison between the SSFRs of low- and high-mass galaxies (left) and between galaxies in the infall and core regions (right).

stellar mass density. In Figure 4.12 we plot the SSFR for low- and high- mass galaxies (split at $3 \times 10^9 M_\odot$, approximately the median of the stellar mass distribution) and for galaxies in the infall and core regions. It is clear that the stellar mass of individual galaxies produces a more significant change in the SSFR than the local stellar mass density. The change in the median-SSFR from low to high mass is ~ 0.53 dex, whereas that from infall to core is ~ 0.44 dex. A K-S test gives p-values $\sim 10^{-14}$ and $\sim 10^{-6}$, respectively, for the samples being drawn from the same distribution. Both mass and environment appear to affect the SSFRs of the galaxies. However, the change of SSFR with environment seen here might be influenced by a change of stellar mass with environment and vice versa. Therefore these two effects need to be isolated to study their separate influence on star formation activity.

For this purpose, we start by using the strong correlation that exists between the SFRs of galaxies and their stellar mass (Brinchmann *et al.*, 2004; Whitaker *et al.*, 2012). This relation holds because high-mass galaxies form stars at higher rates than low-mass ones, as it would be expected from their larger sizes. However, low-mass galaxies tend to have higher SSFRs than high-mass ones. In other words, they tend to be more efficient at forming stars per unit stellar mass. In figure 4.13 we show the SSFR vs stellar mass for all the $H\alpha$-detected galaxies, highlighting the objects classified as bona-fide AGN or star-forming. We also plot two lines showing our detection limits: the dotted line marks the limit in flux at which we are able to detect $H\alpha$, and the dashed line

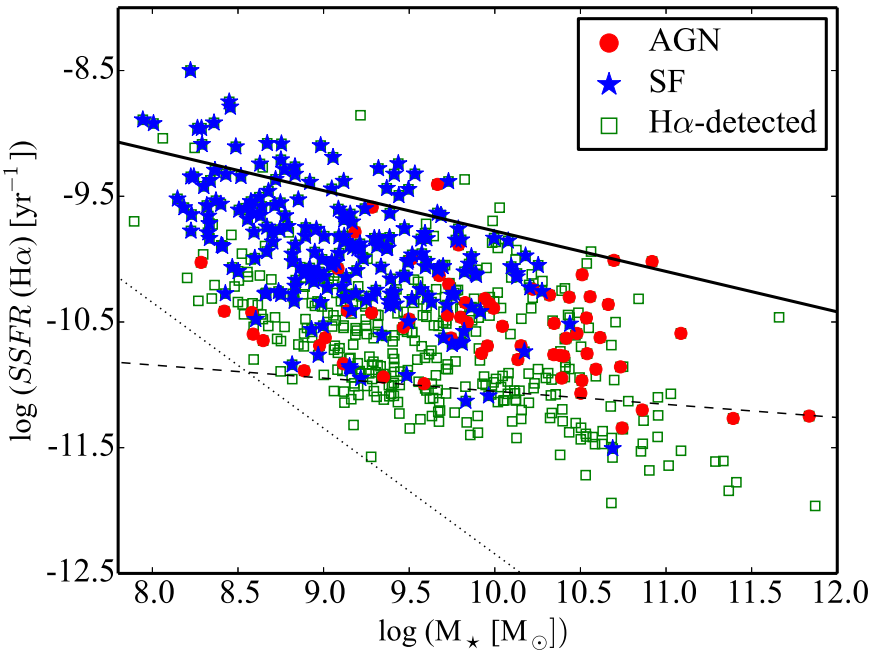

Figure 4.13: SSFR vs stellar mass for the 541 Hα-detected galaxies with available stellar mass densities and reliable mass estimates. Red circles and blue stars correspond to the objects classified as bona-fide AGN and star-forming, respectively. The black solid line marks the Whitaker *et al.* (2012) relation for the field at $z = 0.165$. The dashed and dotted lines show our detections limits (see text for details)

shows the average $W_{\mathrm{H}\alpha}$ detection limit for $W_{\mathrm{H}\alpha}$ = 3Å, after converting stellar masses to R-band luminosities. The equivalent-width limit varies in this plot, depending on the mass-to-light ratio of the galaxy in question. We only show the line for the *dusty red* galaxies, while the same line for the *blue cloud* galaxies is slightly higher, but we do not plot it for clarity. These lines are not straight, and thefore equivalent-widths are not equivalent to SSFRs, because the mass-to-light ratio decreases with R-band luminosity. As a comparison we show the SFR-stellar mass relation in the field, using the relation found by Whitaker *et al.* (2012), which for star-forming galaxies at $z = 0.165$ is given by

$$\log \mathrm{SSFR} = -6.56 - 0.32 \log M_\star. \tag{4.3}$$

The stellar masses used by Whitaker et al. are derived from medium-band photometry using Bruzual & Charlot (2003) models that assume a Chabrier (2003) initial mass function (IMF), solar metallicity, and the Calzetti *et al.* (2000) extinction law. The stellar masses that we use were estimated by Borch *et al.* (2006) using the COMBO-17 photometry in conjunction with a template library derived using the PEGASE stellar population models (Fioc & Rocca-Volmerange, 1997) with solar metallicity and

a Kroupa (2001) IMF. The different IMFs used by Whitaker et al. and Borch et al. would only change the stellar masses by $\sim 10\%$. Moreover, the stellar masses derived in these works are quantitatively consistent with those derived using a simple colour-based stellar mass-to-light ratio (Bell *et al.*, 2003). We are therefore confident that the stellar masses used here can be directly compared, and that any systematic differences will not affect our conclusions. The SFRs estimated by Whitaker et al. are based on UV+IR indicators, and are therefore expected to be ~ 0.3 dex higher, on average, that the $\mathrm{H}\alpha$-based ones.

Even though we expect the Whitaker et al. relation to be ~ 0.3 higher, the majority of our $\mathrm{H}\alpha$-detected galaxies would still fall clearly below the field SFR-mass relation. This confirms that a large fraction of the galaxies in the cluster at all masses, including those in the infall regions, have reduced their SFR significantly relative to the field, as also found by (Poggianti *et al.*, 2008; Vulcani *et al.*, 2010). At first sight, this seems to contradict previous results which suggest that the average SFR in SF galaxies remains roughly constant with environment, and it is only the fraction of SF galaxies that changes (Balogh *et al.*, 2004a; Verdugo, Ziegler & Gerken, 2008; Bamford *et al.*, 2008). However, this contradiction is only apparent. The relative fraction of SF and non-SF galaxies depends on the depth of the survey. Because we are able to detect very low $\mathrm{H}\alpha$ fluxes (and thus very low levels of star formation), our sample contains $\mathrm{H}\alpha$-emitting galaxies that would have been missed by most other surveys. Therefore, strongly suppressed galaxies still appear as $\mathrm{H}\alpha$ emitters in our sample. Cluster galaxies with strong star formation have levels of star formation comparable with those found in the field. If only galaxies with strong star formation are detected in a survey, it would appear that their star formation has not been suppressed. Since galaxies with very low levels of star formation would not have been detected in $\mathrm{H}\alpha$ in most other surveys, they would have been (erroneously) classified as non-SF and one would conclude that only the relative fraction of SF and non-SF galaxies has been affected by the environment.

Despite the clear difference shown here, we still want to obtain a clean estimate of the change of SSFR with environment, eliminating, as much as possible, the effect of mass. This can be done using the SSFR vs mass relation for the field as a reference, since it provides the expected SSFR of a galaxy with a given stellar mass in low-density

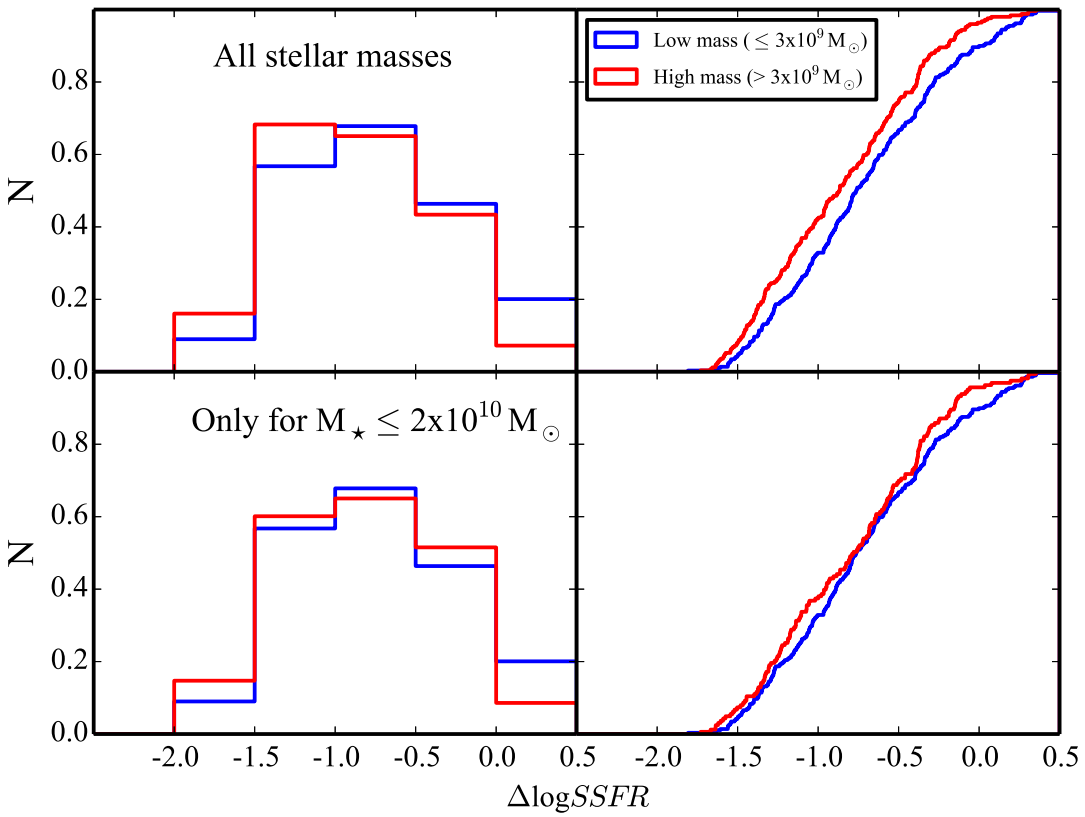

Figure 4.14: Non-cumulative and cumulative histograms of $\Delta\log SSFR$ for high- and low-mass galaxies (see text for details). In the top plots we include all the Hα-detected galaxies whereas in the bottom we only consider those galaxies with stellar mass $< 2 \times 10^{10}$M$_{\odot}$.

environments. Then, if for a given galaxy, we 'subtract' the SSFR governed by its mass, we could study the effect of the environment on the remaining star formation. If we define $\Delta\log SSFR$ as the logarithmic distance to the field relation;

$$\Delta \log SSFR = \log SSFR + 6.56 + 0.32 \log M_{\star}, \tag{4.4}$$

(c.f. equation 4.3), we can repeat now the same comparison as we did using the SSFRs, but now using $\Delta\log SSFR$. The top panel of figure 4.14 shows the distribution of $\Delta\log SSFR$ for high and low mass galaxies. The K-S test in this case provides a 3% probability of them being drawn from the same distribution. The difference is much smaller but the mass is still having an effect in the SSFRs, as massive galaxies are further away from the field relation than low-mass ones.

However, we have not considered yet the fact that massive galaxies stop forming stars at masses 2–3 $\times$ 10^{10}M$_{\odot}$, as suggested by, e.g., Bundy *et al.* (2006), and therefore they do not follow the SSFR-mass relation. This might be the reason why we still

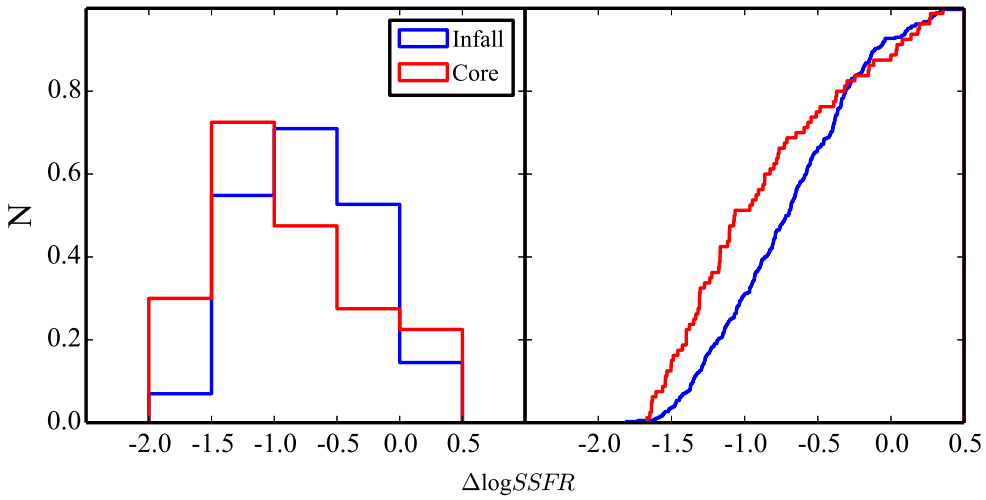

Figure 4.15: Non-cumulative and cumulative histograms of $\Delta\log SSFR$ for infall and core galaxies. We only include galaxies with $M_\star < 2 \times 10^{10} M_\odot$.

see a difference between the SSFRs of low- and high-mass galaxies. To take this into account, we perform the same comparison but now considering only galaxies with stellar mass $< 2 \times 10^{10} M_\odot$. In the bottom of figure 4.14 we show $\Delta\log SSFR$ for low- and high- masses (again split at $3 \times 10^9 M_\odot$) but now removing the highest mass ones. A K-S test gives a probability of them being drawn from the same population of 37%. Therefore, we can confidently expect the mass effect to be removed by this procedure and hence we can study the environmental effects in isolation. Using this new selection cut, the sample is reduced to 455 objects but now we can confirm that the mass dependence is efficiently removed. From now on, instead of using global SSFRs we use $\Delta\log SSFR$ and concentrate on the $M_\star < 2 \times 10^{10} M_\odot$ sample.

We now repeat the analysis of the change in SSFR from the infall to the core, but now using $\Delta\log SSFR$ for the re-defined sample of 455 galaxies. The result is shown in figure 4.15. The K-S statistics yield a p-value $< 1 \times 10^{-3}$, whereas the difference between the median values is ~ 0.37 dex. Therefore, after removing the effect of the mass, there is still a clear statistical decrease in the SSFRs from the infall regions to the core.

4.3.4 Morphologies and colours as indicators of changes in SSFR

So far we have shown that there is a clear change in the SSFR from the infall to the core, even after the mass effects are removed. However, we still do not know in detail

how galaxies are affected by the environment (besides reducing their SSFR), how they stop forming stars and what other changes are shown by the galaxies. To try to answer these questions we now turn our attention to the properties of the galaxies that might correlate with the change in SSFR.

In Figure 4.16 we show the SSFR vs stellar mass in four different density bins for all the 541 $\mathrm{H}\alpha$-detected galaxies with available stellar mass densities and reliable mass estimates. Symbols and colours correspond to different morphologies and SED types, respectively, as explained in the legend. The black lines are the same ones shown in figure 4.13.

By exploring the different density bins in this figure we can observe how different types of galaxies populate them and how they are affected by environment. As expected, the SED types seem to generally correspond to different levels of SSFRs: *blue cloud* galaxies have high SSFRs, *old red* ones appear at the bottom in the four density bins whereas *dusty reds* tend to be in between these two. We now investigate whether galaxies with the same SED types change their levels of star formation as they fall into regions with higher density. We explore this possibility by comparing the $\Delta\log SSFR$ of galaxies of the same SED type residing in the infall region with those in the core, shown in the left plot of Figure 4.17. None of the three SED types change significatively their $\Delta\log SSFR$ from the infall to the core, which supports the idea that a change in colour has to be associated with a change in the $\Delta\log SSFR$ and therefore in the SSFRs. Different density bins also show differences in morphologies, which might be associated with changes in the SSFRs. In the right two panels of figure 4.17 we show the $\Delta\log SSFR$ of ellipticals, S0s, spirals (Sabs and Scds) and irregulars, in the core and in the infall region. No significant variation is found for any morphological types, which all show K-S probabilities $> 10\%$. Looking at figure 4.17, ellipticals and S0s seem to show a variation in $\Delta\log SSFR$ from the infall to the core, but the low numbers of galaxies make any difference statistically insignificant. Consequently, when a galaxy changes its SSFR it must also change its SED type and/or its morphology.

To verify this idea, we show in figures 4.18 and 4.19 the global fraction of different SED and morphological types, respectively, where we consider all the cluster galaxies.

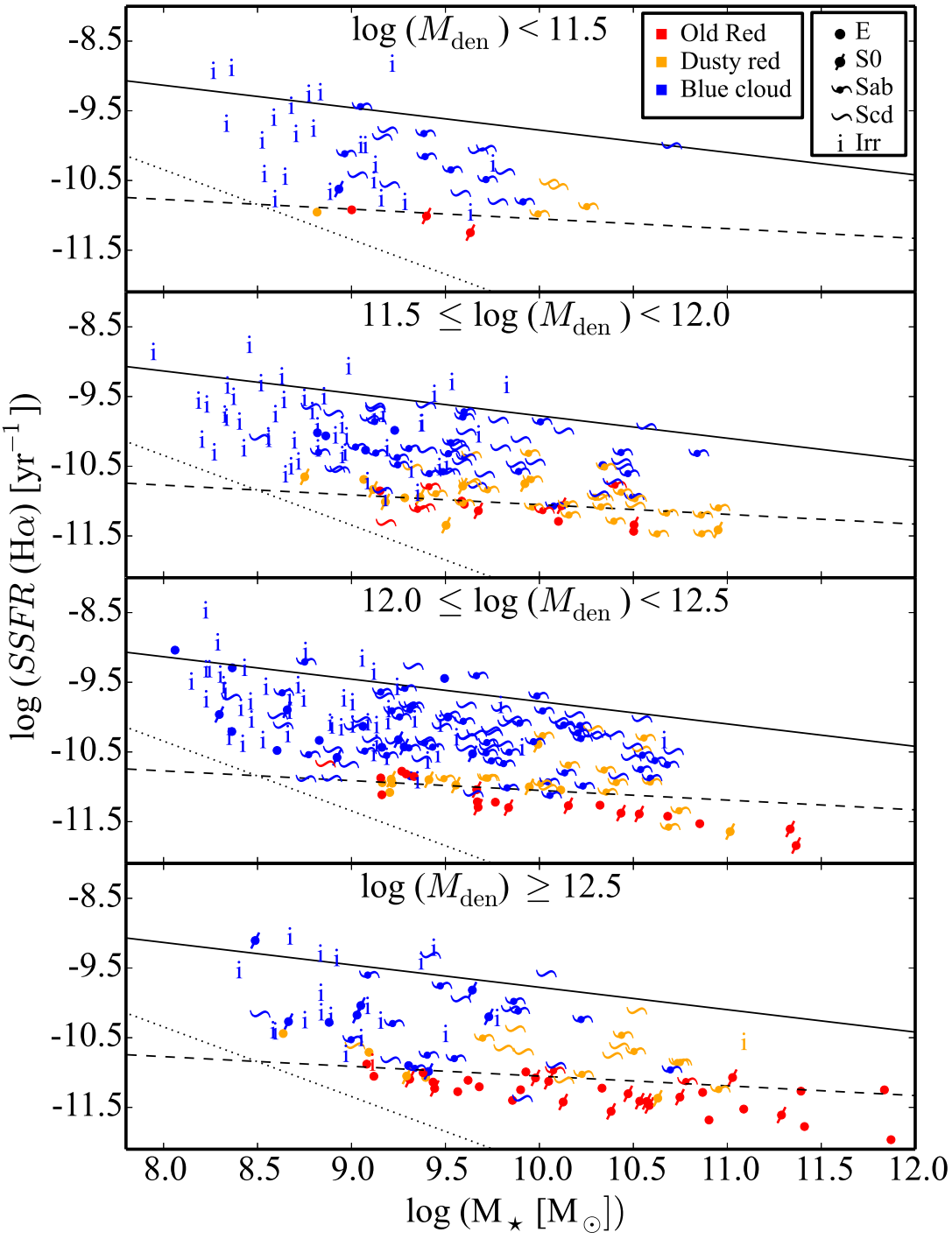

Figure 4.16: SSFR vs stellar mass for the 541 Hα-detected galaxies with available stellar mass densities and reliable mass estimates, split in four density bins. Symbols and colours correspond to different morphologies and SED types, respectively, as explained in the legend. The black line marks the Whitaker *et al.* (2012) relation for the field at $z = 0.165$. The dashed lines show our detections limits (see text for details).

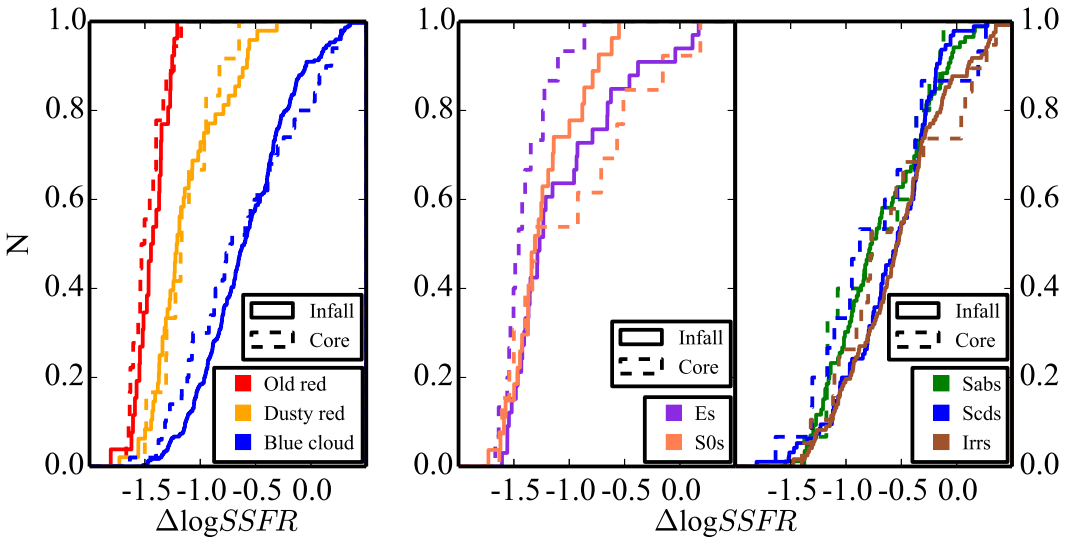

Figure 4.17: Comparison between $\Delta\log SSFR$ in the infall and core regions for different SED types (left) and morphologies (right).

As expected, the fraction of *blue cloud* galaxies decreases with density at all masses, while the *old red* fraction increases. The *dusty red* galaxies show an interesting behaviour: the fractions of low-mass ones ($< 10^{10}\mathrm{M}_{\odot}$) are low and remain constant with a slight increase with density; however, the high-mass ones show a significant decrease with density. A different behaviour between low- and high-mass *dusty reds* is also seen in the $\mathrm{H}\alpha$-detected sample shown in figure 4.16: the *dusty red* galaxies at low masses have generally low SSFRs and tend to be more bulge-dominated systems, whereas at high masses they have higher SSFRs and disk morphologies. This trend might be a consequence of a different origin of the *dusty red* feature depending on the stellar mass: on one hand, star formation in low-mass galaxies might be very rapidly suppressed and accompanied by morphological changes; on the other hand, at high masses the environmental effect on star formation is more subtle, therefore not implying a change in morphology.

We test the apparent difference in SSFRs between low- and high-mass *dusty reds* by comparing their $\Delta\log SSFR$. This comparison is shown in figure 4.20 for all SED types. While *old red* and *blue cloud* galaxies have the same $\Delta\log SSFR$ for low and high masses, the *dusty red* galaxies show a very significant difference, with low-mass galaxies having much lower values of $\Delta\log SSFR$ than high-mass ones. A K-S test gives a probability $< 0.01\%$ of them coming from the same distribution, and the median values differ in ~ 0.3dex. Therefore, the *dusty red* feature in low-mass galaxies

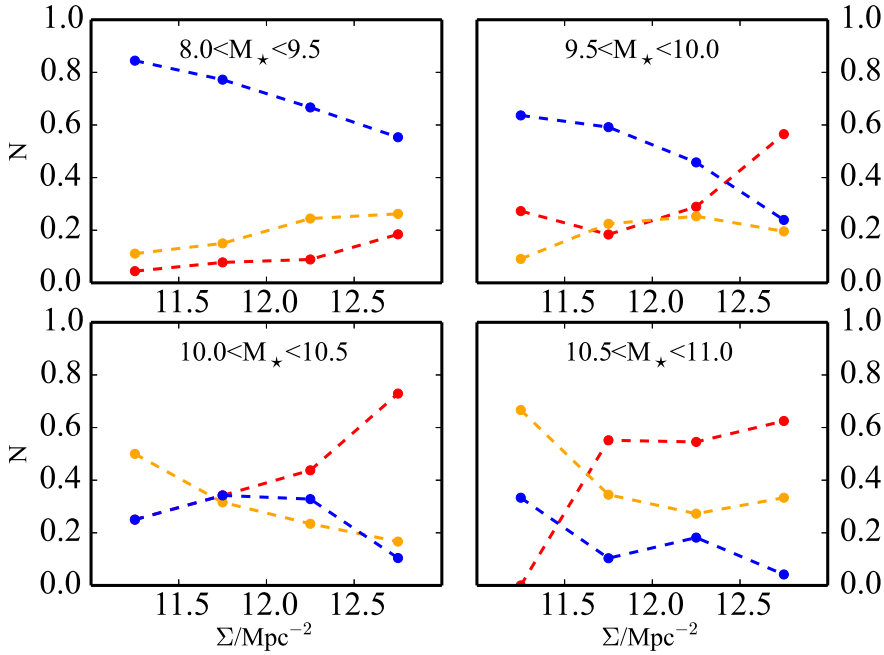

Figure 4.18: Global fraction of each SED type as a function of stellar mass density in different mass bins: *blue cloud* (blue), *dusty reds* (orange) and *old reds* (red).

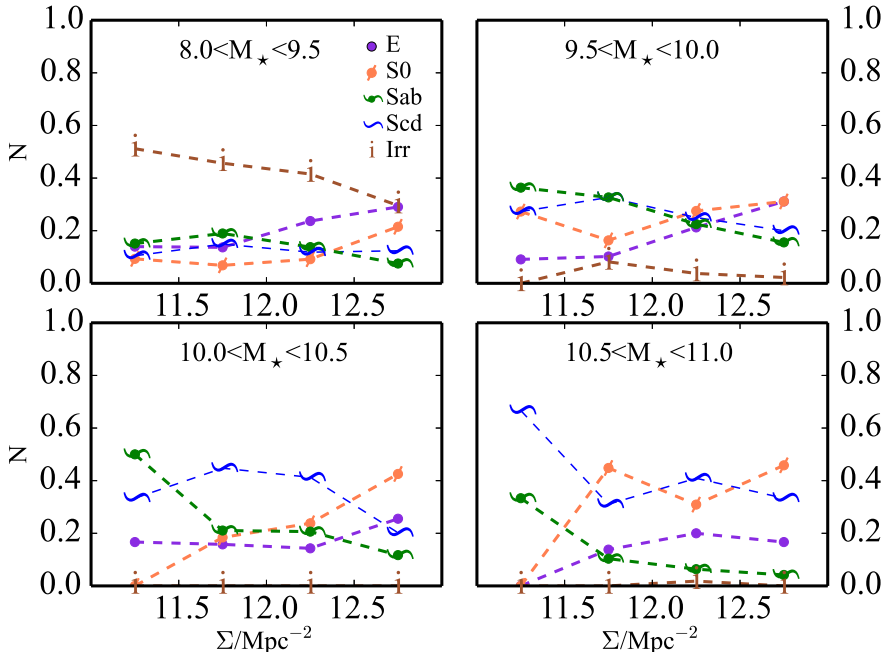

Figure 4.19: Global fraction of the different morphological types as a function of stellar mass density in different mass bins. Different morphologies are shown with different symbols and colors, as explained in the legend.

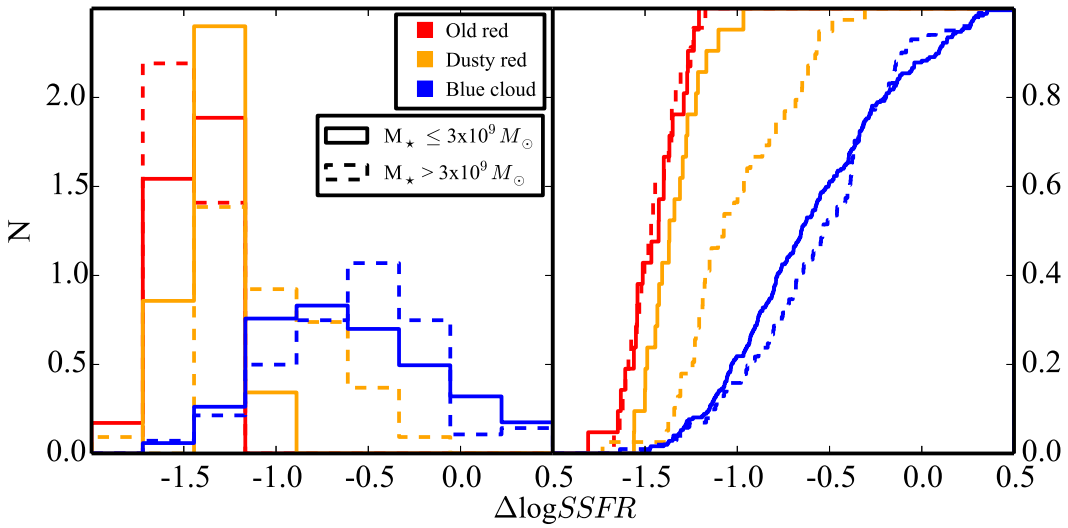

Figure 4.20: Comparison between the $\Delta\log SSFR$ of low- and high-mass galaxies for different SED types.

appears at much lower levels of star formation than in high-mass ones. With respect to the different morphologies at low and high mass, we have to bear in mind that our visual morphologies might be less certain for low-mass systems with low SSFRs, which are difficult objects to classify. As a sanity check, we look at the structural parameters of these galaxies obtained from GALAPAGOS (Barden *et al.*, 2012) fitting of the HST images, which are also available in the STAGES catalogue (Gray *et al.*, 2009). *Dusty red* galaxies with stellar masses $M_\star < 10^{9.5} M_\odot$ have Sérsic indices between 1 and 3.5. Although n < 4 does not necessarily imply a disk for low-mass galaxies, some of these objects might be visually misclassified as early-types when they still retain a disk. As a consequence, there might not be such a strong morphological change in the formation of the *dusty red* feature at low masses.

Apart from changes in the fraction of each SED type, there are also changes in the fractions of each morphological type both for the Hα-detected objects (figure 4.16) and also for the global cluster population, as shown in figure 4.19.

Hα-detected irregular galaxies dominate at low masses in all the density bins, although few are found in the core. This lack of low-mass star-forming galaxies in the core might be produced by the quenching of the star formation in these small objects which, not being that bright any more, go beyond our detection limits. A similar trend is followed by the global irregular population, only appearing at low masses and decreasing

monotonically towards high density regions, where they probably contribute to the increasing fraction of ellipticals. Furthermore, irregulars are also the main morphological type above the SSFR vs mass relation of the field, implying that some of them might be disturbed objects (mergers or ICM interactions) where star formation has been enhanced.

Spiral galaxies dominate the high-SSFR population for masses above 10^9, although they are less common in the core, where they might have transformed into the low-SSFR early-type galaxies that populate the core at high masses. The cluster spiral population also decreases towards the core, with the exception of the highest mass bin, as the ellipticals, and especially S0s become more dominant towards high density regions. These galaxies are probably responsible for the increasing fraction of *old reds* at these masses shown above in figure 4.18. At very high masses, most of the galaxies have disk morphologies, although the fraction of the different morphological types does not change much with density.

In figure 4.17 (right), we showed that star-forming spiral galaxies do not change their values of $\Delta\log SSFR$ from the infall to the core. However, in figure 4.16 their colours seem to vary at different masses and densities. As different colours and morphologies imply different levels of star formation, these properties might be changing in spiral galaxies as they evolve towards more passive systems. We investigate this variation in figure 4.21 where we show the number of star-forming spiral galaxies with different SED type for different mass bins as a function of stellar mass density. The *dusty red* spirals become as common as the *blue cloud* ones, and even dominate at the cores at high masses. The *dusty red* is then a very common feature in the high-mass, star-forming spiral galaxies in A901/2. These findings agree with the results obtained by Bamford *et al.* (2009) and Wolf *et al.* (2009, also in A901/2), who detected an increasing fraction of red spirals with increasing density.

From the analysis of the integrated star formation based on the $\mathrm{H}\alpha$ estimates, we summarize our findings as follows:

• The $\mathrm{H}\alpha$ luminosity function of A901/2 lies in between that of the more evolved cluster A1689 and the field at a similar redshift. Our cluster contains a smaller fraction of star-forming galaxies than the field at both faint and bright ends. However, it con-

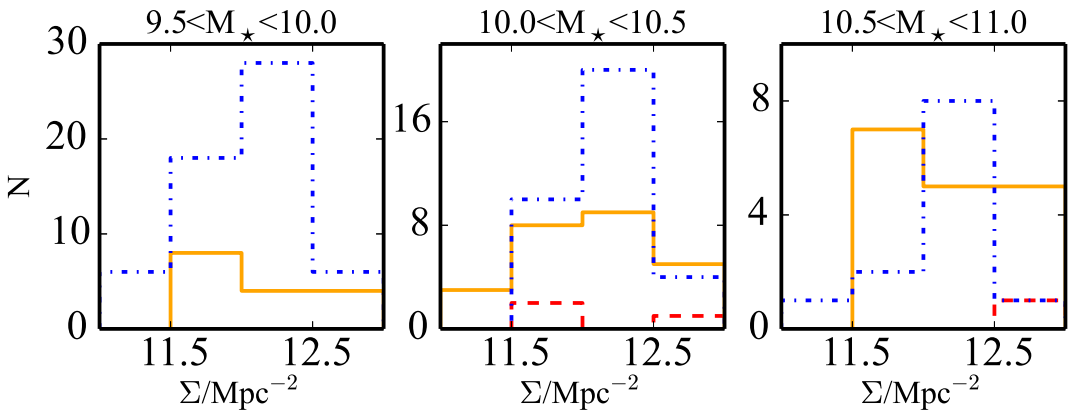

Figure 4.21: Total number of spiral galaxies with different SED types as a function of stellar mass density for three different stellar mass density bins: *blue cloud* (blue), *dusty reds* (orange) and *old reds* (red)

tains larger fractions of high star-forming objects than denser, more evolved clusters.

• The majority of the galaxies with detected emission in Hα show suppressed SSFRs with respect to the field. The cluster galaxies have a wide range of levels of SSFR, implying that the SSFR in star-forming galaxies does not remain constant with environment, contrary to that found in previous works (Balogh *et al.*, 2004a; Verdugo, Ziegler & Gerken, 2008; Bamford *et al.*, 2008) but supported by others (Poggianti *et al.*, 2008; Vulcani *et al.*, 2010).

• Both mass and environment contribute to the suppression of star formation in the galaxies in A901/2, the mass being probably more dominant. Once the mass effect on star formation is removed, there is still a decrease of a factor of ~ 2 in the average SSFRs from the infall regions to the core.

• For a given SED type or morphological type, there is no change in SSFR from the infall to the core. The global change in SSFR is driven by changes in the fractions of galaxies with different SED types and morphologies. At intermediate masses there is a decrease in the fraction of star-forming spiral galaxies, which are replaced by galaxies with early-type morphologies (ellipticals and S0s) that are passive or have low SSFR.

• The effect of environment at low and high masses is significantly different. At low masses, star formation is rapidly quenched, probably leading to morphological changes. At high masses, galaxies show a slower transition in which there are not morphological changes but galaxies still retain relatively high SSFRs. The high number of

high-mass S0s in the core supports this idea.

• High-mass ($M_\star > 10^{9.5} M_\odot$) spiral galaxies in A901/2 evolve into a phase of relatively high SSFRs and red colours while they still retain their disk morphology. These galaxies survive until the very core of the multi-cluster system. The *dusty red* feature is then a very common phenomenon in spiral galaxies at high masses. The increasing fraction of S0s at this masses indicates that *dusty red* spirals are probably an intermediate stage in the transformation of spirals into S0s.

Chapter 5

OMEGA – OSIRIS Mapping of Emission-line Galaxies in A901/2: III.– Spatial analysis of the star formation

In this chapter we introduce the analysis of the spatially resolved properties of galaxies in OMEGA. As mentioned previously, the characteristics of our observations are ideal to study not only the integrated properties of the galaxies, but also to perform detailed spatial analysis. Integrated values can give us an estimate of the global star-forming properties of the galaxies, but it does not provide information about where in the galaxies the star formation is taking place, and most importantly, how the properties of the star-forming regions change as a function of environment and stellar mass. With this information we will be able to answer the question of whether the global decrease in SSFR happens because galaxies as a whole reduce the rate at which they form stars or because, perhaps, the regions of star formation become smaller in denser environments. The study of the distribution of ongoing star formation throughout the galaxies is essential to understand the mechanisms that are altering the gas and suppressing star formation. However, this type of analysis requires high-quality data and only a few works are found in the literature (e.g., Moss & Whittle, 2000; Koopmann & Kenney, 2004a,b; Bamford, Milvang-Jensen & Aragón-Salamanca, 2007; Jaffé *et al.*, 2011; Bretherton, Moss & James, 2013). These works have been able to show how relevant this type of analysis is, already providing some evidence that star formation

in cluster galaxies is more concentrated than in their field counterparts. We start by describing the procedure adopted for the creation of the pure $\mathrm{H}\alpha$ images, and the subsequent estimation of sizes and concentrations of the star-forming regions.

5.1 Creation of the $\mathrm{H}\alpha$ images

As explained in previous chapters, for a single galaxy we have several images, each one corresponding to the light observed at a narrow wavelength range. Therefore we know which images contain the $\mathrm{H}\alpha$, the $[\mathrm{NII}]$ and the continuum emission, respectively. With this information we can build 'pure $\mathrm{H}\alpha$' and 'pure $[\mathrm{NII}]$' images containing only the light contributing to line emission. Figure 5.1 shows the spectrum of one galaxy where we have highlighted the points that we select as part of the $\mathrm{H}\alpha$ emission (blue), $[\mathrm{NII}]$[1] emission (green) and continuum (red). For the two emission lines we only consider the points within the FWHM of the line, as shown by the dotted lines in the same figure. For the continuum we use the points where the absolute continuum-subtracted flux (using the continuum value from the fit) is $< 10\%$ of the continuum-subtracted peak of the emission. We then create a 'mean-$\mathrm{H}\alpha$' stamp and 'mean-$[\mathrm{NII}]$' stamp using all the images within the FWHM of each emission line, and from it we subtract a 'mean-continuum' stamp obtained from the continuum images. We only create an emission-line image when at least five individual monochromatic images contain the flux contributing to the line in question and the continuum, respectively.

This method of obtaining an $\mathrm{H}\alpha$-emission image avoids contamination from the [N II] line, which becomes an issue for many narrow band observations (e.g., Villar *et al.*, 2008; Sobral *et al.*, 2009). Regarding the $[\mathrm{NII}]$ image, in some cases there may be significant contamination coming from the red wing of the $\mathrm{H}\alpha$ line. At this stage, we do not correct the $[\mathrm{NII}]$ images from this contamination, but we will address this issue later. The images corresponding to the spiral galaxy 60598 are shown in Figure 5.2, where we can clearly see that the distribution of the star formation is more extended than the $[\mathrm{NII}]$ and the continuum. Of the 618 $\mathrm{H}\alpha$ detected galaxies, we are able to generate $\mathrm{H}\alpha$ images for 492, and $[\mathrm{NII}]$ images for 365. The remainder galaxies did

[1] Only the stronger $[\mathrm{NII}]$ $\lambda 6583$ line is used in this analysis.

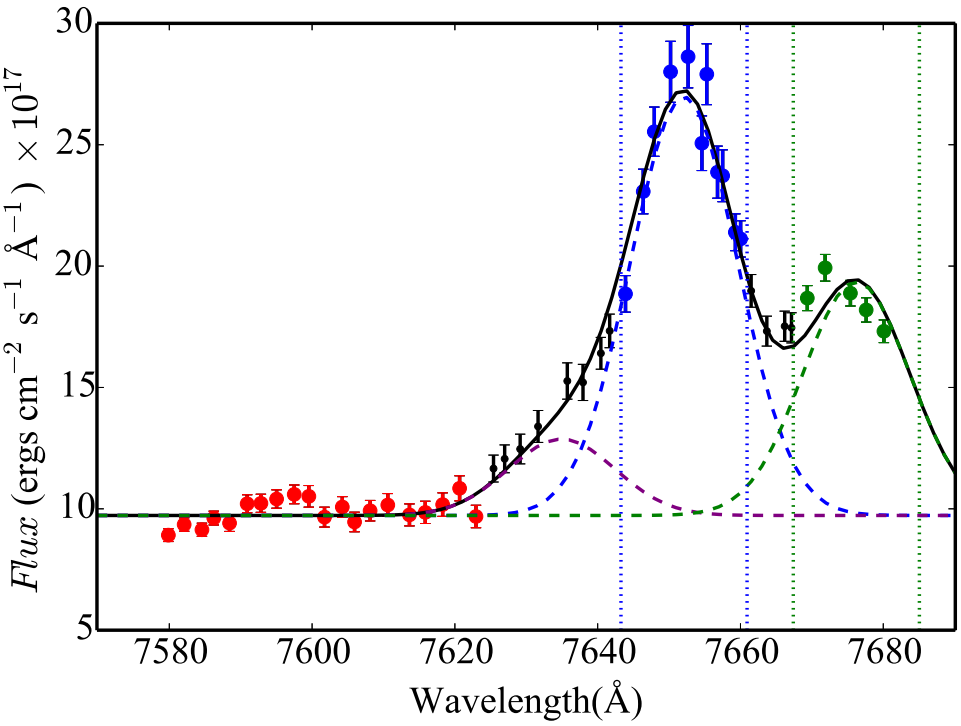

Figure 5.1: Spectrum of galaxy 60598. In different colours we have highlighted the images that are used to create the 'pure-Hα' (blue) and 'pure-[NII]' (green) images, and those used as continuum images (red). Each emission line is also shown with dashed lines. The dotted-blue and dotted-green lines mark the FWHM around Hα and [NII] λ6583.

not have at least five images contributing to the emission lines or to the continuum, as explained above.

When building the Hα and [NII] images we should ensure that the flux they contain is the same as that measured when fitting the integrated spectra. To test that this is the case, we measure the flux in the continuum, Hα and [NII] images using the same $R_{\rm tot}$ aperture and compare them with the flux measured for the continuum and within the FWHM of each line from the spectral fits. This comparison is shown in figure 5.3. The scatter in the continuum, Hα and [NII] are $\sim 5\%$, $\sim 11\%$ and $\sim 26\%$ respectively. For the [NII] images, in some cases we measured higher fluxes in the 'pure-[NII]' image than in the spectral fit, particularly for faint [NII] lines. As mentioned above, a potential reason for this difference is the contamination of the [NII] line from the red wing of Hα. This problem is worse for the [NII] line than for Hα because the latter is generally much stronger than the former. We have tested the effect of this contamination by computing the flux of Hα within the FWHM of the [NII] λ6583 line and adding it to the flux of [NII] from the spectral fit. The result is shown in the bottom-right panel

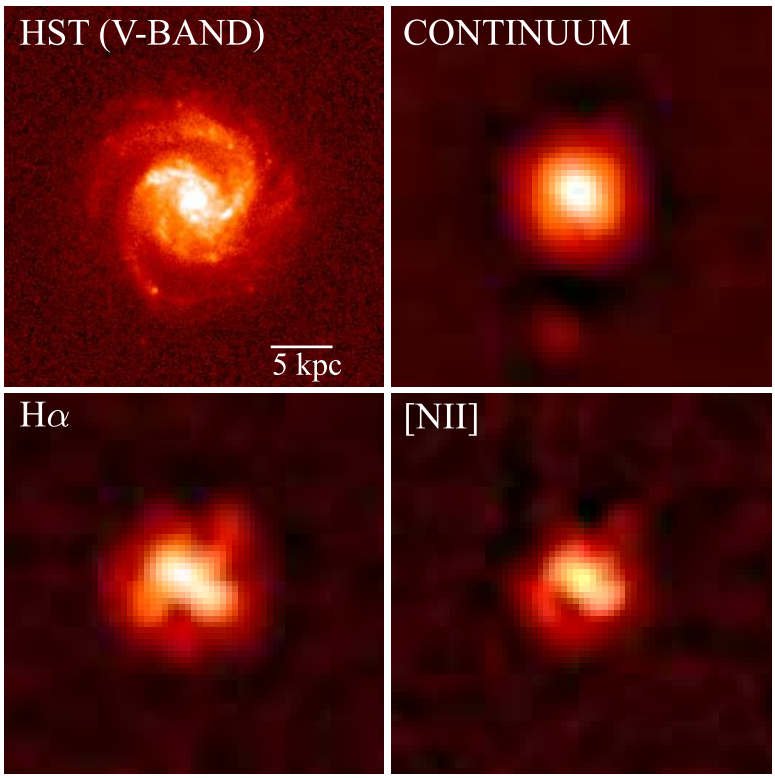

Figure 5.2: Galaxy 60598 as observed by the HST in the V-BAND, as well as the continuum, Hα and [NII] images.

of figure 5.3, where we can see that the bias towards higher fluxes in the [NII] images compared with the spectral fits has been removed when the contamination is taken into account. These tests indicate that the method to generate pure emission-line images works quantitatively, yielding fluxes that agree with those measured in the integrated spectra. Nevertheless, the Hα contamination of the [NII] line is typically $\sim 3\%$, and should have limited effect on our images.

5.2 Sizes and concentrations of the emission-line regions

We now use the images we have created to study the distribution of the Hα emitting regions and compare them with that of the underlying stellar populations. First we need to define the area of the galaxies that will be used to compare these distributions. We adopt the same procedure used by previous works to study the concentration of galaxies, which uses an isophotal radius corresponding to a surface brightness of 24 magnitudes per arcsec^2 (Koopmann, Kenney & Young, 2001; Koopmann & Kenney, 2004b; Bretherton, Moss & James, 2013). To estimate the isophotal radius in our

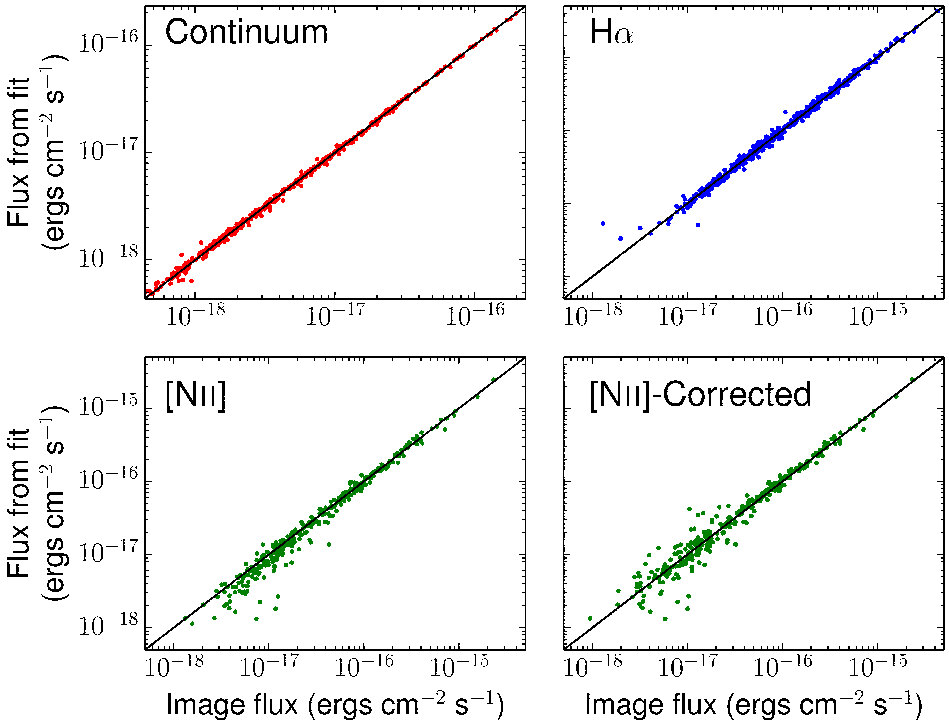

Figure 5.3: Comparison of the fluxes of the continuum, Hα and [NII] emission lines from the spectral fit with the fluxes measured in the corresponding images. We also show the comparison for the [NII] after correcting for contamination from Hα.

images we make use of the structural parameters previously estimated for the HST images, which are available in the STAGES catalogue of Gray *et al.* (2009). The light profiles of the galaxies are derived using the half-light radius, $R_{\rm e}$, Sérsic index, n, and total magnitude within $R_{\rm e}$, $m_{\rm tot}$, which, in combination with equations 6, 9 and 11 from Graham & Driver (2005), allow us to estimate the isophotal radius R for a given surface brightness $\mu(R)$:

$$R = \left[\mu(R) - m_{tot} - 2.5\ \log[f(n)] - 2.5\ \log(2R_e^2)\right] \frac{\ln(10)}{2.5b_n}, \tag{5.1}$$

where b_n can be approximated by $b_n \simeq 2n - 0.324$ and $f(n)$ is given by:

$$f(n) = \frac{ne^b}{b^{2n}}\Gamma(2n), \tag{5.2}$$

where Γ is the Gamma function. When measuring the concentrations, we want to make sure that we cover the full extent of the galaxies. Initially, we tried using a 24 magnitudes per arcsec^2 isophotal radius. However, after visual inspection of the images we decided to use a 26 magnitudes per arcsec^2 isophote, r_{26}, which successfully encompasses most of the galaxies' light. This is more appropiate for our work since

both our continuum and $\mathrm{H}\alpha$ images are deeper than in previous studies. Accounting for redshift dimming this magnitude corresponds to ~ 25.2 magnitudes per arcsec^2 in the cluster rest frame.

5.2.1 Sizes

We start our study of the distribution of the $\mathrm{H}\alpha$-emitting region by estimating the area of each galaxy that is hosting star formation. However, the measurement of the sizes of the $\mathrm{H}\alpha$-emitting regions is not a straightforward procedure as their distribution has generally a high degree of irregularity and clumpiness. As a first approach we calculate sizes by considering all the regions of the galaxy within r_{26} that are above a certain threshold of SFR per unit area. This threshold is estimated by evaluating the background noise in the $\mathrm{H}\alpha$ images and, by visual inspection, determining the threshold in flux per unit area that removes the noisy features in the images. From this analysis we start by using a SFR threshold that corresponds to $\sim 5 \times 10^{-5}\mathrm{M}_{\odot}\mathrm{yr}^{-1}\mathrm{kpc}^{-2}$ (15 times the standard deviation of the background noise). Because this is a conservative limit, some galaxies do not have any regions with ongoing star formation above this threshold. From the area covered by the pixels selected above the threshold, $A_{\mathrm{H}\alpha}$, we define a radius $r_{\mathrm{H}\alpha} = \sqrt{\frac{A_{\mathrm{H}\alpha}}{\pi}}$. In Appendix B we show the SFR contours on top of the V-band HST images, together with the spectrum and some relevant galaxy properties for the galaxies with star-forming regions larger than the area encompassed by twice the FWHM of the PSF, which corresponds to 79 pixels ($40\mathrm{kpc}^2$ at $z = 0.165$).

5.2.2 Concentrations

The above estimation of the sizes of the star-forming regions provides very relevant information. However, it has the caveat that it depends on the chosen threshold value. A complementary way of studying the $\mathrm{H}\alpha$ distribution that does not depend on any SFR threshold is given by the concentration of the $\mathrm{H}\alpha$ light, which can be compared with that of the underlying stellar populations. Moreover, measurements of the concentration provide information about the light distribution in the galaxies in a more objective way than qualitative visual inspections, although these are also useful. In

our work we employ a similar concentration index to the one used in previous studies (Koopmann, Kenney & Young, 2001; Koopmann & Kenney, 2004b; Bretherton, Moss & James, 2013), which is defined as:

$$C_{30} = \frac{F_R(0.3r_m)}{F_R(r_m)}, \tag{5.3}$$

where $F_R(r_m)$ is the flux within the isophote corresponding to a surface brightness of m magnitudes per arcsec^2 and $F_R(0.3r_m)$ is the flux within $0.3r_m$. As stated above, in our study we use r_{26}. The concentration of our galaxies is then calculated using an ellipse with a semi-major axis equal to this isophotal radius, and a major-to-minor axis ratio Q which was determined by SExtractor and is provided by Gray *et al.* (2009). We limit the measurement of the concentration to objects whose major axis is equal to or larger than the FWHM of the PSF in our images, which is 5 pixels or 1.27 arcsec. Due to the high spatial resolution of the HST images that were used to extract the structural parameters, highly-inclined galaxies have semi-minor axes that are often very small compared with the ground-based seeing. In these cases we force the semi-minor axis to be equal to the FWHM. We measure the $\mathrm{H}\alpha$ concentrations in a total of 389 galaxies.

We also have to keep in mind that the COMBO-17 R-band image that we are using as reference was observed in different seeing conditions from the OMEGA ones. The FWHM of the R-band image is 0.7 arcsecs, which is significantly lower than that of our images. Differences in the FWHM of the images can affect the estimation of the concentration in such a way that a source observed with a larger seeing would look less concentrated than the same source observed in lower seeing conditions. For that reason, we convolve the R-band image with a Gaussian function to match the FWHM of the OMEGA images, using the `IRAF` task `gauss`.

To study the concentration of the $\mathrm{H}\alpha$ emission we define a similar concentration index, using as reference the r_{26} obtained for the R-band image. $C_{\mathrm{H}\alpha}$ is therefore defined as:

$$C_{\mathrm{H}\alpha} = \frac{F_{\mathrm{H}\alpha}(0.3r_{26})}{F_{\mathrm{H}\alpha}(r_{26})}. \tag{5.4}$$

5.2.3 First results

In this section we present the first results from the spatial analysis, although there is still much to come, as this is still work in progress. Moreover, when performing the

analysis of the $\mathrm{H}\alpha$ and $[\mathrm{NII}]$ images, we noticed that in some galaxies a significant number of negative pixels were found. The value of the negative pixels is always smaller than $\sim 3\%$ of the peak value in the image. This is due to sky subtraction uncertainties which affect mostly large galaxies. Recall that the sky was estimated by dithering the images by a few arcsecs (section 3.3.1), and the light of the objects was eliminated by median filtering. Some residual light from large objects may still be present in the sky image, and the sky may have been marginally over-subtracted for the largest objects. This problem may have a small effect in the estimation of the concentrations and sizes, and deserves further investigation. Nevertheless, the level of the problem seems relatively small. We will address this issue as part of our planned future work that we describe in the final chapter of this thesis.

We start by showing in figure 5.4 an example of the distribution of the $\mathrm{H}\alpha$ emission in different galaxies, on top of the V-band HST images. In each column we show galaxies in the infall regions, in the core, and those classified as bona-fide star-forming or AGN (see section 4.2.1). Overall, the $\mathrm{H}\alpha$ emission is quite clumpy, and does not always have the same distribution as the underlying stellar population. The distribution of the $\mathrm{H}\alpha$ emission in galaxies in the infall and core regions is quite similar. In both environments there are objects where the $\mathrm{H}\alpha$ emission is spread throughout the galaxy and some where the galaxies' centres are devoid of $\mathrm{H}\alpha$ emission. With respect to the difference between star-forming galaxies and those hosting an AGN, $\mathrm{H}\alpha$ emission tends to be more extended in the former ones and more centrally concentrated in the latter.

We now look at the sizes of the star-forming regions, estimated in section 5.2.1, where we defined the radius $r_{\mathrm{H}\alpha}$ from the total area of a galaxy that is hosting star formation. To compare this radius with the total area of the galaxy, we define a similar radius for the continuum emission, $r_{\mathrm{cont}} = \sqrt{\frac{A_{\mathrm{cont}}}{\pi}}$, where A_{cont} is the area of the ellipse within the 26 mag per arcsec^2 isophote, r_{26}. To investigate the effect of environment on the star formation we compare the values of $r_{\mathrm{H}\alpha}/r_{\mathrm{cont}}$ for galaxies at different densities. This is shown in figure 5.5, where $r_{\mathrm{H}\alpha}/r_{\mathrm{cont}}$ is plotted against r_{cont} in three different mass-density bins. Morphologies and SED types are shown with different symbols and colours, respectively, as we did in figure 4.16. In all the density bins, almost all the

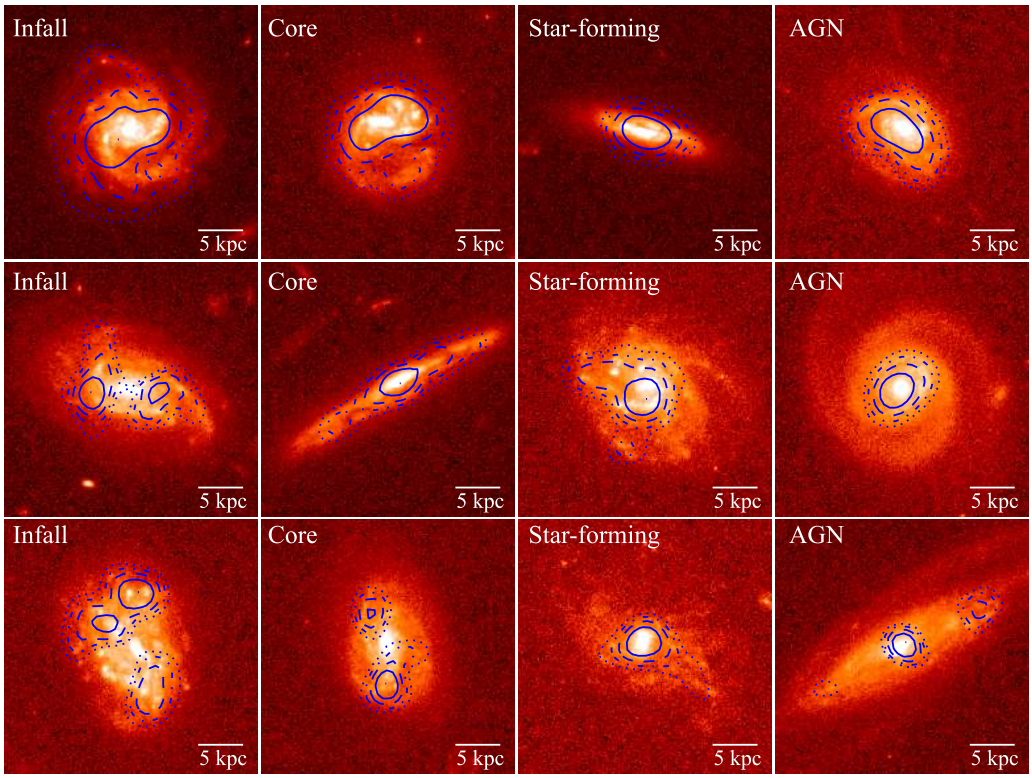

Figure 5.4: Hα contours overlayed on top of the HST images for 12 of the galaxies in our sample. The contours are logaritmically spaced from the star-forming threshold to the maximum pixel value. In each column we show galaxies in the infall and core regions, and those classified as bona-fide star-forming or AGN (see section 4.2.1).

galaxies have star-forming regions that are significantly smaller than the sizes of the galaxies (as determined by $r_{\rm cont}$). However, these sizes only account for star formation above the chosen threshold, and we have not computed yet the fraction of the total SFR of a galaxy contained in those regions. These fractions will be very useful to evaluate how significant are the differences between the Hα and continuum extents. Moreover, we find no significant changes with environment for the values of $r_{\rm H\alpha}/r_{\rm cont}$, with a K-S test yielding a 57% probability of them being drawn from the same population.

As previous studies have used only galaxies with disk morphologies, we focus on these morphological types and further investigate the changes of $r_{\rm H\alpha}/r_{\rm cont}$ with mass and environment. In fact, these galaxies dominate the star-forming population at intermediate and high masses (see Sec. 4.3.4), and therefore they are the objects more likely to show any significant variation. Thus, we limit our study to galaxies with S0 to Sd morphologies and investigate any changes in their values of $r_{\rm H\alpha}/r_{\rm cont}$ with environment and mass. In Table 5.1 we show the values of $r_{\rm H\alpha}/r_{\rm cont}$ for different disk morphological types together with those for different SED types considering only disk

galaxies. We compare infall and core, and low- and high-mass disk galaxies. Generally, all disk morphologies show similar $r_{\mathrm{H}\alpha}/r_{\mathrm{cont}}$ of $\sim 0.3 - 0.45$ implying that the star-forming regions cover between one third and half of the total galaxy area. Although again we do not find any statistically significant trend, galaxies in the core tend to have slightly larger star-forming regions relative to the galaxy area. The Sd types show the largest change from infall to core. However, there are only 3 objects of this type detected in the core and 17 in the infall regions, and therefore this difference is probably not significant. Moreover, none of the morphological types considered here shows a significant variation with mass. Regarding the SED types, *blue cloud* galaxies have always higher values of $r_{\mathrm{H}\alpha}/r_{\mathrm{cont}}$ than the other two types, with a small but still not significant increase from the infall regions to the core.

From these analysis, the sizes of the star-forming regions in the cluster galaxies seem to always be significantly smaller than the sizes of the host galaxies, although possible caveats in our estimation of the sizes may produce a weaker trend. Furthermore, we find no significant variation of $r_{\mathrm{H}\alpha}/r_{30}$ between the three different mass density bins that we explore. These findings imply that the star formation is not distributed in the same way as the underlying stellar population, and that the difference between their distributions does not depend on the environment, as estimated by stellar mass density, at least within the ranges explored in our study. However, we bear in mind that there might be some galaxies in high-density regions seen in projection and that only galaxies with $r_{\mathrm{H}\alpha} > 0$ are considered in our study. In chapter 4, we concluded that a change in SSFR must be accompanied by a change in morphology or SED type. Therefore, we would not expect an environmental variation of $r_{\mathrm{H}\alpha}/r_{30}$ in each class, but would overall. A possible explanation for these findings is the fading of the stellar populations in the outer disk of our galaxies, accompanying a slow suppression of star formation.

Since the sizes of the star-forming regions depend on the SFR threshold, we also study the distribution of the star-forming regions using the concentration of the light coming from the $\mathrm{H}\alpha$ emission and that from the stellar continuum. This method, which avoids the need for a SFR threshold, can also be used to explore the differences between galaxies in different environments. Although the concentration index is a useful

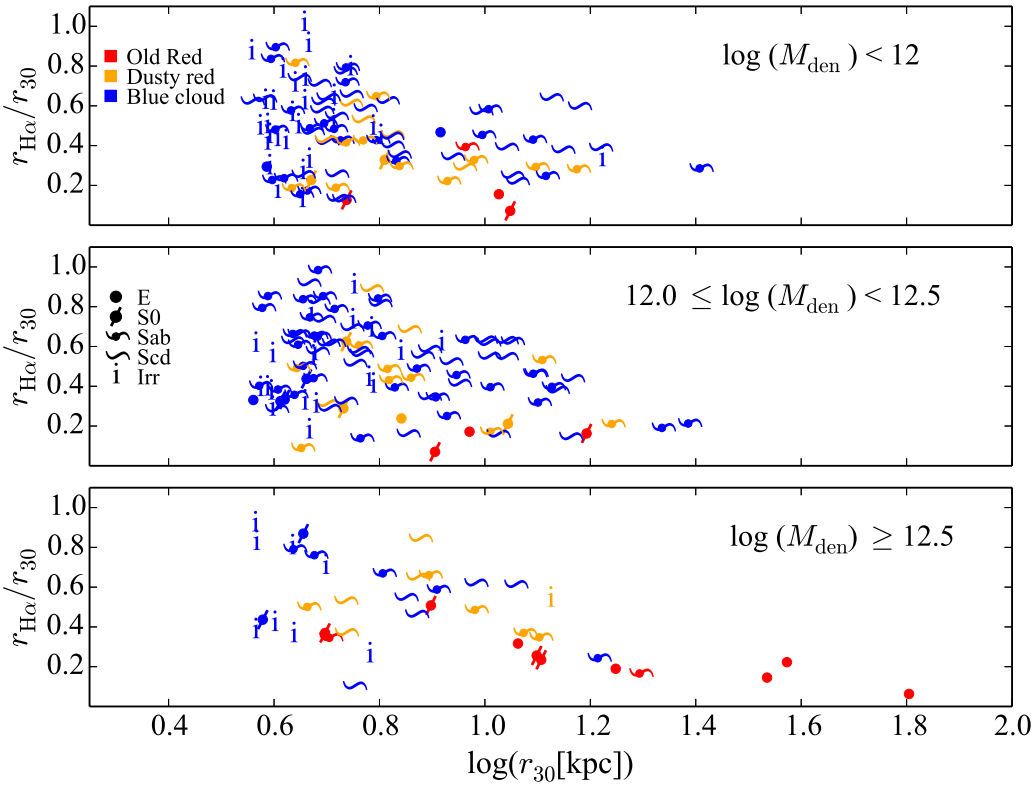

Figure 5.5: $r_{\rm H\alpha}/r_{cont}$ versus r_{cont} in three different stellar mass density bins. The two lowest density bins correspond to the infall regions. We only show galaxies with $r_{\rm H\alpha} > 0$. We plot morphological and SED types with different symbols and colours, respectively, as explained in the legend.

$r_{\rm H\alpha}/r_{\rm cont}$	All galaxies Med. (σ)	Infall Med. (σ)	Core Med. (σ)	K-S p-value	$M_\star < 10^{9.5} M_\odot$ Med. (σ)	$M_\star > 10^{9.5} M_\odot$ Med. (σ)	K-S p-value
S0	0.31 (0.19)	0.26 (0.15)	0.40 (0.21)	0.19	0.33 (0.05)	0.26 (0.21)	0.21
Sa	0.41 (0.20)	0.40 (0.20)	0.51 (-)	-	0.23 (0.21)	0.44 (0.18)	0.17
Sb	0.43 (0.21)	0.43 (0.22)	0.43 (0.21)	0.85	0.64 (0.22)	0.40 (0.20)	0.06
Sc	0.44 (0.19)	0.46 (0.19)	0.46 (0.18)	0.45	0.61 (0.18)	0.44 (0.19)	0.15
Sd	0.37 (0.19)	0.35 (0.16)	0.65 (0.10)	0.01	0.33 (0.20)	0.42 (0.18)	0.57
old red	0.24 (0.14)	0.13 (0.12)	0.30 (0.11)	0.03	-	0.24 (0.14)	-
dusty red	0.44 (0.19)	0.43 (0.19)	0.51 (0.16)	0.07	-	0.44 (0.19)	-
blue cloud	0.53 (0.20)	0.52 (0.20)	0.59 (0.21)	0.87	0.58 (0.21)	0.52 (0.20)	0.32

Table 5.1: Values of $r_{\rm H\alpha}/r_{\rm cont}$ for different SED and morphological types, in the infall, core and at low and high masses. We also show the p-value obtained in the comparison between infall/core and low/high mass for each type.

parameter to compare the distribution of the star-forming regions with respect to the older stars, we have to bear in mind that the same change in concentration can be produced in different ways, and therefore it might be difficult to identify the responsible process. An increase in the central luminosity while the outer parts remain constant will produce a higher concentration, but an increase in concentration will also result from a decrease in the luminosity of the outer parts with a constant central luminosity (e.g., 'quenched' disk).

Previous studies have found that disk galaxies in clusters tend to have higher concentrations than those residing in the field (Koopmann & Kenney, 2004b; Bamford *et al.*, 2008; Jaffé *et al.*, 2011; Bretherton, Moss & James, 2013). Since our study does not include any field galaxies, we investigate the changes in concentration and size of the star-forming regions with galaxy stellar mass density. First, we study the variation of $C_{\mathrm{H}\alpha}$ and C_{30} with environment separately. In both cases we find the concentrations to be slightly higher in the core than in the infall regions. For the $\mathrm{H}\alpha$ emission a K-S test yields a probability of $\sim 8\%$ for the concentration distributions in the infall and core being regions drawn from the same population, whereas the difference in the median values is $\sim 0.04 \pm 0.03$. For the continuum emission, the K-S probability is $\sim 4\%$ and the median difference $\sim 0.03 \pm 0.02$. This increase in the concentration of the light coming from the $\mathrm{H}\alpha$ emission and from the continuum is probably a consequence of a change in morphology with environment, as galaxies in higher density regions tend to have earlier-type morphologies that are more concentrated (Dressler, 1980; Bamford *et al.*, 2009). We use now the ratio between $C_{\mathrm{H}\alpha}$ and C_{30}, which will tell us how concentrated the $\mathrm{H}\alpha$ emission is with respect to the R-band emission. This is shown in figure 5.6, where we plot $C_{\mathrm{H}\alpha}/C_{30}$ vs C_{30} in three different mass-density bins. Again, morphologies and SED types are shown with different symbols and colours, respectively.

In all the density bins, almost all the galaxies show more concentrated $\mathrm{H}\alpha$ than R-band emission. This confirms the tentative results obtained from the relative size comparison discussed above. Moreover, the comparison between the values of $C_{\mathrm{H}\alpha}/C_{30}$ in the infall and core regions yields no significant difference between them, neither using all the morphologies nor restricting to only disk galaxies (K-S test p-values of 0.91 and

0.68, respectively). These two findings, together with the results from previous works which found an increase in the concentration of $\mathrm{H}\alpha$ from the field to the cluster regions, implies that most of our galaxies must have already increased their $\mathrm{H}\alpha$ concentrations by the time they reached the cluster environment we explore. To support this idea, we compare the values of $C_{\mathrm{H}\alpha}/C_{30}$ for our cluster disk galaxies with those found for isolated disk galaxies by Koopmann & Kenney (2004b, figure 3) and for field disk galaxies by Bretherton, Moss & James (2013, figure 5). They find that $C_{\mathrm{H}\alpha}/C_{30} \sim 1$, implying that for field galaxies the distribution of the star-forming regions is quite similar to that of the continuum. In their sample of cluster galaxies, as in ours, $C_{\mathrm{H}\alpha}$ is almost always significantly larger than C_{30}. Therefore, the process responsible for the increase in the concentration of the star formation took place, for the majority of the cluster galaxies, in lower density regions than the ones we sample. In other words, their star-forming regions were already truncated or concentrated before entering the multi-cluster system of our study.

In addition to these global trends, figure 5.6 also shows that in the two lowest density bins, disk galaxies stand out from the rest showing high $C_{\mathrm{H}\alpha}$ and high C_{30}. In the core regions, the galaxies that show the highest concentration in both $\mathrm{H}\alpha$ and the R-band are *old reds*. Four of them have elliptical morphology, of which two (46643 and 39020) are classified in 4.2.1 as bona-fide optical AGN, which would explain why they have such high concentration. The other two *old red* ellipticals (14868 and 41990) are not classified as AGN but still show more centrally concentrated $\mathrm{H}\alpha$ and continuum emission.

As we did with the sizes of the star-forming regions, we explore in Table 5.2 the values of $C_{\mathrm{H}\alpha}/C_{30}$ for different disk morphological types together with those for different SED types considering only disk galaxies. We compare infall and core, and low- and high-mass disk galaxies. As was already pointed out above, almost all galaxy types show higher concentrations in $\mathrm{H}\alpha$ than in the continuum. Among the different disk morphologies, the Sd types show the lowest concentration of $\mathrm{H}\alpha$ with respect to the older stellar populations, whereas the earlier-type ones show progressively higher concentrations. We speculate that the process that increases the concentration in disk galaxies also results in a morphological transformation. The galaxies for which the

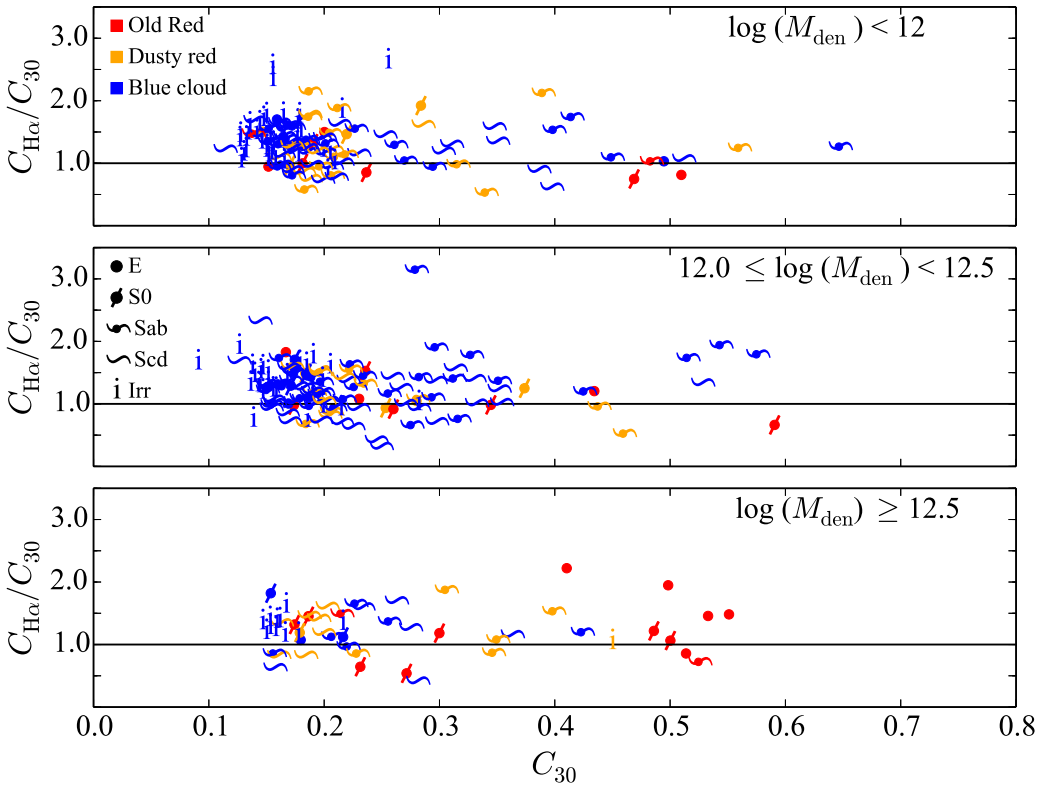

Figure 5.6: $C_{H\alpha}/C_{30}$ vs C_{30} in three different stellar mass density bins. We plot morphological and SED types with different symbols and colours, respectively, as explained in the legend.

concentration has increased are also of earlier morphological types. Later types are, perhaps, the galaxies for which this process is less advanced.

However, none of the morphological types show a significant difference from the infall to the core, or between low- and high-mass objects. Regarding SED types, *blue cloud* and *dusty red* disk galaxies show similar concentrations, and again no significant variation with density or mass is found.

5.2.4 Emission-line distribution for 'retired-galaxies' and AGN

We finish the introduction of the first results on the spatial distribution of the line emission by addressing the issue of the extension of the emission-line regions in 'retired-galaxies' (RG, see section 4.2.1). These are galaxies that have stopped formed stars and the radiation is believed to come from hot low-mass stars in the post-AGB phase (Cid Fernandes *et al.* 2011, Yan & Blanton 2012, Stasińska *et al.* 2015). From their definition, the line-emitting region does not have to be nuclear, and therefore we might

$C_{\rm H\alpha}/C_{30}$	All galaxies Med. (σ)	Infall Med. (σ)	Core Med. (σ)	K-S p-value	$M_\star < 10^{9.5} M_\odot$ Med. (σ)	$M_\star > 10^{9.5} M_\odot$ Med. (σ)	K-S p-value
S0	1.20 (0.34)	1.25 (0.34)	1.19 (0.35)	0.64	1.39 (0.26)	1.06 (0.34)	0.08
Sa	1.32 (0.36)	1.21 (0.36)	1.56 (0.10)	0.14	1.39 (0.38)	1.18 (0.35)	0.82
Sb	1.17 (0.47)	1.26 (0.49)	1.02 (0.33)	0.44	1.27 (0.37)	1.18 (0.49)	0.65
Sc	1.16 (0.40)	1.16 (0.41)	1.21 (0.38)	0.74	1.07 (0.38)	1.17 (0.41)	0.87
Sd	0.93 (0.39)	0.89 (0.38)	1.01 (0.36)	0.96	1.00 (0.41)	0.83 (0.34)	0.99
old red	1.03 (0.32)	0.98 (0.27)	1.18 (0.33)	0.33	1.45 (0.07)	0.98 (0.28)	0.01
dusty red	1.19 (0.38)	1.19 (0.40)	1.19 (0.33)	0.94	1.14 (0.11)	1.21 (0.38)	0.33
blue cloud	1.28 (0.35)	1.28 (0.36)	1.23 (0.40)	0.67	1.30 (0.30)	1.26 (0.39)	0.43

Table 5.2: Value of $C_{\rm H\alpha}/C_{30}$ for different SED and morphological types, in the infall, core and at low and high masses. We also show the p-value obtained in the comparison between infall/core and low/high mass for each type

expect it to be more extended than in galaxies hosting an AGN. Although we did not classify any galaxy as bona-fide RG given the line-ratio uncertainties, we still found some objects in the corresponding area of the WHAN diagram. We could only generate emission-line images for two of these objects (31013 and 53201), and for them we show in figure 5.7 the distribution of $\rm H\alpha$ and $[\rm NII]$ in blue and red, respectively. For comparison, we also show the same distributions for two bona-fide AGN (19305 and 45654). Although the numbers are too low for an statistical comparison, the two 'retired-galaxies' seem to have offset $\rm H\alpha$ and $[\rm NII]$ emission, whereas in AGN these two lines come from the same regions. This might be a consequence of the $\rm H\alpha$ emission in 'retired-galaxies' being not associated with nuclear sources, but instead being distributed in the outer parts of the galaxies. The origin of the ionising radiation in these galaxy types is very interesting, but our sample is too small to address it. Integral Field Spectroscopic surveys like MaNGA (Bundy *et al.*, 2015) are shedding more light into this issue, and are already producing interesting results (Belfiore *et al.*, 2014).

5.2.5 Summary

In this section we have succesfully created emission-line images of $\rm H\alpha$ and $[\rm NII]$. We have developed a method to estimate the sizes and concentrations of the star-forming regions in our cluster galaxies, and we have compared them for galaxies in different densities and with different masses. We find no significant changes in the sizes or concentrations of the $\rm H\alpha$-emitting regions from the infall to the core regions. In most of the galaxies the extent of the star-forming regions is between 30% and 45% of that

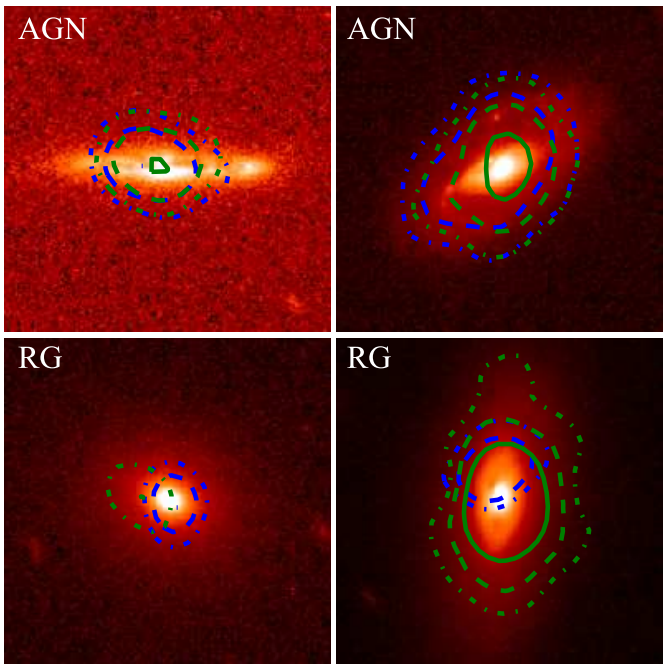

Figure 5.7: Hα (blue) and [NII] (green) contours overlayed on top of the HST images for 2 AGN and 2 'retired-galaxies' (RG). The contours are logaritmically spaced from the star-forming threshold to the maximum pixel value.

of the underlying stellar population, and therefore always covers less than half of the galaxy. Moreover, the majority of the galaxies have higher concentrations in Hα than in the continuum at all densities and masses. This finding complements previous results that showed the concentrations of Hα with respect to the continuum to be higher in cluster disk galaxies than in field ones (Koopmann & Kenney, 2004b; Bamford *et al.*, 2008; Jaffé *et al.*, 2011; Bretherton, Moss & James, 2013). Furthermore, since these works also showed that the concentration of Hα emission in field galaxies is similar to that of the continuum (Koopmann & Kenney, 2004a; Bretherton, Moss & James, 2013), our findings imply that the star-forming regions of galaxies in the multi-cluster system A901/2 have already been influenced by the environment, since the current star formation is less extended than the older stellar population. We therefore conclude that the physically responsible mechanism acts at lower densities than the ones explored here. Extending this type of study to the infall regions with lower densities would therefore be desirable.

We have also shown that our data allow us to perform a comparison between the distribution of the Hα and [NII] emission. This type of analysis is very interesting to study the origin of the ionising radiation in 'retired-galaxies'.

With the results presented here we have shown that spatial studies of the emission-line regions in OMEGA can provide useful information about the galaxies' properties and how they might change with mass and environment. We are eager to dig deeply into this analysis and discover what it can tell us about the fate of the galaxies in A901/2, but this work is beyond the scope of this thesis. Our plans for future work are explained in chapter 6.

Chapter 6

Conclusions and future work

6.1 Conclusions

The work presented in this thesis has been aimed at obtaining a better understanding of the processes that affect galaxies that reside in clusters. In particular we have investigated the effects of environment on the star formation within galaxies. We have studied the suppression of star formation in cluster galaxies at two different stages of their evolution. On the one hand, we have looked at cluster galaxies while they are still forming stars but are already going through a process, or multiple processes, that affect the rates at which they form stars. On the other hand, we have observed galaxies just after their star formation has been strongly suppressed, and explored the different mechanisms that drove the transformation from actively star-forming to passive. In the following we summarize our results.

6.1.1 Cluster 'k+a' galaxies as a link between spirals and S0s in clusters

In chapter 2 we looked at a sample of disk galaxies which had recently stopped forming stars in a cluster at $z \sim 0.3$. These galaxies were selected by the presence of the 'k+a' feature in their spectrum, which indicates that the galaxies host a combination of young and old populations. By using Integral Field Spectroscopic observations

(FLAMES/VLT), we analysed the distributions and kinematics of the young and old stellar populations inhabiting these galaxies. From our analysis, the young stellar populations were found to have similar or more concentrated distributions than the older stars. The kinematics of the young populations are consistent with being rotationally supported, and therefore they must have been formed in a disk. In the few cases where we could kinematically separate the young and old populations, we found that they behave similarly. These findings indicate that the stellar disk is preserved and remains largely undisturbed through the process that suppresses star formation. Interestingly, galaxies with concentrated young populations were identified to have close companions, therefore suggesting that they might have experienced galaxy-galaxy interactions. The results from this study led us to conclude that the process or processes responsible for the suppression of the star-formation in cluster disk galaxies, and the transformation of spirals into S0s, must have been reasonably gentle. Moreover, the driving process favours a centrally-concentrated (but not nuclear) last episode of star formation in the cluster disk galaxies. This may contribute to the growth of the bulge. Finally, galaxy-galaxy interactions also seem to have contributed to the exhaustion of the cold gas in the galaxies.

6.1.2 Integrated star formation and AGN activity in the multi-cluster system A901/2

In chapter 3 we turned our attention to the study of the ongoing star formation and AGN activity of galaxies in the multi-cluster system A901/2, at $z = 0.165$. We introduced the OMEGA survey, whose goal is to study emission-line galaxies over a wide range of stellar masses and environments. We explained the procedures adopted for the reduction of the data and the building of the spectra containing the $\mathrm{H}\alpha$ and $[\mathrm{NII}]$ lines. Both the quantity and quality of the spectra generated showed that Tuneable Filter observations are a very powerful tool to obtain spectral information for a large number of galaxies at a single redshift. Furthermore, we presented a method to fit the spectra of the galaxies and to generate the probability density distributions of the model parameters. Thanks to the proximity of the two spectral lines $\mathrm{H}\alpha$ and $[\mathrm{NII}]$ we were able to measure both of their fluxes and equivalent widths. The probability den-

sity distributions were used to define robust samples of galaxies. We finished chapter 3 by explaining the detection limits and completeness of our observations.

The results from the analysis of the integrated properties of the emission-line galaxies were presented in chapter 4. First, using the spectra from the central regions of the galaxies, we classified galaxies as star-forming or AGN based on the WHAN emission-line diagnostic diagram from Cid Fernandes *et al.* (2010, 2011). We compared our sample of optically-detected AGN with the galaxies in A901/2 that were detected as XMM X-ray point sources by Gilmour *et al.* (2007). Moreover, we investigated properties such as SED types, stellar masses and morphologies of the galaxies hosting AGN, and compared them with the star-forming population. Finally, we studied the environmental dependence of AGN activity by computing the stellar mass densities of the regions where they reside. The results from these analyses can be summarized as follows:

• We detect a large number of optical AGN that do not have an X-ray counterpart. Only one of the 12 galaxies detected as X-ray point sources is classified as a bona-fide optical AGN, although some remain unclassified because we do not have the required wavelength coverage. The lack of optical counterparts is attributed to heavily obscured Compton-thick AGN with no or weak emission lines.

• AGN galaxies have generally disk morphologies, with only a few AGN having early-type morphologies. Moreover, they present a wide range of stellar masses and dominate the high-mass end of the emission-line population.

• We find no dependence of the AGN fraction with environment, from the outskirts to the core of the clusters. The comparison between the distribution of AGN hosts and star-forming galaxies indicates that, perhaps, they distribute differently in the cluster environment. This difference is more significant for the most securely classified AGN, which may also be those in which the AGN is most dominant.

We also measured global integrated $\mathrm{H}\alpha$ fluxes that were then used to estimate the star formation rates (SFRs) of our cluster galaxies. We studied the variation of the specific star formation rates (SSFRs, i.e., SFR per unit stellar mass) with stellar mass and environment, finding that both drivers contribute to the suppression of the star

formation in the galaxies in A901/2. However, stellar mass seems to play the strongest role: more massive galaxies tend to have very significantly higher SSFRs.

When comparing the SSFRs of our cluster galaxies with the field relation at a similar redshift, provided by Whitaker *et al.* 2012, we find that the majority of our galaxies show suppressed SSFRs with respect to the field. These results indicate that, contrary to previous results (Balogh *et al.*, 2004a; Verdugo, Ziegler & Gerken, 2008; Poggianti *et al.*, 2008; Bamford *et al.*, 2008), the SSFRs of galaxies do not remain constant with increasing density. We associate this apparent contradiction to our ability to detect much lower levels of star formation than in previous studies, and therefore detecting galaxies with low star formation rates that would have been missed by other surveys.

To study in isolation the effects of the environment on the properties of the star-forming galaxies, we successfuly removed the contribution of the stellar mass of the galaxies to the suppression of the star formation. Even when the mass effect was removed, we still detected a significant difference between the SSFRs of galaxies in the infall regions and those in the core: on average, galaxies in the core have their SSFRs suppressed by a factor of ~ 2 compared to those in the infall regions. We then explored the variation in SSFR for galaxies with different SED types and morphologies, and studied the changing fractions of these galaxy types as a function of stellar mass and density for the global cluster population. The main findings from these analyses are:

• For a given SED or morphological type, once the mass effect is removed, there is no statistically significant variation in the SSFR from the infall regions to the core. A variation in the SSFR of a galaxy must be accompanied by a change in SED type or morphology, and therefore the global change in SSFR is driven by changes in the fractions of galaxies with different SED types and morphologies. This idea is supported by the decrease in the fraction of star-forming spiral galaxies at intermediate masses, which are replaced by galaxies with early-type morphologies (ellipticals and S0s) that are passive or have low SSFRs.

• Low and high mass galaxies experience different transformations when they join the cluster environment. On the one hand, in low-mass objects the star formation is rapidly quenched and morphological transformations are likely to happen. On the other hand, at high masses galaxies show a slower transition from active to pas-

sive preserving their disk morphologies and intermediate levels of star formation. The increasing fraction of S0s towards higher density regions supports this idea.

• Finally, high-mass ($M_\star > 10^{9.5} M_\odot$) spiral galaxies in A901/2 evolve into a phase of relatively high SSFRs and red colours while they still retain their disk morphology. These galaxies survive until the very core of the multi-cluster system. The fraction of spiral galaxies with *dusty red* feature increases with stellar mass density, as found by previous studies (Bamford *et al.*, 2009; Wolf *et al.*, 2009). The increasing fraction of S0s at these masses indicates that *dusty red* spirals are probably an intermediate stage in the transformation of spirals into S0s.

6.1.3 Spatial studies of the emission-line regions in A901/2

The last chapter of this thesis has been devoted to the spatial analysis of the emission-line regions in the galaxies in A901/2. In this chapter we explained the procedure adopted for the creation of the emission-line images and provided quantitative tests that confirmed its efficacy. Different methods to study the distribution of the star-forming regions in our galaxies were proposed, which include the measurement of the area of the galaxies hosting ongoing star formation and the calculation of the concentration of the $\mathrm{H}\alpha$ and continuum light.

We find no statistically significant changes in the sizes or concentrations of the star-forming regions of our cluster galaxies from the infall to the core regions, or from low to high masses. In the majority of the galaxies the extent of the star-forming regions is significantly smaller than that of the underlying stellar population. Moreover, most of the galaxies at all densities and masses have higher concentrations in $\mathrm{H}\alpha$ than in the continuum. Since previous works (Koopmann & Kenney, 2004a; Bretherton, Moss & James, 2013) have found that the concentration of $\mathrm{H}\alpha$ in field disk galaxies is very similar to that of the continuum, our results indicate that in our cluster system, disk galaxies have already experienced a process that has truncated or concentrated the star-forming regions. We therefore conclude that the responsible mechanism acts at lower densities than the ones we explore in our study.

The results obtained from the analysis of the cluster 'k+a' galaxies and the star-forming

galaxies in A901/2 provide us with an overall picture of how star formation in galaxies is influenced by environment. As galaxies fall into clusters, their star formation is affected by the environment in a way that, besides suppressing it, also truncates or concentrates the remainder star formation. These effects lead to a more centrally concentrated last episode of star formation before it is suppressed. As a consequence, the young populations in galaxies where star formation has been recently suppressed have a centrally-concentrated distribution compared with the more extended old stellar populations. This series of events may lead to the formation of S0s out of spiral galaxies in clusters.

6.2 Future work

A lot of work has already been devoted to the study of star formation in cluster galaxies and the transformation of spirals into S0s, producing many significant results. However, the studies presented here can still be expanded using new Integral Field Spectroscopic instruments such as MUSE and KMOS. The capabilities of these instruments will allow us to obtain even more detailed information about the environmental processes driving the suppression of star formation in galaxies at different cosmic times.

Moreover, although the OMEGA survey has also been intensively studied, there is still much to explore in the data from the A901/2 multi-cluster system.

The first analysis of the properties of the spatially-resolved emission-line regions in the galaxies in A901/2 have already produced very interesting results. However, more work is expected to be devoted to their study. Although the results presented in this thesis may not change, our next step is to correct the problems that have arisen regarding the sky subtraction mentioned at the beginning of section 5.2.3, and obtain emission-line images clean from these effects. We will repeat the same analysis presented in chapter 5 to test if any of the conclusions are affected. We will also investigate if the choice of a different SFR threshold for the estimation of the sizes of the star-forming regions provides more information on the star-forming properties of the galaxies. Introducing a higher threshold might yield different results, as only the regions with the highest SFRs would be considered. These regions may show a different trend with

environment. In a similar way, a lower SFR threshold can be used to study variations at lower levels of star formation.

As an alternative tool to analyze the emission-line images, we will inspect them visually to look for differences in the distribution of different levels of star formation. This way of analysing our images will provide more insights into our understanding of the processes that are affecting the star-forming regions, as we will be able to evaluate when they are clumpy or off-centred. Additionally, quantitative methods to estimate the degree of clumpiness of the star formation (e.g., Hoyos *et al.* 2012) will be implemented. The visual inspection of the galaxies will include the study of the dynamical state of the galaxies. We will identify whether galaxies are interacting with other objects or with the ICM, by looking for tidal tails or signs of ram pressure stripping, which have already been found to be present in A901/2 galaxies (Bösch *et al.*, 2013a). With these analyses we will be able to assess for individual galaxies which processes are affecting their star formation.

Appendices

Appendix A

Individual analysis of ‘k+a’ galaxies

In this section we include the analysis of each of the galaxies in the sample, with a qualitative description and the figures with individual analysis of each galaxy. In the figures we show the distribution of light in the individual IFUs, the integrated spectra of the galaxies, the distribution of the three different indicators $\mathrm{H}\delta_{\mathrm{F}}$, A/(AFGKM) and f_{young} throughout the galaxies, as well as the maps of velocity and σ for the whole galaxy and for the old and young populations, as obtained with the simultaneous fitting procedure.

A.1 CN4

This elliptical galaxy has low values of $\mathrm{H}\delta_{\mathrm{F}}$ and f_{young}, therefore being possibly misclassified as ‘k+a’ galaxy by CS87. However, there seems to be a relatively important population of B and A stars in the stellar template histograms. No pattern of rotation was found in the kinematic analysis. It is isolated.

A.2 CN22

This galaxy, which is classified as peculiar, seems to be an ongoing merger from inspection of the HST/WFPC2 images. Its distributions of A/(AFGKM) and f_{young} are consistent with the young population been concentrated in the centre of the galaxy,

although the H$\delta_{\rm F}$ maps show a more extended distribution. The value of H$\delta_{\rm F}$ = 6.4 ± 0.4 Å implies the occurrence of a starburst to produce the k+a feature and not a simple truncation of the star formation in the galaxy. The starburst may have taken place in the centre of the galaxy although the distribution of H$\delta_{\rm F}$ implies a more extended young population. Rotation was found in this galaxy together with higher values of σ in the centre. The two populations found in the kinematic decomposition are rotating in the same direction and both show higher values of σ in the centre.

The merger appears to be responsible for producing a centrally-concentrated young stellar population before halting star-formation, resulting in the 'k+a' spectrum observed.

A.3 CN24

This galaxy has low global values for the three young population indicators. In particular H$\delta_{\rm F}$ = 1.0 ± 0.4 Å and therefore it appears to have been misclassified as 'k+a' by CS87. The velocity maps do not show a clear pattern of rotation. The galaxy is isolated. CN24 is consistent with being a passive spiral galaxy.

A.4 CN74

With low values of all the young population indicators, this galaxy also appears to have an unreliable Hδ measurement by CS87. We measure a global value of H$\delta_{\rm F}$ = 1.0 ± 0.3 Å. CS87 detect emission in [OII], although there were no emission features found in our spectra of the galaxy. It presents clear rotation. This galaxy does not show signs of recent interaction and is isolated.

A.5 CN89

This elliptical galaxy has very low values of A/(AFGKM) and $f_{\rm young}$ although its global H$\delta_{\rm F}$ = 2.1 ± 0.9 Å, showing a uniform distribution of the young population.

No kinematic analysis could be performed for this galaxy.

A.6 CN119

The global values of the young population indicators in this galaxy are low, with $\mathrm{H}\delta_{\mathrm{F}} = 1.0 \pm 0.5$ Å. However, the value of $f_{\mathrm{young}} = 0.4$ does suggest the presence of a young population in the galaxy that is not dominant enough to present clear spectral features.

The weights of the different SSP templates suggest that there are two dominant populations, one with ages between 0.5 and 1.5 Gyr and the other one older than 7 Gyr, which are also found in the kinematic decomposition. Both populations have similar velocity distributions although the old population show generally higher values of sigma. Although this galaxy would be consistent with a rotating system, the analysis of the individual IFU elements did not provide enough information for its confirmation. The galaxy is not interacting.

A.7 CN143

Very high values of all the young population indicators, imply the occurrence of a recent (< 1.5 Gyr) starburst in the galaxy. The distribution maps show the young population extended throughout the whole galaxy. Rotation is detected in this galaxy although no kinematic decomposition could be performed. The galaxy is isolated.

These findings are consistent with this system being a spiral galaxy where the gas has been depleted and used up in a starburst. Because there are no signs of interaction, this depletion may have been due to the interaction with the intracluster medium.

A.8 CN146

This galaxy has detected emission in [OII] by CS87, and emission lines can be seen in its Balmer absorption features in our spectrum. The values of the indicators are consistent with the presence of a young population in the galaxy. This population appears

spatially extended in the galaxy although the $f_{\rm young}$ maps show higher concentration in the centre. No clear pattern of rotation or trend of sigma is found in the maps of the kinematics. Alhough there are few individual IFU elements with good S/N, the kinematic decomposition shows higher values of sigma in the outskirts for the young population whereas the old population has higher velocity dispersions in the centre. This galaxy is not interacting.

The characteristics of this galaxy imply star formation that is gradually declining but has not been entirely truncated yet, consistent with the depletion of gas due to interaction with the ICM.

A.9 CN155

This galaxy has [OII] emission detected by CS87, and emission lines can be seen in its Balmer absorption features in our spectrum. The distribution of the young population indicators is consistent with the young population being more dominant in the central regions. The strong value of H$\delta_{\rm F}$ implies the occurrence of a starburst. No clear pattern of rotation was found and no kinematic decomposition could be performed in this galaxy. In the HST/WFPC2 image this galaxy is interacting with a smaller object. The post-starburst feature may be associated with an interaction with this companion. The star formation in the galaxy has not been truncated yet, therefore this galaxy could be similar to the progenitors of the k+a galaxies in our sample.

A.10 CN187

The global values of the young population indicators in this galaxy are low, with H$\delta_{\rm F} = 1.0 \pm 0.5$ Å. The kinematics of this galaxy could not be analysed due to the low number of IFU elements available and their distribution. This galaxy is isolated. This galaxy appears to have been misclassified as a 'k+a' galaxy by CS87.

A.11 CN191

This galaxy presents high values of all the young population indicators, with H$\delta_{\rm F}$ = 5.1 ± 0.3 Å, showing flat distributions. Although the H$\delta_{\rm F}$ value is not exceptionally high, it could be consistent with the occurrence of a starburst in the galaxy between 0.5 and 1.5 Gyr ago. The galaxy shows clear rotation and its kinematical decomposition shows two populations (young and old) rotating in the same direction, with the young population having higher values of sigma in the centre. This galaxy is not found to be interacting.

The presence of rotation implyes that the process responsible for the truncation of the star formation did not affect the kinematic state of the galaxy. The distribution of the young population implies a that the final episode of star formation occured throughout the galaxy.

A.12 CN228

The young population in this galaxy is concentrated in the central regions with high global values of the indicators. It displays rotation and the two distinct stellar populations are rotating in the same direction. It has a very close satellite.

The presence of a close satellite and the distribution of the young population suggest the interaction with the other object as the responsible mechanism for the truncation of the star formation, which has not affected the kinematics of the galaxy.

A.13 CN229

This galaxy, which was observed instead of CN254 by P05, is a disk system which has very low values of H$\delta_{\rm F} = 0.1 \pm 1.1$ Å, but whose histograms show the presence of a very young 'O' stars, and a population with age < 0.5 Gyr. Although no [OII] has been measured in this galaxy, this dominant young population would be consistent with ongoing star formation. This galaxy therefore does not fulfill the 'k+a' criteria, nor does it show evidence of rapidly declining star-fomation.

A.14 CN232

Very low global values of all the indicators, with $H\delta_F = 1.1 \pm 0.6$ Å imply there is no dominant young population. This galaxy presents rotation but it could not be kinematically decomposed. In the images it is found with a close satellite. This galaxy seems to have been misclassified by CS87 and is not an actual k+a.

A.15 CN243

This galaxy has two broken fibres in the centre, and therefore no spatial analysis could be performed. Its has a global value of $H\delta_F = 3.1 \pm 0.3$ Å and it CS87 detected emission in OII. Due to the broken fibres we could not obtain maps of the kinematics. This galaxy is in a close encounter with other object, with which it seems to be exchanging material.

A.16 CN247

An elliptical galaxy with very low values of all the indicators. One fibre has $H\delta_F \sim 3.0$ Å, although the global value is much lower at 1.0 ± 0.4 Å. No kinematic analysis could be performed for this galaxy. Its characteristics are consistent with an old, passive galaxy.

A.17 CN254

Although this galaxy was meant to be observed by P05 as well as us, their observation actually corresponded to galaxy CN229. $H\delta_F$ is the only young population indicator with high values and it shows similar values throughout the galaxy, with a global value of 2.1 ± 0.5 Å. This galaxy shows rotation and and two distinct populations that are rotating in the same direction. The old population shows higher values of sigma than the young in the whole galaxy. This galaxy is surrounded by smaller objects but does not show signs of interaction.

The values of $H\delta_F$, the presence of rotation in both populations and the fact that the galaxy is not interacting suggest that the truncation of the star formation was produced by the gradual removal of the gas in the disk of the galaxy due to an interaction with the ICM.

A.18 CN667

Disk galaxy with low values of A/(AFGKM) and $f_{\rm young}$ and very low $H\delta_F = 0.6 \pm 0.4$ Å. No kinematic analysis could be performed in this galaxy. This galaxy is possibly interacting with two close satellites.

A.19 CN849

A disk galaxy with relatively low values of the young population indicators, with $H\delta_F = 2.3 \pm 0.4$ Å. The distribution of the indicators suggest a concentration of the young population in the outskirts, but $H\delta_F$ is also prominent in the central pixel. The histograms of the SSP models show two populations, one young and one old, which are also found in the kinematic decomposition to be rotating in the same direction, although the young component appears to rotate faster. This galaxy is clearly exchanging material with another object, and therefore this interaction could be responsible for the cessation of star formation.

A.20 CN858

This elliptical galaxy has a zero value of A/(AFGKM) and $f_{\rm young}$ and negative $H\delta_F$, implying that it is a passive galaxy. It is not interacting.

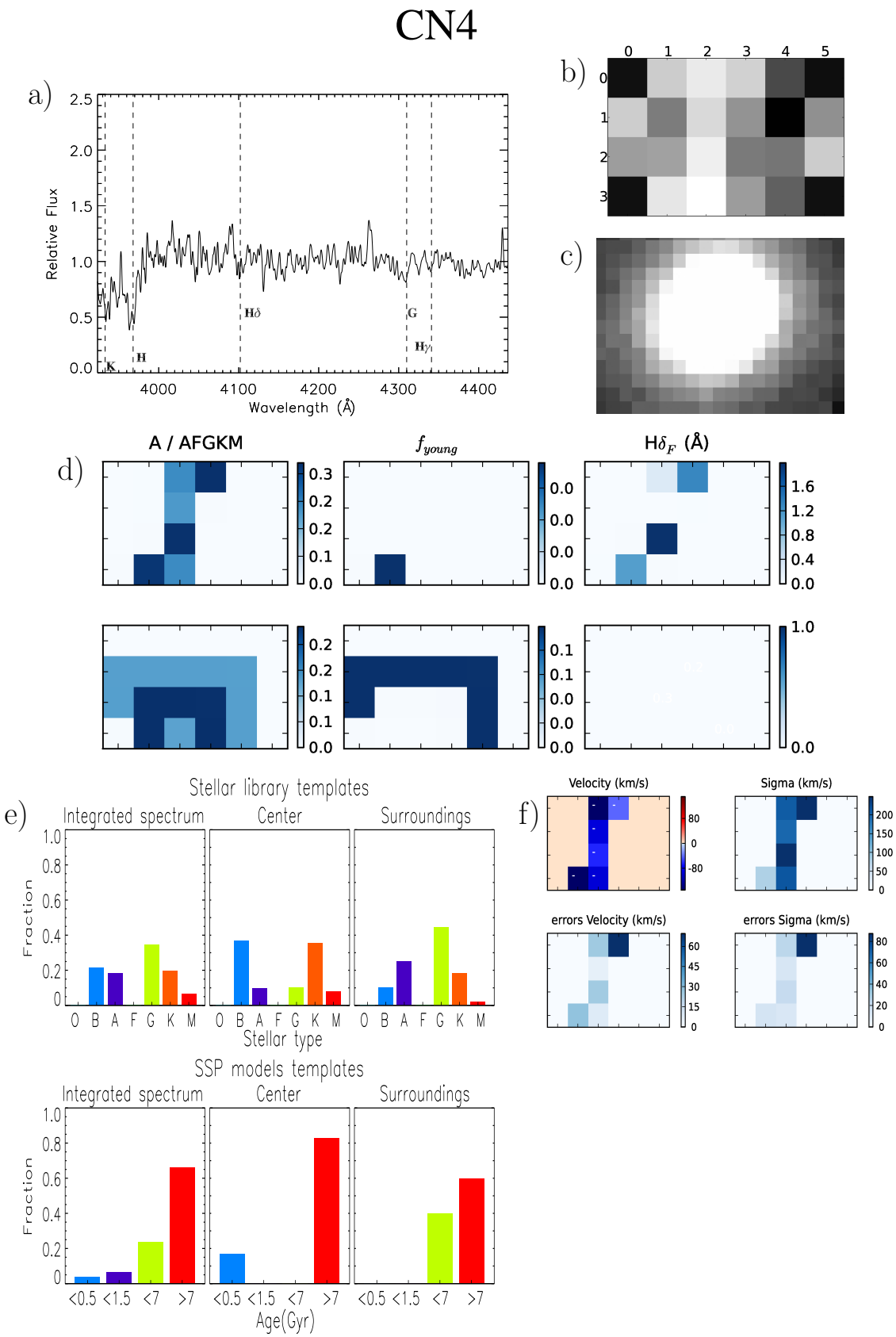

Figure A.1: Individual analysis of each galaxy. (a) Integrated spectra, (b) distribution of light in the IFU, (c) HST/WFPC2 image of the galaxy, (d) maps of the individual fibre values of A/(AFGKM), $f_{\rm young}$ and $H\delta_F$ index (top) and the corresponding values for the integrated regions 'centre', 'surroundings' and 'outskirts' when available (bottom). Errors of the $H\delta_F$ index are printed over the regions. Each spatial pixel has a size of 0.52 x 0.52 which corresponds to $\sim$ 2.3 x 2.3 kpc^2 at the redshift of AC114. (e) Histograms of stellar type and stellar population age obtained with pPXF for the integrated spectra, 'centre', 'surroundings' and 'outskirts' when available. (f) Maps of velocity and σ for the galaxy. (g) Maps of velocity and sigma for the old and young populations (not available for CN4). Blank spaces are left when the respective analysis could not be performed in a galaxy.

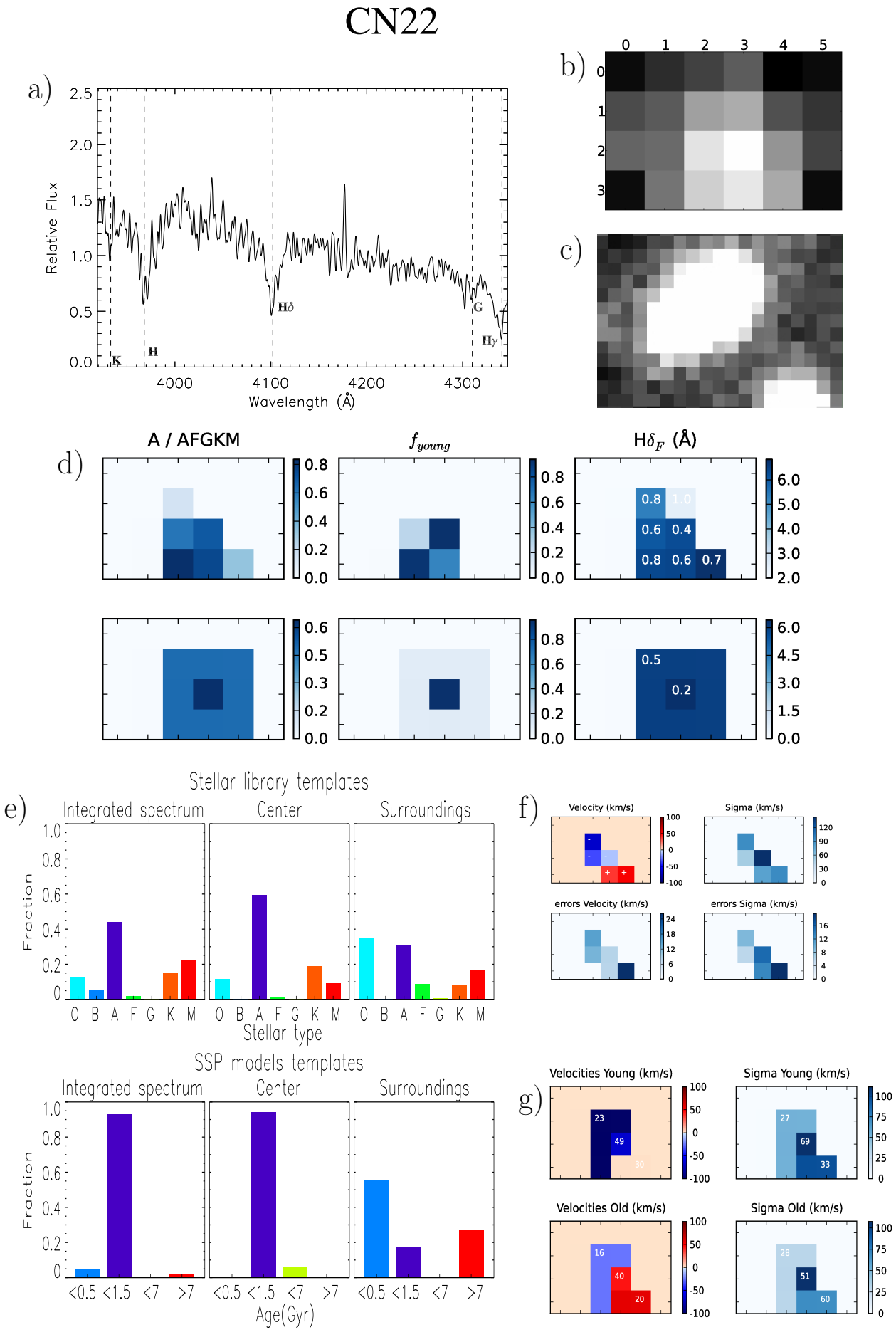
CN22
a)
Relative Flux
Wavelength (Å)
K
H
Hδ
G
Hγ
b)
c)
d)
A / AFGKM
f_{young}
$H\delta_F$ (Å)
e)
Stellar library templates
Integrated spectrum
Center
Surroundings
Fraction
O B A F G K M
Stellar type
SSP models templates
<0.5 <1.5 <7 >7
Age(Gyr)
f)
Velocity (km/s)
Sigma (km/s)
errors Velocity (km/s)
errors Sigma (km/s)
g)
Velocities Young (km/s)
Sigma Young (km/s)
Velocities Old (km/s)
Sigma Old (km/s)

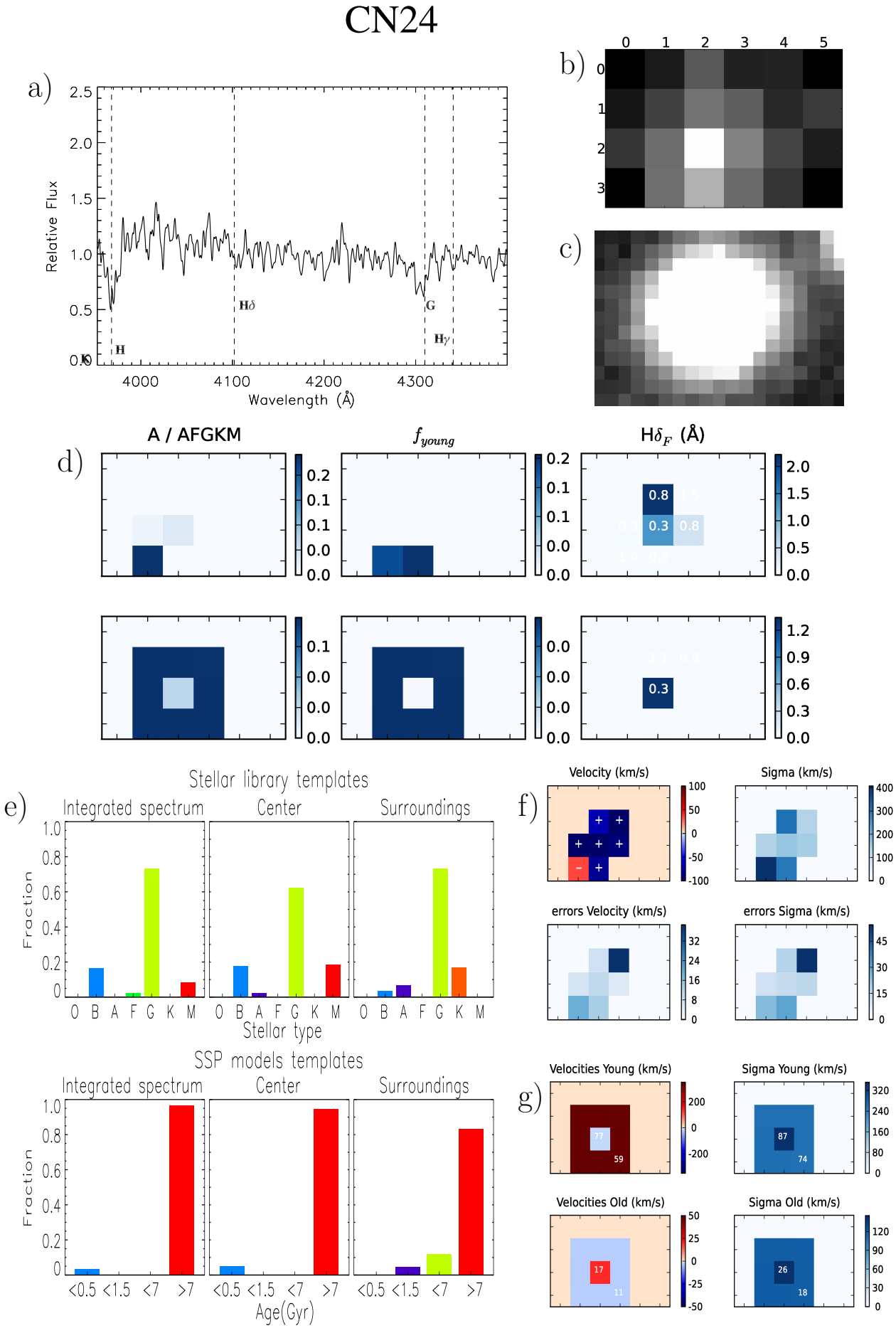
CN24
a)
Relative Flux
Wavelength (Å)
H
Hδ
G
Hγ
b)
c)
d)
A / AFGKM
f_{young}
$H\delta_F$ (Å)
e)
Stellar library templates
Integrated spectrum
Center
Surroundings
Fraction
O B A F G K M
Stellar type
SSP models templates
<0.5 <1.5 <7 >7
Age(Gyr)
f)
Velocity (km/s)
Sigma (km/s)
errors Velocity (km/s)
errors Sigma (km/s)
g)
Velocities Young (km/s)
Sigma Young (km/s)
Velocities Old (km/s)
Sigma Old (km/s)

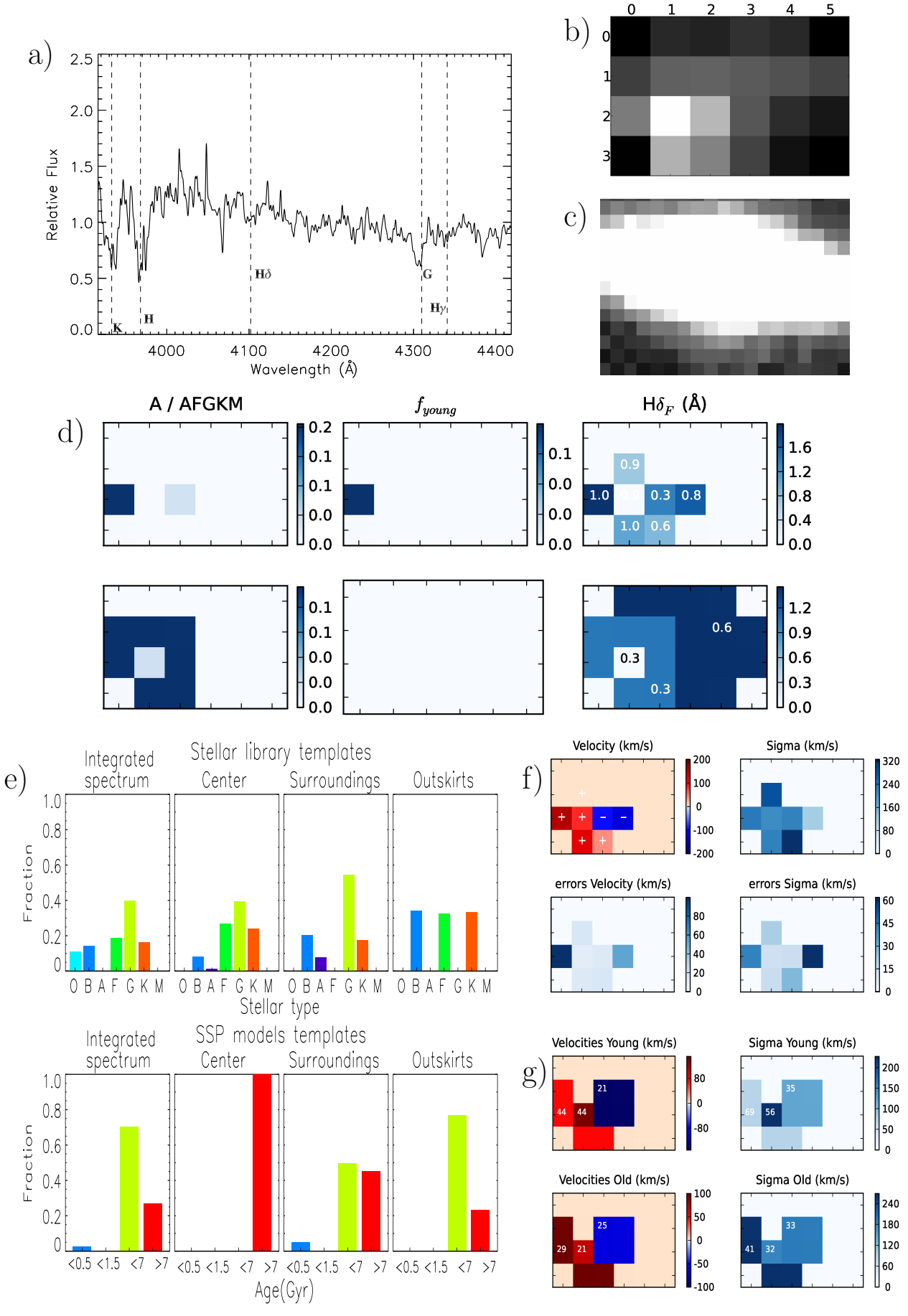
CN74
a)
Relative Flux
Wavelength (Å)
K
H
Hδ
G
Hγ
b)
c)
d)
A / AFGKM
f_{young}
$H\delta_F$ (Å)
e)
Integrated spectrum
Stellar library templates
Center
Surroundings
Outskirts
Fraction
O B A F G K M
Stellar type
SSP models templates
<0.5 <1.5 <7 >7
Age(Gyr)
f)
Velocity (km/s)
Sigma (km/s)
errors Velocity (km/s)
errors Sigma (km/s)
g)
Velocities Young (km/s)
Sigma Young (km/s)
Velocities Old (km/s)
Sigma Old (km/s)

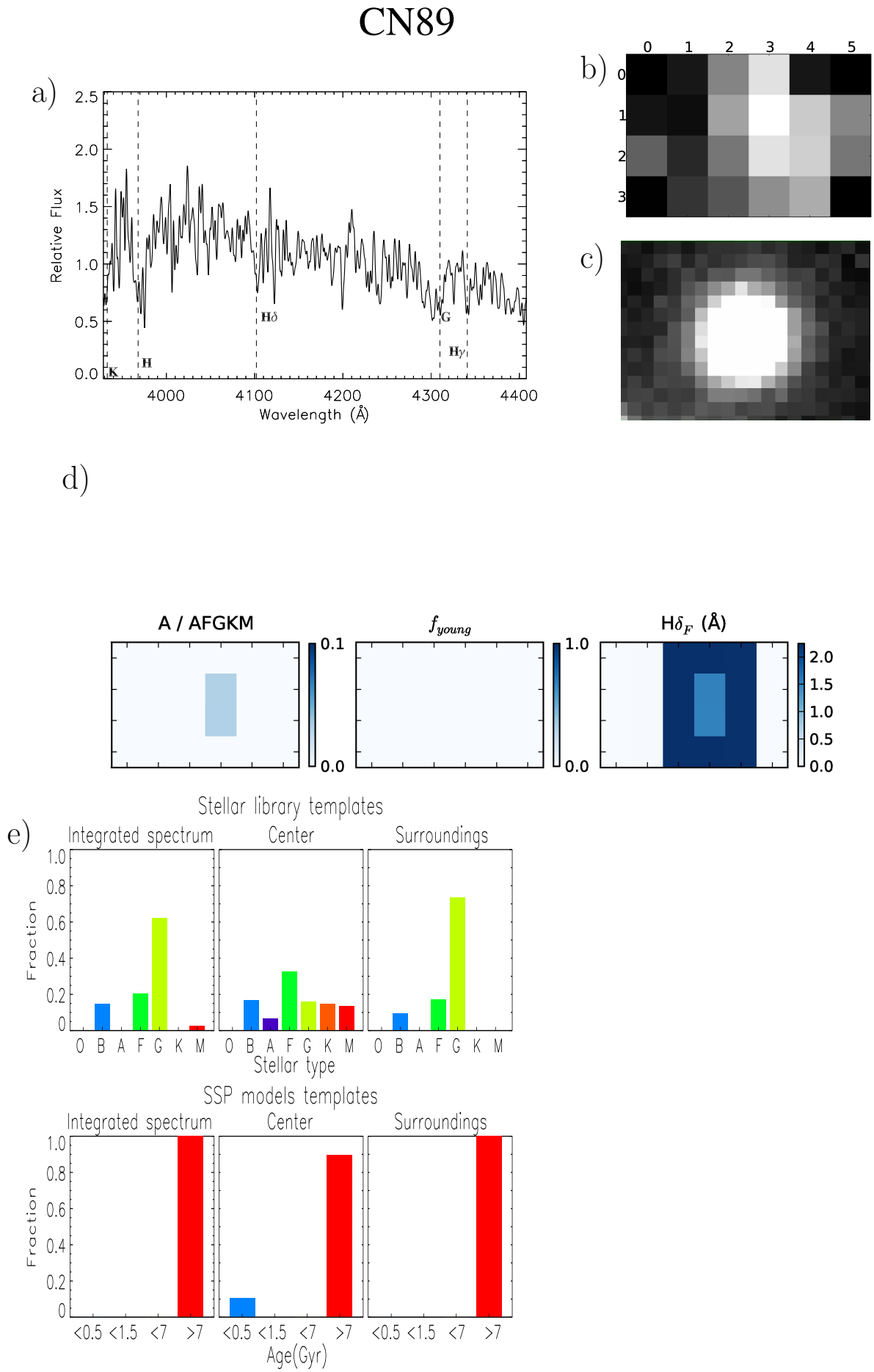
CN89
a)
Relative Flux
Wavelength (Å)
K
H
Hδ
G
Hγ
b)
c)
d)
A / AFGKM
f_{young}
Hδ$_F$ (Å)
e)
Stellar library templates
Integrated spectrum
Center
Surroundings
Fraction
O B A F G K M
Stellar type
SSP models templates
<0.5 <1.5 <7 >7
Age(Gyr)

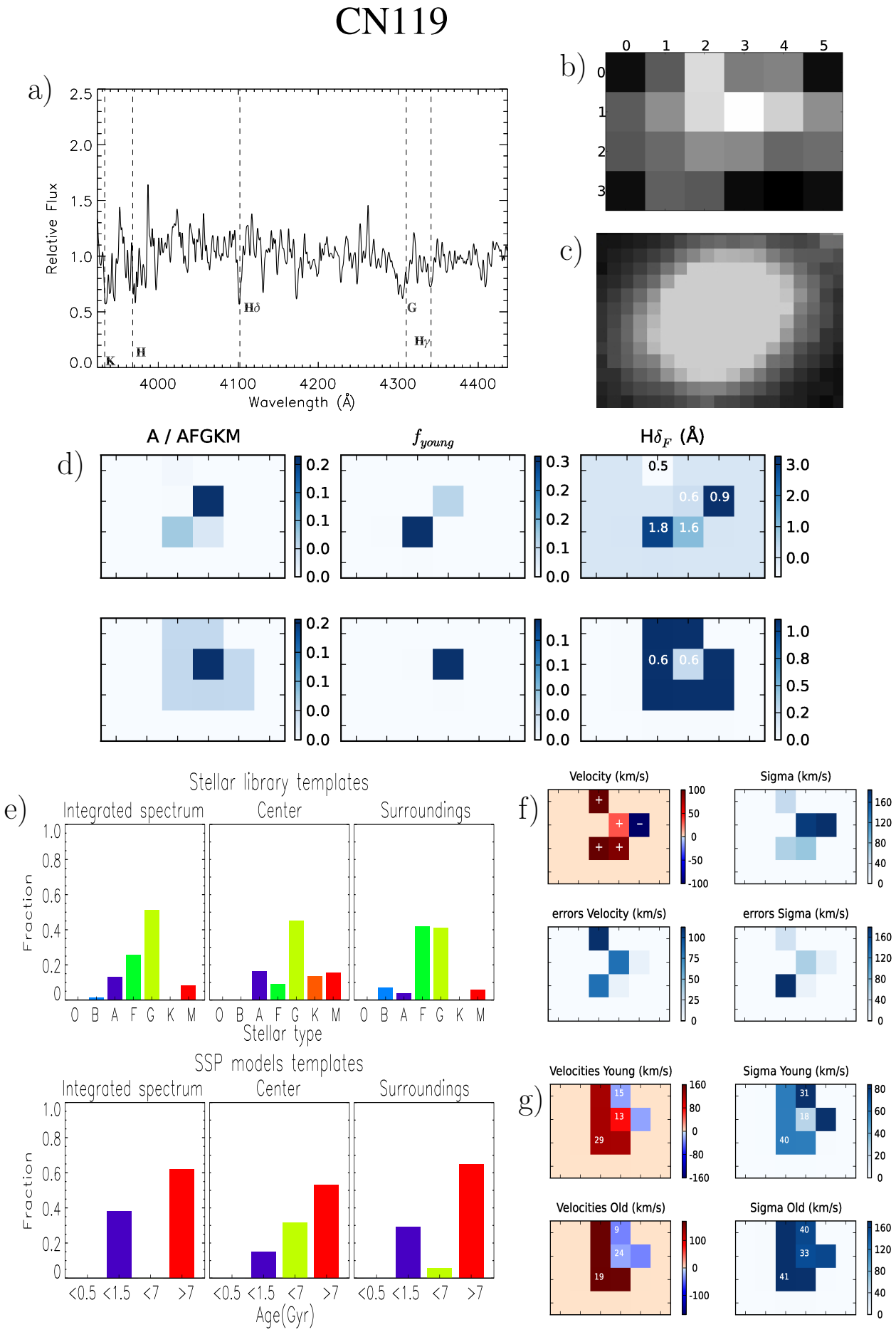
CN119
a)
Relative Flux
Wavelength (Å)
K
H
Hδ
G
Hγ
b)
c)
d)
A / AFGKM
f_{young}
$H\delta_F$ (Å)
e)
Stellar library templates
Integrated spectrum
Center
Surroundings
Fraction
O B A F G K M
Stellar type
SSP models templates
<0.5 <1.5 <7 >7
Age(Gyr)
f)
Velocity (km/s)
Sigma (km/s)
errors Velocity (km/s)
errors Sigma (km/s)
g)
Velocities Young (km/s)
Sigma Young (km/s)
Velocities Old (km/s)
Sigma Old (km/s)

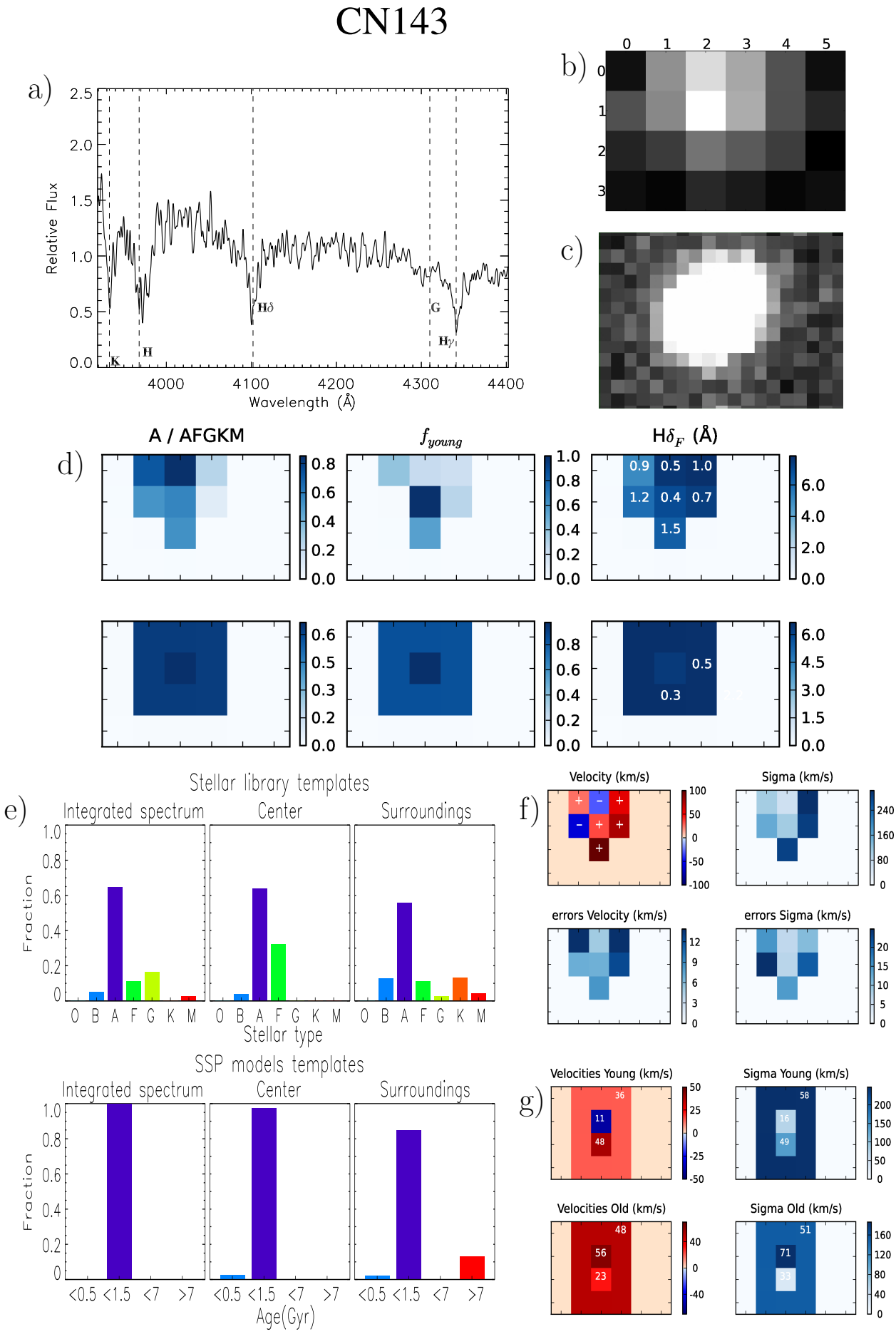
CN143
a)
Relative Flux
Wavelength (Å)
K
H
Hδ
G
Hγ
b)
c)
d)
A / AFGKM
f_{young}
$H\delta_F$ (Å)
e)
Stellar library templates
Integrated spectrum
Center
Surroundings
Fraction
O B A F G K M
Stellar type
SSP models templates
<0.5 <1.5 <7 >7
Age(Gyr)
f)
Velocity (km/s)
Sigma (km/s)
errors Velocity (km/s)
errors Sigma (km/s)
g)
Velocities Young (km/s)
Sigma Young (km/s)
Velocities Old (km/s)
Sigma Old (km/s)

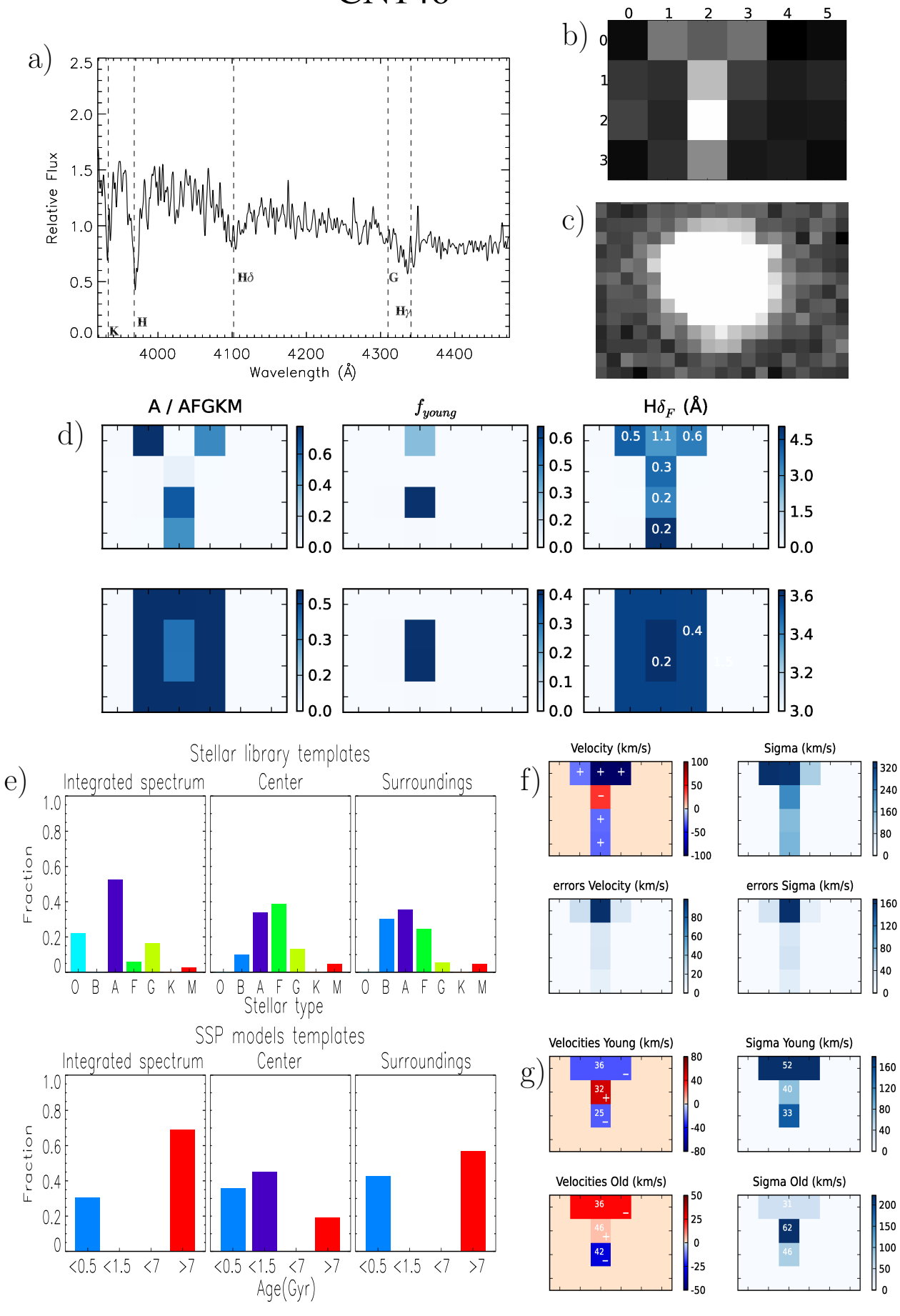
CN146
a)
Relative Flux
Wavelength (Å)
K
H
Hδ
G
Hγ
b)
c)
d)
A / AFGKM
f_{young}
$H\delta_F$ (Å)
e)
Stellar library templates
Integrated spectrum
Center
Surroundings
Fraction
O B A F G K M
Stellar type
SSP models templates
<0.5 <1.5 <7 >7
Age(Gyr)
f)
Velocity (km/s)
Sigma (km/s)
errors Velocity (km/s)
errors Sigma (km/s)
g)
Velocities Young (km/s)
Sigma Young (km/s)
Velocities Old (km/s)
Sigma Old (km/s)

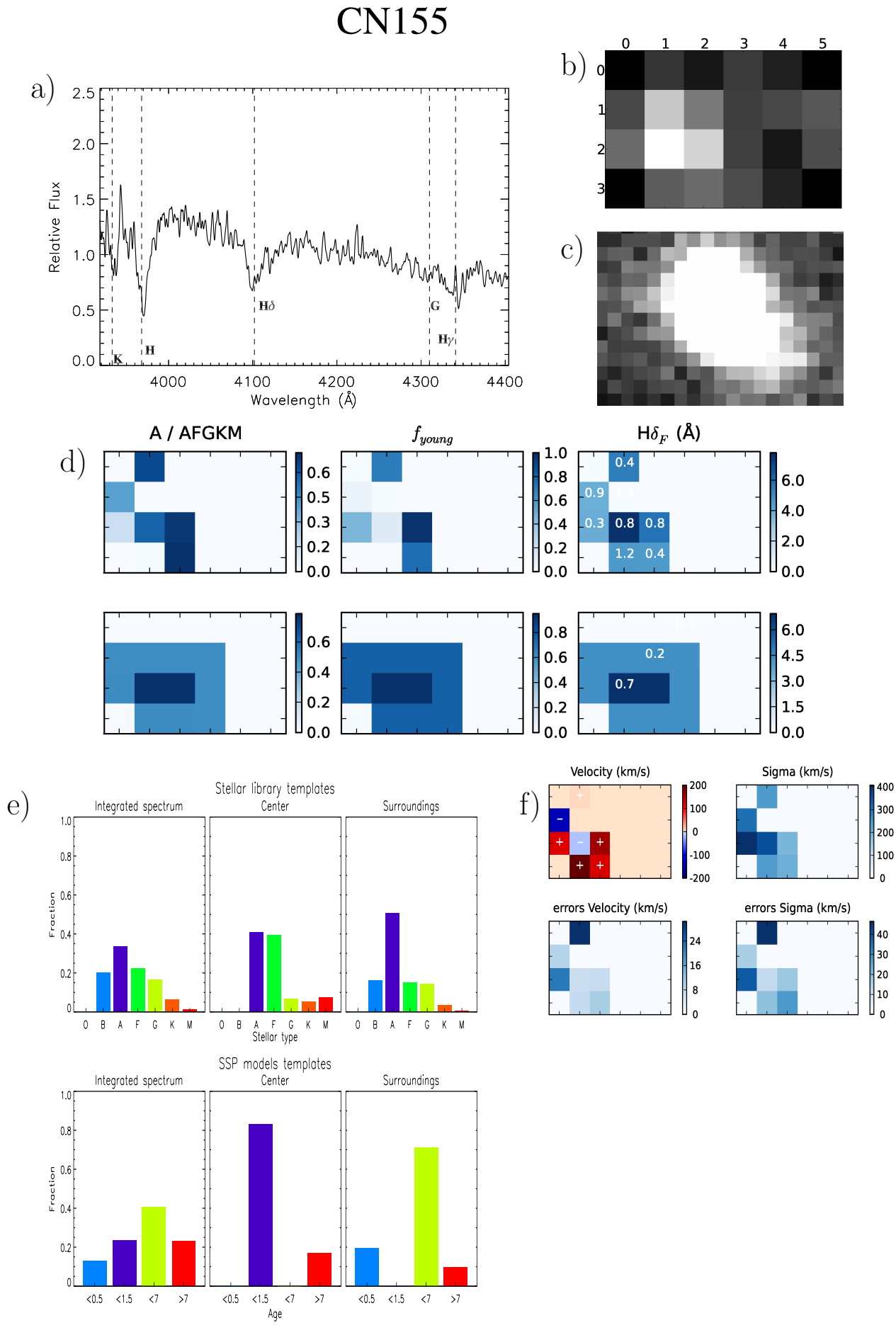
CN155
a)
Relative Flux
Wavelength (Å)
K
H
Hδ
G
Hγ
b)
c)
d)
A / AFGKM
f_{young}
$H\delta_F$ (Å)
e)
Stellar library templates
Integrated spectrum
Center
Surroundings
Fraction
Stellar type
SSP models templates
Age
f)
Velocity (km/s)
Sigma (km/s)
errors Velocity (km/s)
errors Sigma (km/s)

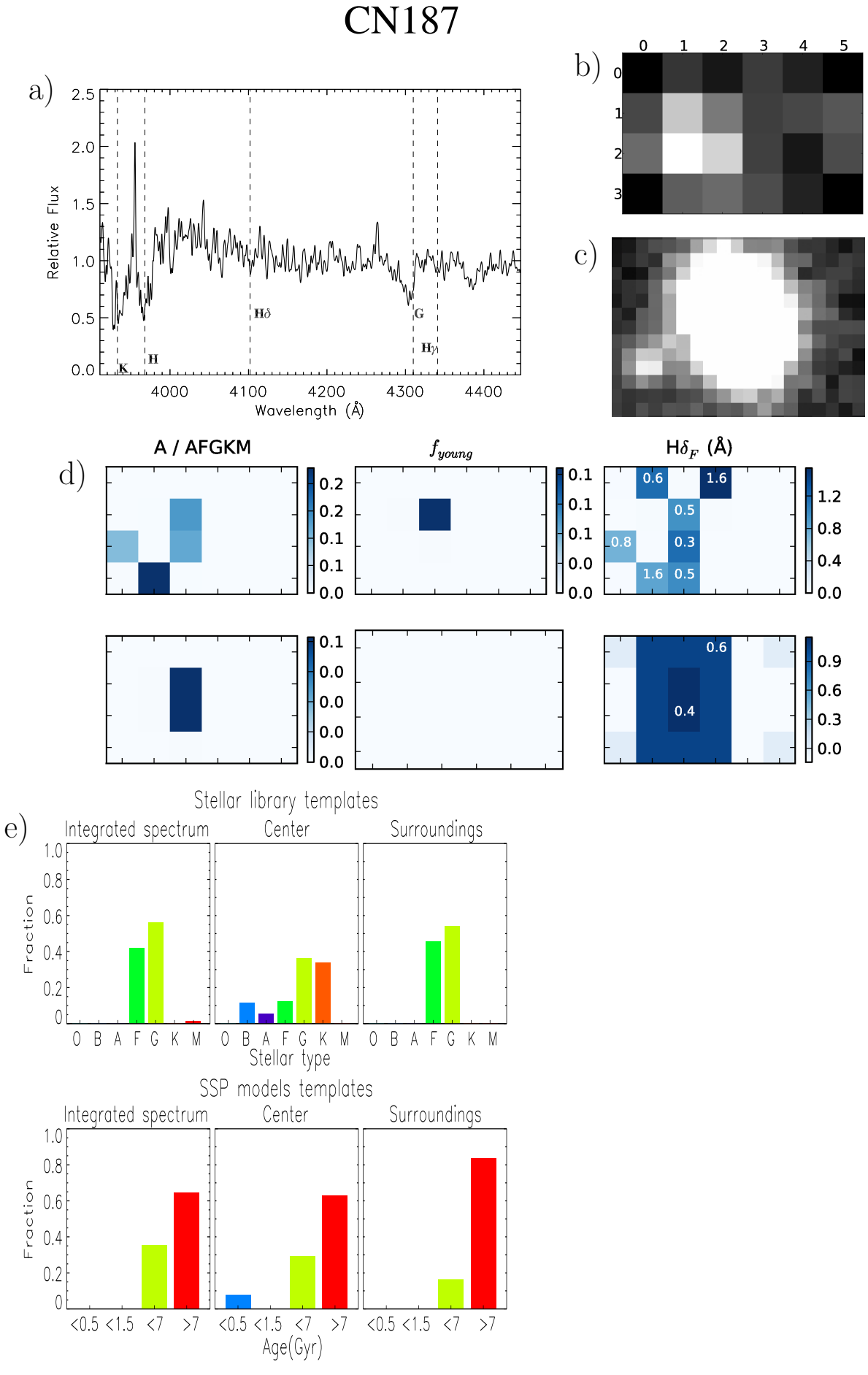
CN187
a)
Relative Flux
Wavelength (Å)
K
H
Hδ
G
Hγ
b)
c)
d)
A / AFGKM
f_{young}
$H\delta_F$ (Å)
e)
Stellar library templates
Integrated spectrum
Center
Surroundings
Fraction
O B A F G K M
Stellar type
SSP models templates
<0.5 <1.5 <7 >7
Age(Gyr)

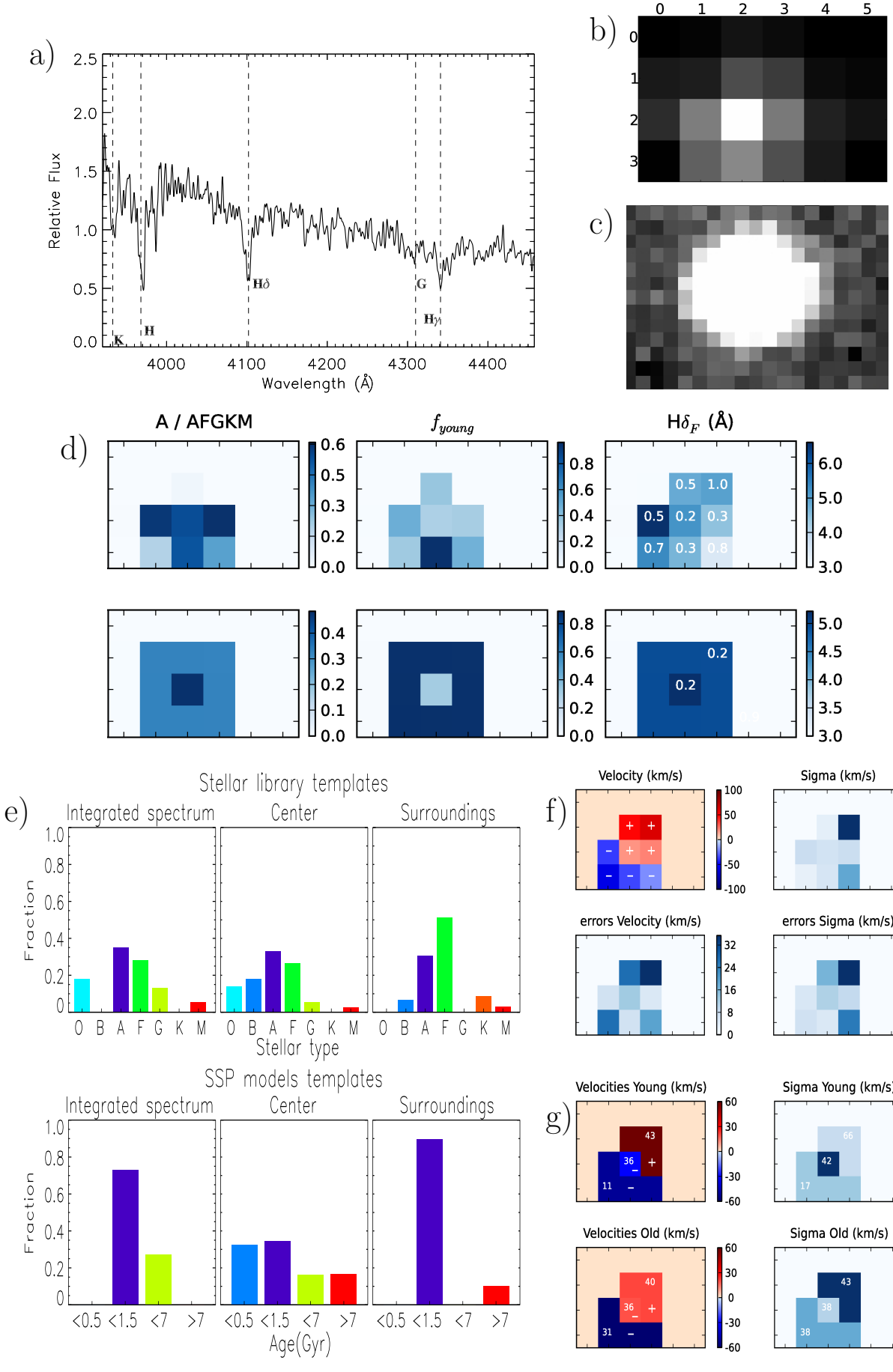
CN191
a)
Relative Flux
Wavelength (Å)
K
H
Hδ
G
Hγ
b)
c)
d)
A / AFGKM
f_{young}
$H\delta_F$ (Å)
e)
Stellar library templates
Integrated spectrum
Center
Surroundings
Fraction
O B A F G K M
Stellar type
SSP models templates
<0.5 <1.5 <7 >7
Age(Gyr)
f)
Velocity (km/s)
Sigma (km/s)
errors Velocity (km/s)
errors Sigma (km/s)
g)
Velocities Young (km/s)
Sigma Young (km/s)
Velocities Old (km/s)
Sigma Old (km/s)

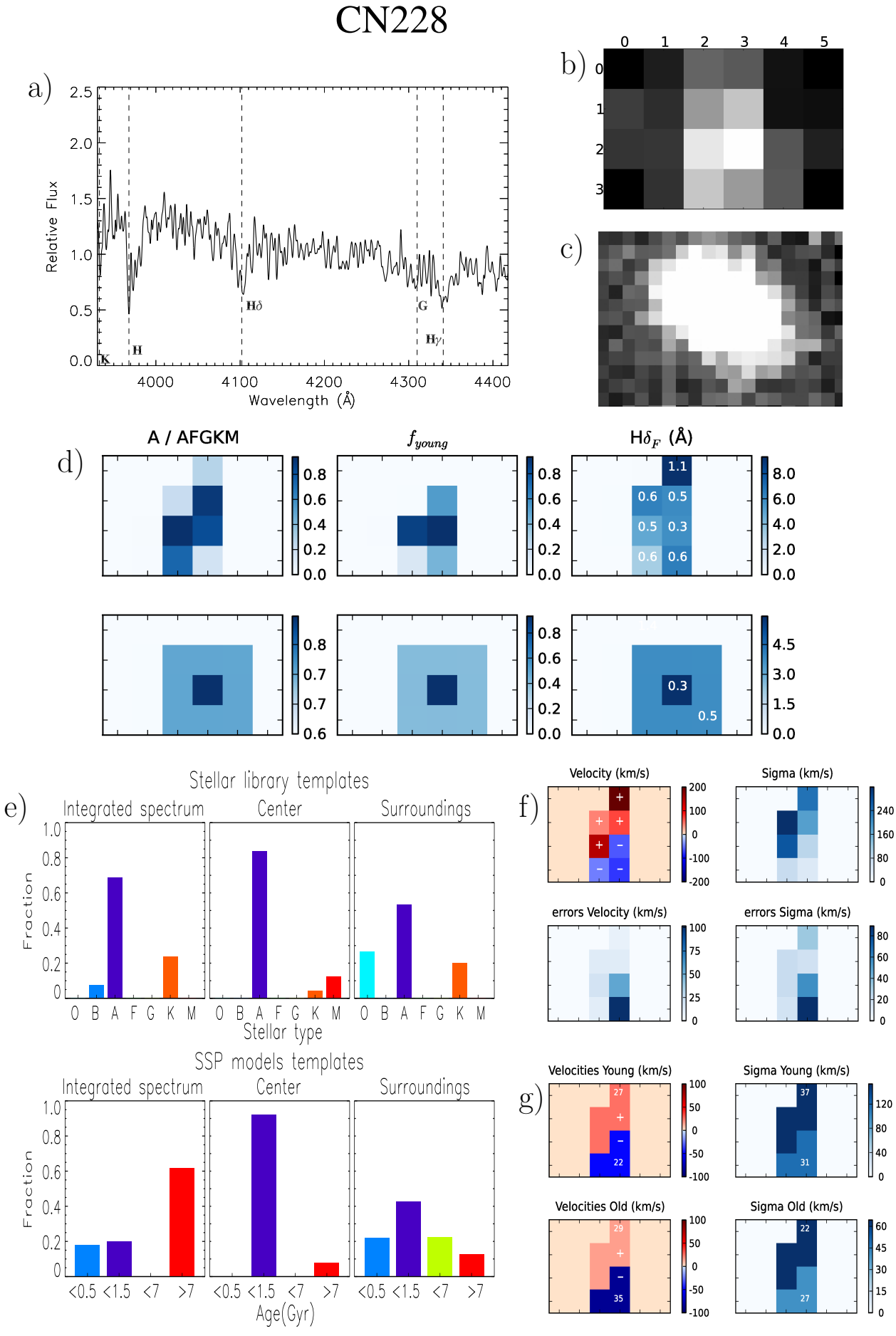
CN228
a)
Relative Flux
Wavelength (Å)
K
H
Hδ
G
Hγ
b)
c)
d)
A / AFGKM
f_{young}
$H\delta_F$ (Å)
e)
Stellar library templates
Integrated spectrum
Center
Surroundings
Fraction
O B A F G K M
Stellar type
SSP models templates
<0.5 <1.5 <7 >7
Age(Gyr)
f)
Velocity (km/s)
Sigma (km/s)
errors Velocity (km/s)
errors Sigma (km/s)
g)
Velocities Young (km/s)
Sigma Young (km/s)
Velocities Old (km/s)
Sigma Old (km/s)

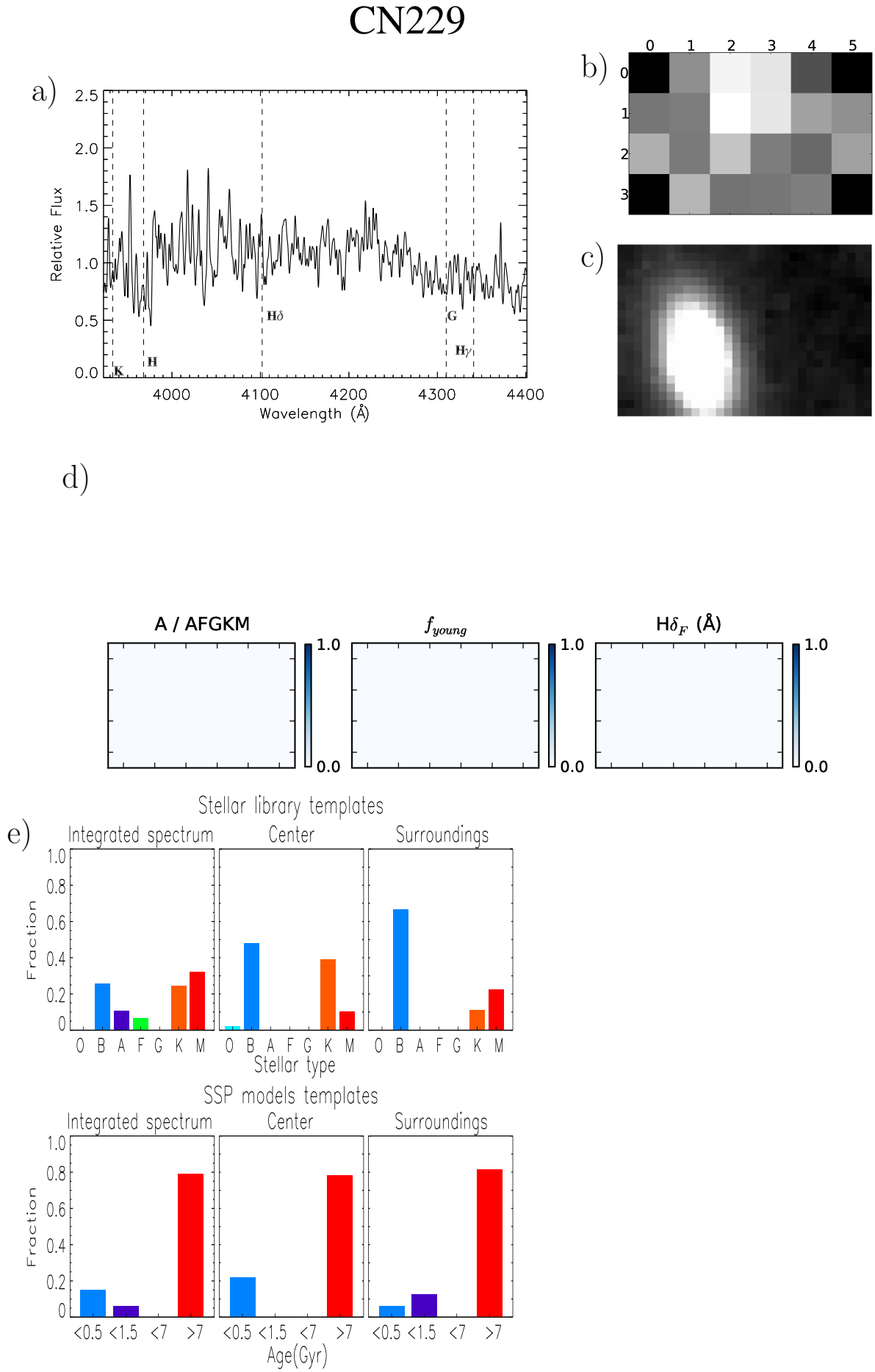
CN229
a)
Relative Flux
Wavelength (Å)
K
H
Hδ
G
Hγ
b)
c)
d)
A / AFGKM
f_{young}
$H\delta_F$ (Å)
1.0
0.0
e)
Stellar library templates
Integrated spectrum
Center
Surroundings
Fraction
O B A F G K M
Stellar type
SSP models templates
<0.5 <1.5 <7 >7
Age(Gyr)

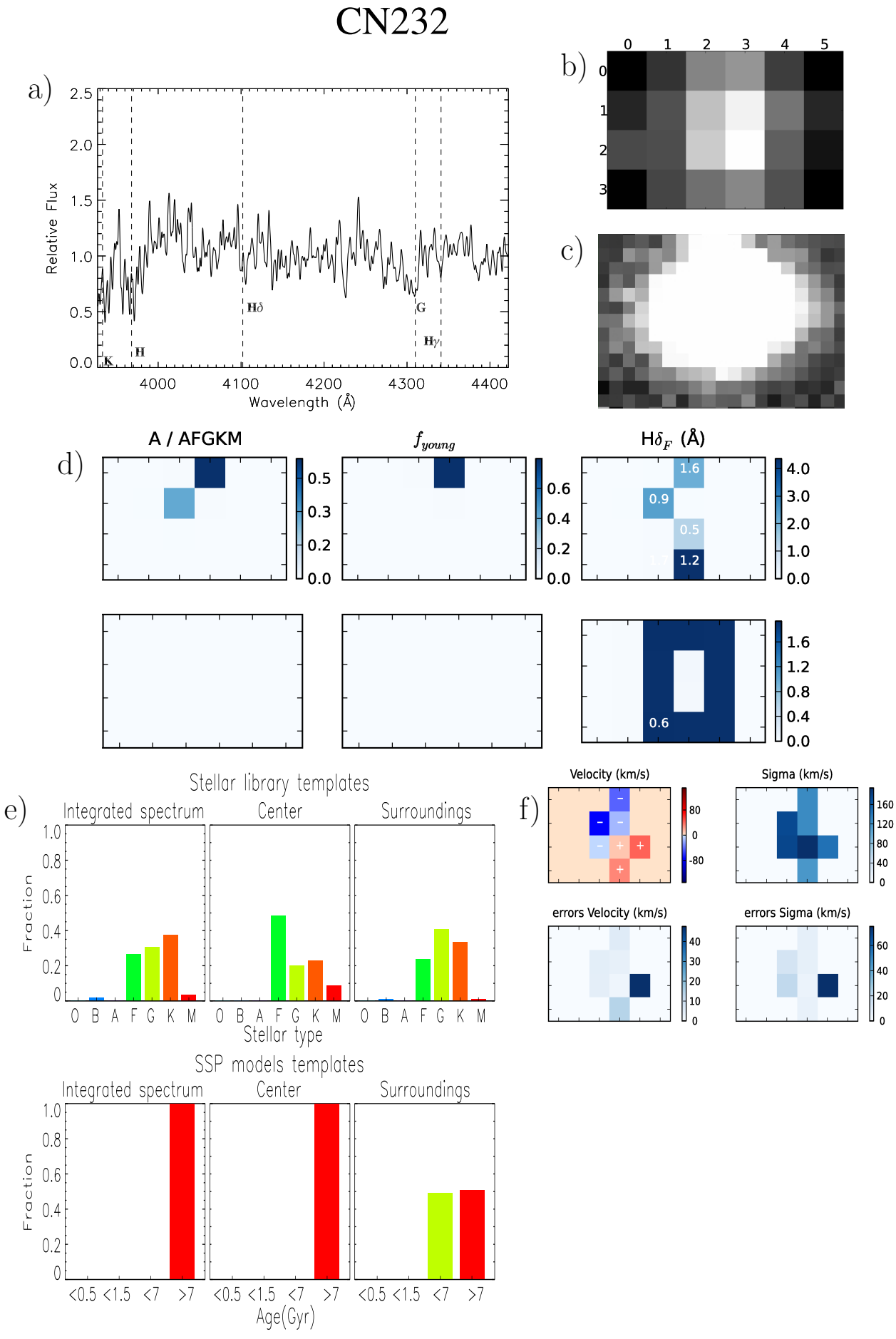
CN232
a)
Relative Flux
Wavelength (Å)
K
H
Hδ
G
Hγ
b)
c)
d)
A / AFGKM
f_{young}
$H\delta_F$ (Å)
e)
Stellar library templates
Integrated spectrum
Center
Surroundings
Fraction
O B A F G K M
Stellar type
SSP models templates
<0.5 <1.5 <7 >7
Age(Gyr)
f)
Velocity (km/s)
Sigma (km/s)
errors Velocity (km/s)
errors Sigma (km/s)

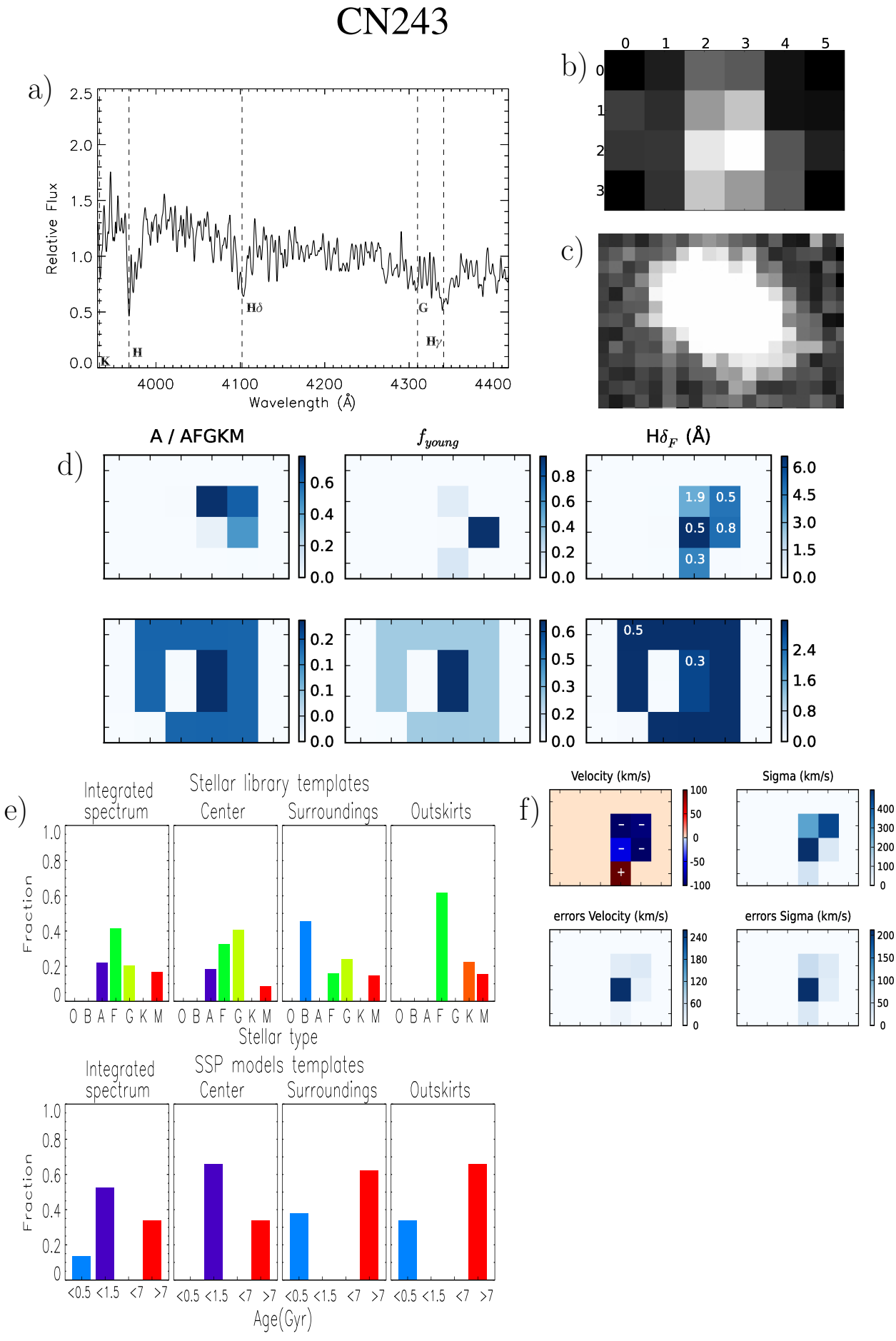
CN243
a)
Relative Flux
Wavelength (Å)
K
H
Hδ
G
Hγ
b)
c)
d)
A / AFGKM
f_{young}
$H\delta_F$ (Å)
e)
Integrated spectrum
Stellar library templates
Center
Surroundings
Outskirts
Fraction
O B A F G K M
Stellar type
SSP models templates
<0.5 <1.5 <7 >7
Age(Gyr)
f)
Velocity (km/s)
Sigma (km/s)
errors Velocity (km/s)
errors Sigma (km/s)

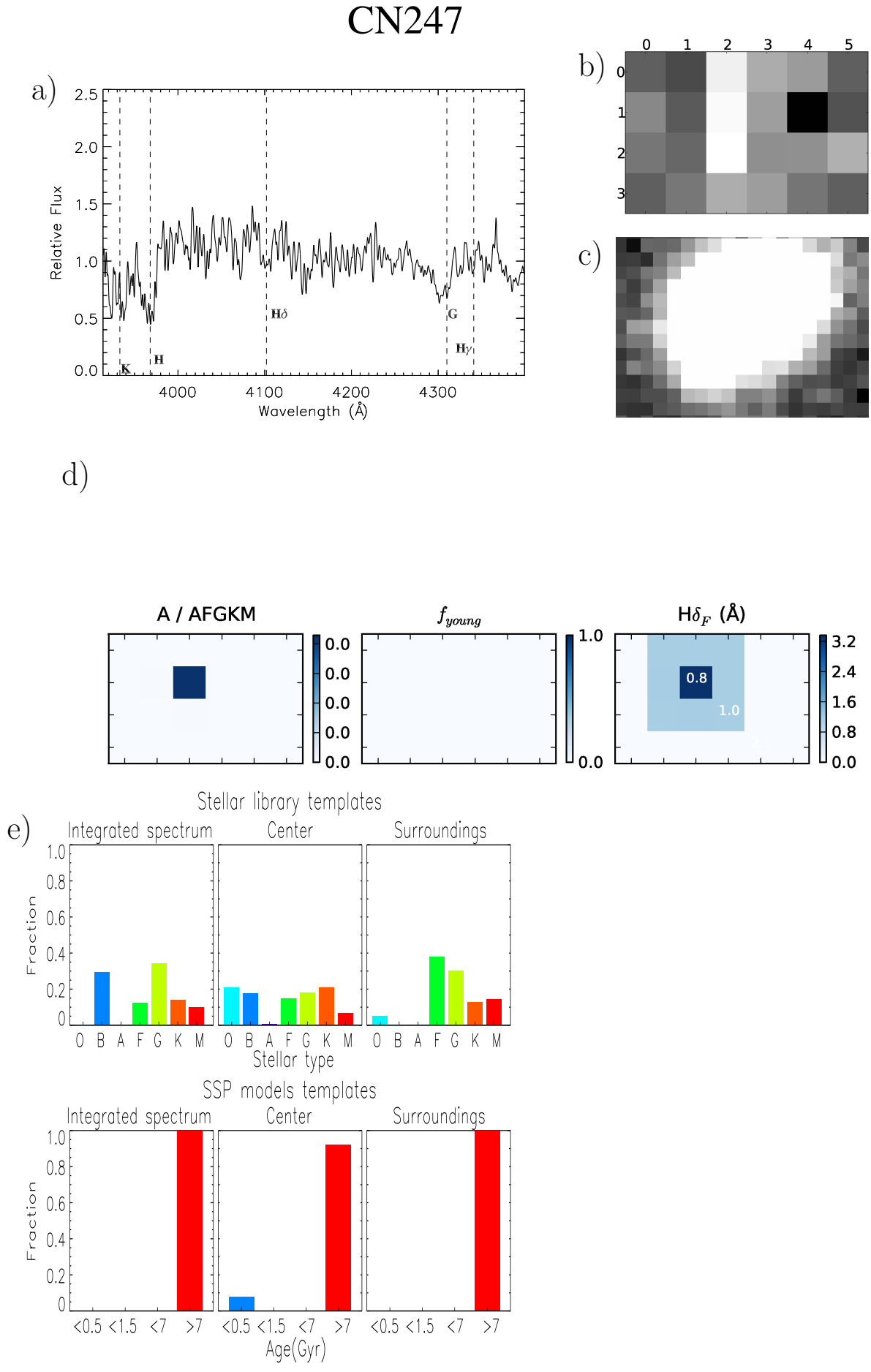
CN247
a)
Relative Flux
Wavelength (Å)
K
H
Hδ
G
Hγ
b)
c)
d)
A / AFGKM
f_{young}
$H\delta_F$ (Å)
0.8
1.0
e)
Stellar library templates
Integrated spectrum
Center
Surroundings
Fraction
O B A F G K M
Stellar type
SSP models templates
<0.5 <1.5 <7 >7
Age(Gyr)

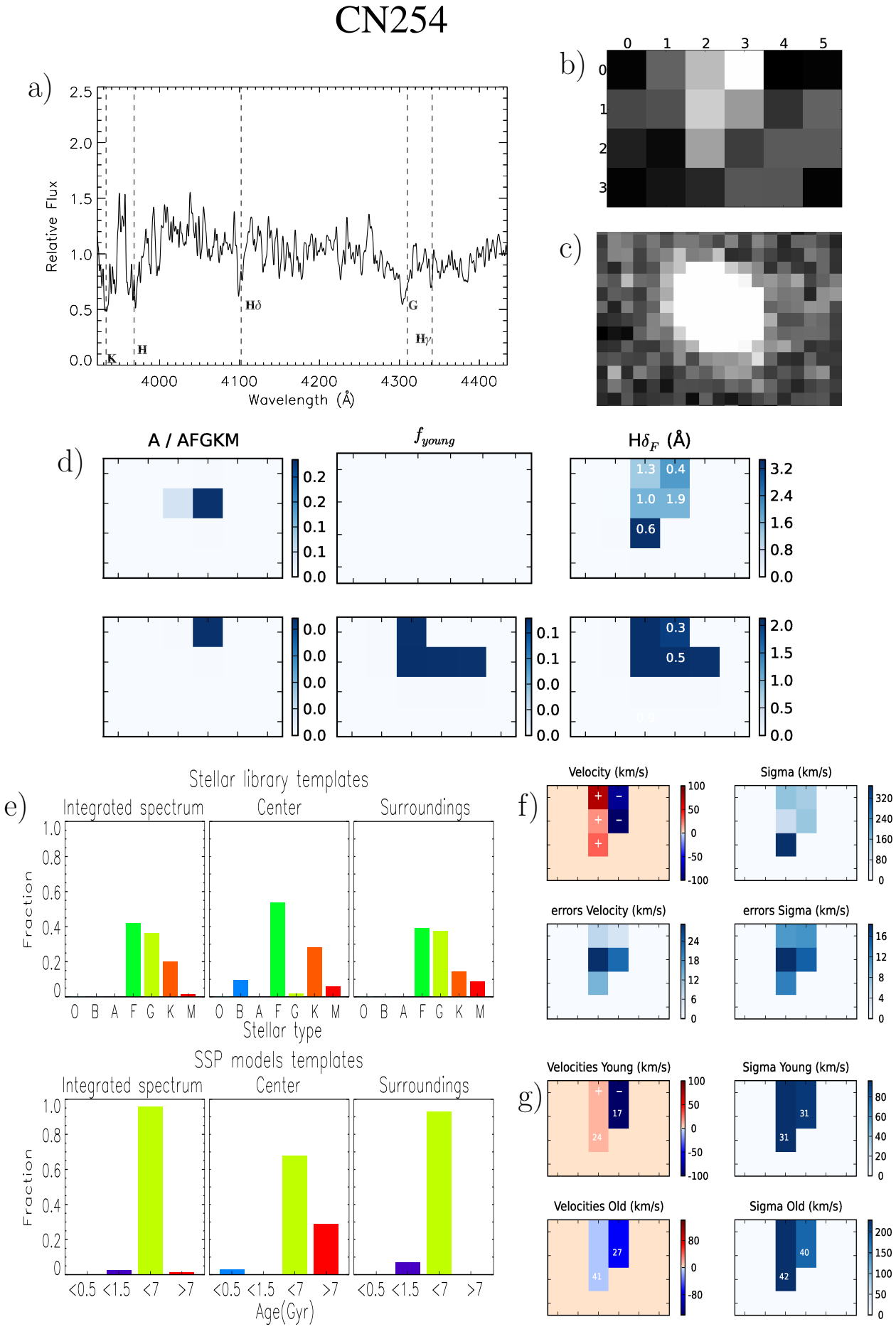
CN254
a)
Relative Flux
Wavelength (Å)
K
H
Hδ
G
Hγ
b)
c)
d)
A / AFGKM
f_{young}
$H\delta_F$ (Å)
e)
Stellar library templates
Integrated spectrum
Center
Surroundings
Fraction
O B A F G K M
Stellar type
SSP models templates
<0.5 <1.5 <7 >7
Age(Gyr)
f)
Velocity (km/s)
Sigma (km/s)
errors Velocity (km/s)
errors Sigma (km/s)
g)
Velocities Young (km/s)
Sigma Young (km/s)
Velocities Old (km/s)
Sigma Old (km/s)

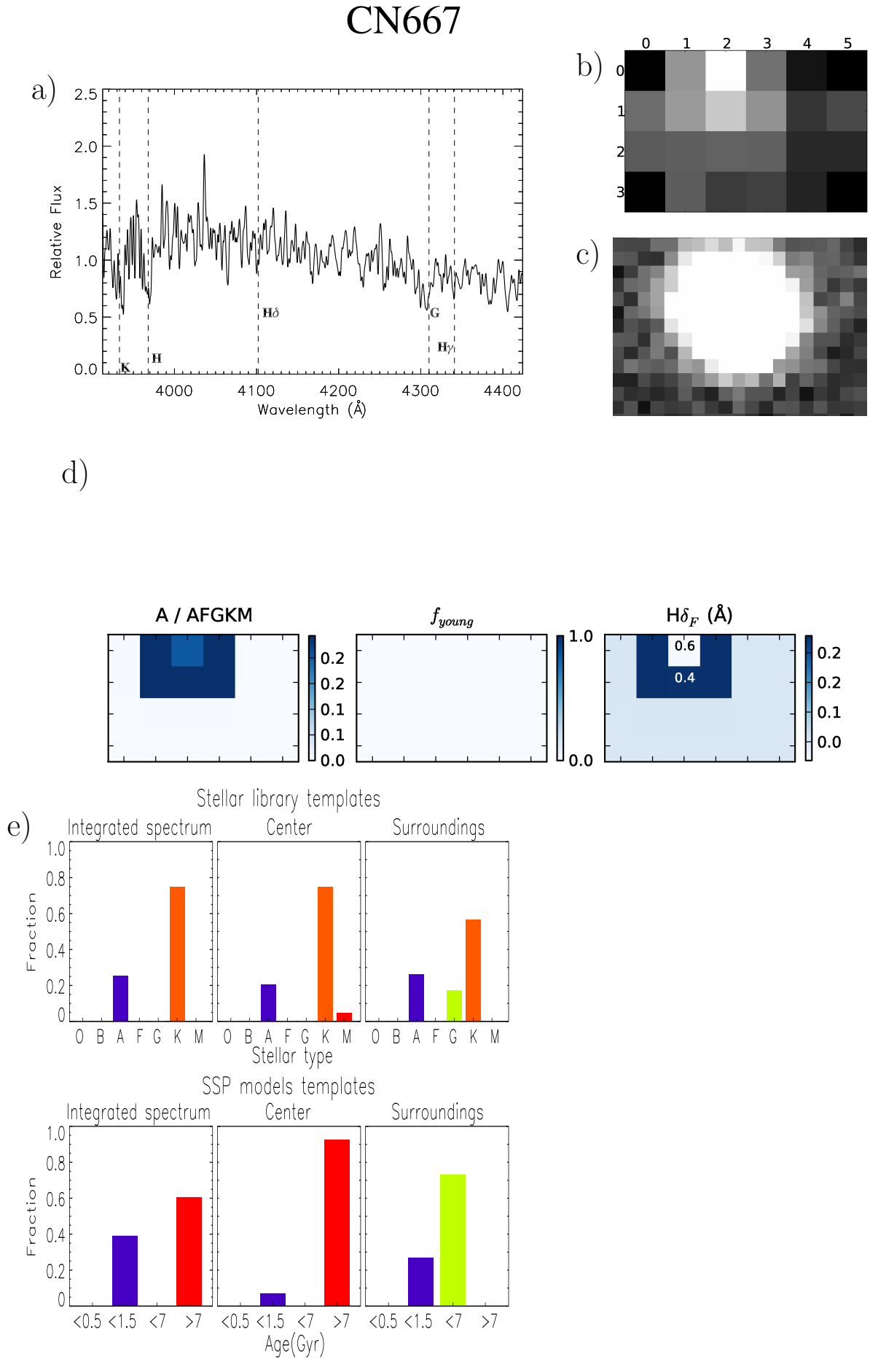
CN667
a)
Relative Flux
Wavelength (Å)
K
H
Hδ
G
Hγ
b)
c)
d)
A / AFGKM
f_{young}
$H\delta_F$ (Å)
e)
Stellar library templates
Integrated spectrum
Center
Surroundings
Fraction
O B A F G K M
Stellar type
SSP models templates
<0.5 <1.5 <7 >7
Age(Gyr)

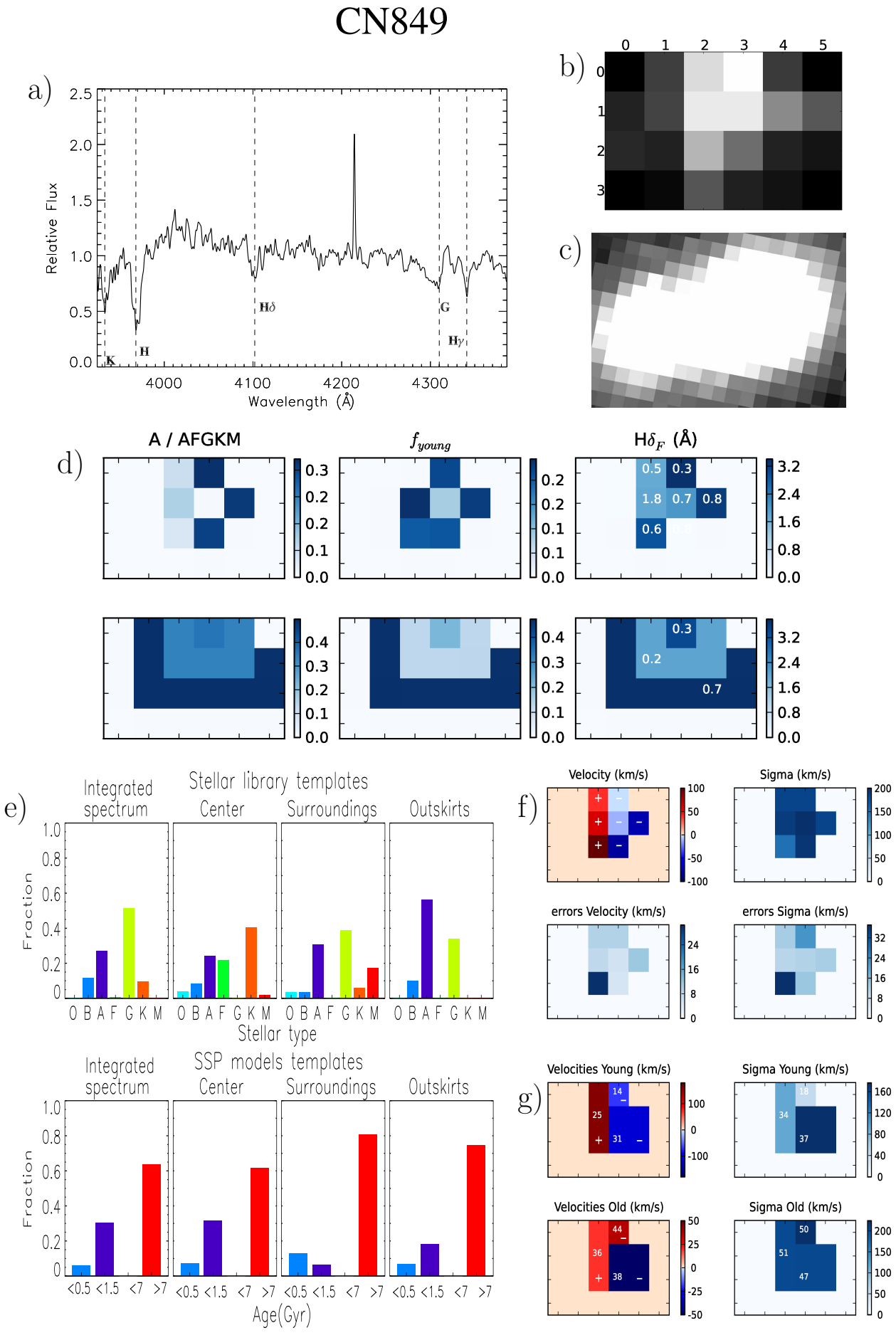
CN849
a)
Relative Flux
Wavelength (Å)
K
H
Hδ
G
Hγ
b)
c)
d)
A / AFGKM
f_{young}
$H\delta_F$ (Å)
e)
Integrated spectrum
Stellar library templates
Center
Surroundings
Outskirts
Fraction
O B A F G K M
Stellar type
SSP models templates
<0.5 <1.5 <7 >7
Age(Gyr)
f)
Velocity (km/s)
Sigma (km/s)
errors Velocity (km/s)
errors Sigma (km/s)
g)
Velocities Young (km/s)
Sigma Young (km/s)
Velocities Old (km/s)
Sigma Old (km/s)

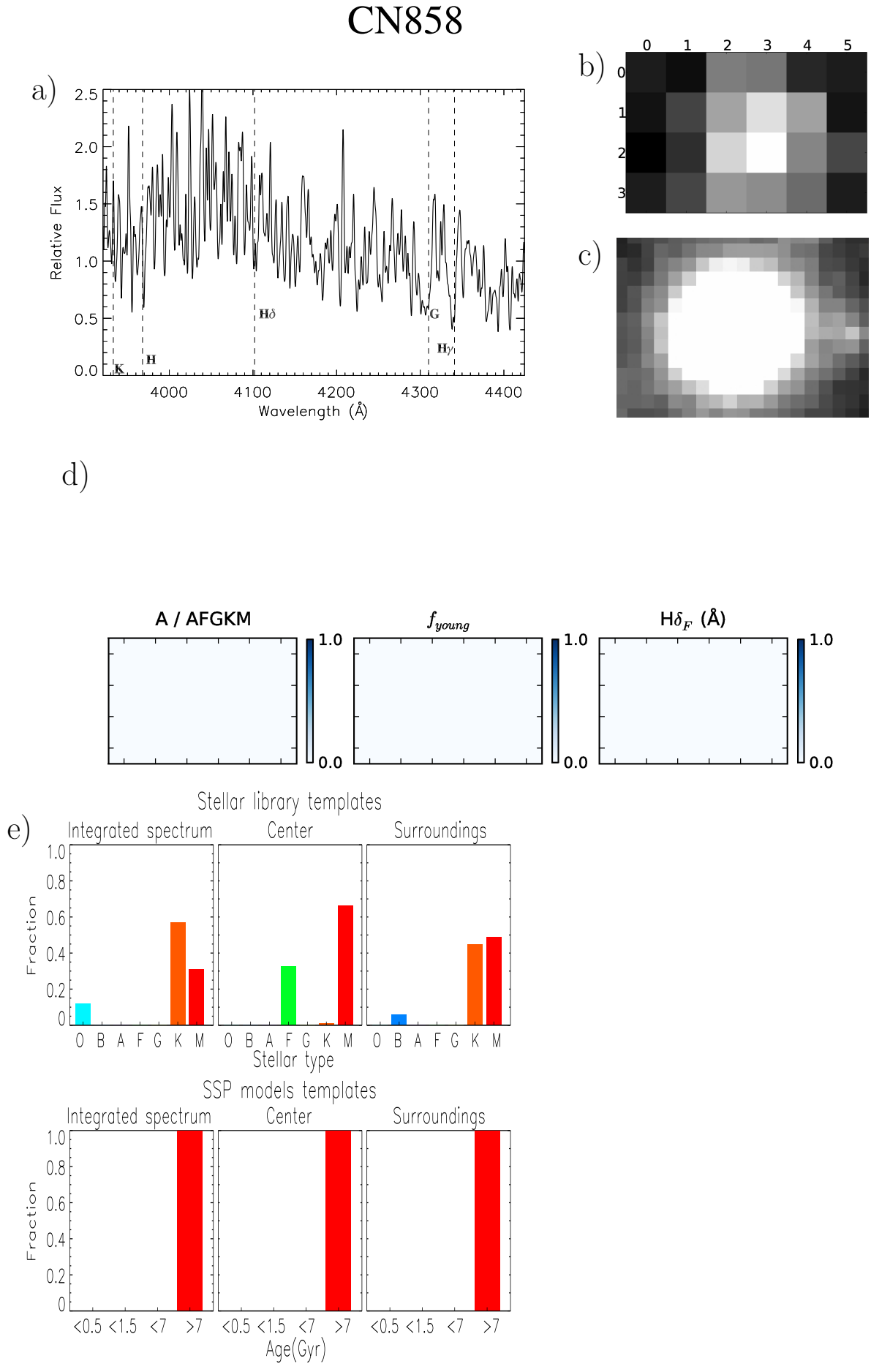
CN858
a)
Relative Flux
Wavelength (Å)
K
H
Hδ
G
Hγ
b)
c)
d)
A / AFGKM
f_{young}
$H\delta_F$ (Å)
1.0
0.0
e)
Stellar library templates
Integrated spectrum
Center
Surroundings
Fraction
O B A F G K M
Stellar type
SSP models templates
<0.5 <1.5 <7 >7
Age(Gyr)

Appendix B

OMEGA $\mathrm{H}\alpha$ maps

In this appendix we show the $\mathrm{H}\alpha$ emission-line regions overlaid on top of the V-band HST images for all the OMEGA galaxies with star-forming regions larger than the PSF (79 pixels, ~ 5arcsec^2, 40kpc^2 at $z = 0.165$). To determine if there is star formation in a pixel we adopt a threshold that corresponds to $\sim 5 \times 10^{-5}$M$_\odot$yr^{-1}kpc^{-2} (15 times the standard deviation of the background noise in the $\mathrm{H}\alpha$ stamps). The contour levels correspond to logaritmically-binned values of SFR from the chosen threshold to the peak value of the flux in each image. We have accompanied the images with the spectrum of the galaxies and the spectral fit, and some relevant galaxies' properties measured in OMEGA and also provided by STAGES (Gray *et al.*, 2009).

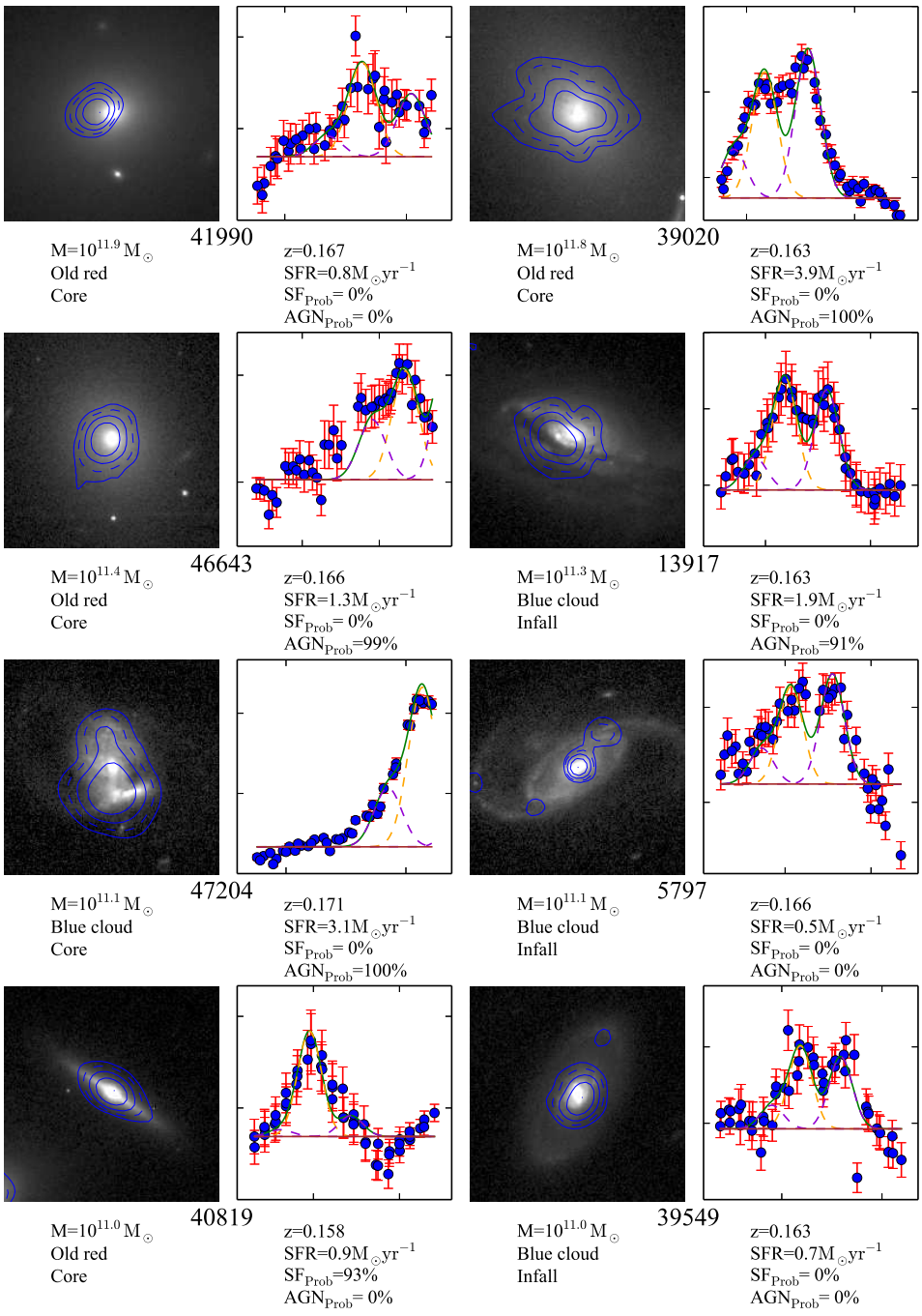

Figure B.1: SFR contours overlaid on top of the V-band HST images for the galaxies with star-forming regions larger than the PSF (79 pixels, $\sim$ 5arcsec^2, 40kpc^2 at $z = 0.165$). The contour levels correspond to logaritmically-binned values of SFR from the chosen threshold to the peak value of the flux in each image. We also show some of the galaxy properties we have measured in OMEGA together with that from STAGES (Gray *et al.*, 2009). Galaxies are sorted by stellar mass.

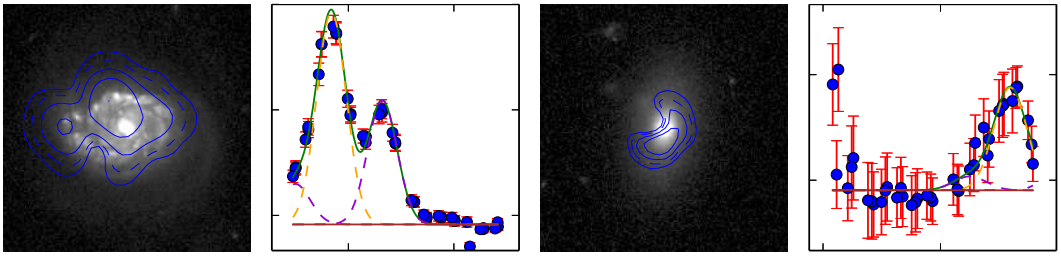

31772
M=$10^{10.9}$ M$_\odot$
Blue cloud
Infall
z=0.164
SFR=7.9M$_\odot$yr^{-1}
SF$_{\rm Prob}$= 0%
AGN$_{\rm Prob}$=100%

38105
M=$10^{10.9}$ M$_\odot$
Old red
Core
z=0.170
SFR=0.4M$_\odot$yr^{-1}
SF$_{\rm Prob}$= 9%
AGN$_{\rm Prob}$= 0%

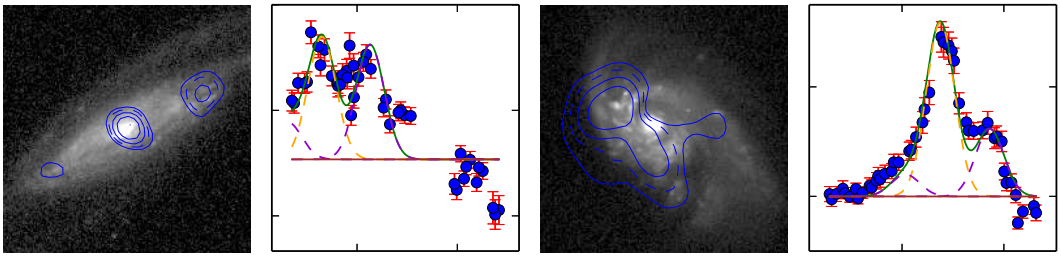

19108
M=$10^{10.9}$ M$_\odot$
Blue cloud
Infall
z=0.163
SFR=0.5M$_\odot$yr^{-1}
SF$_{\rm Prob}$= 0%
AGN$_{\rm Prob}$=99%

11827
M=$10^{10.8}$ M$_\odot$
Blue cloud
Infall
z=0.169
SFR=3.3M$_\odot$yr^{-1}
SF$_{\rm Prob}$= 0%
AGN$_{\rm Prob}$=67%

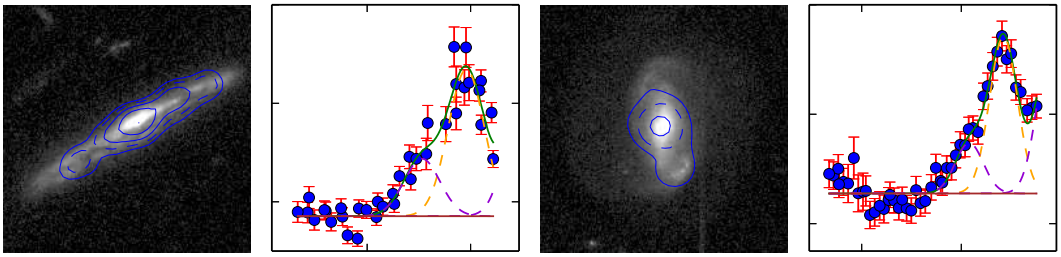

9721
M=$10^{10.7}$ M$_\odot$
Blue cloud
Core
z=0.170
SFR=0.8M$_\odot$yr^{-1}
SF$_{\rm Prob}$= 0%
AGN$_{\rm Prob}$=59%

15698
M=$10^{10.7}$ M$_\odot$
Blue cloud
Core
z=0.169
SFR=0.8M$_\odot$yr^{-1}
SF$_{\rm Prob}$= 0%
AGN$_{\rm Prob}$=100%

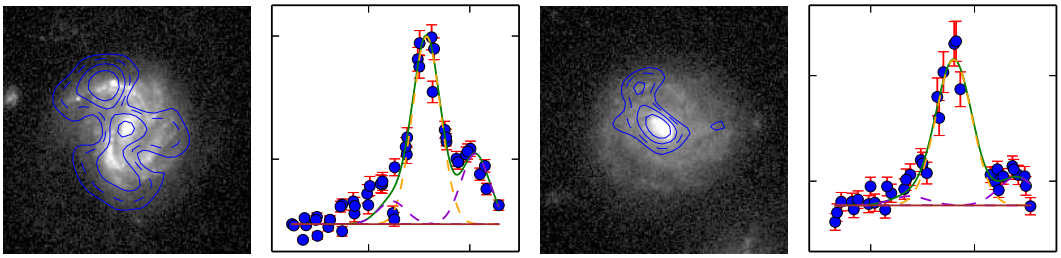

52549
M=$10^{10.7}$ M$_\odot$
Blue cloud
Infall
z=0.162
SFR=1.6M$_\odot$yr^{-1}
SF$_{\rm Prob}$=89%
AGN$_{\rm Prob}$=10%

12938
M=$10^{10.7}$ M$_\odot$
Blue cloud
Core
z=0.169
SFR=0.5M$_\odot$yr^{-1}
SF$_{\rm Prob}$=68%
AGN$_{\rm Prob}$=31%

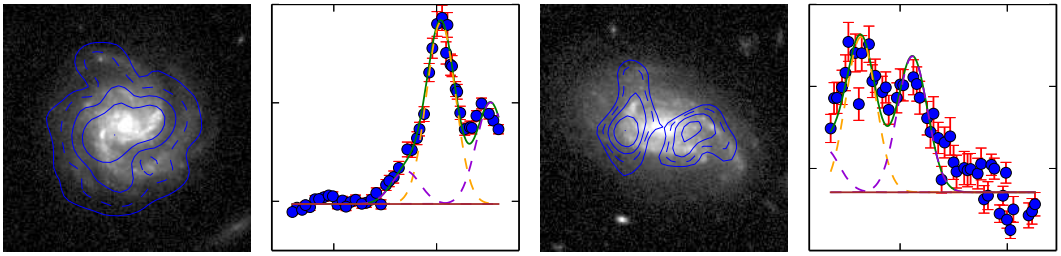

60598
M=$10^{10.7}$ M$_\odot$
Blue cloud
Infall
z=0.166
SFR=4.9M$_\odot$yr^{-1}
SF$_{\rm Prob}$= 0%
AGN$_{\rm Prob}$=100%

34219
M=$10^{10.7}$ M$_\odot$
Blue cloud
Infall
z=0.163
SFR=1.0M$_\odot$yr^{-1}
SF$_{\rm Prob}$= 0%
AGN$_{\rm Prob}$=31%

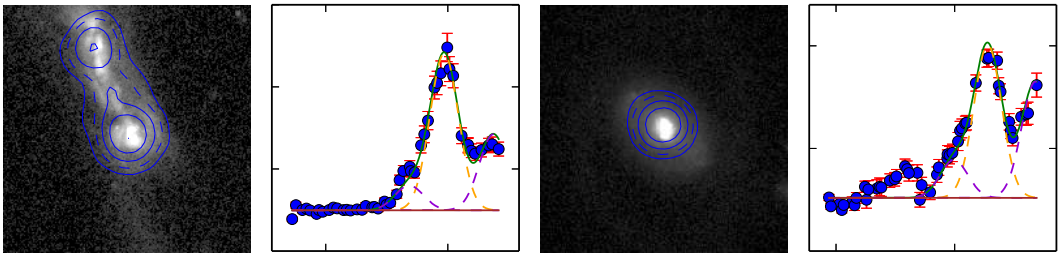

13416
M=$10^{10.7}$ M$_\odot$
Blue cloud
Infall
z=0.170
SFR=2.0M$_\odot$yr^{-1}
SF$_{\rm Prob}$= 0%
AGN$_{\rm Prob}$=99%

40199
M=$10^{10.6}$ M$_\odot$
Blue cloud
Infall
z=0.164
SFR=1.0M$_\odot$yr^{-1}
SF$_{\rm Prob}$= 0%
AGN$_{\rm Prob}$=100%

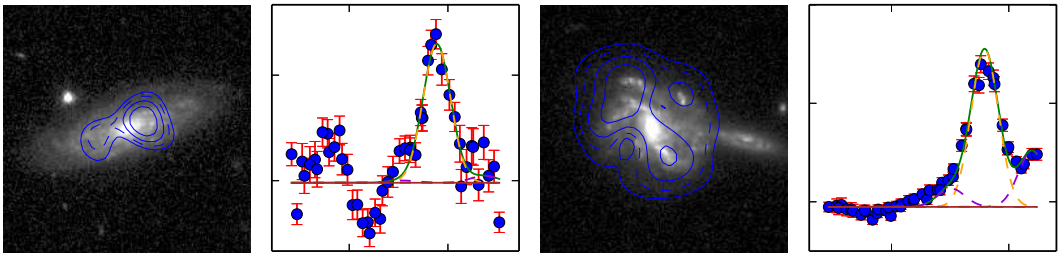

41939
M=$10^{10.6}$ M$_\odot$
Blue cloud
Infall
z=0.165
SFR=0.5M$_\odot$yr^{-1}
SF$_{\rm Prob}$= 0%
AGN$_{\rm Prob}$=99%

23924
M=$10^{10.6}$ M$_\odot$
Blue cloud
Infall
z=0.168
SFR=4.2M$_\odot$yr^{-1}
SF$_{\rm Prob}$=19%
AGN$_{\rm Prob}$=80%

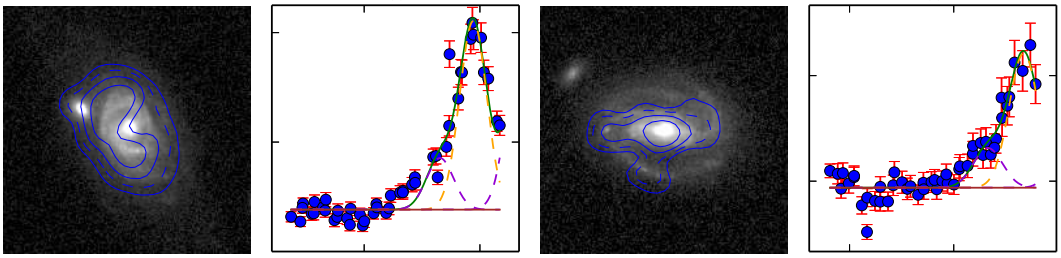

34839
M=$10^{10.6}$ M$_\odot$
Blue cloud
Infall
z=0.170
SFR=1.8M$_\odot$yr^{-1}
SF$_{\rm Prob}$= 0%
AGN$_{\rm Prob}$=99%

35412
M=$10^{10.5}$ M$_\odot$
Blue cloud
Infall
z=0.171
SFR=1.0M$_\odot$yr^{-1}
SF$_{\rm Prob}$= 0%
AGN$_{\rm Prob}$=96%

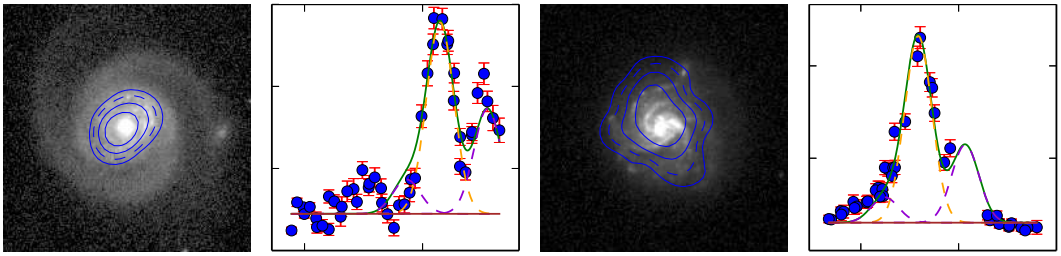

48706
M=$10^{10.5}$ M$_\odot$
Blue cloud
Infall
z=0.162
SFR=0.6M$_\odot$yr^{-1}
SF$_{\rm Prob}$= 0%
AGN$_{\rm Prob}$=100%

19140
M=$10^{10.5}$ M$_\odot$
Blue cloud
Infall
z=0.163
SFR=3.2M$_\odot$yr^{-1}
SF$_{\rm Prob}$=13%
AGN$_{\rm Prob}$=86%

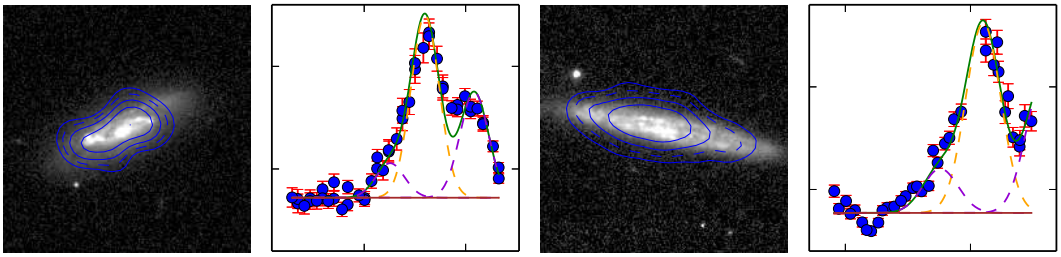

17155
M=$10^{10.5}$ M$_\odot$
Blue cloud
Infall
z=0.170
SFR=1.2M$_\odot$yr^{-1}
SF$_{\rm Prob}$= 0%
AGN$_{\rm Prob}$=100%

20593
M=$10^{10.5}$ M$_\odot$
Blue cloud
Core
z=0.166
SFR=2.4M$_\odot$yr^{-1}
SF$_{\rm Prob}$= 0%
AGN$_{\rm Prob}$=99%

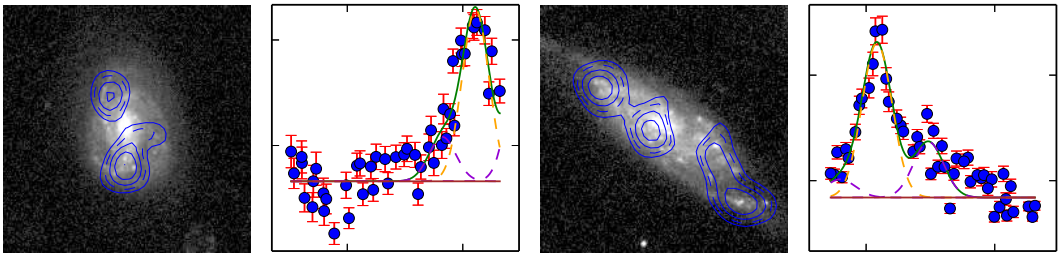

14192
M=$10^{10.5}$ M$_\odot$
Blue cloud
Core
z=0.171
SFR=0.6M$_\odot$yr^{-1}
SF$_{\rm Prob}$= 2%
AGN$_{\rm Prob}$= 0%

36437
M=$10^{10.5}$ M$_\odot$
Blue cloud
Infall
z=0.162
SFR=1.2M$_\odot$yr^{-1}
SF$_{\rm Prob}$=80%
AGN$_{\rm Prob}$=19%

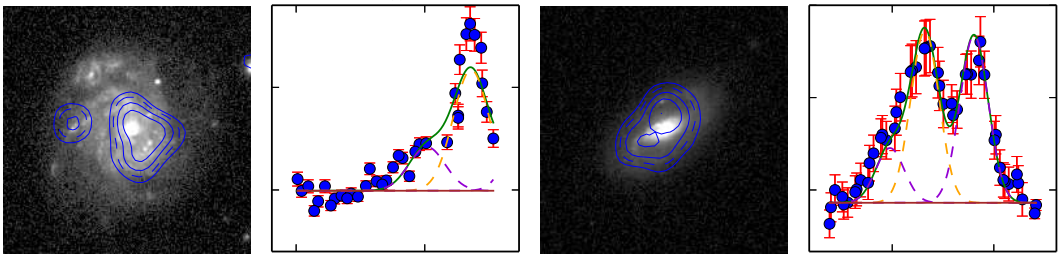

9524
M=$10^{10.5}$ M$_\odot$
Blue cloud
Infall
z=0.168
SFR=0.8M$_\odot$yr^{-1}
SF$_{\rm Prob}$= 0%
AGN$_{\rm Prob}$=100%

19305
M=$10^{10.5}$ M$_\odot$
Blue cloud
Infall
z=0.168
SFR=0.7M$_\odot$yr^{-1}
SF$_{\rm Prob}$= 0%
AGN$_{\rm Prob}$=79%

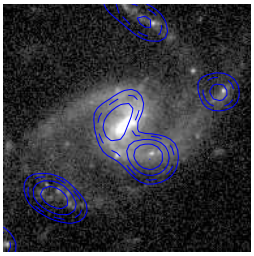
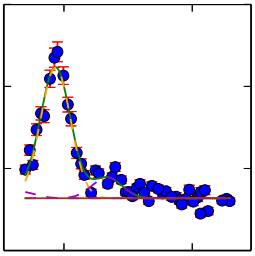

27886

M=$10^{10.4}$ M$_\odot$
Blue cloud
Infall

z=0.160
SFR=0.8M$_\odot$yr^{-1}
SF$_{\rm Prob}$=100%
AGN$_{\rm Prob}$= 0%

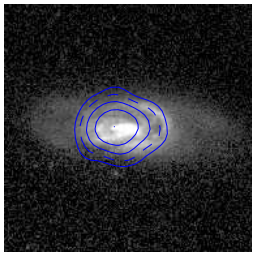
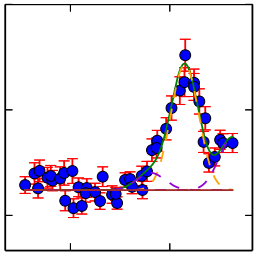

11633

M=$10^{10.4}$ M$_\odot$
Blue cloud
Core

z=0.167
SFR=0.9M$_\odot$yr^{-1}
SF$_{\rm Prob}$=39%
AGN$_{\rm Prob}$=60%

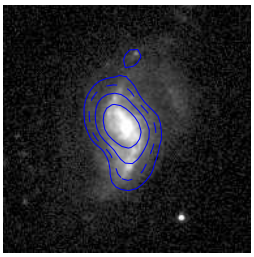
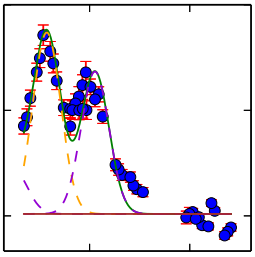

18509

M=$10^{10.4}$ M$_\odot$
Blue cloud
Infall

z=0.162
SFR=1.4M$_\odot$yr^{-1}
SF$_{\rm Prob}$= 0%
AGN$_{\rm Prob}$=100%

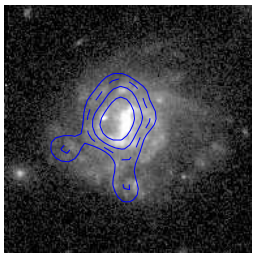
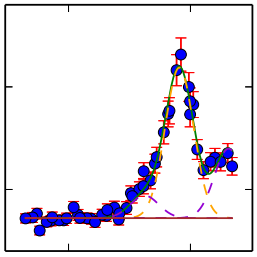

4657

M=$10^{10.4}$ M$_\odot$
Blue cloud
Infall

z=0.169
SFR=1.0M$_\odot$yr^{-1}
SF$_{\rm Prob}$= 1%
AGN$_{\rm Prob}$=98%

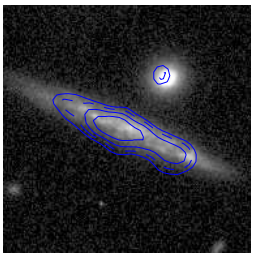
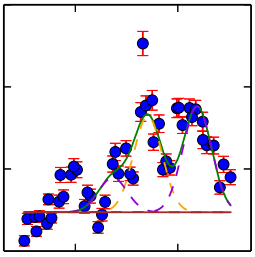

39800

M=$10^{10.4}$ M$_\odot$
Blue cloud
Core

z=0.163
SFR=0.6M$_\odot$yr^{-1}
SF$_{\rm Prob}$= 0%
AGN$_{\rm Prob}$=100%

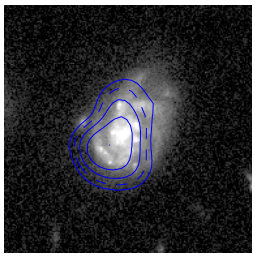
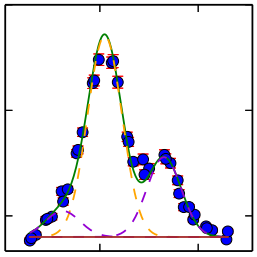

42713

M=$10^{10.4}$ M$_\odot$
Blue cloud
Non-cluster

z=0.164
SFR=1.5M$_\odot$yr^{-1}
SF$_{\rm Prob}$= 2%
AGN$_{\rm Prob}$=97%

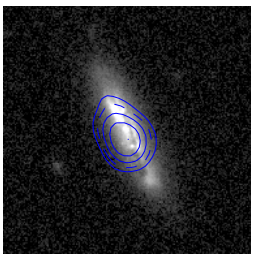
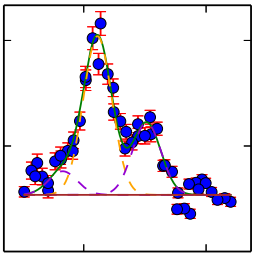

40522

M=$10^{10.4}$ M$_\odot$
Blue cloud
Infall

z=0.162
SFR=0.6M$_\odot$yr^{-1}
SF$_{\rm Prob}$=59%
AGN$_{\rm Prob}$=40%

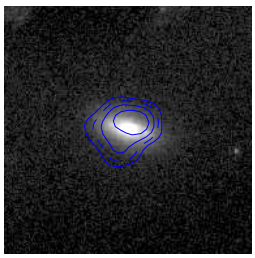
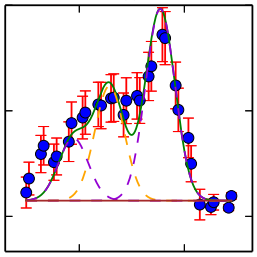

9020

M=$10^{10.4}$ M$_\odot$
Old red
Infall

z=0.168
SFR=0.4M$_\odot$yr^{-1}
SF$_{\rm Prob}$= 0%
AGN$_{\rm Prob}$=99%

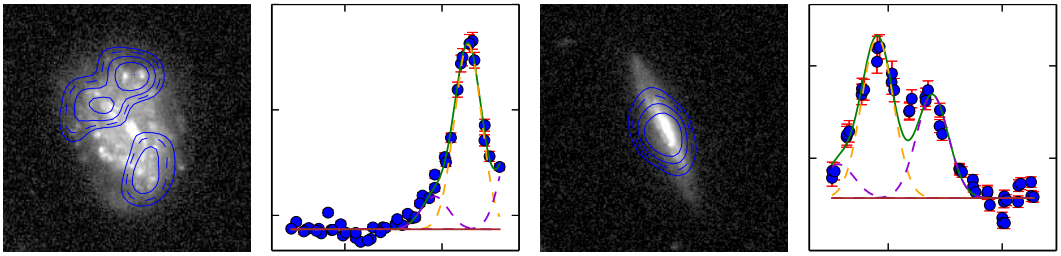

42109
M=$10^{10.4}$ M$_\odot$
Blue cloud
Infall
z=0.168
SFR=1.4M$_\odot$yr^{-1}
SF$_{\rm Prob}$=91%
AGN$_{\rm Prob}$= 8%

57975
M=$10^{10.3}$ M$_\odot$
Blue cloud
Infall
z=0.165
SFR=0.7M$_\odot$yr^{-1}
SF$_{\rm Prob}$= 0%
AGN$_{\rm Prob}$=100%

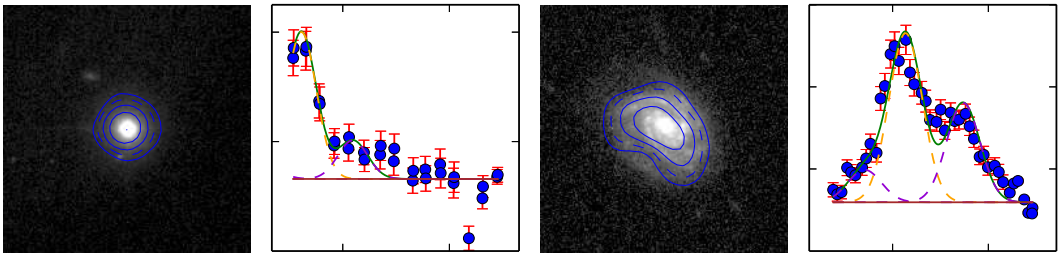

33338
M=$10^{10.3}$ M$_\odot$
Blue cloud
Infall
z=0.163
SFR=0.7M$_\odot$yr^{-1}
SF$_{\rm Prob}$=98%
AGN$_{\rm Prob}$= 1%

47486
M=$10^{10.3}$ M$_\odot$
Blue cloud
Infall
z=0.165
SFR=1.1M$_\odot$yr^{-1}
SF$_{\rm Prob}$= 0%
AGN$_{\rm Prob}$=100%

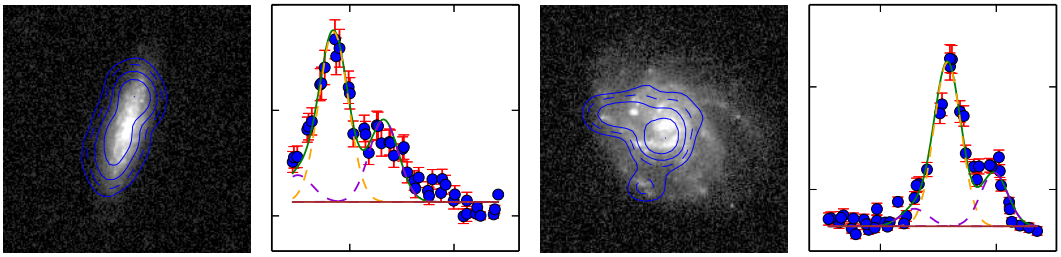

10649
M=$10^{10.3}$ M$_\odot$
Blue cloud
Infall
z=0.164
SFR=1.3M$_\odot$yr^{-1}
SF$_{\rm Prob}$=78%
AGN$_{\rm Prob}$=21%

7005
M=$10^{10.3}$ M$_\odot$
Blue cloud
Infall
z=0.166
SFR=1.0M$_\odot$yr^{-1}
SF$_{\rm Prob}$=100%
AGN$_{\rm Prob}$= 0%

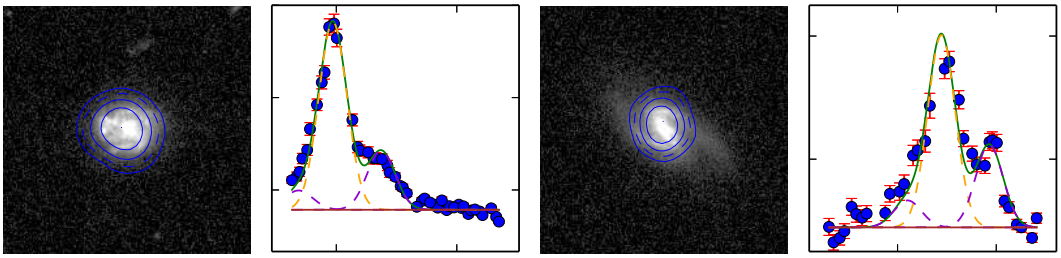

52235
M=$10^{10.3}$ M$_\odot$
Blue cloud
Non-cluster
z=0.161
SFR=1.6M$_\odot$yr^{-1}
SF$_{\rm Prob}$=100%
AGN$_{\rm Prob}$= 0%

9049
M=$10^{10.2}$ M$_\odot$
Blue cloud
Infall
z=0.169
SFR=0.8M$_\odot$yr^{-1}
SF$_{\rm Prob}$=56%
AGN$_{\rm Prob}$=43%

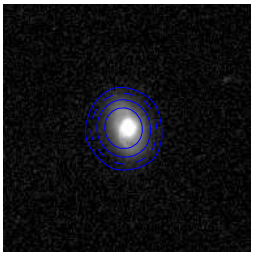
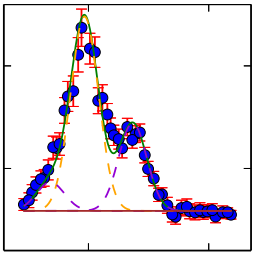

23437
M=$10^{10.2}$ M$_\odot$
Blue cloud
Infall
z=0.161
SFR=1.2M$_\odot$yr^{-1}
SF$_{\rm Prob}$= 2%
AGN$_{\rm Prob}$=97%

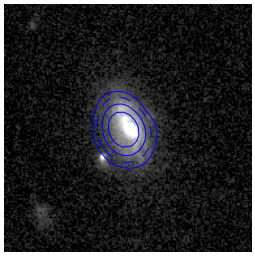
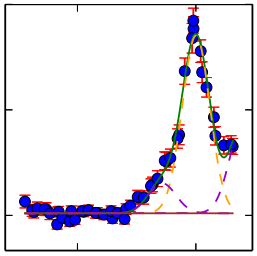

19222
M=$10^{10.2}$ M$_\odot$
Blue cloud
Non-cluster
z=0.170
SFR=0.7M$_\odot$yr^{-1}
SF$_{\rm Prob}$= 0%
AGN$_{\rm Prob}$=99%

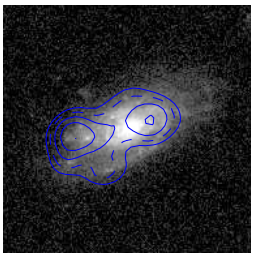
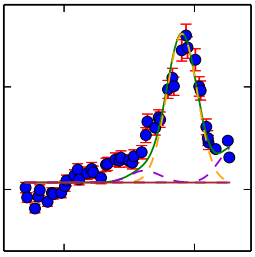

49719
M=$10^{10.2}$ M$_\odot$
Blue cloud
Infall
z=0.169
SFR=1.0M$_\odot$yr^{-1}
SF$_{\rm Prob}$=100%
AGN$_{\rm Prob}$= 0%

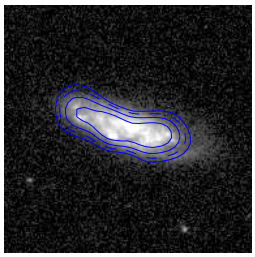
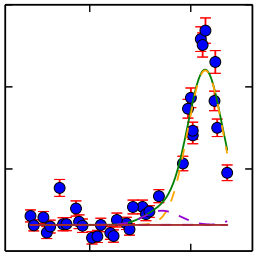

9961
M=$10^{10.2}$ M$_\odot$
Blue cloud
Infall
z=0.165
SFR=1.0M$_\odot$yr^{-1}
SF$_{\rm Prob}$=59%
AGN$_{\rm Prob}$=40%

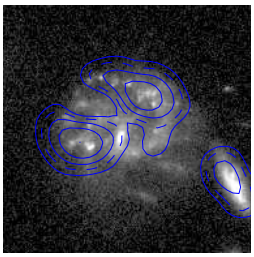
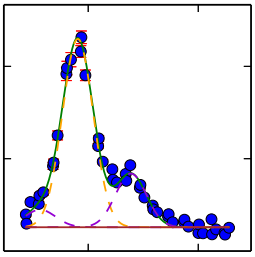

35120
M=$10^{10.2}$ M$_\odot$
Blue cloud
Infall
z=0.165
SFR=1.6M$_\odot$yr^{-1}
SF$_{\rm Prob}$=100%
AGN$_{\rm Prob}$= 0%

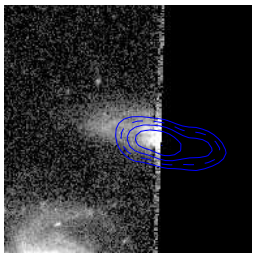
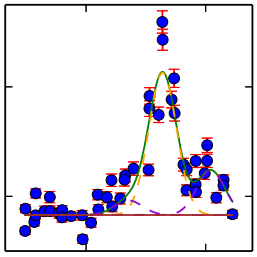

61188
M=$10^{10.2}$ M$_\odot$
Blue cloud
Infall
z=0.167
SFR=0.3M$_\odot$yr^{-1}
SF$_{\rm Prob}$=100%
AGN$_{\rm Prob}$= 0%

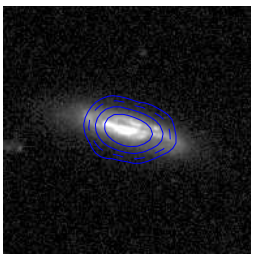
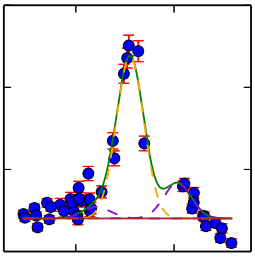

21683
M=$10^{10.1}$ M$_\odot$
Blue cloud
Infall
z=0.162
SFR=1.0M$_\odot$yr^{-1}
SF$_{\rm Prob}$=99%
AGN$_{\rm Prob}$= 0%

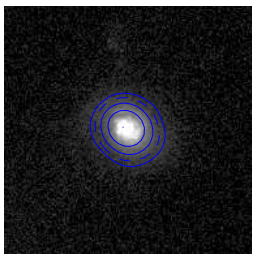
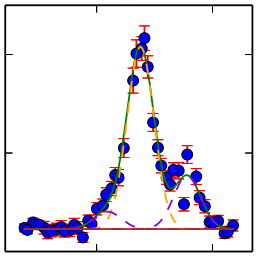

29558
M=$10^{10.1}$ M$_\odot$
Blue cloud
Infall
z=0.165
SFR=1.0M$_\odot$yr^{-1}
SF$_{\rm Prob}$=99%
AGN$_{\rm Prob}$= 0%

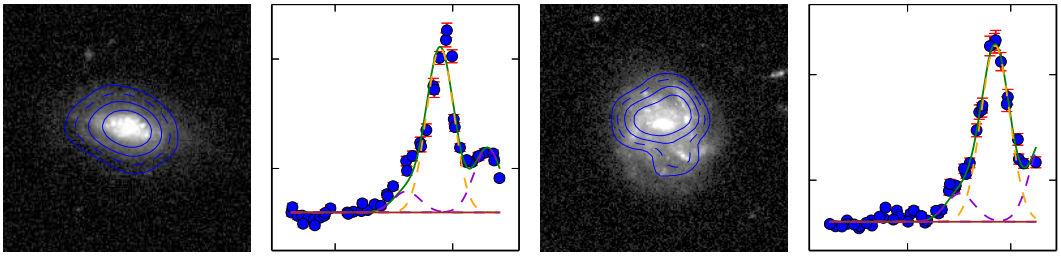

5363
M=$10^{10.1}$ M$_\odot$
Blue cloud
Infall
z=0.169
SFR=1.6M$_\odot$yr^{-1}
SF$_{\rm Prob}$=38%
AGN$_{\rm Prob}$=61%

29826
M=$10^{10.1}$ M$_\odot$
Blue cloud
Infall
z=0.165
SFR=1.3M$_\odot$yr^{-1}
SF$_{\rm Prob}$= 7%
AGN$_{\rm Prob}$=92%

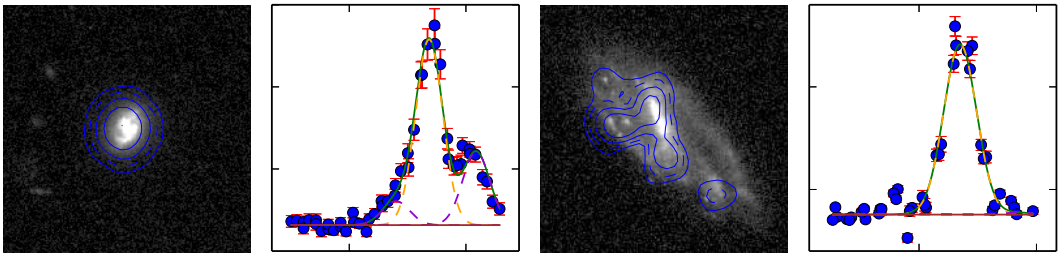

24286
M=$10^{10.1}$ M$_\odot$
Blue cloud
Non-cluster
z=0.167
SFR=0.9M$_\odot$yr^{-1}
SF$_{\rm Prob}$=52%
AGN$_{\rm Prob}$=47%

53418
M=$10^{10.1}$ M$_\odot$
Blue cloud
Infall
z=0.161
SFR=1.1M$_\odot$yr^{-1}
SF$_{\rm Prob}$=100%
AGN$_{\rm Prob}$= 0%

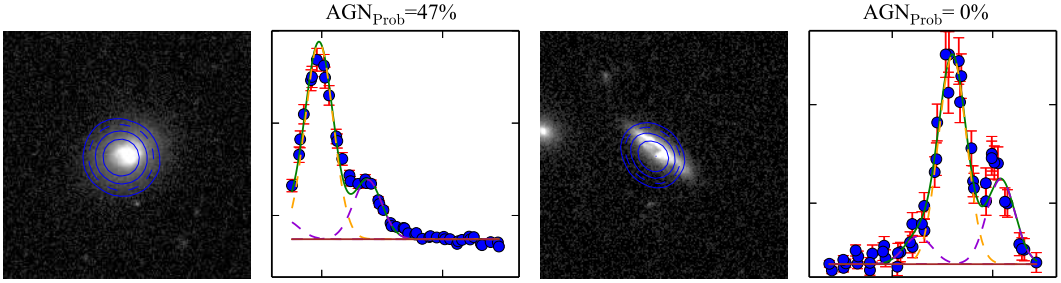

33185
M=$10^{10.1}$ M$_\odot$
Blue cloud
Non-cluster
z=0.161
SFR=1.7M$_\odot$yr^{-1}
SF$_{\rm Prob}$=100%
AGN$_{\rm Prob}$= 0%

7062
M=$10^{10.0}$ M$_\odot$
Blue cloud
Non-cluster
z=0.163
SFR=0.4M$_\odot$yr^{-1}
SF$_{\rm Prob}$=37%
AGN$_{\rm Prob}$=62%

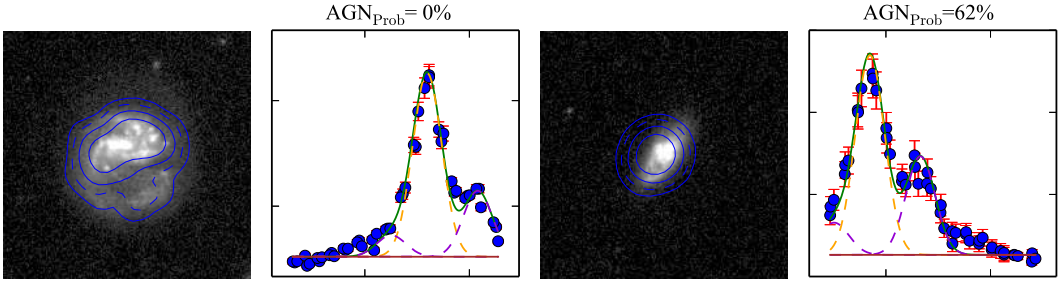

36376
M=$10^{10.0}$ M$_\odot$
Blue cloud
Core
z=0.170
SFR=2.7M$_\odot$yr^{-1}
SF$_{\rm Prob}$= 4%
AGN$_{\rm Prob}$=95%

10565
M=$10^{10.0}$ M$_\odot$
Blue cloud
Infall
z=0.165
SFR=1.3M$_\odot$yr^{-1}
SF$_{\rm Prob}$= 1%
AGN$_{\rm Prob}$=98%

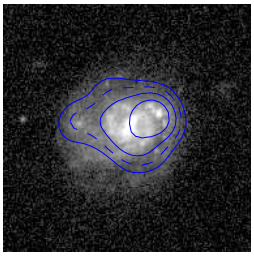
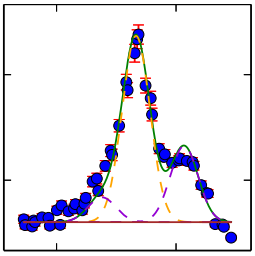

25122
M=$10^{10.0}$ M$_\odot$
Blue cloud
Infall
z=0.167
SFR=1.4M$_\odot$yr^{-1}
SF$_{\rm Prob}$= 3%
AGN$_{\rm Prob}$=96%

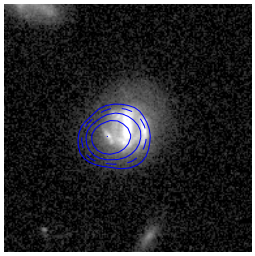
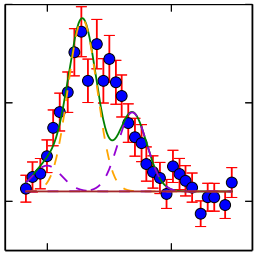

9010
M=$10^{10.0}$ M$_\odot$
Blue cloud
Non-cluster
z=0.164
SFR=0.5M$_\odot$yr^{-1}
SF$_{\rm Prob}$=15%
AGN$_{\rm Prob}$=84%

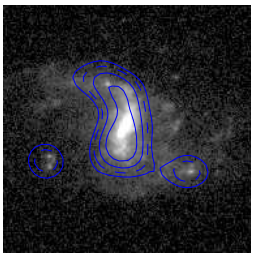
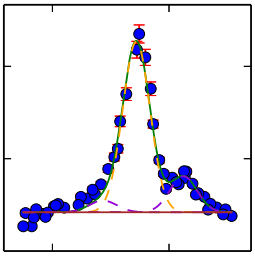

7431
M=$10^{10.0}$ M$_\odot$
Blue cloud
Infall
z=0.168
SFR=1.5M$_\odot$yr^{-1}
SF$_{\rm Prob}$=100%
AGN$_{\rm Prob}$= 0%

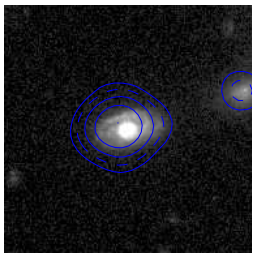
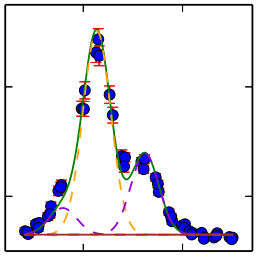

8029
M=$10^{10.0}$ M$_\odot$
Blue cloud
Infall
z=0.167
SFR=2.0M$_\odot$yr^{-1}
SF$_{\rm Prob}$=51%
AGN$_{\rm Prob}$=48%

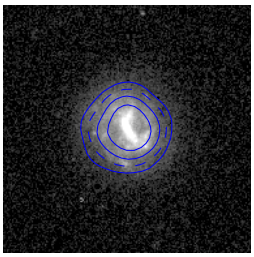
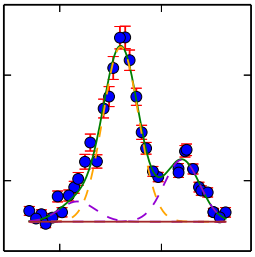

17849
M=$10^{10.0}$ M$_\odot$
Blue cloud
Non-cluster
z=0.162
SFR=1.3M$_\odot$yr^{-1}
SF$_{\rm Prob}$=98%
AGN$_{\rm Prob}$= 1%

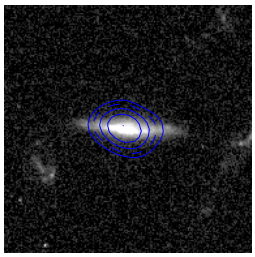
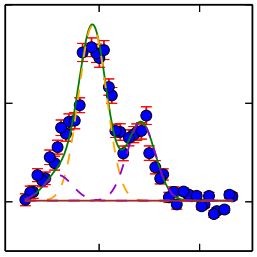

17536
M=$10^{10.0}$ M$_\odot$
Blue cloud
Non-cluster
z=0.165
SFR=0.5M$_\odot$yr^{-1}
SF$_{\rm Prob}$= 4%
AGN$_{\rm Prob}$=95%

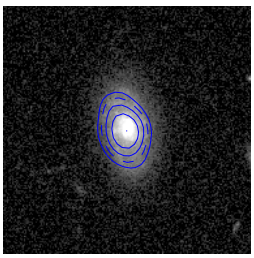
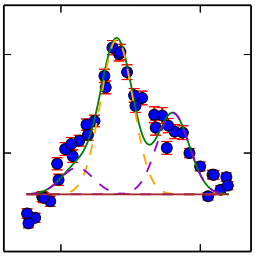

45653
M=$10^{10.0}$ M$_\odot$
Blue cloud
Infall
z=0.165
SFR=0.4M$_\odot$yr^{-1}
SF$_{\rm Prob}$= 0%
AGN$_{\rm Prob}$=100%

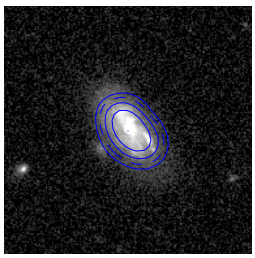
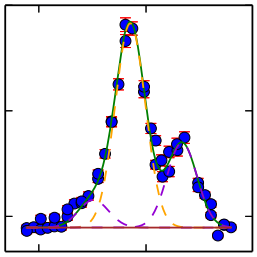

40968
M=$10^{10.0}$ M$_\odot$
Blue cloud
Non-cluster
z=0.165
SFR=0.8M$_\odot$yr^{-1}
SF$_{\rm Prob}$=48%
AGN$_{\rm Prob}$=51%

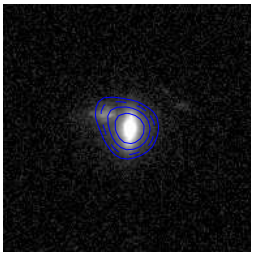
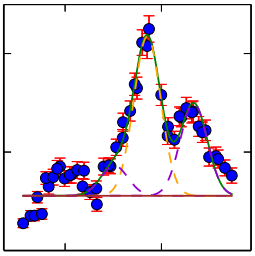

37116

M=$10^{9.9}$ M$_\odot$
Blue cloud
Infall

z=0.165
SFR=0.4M$_\odot$yr^{-1}
SF$_{\rm Prob}$= 0%
AGN$_{\rm Prob}$=100%

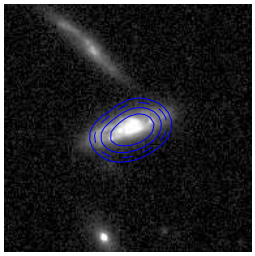
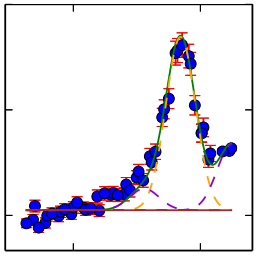

39977

M=$10^{9.9}$ M$_\odot$
Blue cloud
Infall

z=0.169
SFR=0.6M$_\odot$yr^{-1}
SF$_{\rm Prob}$=92%
AGN$_{\rm Prob}$= 7%

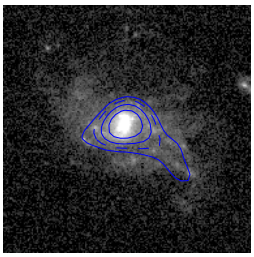
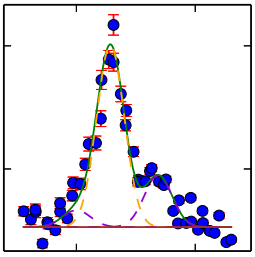

35964

M=$10^{9.9}$ M$_\odot$
Blue cloud
Infall

z=0.164
SFR=0.6M$_\odot$yr^{-1}
SF$_{\rm Prob}$=100%
AGN$_{\rm Prob}$= 0%

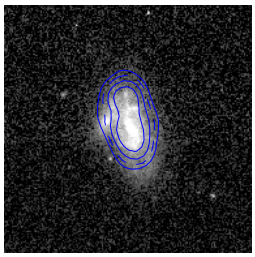
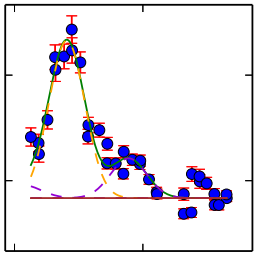

18385

M=$10^{9.9}$ M$_\odot$
Blue cloud
Core

z=0.161
SFR=0.6M$_\odot$yr^{-1}
SF$_{\rm Prob}$=100%
AGN$_{\rm Prob}$= 0%

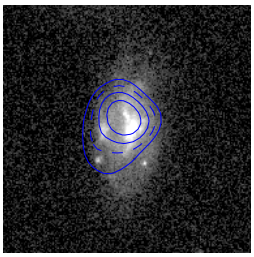
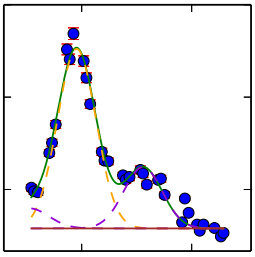

46664

M=$10^{9.9}$ M$_\odot$
Blue cloud
Core

z=0.164
SFR=0.8M$_\odot$yr^{-1}
SF$_{\rm Prob}$=99%
AGN$_{\rm Prob}$= 0%

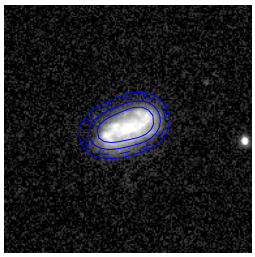
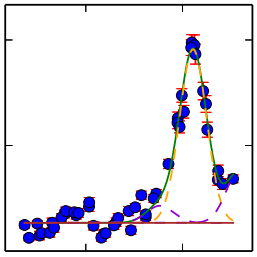

51433

M=$10^{9.8}$ M$_\odot$
Blue cloud
Infall

z=0.166
SFR=0.6M$_\odot$yr^{-1}
SF$_{\rm Prob}$=99%
AGN$_{\rm Prob}$= 0%

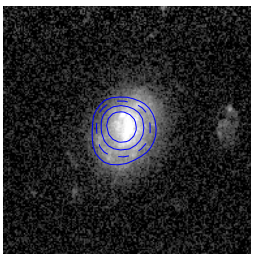
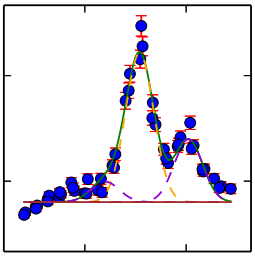

40107

M=$10^{9.8}$ M$_\odot$
Blue cloud
Core

z=0.162
SFR=0.6M$_\odot$yr^{-1}
SF$_{\rm Prob}$=64%
AGN$_{\rm Prob}$=35%

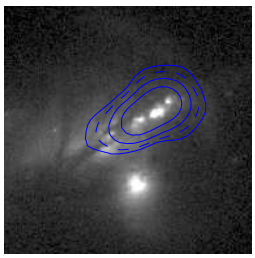
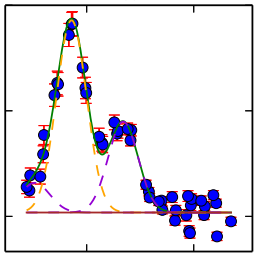

54417

M=$10^{9.8}$ M$_\odot$
Blue cloud
Infall

z=0.165
SFR=2.9M$_\odot$yr^{-1}
SF$_{\rm Prob}$= 7%
AGN$_{\rm Prob}$=92%

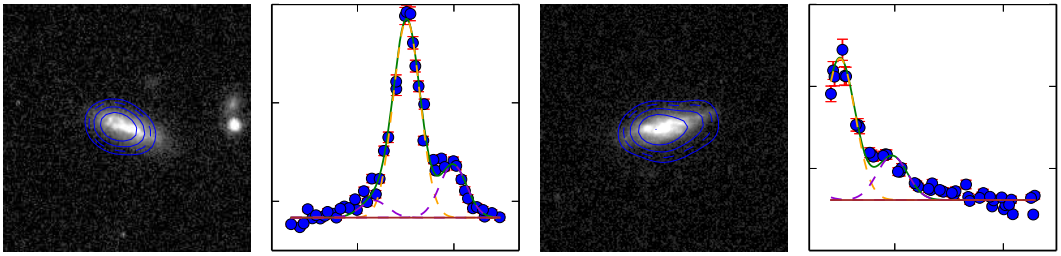

39628
M=$10^{9.8}$ M$_\odot$
Blue cloud
Infall
z=0.162
SFR=0.5M$_\odot$yr^{-1}
SF$_{\rm Prob}$=100%
AGN$_{\rm Prob}$= 0%

29925
M=$10^{9.8}$ M$_\odot$
Blue cloud
Non-cluster
z=0.162
SFR=0.9M$_\odot$yr^{-1}
SF$_{\rm Prob}$=99%
AGN$_{\rm Prob}$= 0%

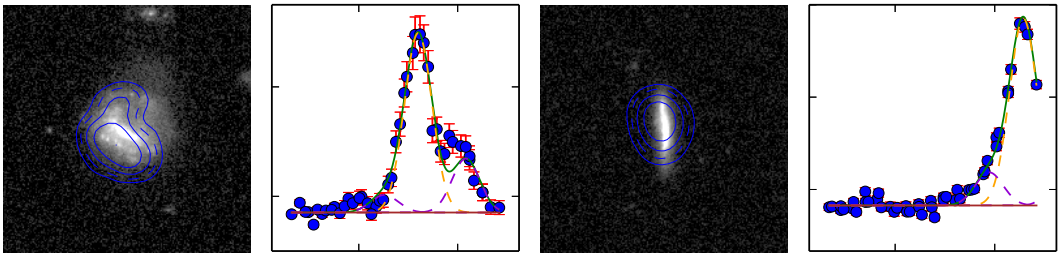

13968
M=$10^{9.8}$ M$_\odot$
Blue cloud
Infall
z=0.163
SFR=0.9M$_\odot$yr^{-1}
SF$_{\rm Prob}$=99%
AGN$_{\rm Prob}$= 0%

34349
M=$10^{9.8}$ M$_\odot$
Blue cloud
Infall
z=0.168
SFR=0.8M$_\odot$yr^{-1}
SF$_{\rm Prob}$= 0%
AGN$_{\rm Prob}$=99%

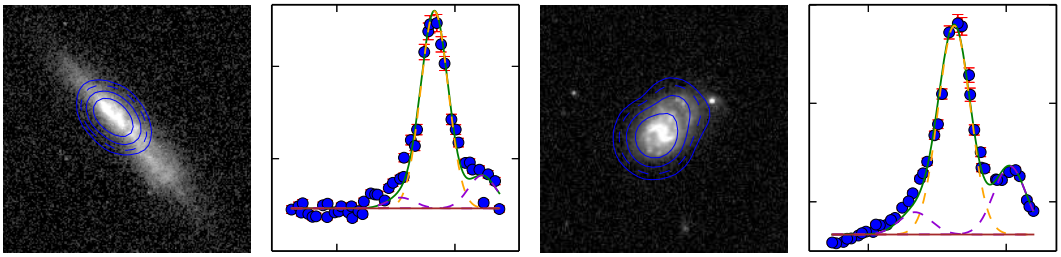

23457
M=$10^{9.8}$ M$_\odot$
Blue cloud
Infall
z=0.169
SFR=0.8M$_\odot$yr^{-1}
SF$_{\rm Prob}$=100%
AGN$_{\rm Prob}$= 0%

42742
M=$10^{9.7}$ M$_\odot$
Blue cloud
Infall
z=0.167
SFR=2.2M$_\odot$yr^{-1}
SF$_{\rm Prob}$=100%
AGN$_{\rm Prob}$= 0%

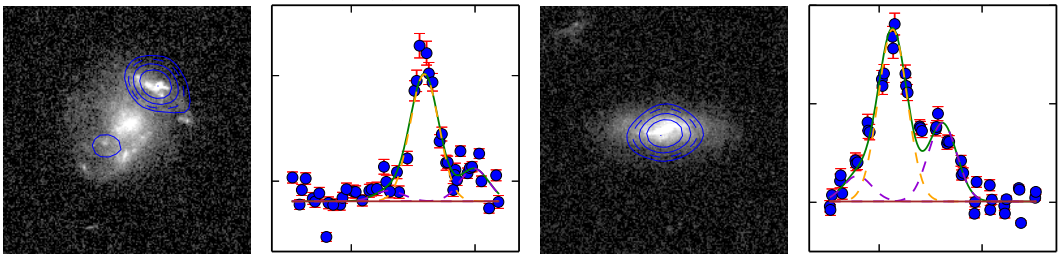

50962
M=$10^{9.7}$ M$_\odot$
Blue cloud
Infall
z=0.166
SFR=0.2M$_\odot$yr^{-1}
SF$_{\rm Prob}$= 0%
AGN$_{\rm Prob}$=99%

21669
M=$10^{9.7}$ M$_\odot$
Blue cloud
Infall
z=0.167
SFR=0.5M$_\odot$yr^{-1}
SF$_{\rm Prob}$=20%
AGN$_{\rm Prob}$=79%

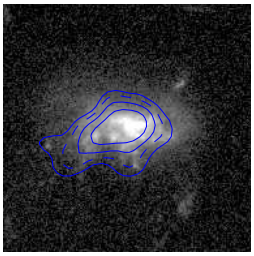
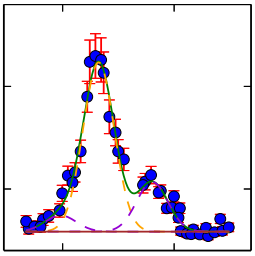

45301
M=$10^{9.7}$ M$_\odot$
Blue cloud
Non-cluster
z=0.161
SFR=1.1M$_\odot$yr^{-1}
SF$_{\rm Prob}$=99%
AGN$_{\rm Prob}$= 0%

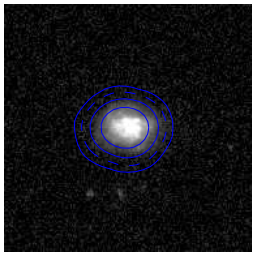
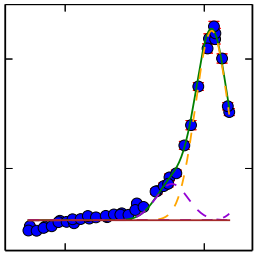

49240
M=$10^{9.7}$ M$_\odot$
Blue cloud
Infall
z=0.171
SFR=1.8M$_\odot$yr^{-1}
SF$_{\rm Prob}$= 0%
AGN$_{\rm Prob}$=100%

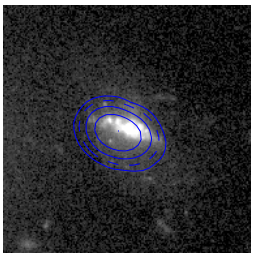
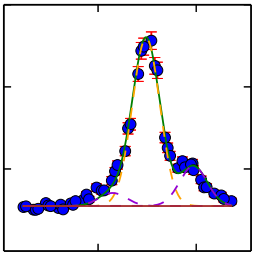

15639
M=$10^{9.7}$ M$_\odot$
Blue cloud
Core
z=0.162
SFR=1.1M$_\odot$yr^{-1}
SF$_{\rm Prob}$=100%
AGN$_{\rm Prob}$= 0%

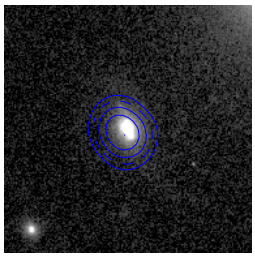
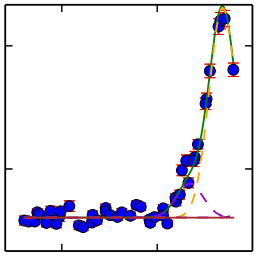

14270
M=$10^{9.6}$ M$_\odot$
Blue cloud
Core
z=0.171
SFR=0.7M$_\odot$yr^{-1}
SF$_{\rm Prob}$= 1%
AGN$_{\rm Prob}$=98%

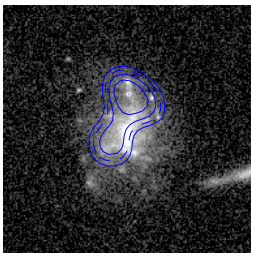
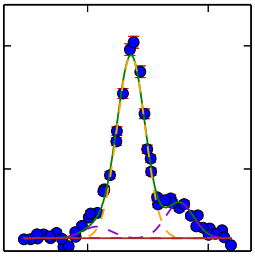

41324
M=$10^{9.6}$ M$_\odot$
Blue cloud
Infall
z=0.164
SFR=0.6M$_\odot$yr^{-1}
SF$_{\rm Prob}$=100%
AGN$_{\rm Prob}$= 0%

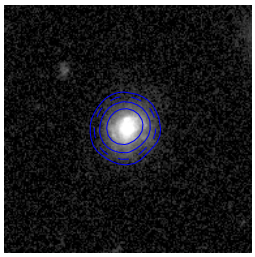
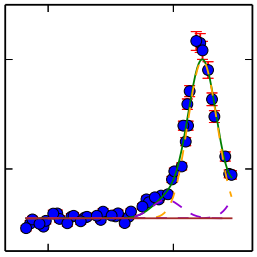

52612
M=$10^{9.6}$ M$_\odot$
Blue cloud
Infall
z=0.172
SFR=0.8M$_\odot$yr^{-1}
SF$_{\rm Prob}$=89%
AGN$_{\rm Prob}$=10%

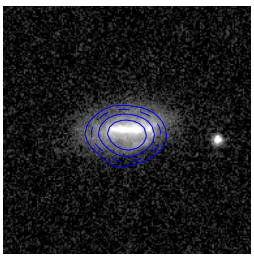
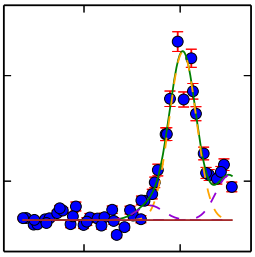

40078
M=$10^{9.6}$ M$_\odot$
Blue cloud
Infall
z=0.166
SFR=0.6M$_\odot$yr^{-1}
SF$_{\rm Prob}$=100%
AGN$_{\rm Prob}$= 0%

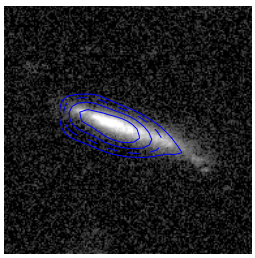
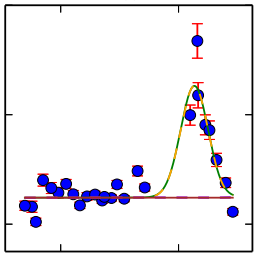

8778
M=$10^{9.6}$ M$_\odot$
Blue cloud
Infall
z=0.171
SFR=0.5M$_\odot$yr^{-1}
SF$_{\rm Prob}$=99%
AGN$_{\rm Prob}$= 0%

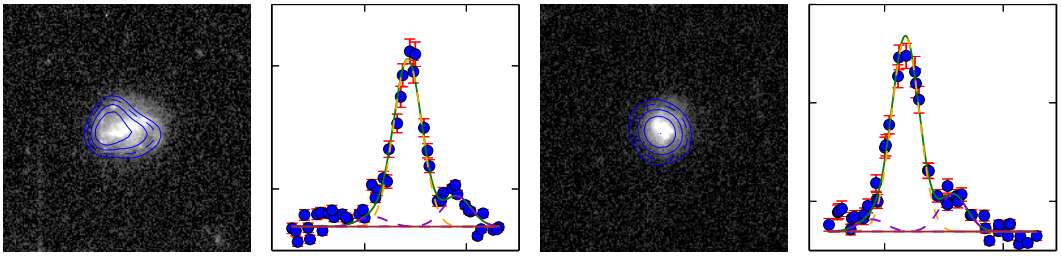

19244
M=$10^{9.5}$ M$_\odot$
Blue cloud
Infall
z=0.169
SFR=0.4M$_\odot$yr^{-1}
SF$_{\rm Prob}$=100%
AGN$_{\rm Prob}$= 0%

8559
M=$10^{9.5}$ M$_\odot$
Blue cloud
Core
z=0.163
SFR=0.5M$_\odot$yr^{-1}
SF$_{\rm Prob}$=100%
AGN$_{\rm Prob}$= 0%

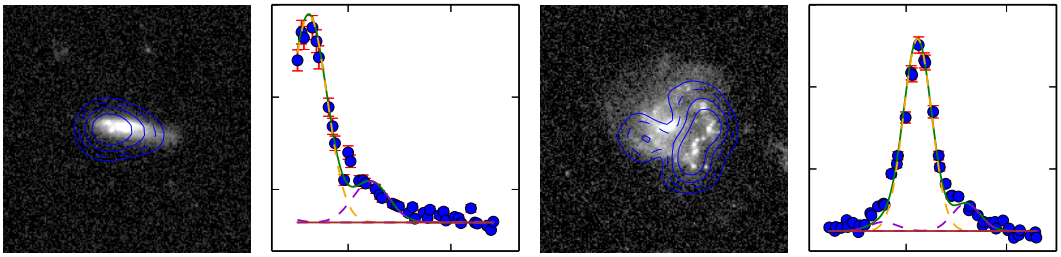

46149
M=$10^{9.4}$ M$_\odot$
Blue cloud
Infall
z=0.162
SFR=0.9M$_\odot$yr^{-1}
SF$_{\rm Prob}$=100%
AGN$_{\rm Prob}$= 0%

33534
M=$10^{9.4}$ M$_\odot$
Blue cloud
Core
z=0.167
SFR=1.2M$_\odot$yr^{-1}
SF$_{\rm Prob}$=100%
AGN$_{\rm Prob}$= 0%

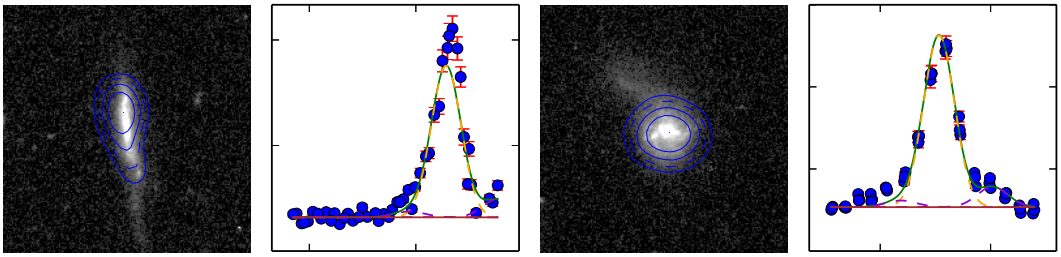

27469
M=$10^{9.4}$ M$_\odot$
Blue cloud
Infall
z=0.168
SFR=0.6M$_\odot$yr^{-1}
SF$_{\rm Prob}$=100%
AGN$_{\rm Prob}$= 0%

20056
M=$10^{9.3}$ M$_\odot$
Blue cloud
Infall
z=0.170
SFR=1.1M$_\odot$yr^{-1}
SF$_{\rm Prob}$=100%
AGN$_{\rm Prob}$= 0%

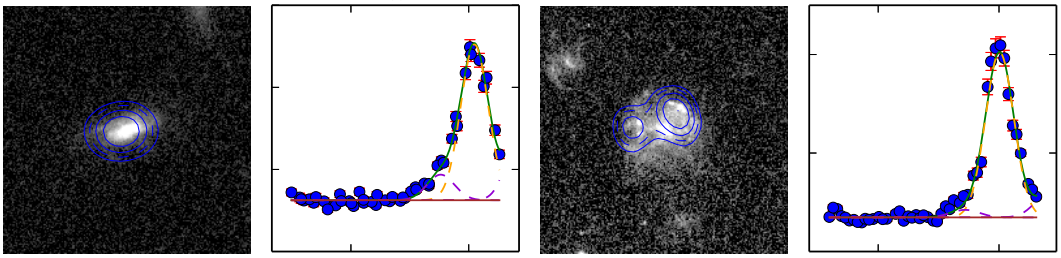

15732
M=$10^{9.3}$ M$_\odot$
Blue cloud
Infall
z=0.171
SFR=0.5M$_\odot$yr^{-1}
SF$_{\rm Prob}$= 0%
AGN$_{\rm Prob}$=99%

17974
M=$10^{9.2}$ M$_\odot$
Blue cloud
Infall
z=0.170
SFR=0.4M$_\odot$yr^{-1}
SF$_{\rm Prob}$=100%
AGN$_{\rm Prob}$= 0%

Bibliography

Abell G. O., Corwin, Jr. H. G., Olowin R. P., 1989. ApJS, **70**, 1. *A catalog of rich clusters of galaxies*.

Abell G. O., 1965. ARAA, **3**, 1. *Clustering of Galaxies*.

Alamo-Martínez K. A., Blakeslee J. P., Jee M. J., Côté P., Ferrarese L., González-Lópezlira R. A., Jordán A., Meurer G. R., Peng E. W., West M. J., 2013. ApJ, **775**, 20. *The Rich Globular Cluster System of Abell 1689 and the Radial Dependence of the Globular Cluster Formation Efficiency*.

Aragón-Salamanca A., Bedregal A. G., Merrifield M. R., 2006. AA, **458**, 101. *Measuring the fading of S0 galaxies using globular clusters*.

Bacon R., Accardo M., Adjali L., Anwand H., Bauer S., Biswas I., Blaizot J., Boudon D., Brau-Nogue S., Brinchmann J., Caillier P., Capoani L., Carollo C. M., Contini T., Couderc P., Daguisé E., Deiries S., Delabre B., Dreizler S., Dubois J., Dupieux M., Dupuy C., Emsellem E., Fechner T., Fleischmann A., François M., Gallou G., Gharsa T., Glindemann A., Gojak D., Guiderdoni B., Hansali G., Hahn T., Jarno A., Kelz A., Koehler C., Kosmalski J., Laurent F., Le Floch M., Lilly S. J., Lizon J.-L., Loupias M., Manescau A., Monstein C., Nicklas H., Olaya J.-C., Pares L., Pasquini L., Pécontal-Rousset A., Pelló R., Petit C., Popow E., Reiss R., Remillieux A., Renault E., Roth M., Rupprecht G., Serre D., Schaye J., Soucail G., Steinmetz M., Streicher O., Stuik R., Valentin H., Vernet J., Weilbacher P., Wisotzki L., Yerle N., 2010. *The MUSE second-generation VLT instrument*, In: *Society of Photo-Optical Instrumentation Engineers (SPIE) Conference Series*, 8.

Baldry I. K., Balogh M. L., Bower R. G., Glazebrook K., Nichol R. C., Bamford S. P., Budavari T., 2006. *MNRAS*, **373**, 469. *Galaxy bimodality versus stellar mass and environment*.

Baldwin J. A., Phillips M. M., Terlevich R., 1981. PASP, **93**, 5. *Classification parameters for the emission-line spectra of extragalactic objects*.

Balogh M. L., Couch W. J., Smail I., Bower R. G., Glazebrook K., 2002. MNRAS, **335**, 10. *An Hα survey of the rich cluster A 1689*.

Balogh M., Eke V., Miller C., Lewis I., Bower R., Couch W., Nichol R., Bland-Hawthorn J., Baldry I. K., Baugh C., Bridges T., Cannon R., Cole S., Colless M., Collins C., Cross N., Dalton G., de Propris R., Driver S. P., Efstathiou G., Ellis R. S., Frenk C. S., Glazebrook K., Gomez P., Gray A., Hawkins E., Jackson C., Lahav

O., Lumsden S., Maddox S., Madgwick D., Norberg P., Peacock J. A., Percival W., Peterson B. A., Sutherland W., Taylor K., 2004a. MNRAS, **348**, 1355. *Galaxy ecology: groups and low-density environments in the SDSS and 2dFGRS*.

Balogh M. L., Baldry I. K., Nichol R., Miller C., Bower R., Glazebrook K., 2004b. *ApJL*, **615**, L101. *The Bimodal Galaxy Color Distribution: Dependence on Luminosity and Environment*.

Bamford S. P., Milvang-Jensen B., Aragón-Salamanca A., Simard L., 2005. MNRAS, **361**, 109. *The Tully-Fisher relation of distant cluster galaxies*.

Bamford S. P., Rojas A. L., Nichol R. C., Miller C. J., Wasserman L., Genovese C. R., Freeman P. E., 2008. *MNRAS*, **391**, 607. *Revealing components of the galaxy population through non-parametric techniques*.

Bamford S. P., Nichol R. C., Baldry I. K., Land K., Lintott C. J., Schawinski K., Slosar A., Szalay A. S., Thomas D., Torki M., Andreescu D., Edmondson E. M., Miller C. J., Murray P., Raddick M. J., Vandenberg J., 2009. *MNRAS*, **393**, 1324. *Galaxy Zoo: the dependence of morphology and colour on environment*.

Bamford S. P., Häußler B., Rojas A., Vika M., Cresswell J., 2012. *Measuring SEDs for individual galaxy components*, In: *IAU Symposium*, p. 301, eds Tuffs R. J., Popescu C. C.

Bamford S. P., Milvang-Jensen B., Aragón-Salamanca A., 2007. MNRAS, **378**, L6. *The sizes of disc galaxies in intermediate-redshift clusters*.

Barden M., Häußler B., Peng C. Y., McIntosh D. H., Guo Y., 2012. MNRAS, **422**, 449. *GALAPAGOS: from pixels to parameters*.

Barnes J. E., Hernquist L. E., 1991. *ApJL*, **370**, L65. *Fueling starburst galaxies with gas-rich mergers*.

Bedregal A. G., Aragón-Salamanca A., Merrifield M. R., 2006. MNRAS, **373**, 1125. *The Tully-Fisher relation for S0 galaxies*.

Bedregal A. G., Cardiel N., Aragón-Salamanca A., Merrifield M. R., 2011. MNRAS, **415**, 2063. *Stellar population gradients in Fornax cluster S0 galaxies: connecting bulge and disc evolution*.

Bekki K., Couch W. J., Shioya Y., 2002. ApJ, **577**, 651. *Passive Spiral Formation from Halo Gas Starvation: Gradual Transformation into S0s*.

Bekki K., Couch W. J., Shioya Y., Vazdekis A., 2005. MNRAS, **359**, 949. *Origin of E+A galaxies - I. Physical properties of E+A galaxies formed from galaxy merging and interaction*.

Bekki K., 1998. ApJ, **502**, L133. *Unequal-Mass Galaxy Mergers and the Creation of Cluster S0 Galaxies*.

Bekki K., 2009. MNRAS, **399**, 2221. *Ram-pressure stripping of halo gas in disc galaxies: implications for galactic star formation in different environments*.

Belfiore F., Maiolino R., Bundy K., Thomas D., Maraston C., Wilkinson D., Sánchez S. F., Bershady M., Blanc G. A., Bothwell M., Cales S. L., Coccato L., Drory N., Emsellem E., Fu H., Gelfand J., Law D., Masters K., Parejko J., Tremonti C., Wake D., Weijmans A., Yan R., Xiao T., Zhang K., Zheng T., Bizyaev D., Kinemuchi K., Oravetz D., Simmons A., 2014. *ArXiv e-prints*. *P-MaNGA Galaxies: Emission Lines Properties - Gas Ionisation and Chemical Abundances from Prototype Observations*.

Bell E. F., McIntosh D. H., Katz N., Weinberg M. D., 2003. ApJS, **149**, 289. *The Optical and Near-Infrared Properties of Galaxies. I. Luminosity and Stellar Mass Functions*.

Bell E. F., Papovich C., Wolf C., Le Floc'h E., Caldwell J. A. R., Barden M., Egami E., McIntosh D. H., Meisenheimer K., Pérez-González P. G., Rieke G. H., Rieke M. J., Rigby J. R., Rix H.-W., 2005. ApJ, **625**, 23. *Toward an Understanding of the Rapid Decline of the Cosmic Star Formation Rate*.

Bertin E., Arnouts S., 1996. AAS, **117**, 393. *SExtractor: Software for source extraction.*

Best P. N., 2004. MNRAS, **351**, 70. *The environmental dependence of radio-loud AGN activity and star formation in the 2dFGRS*.

Blake C., Pracy M. B., Couch W. J., Bekki K., Lewis I., Glazebrook K., Baldry I. K., Baugh C. M., Bland-Hawthorn J., Bridges T., Cannon R., Cole S., Colless M., Collins C., Dalton G., De Propris R., Driver S. P., Efstathiou G., Ellis R. S., Frenk C. S., Jackson C., Lahav O., Lumsden S., Maddox S., Madgwick D., Norberg P., Peacock J. A., Peterson B. A., Sutherland W., Taylor K., 2004. *MNRAS*, **355**, 713.

Blanton M. R., Eisenstein D., Hogg D. W., Schlegel D. J., Brinkmann J., 2005. ApJ, **629**, 143. *Relationship between Environment and the Broadband Optical Properties of Galaxies in the Sloan Digital Sky Survey*.

Booth C. M., Schaye J., 2009. MNRAS, **398**, 53. *Cosmological simulations of the growth of supermassive black holes and feedback from active galactic nuclei: method and tests*.

Borch A., Meisenheimer K., Bell E. F., Rix H.-W., Wolf C., Dye S., Kleinheinrich M., Kovacs Z., Wisotzki L., 2006. AA, **453**, 869. *The stellar masses of 25 000 galaxies at 0.2 < z < 1.0 estimated by the COMBO-17 survey*.

Bösch B., Böhm A., Wolf C., Aragón-Salamanca A., Barden M., Gray M. E., Ziegler B. L., Schindler S., Balogh M., 2013a. *A&A*, **549**, A142. *Ram pressure and dusty red galaxies - key factors in the evolution of the multiple cluster system Abell 901/902*.

Bösch B., Böhm A., Wolf C., Aragón-Salamanca A., Ziegler B. L., Barden M., Gray M. E., Balogh M., Meisenheimer K., Schindler S., 2013b. *ArXiv Astrophysics, preprint (arXiv:1304.6186). Tully-Fisher analysis of the multiple cluster system Abell 901/902*.

Bouwens R. J., Illingworth G. D., Franx M., Ford H., 2007. ApJ, **670**, 928. *UV Luminosity Functions at z˜4, 5, and 6 from the Hubble Ultra Deep Field and Other Deep Hubble Space Telescope ACS Fields: Evolution and Star Formation History*.

Bretherton C. F., Moss C., James P. A., 2013. AA, **553**, A67. *Star-forming galaxies in low-redshift clusters: Effects of environment on the concentration of star formation*.

Brinchmann J., Charlot S., White S. D. M., Tremonti C., Kauffmann G., Heckman T., Brinkmann J., 2004. MNRAS, **351**, 1151. *The physical properties of star-forming galaxies in the low-redshift Universe*.

Bruzual G., Charlot S., 2003. MNRAS, **344**, 1000. *Stellar population synthesis at the resolution of 2003*.

Buitrago F., Trujillo I., Conselice C. J., Bouwens R. J., Dickinson M., Yan H., 2008. ApJ, **687**, L61. *Size Evolution of the Most Massive Galaxies at 1.7 < z < 3 from GOODS NICMOS Survey Imaging*.

Bundy K., Ellis R. S., Conselice C. J., 2005. ApJ, **625**, 621. *The Mass Assembly Histories of Galaxies of Various Morphologies in the GOODS Fields*.

Bundy K., Ellis R. S., Conselice C. J., Taylor J. E., Cooper M. C., Willmer C. N. A., Weiner B. J., Coil A. L., Noeske K. G., Eisenhardt P. R. M., 2006. ApJ, **651**, 120. *The Mass Assembly History of Field Galaxies: Detection of an Evolving Mass Limit for Star-Forming Galaxies*.

Bundy K., Bershady M. A., Law D. R., Yan R., Drory N., MacDonald N., Wake D. A., Cherinka B., Sánchez-Gallego J. R., Weijmans A.-M., Thomas D., Tremonti C., Masters K., Coccato L., Diamond-Stanic A. M., Aragón-Salamanca A., Avila-Reese V., Badenes C., Falcón-Barroso J., Belfiore F., Bizyaev D., Blanc G. A., Bland-Hawthorn J., Blanton M. R., Brownstein J. R., Byler N., Cappellari M., Conroy C., Dutton A. A., Emsellem E., Etherington J., Frinchaboy P. M., Fu H., Gunn J. E., Harding P., Johnston E. J., Kauffmann G., Kinemuchi K., Klaene M. A., Knapen J. H., Leauthaud A., Li C., Lin L., Maiolino R., Malanushenko V., Malanushenko E., Mao S., Maraston C., McDermid R. M., Merrifield M. R., Nichol R. C., Oravetz D., Pan K., Parejko J. K., Sanchez S. F., Schlegel D., Simmons A., Steele O., Steinmetz M., Thanjavur K., Thompson B. A., Tinker J. L., van den Bosch R. C. E., Westfall K. B., Wilkinson D., Wright S., Xiao T., Zhang K., 2015. ApJ, **798**, 7. *Overview of the SDSS-IV MaNGA Survey: Mapping nearby Galaxies at Apache Point Observatory*.

Butcher H., Oemler, Jr. A., 1978. ApJ, **226**, 559. *The evolution of galaxies in clusters. II - The galaxy content of nearby clusters*.

Butcher H., Oemler, Jr. A., 1984. ApJ, **285**, 426. *The evolution of galaxies in clusters. V - A study of populations since Z approximately equal to 0.5*.

Byrd G., Valtonen M., 1990. ApJ, **350**, 89. *Tidal generation of active spirals and S0 galaxies by rich clusters*.

Caldwell N., Rose J. A., Franx M., Leonardi A. J., 1996. AJ, **111**, 78. *Spatial Distribution of the Starbursts in Post-Starburst Coma Cluster Galaxies*.

Caldwell N., Rose J. A., Dendy K., 1999. AJ, **117**, 140. *On the Origins of Starburst and Poststarburst Galaxies in Nearby Clusters*.

Calzetti D., Armus L., Bohlin R. C., Kinney A. L., Koornneef J., Storchi-Bergmann T., 2000. ApJ, **533**, 682. *The Dust Content and Opacity of Actively Star-forming Galaxies*.

Cappellari M., Emsellem E., 2004. PASP, **116**, 138. *Parametric Recovery of Line-of-Sight Velocity Distributions from Absorption-Line Spectra of Galaxies via Penalized Likelihood*.

Cappellari M., Emsellem E., Krajnović D., McDermid R. M., Serra P., Alatalo K., Blitz L., Bois M., Bournaud F., Bureau M., Davies R. L., Davis T. A., de Zeeuw P. T., Khochfar S., Kuntschner H., Lablanche P.-Y., Morganti R., Naab T., Oosterloo T., Sarzi M., Scott N., Weijmans A.-M., Young L. M., 2011. MNRAS, **416**, 1680. *The ATLAS^{3D} project - VII. A new look at the morphology of nearby galaxies: the kinematic morphology-density relation*.

Cardiel N., 2010. *ASCL. indexf: Line-strength Indices in Fully Calibrated FITS Spectra*. Astrophysics Source Code Library.

Casteels K. R. V., Bamford S. P., Skibba R. A., Masters K. L., Lintott C. J., Keel W. C., Schawinski K., Nichol R. C., Smith A. M., 2013. MNRAS, **429**, 1051. *Galaxy Zoo: quantifying morphological indicators of galaxy interaction*.

Cepa J., Bongiovanni A., Pérez García A. M., Ederoclite A., González-Serrano J. I., González J. J., Sánchez-Portal M., Alfaro E. J., Cabrera-Lavers A., 2013a. *OSIRIS/GTC: status and prospects*, In: *Highlights of Spanish Astrophysics VII*, p. 868, eds Guirado J. C., Lara L. M., Quilis V., Gorgas J.

Cepa J., Bongiovanni A., Pérez García A. M., Ederoclite A., Lara-López M. A., Alfaro E. J., Gallego J., González J. J., González-Serrano J. I., Sánchez-Portal M., Castañeda H. O., Bland-Hawthorn J., Rodríguez-Espinosa J. M., Fernández-Lorenzo M., Povic M., 2013b. *The OTELO Project*, In: *Revista Mexicana de Astronomia y Astrofisica Conference Series*, p. 70.

Chabrier G., 2003. PASP, **115**, 763. *Galactic Stellar and Substellar Initial Mass Function*.

Chien L.-H., Barnes J. E., 2010. *MNRAS*, **407**, 43. *Dynamically driven star formation in models of NGC 7252*.

Christlein D., Zabludoff A. I., 2004. ApJ, **616**, 192. *Can Early-Type Galaxies Evolve from the Fading of the Disks of Late-Type Galaxies?*

Cid Fernandes R., Stasińska G., Schlickmann M. S., Mateus A., Vale Asari N., Schoenell W., Sodré L., 2010. MNRAS, **403**, 1036. *Alternative diagnostic diagrams and the 'forgotten' population of weak line galaxies in the SDSS*.

Cid Fernandes R., Stasińska G., Mateus A., Vale Asari N., 2011. MNRAS, **413**, 1687. *A comprehensive classification of galaxies in the Sloan Digital Sky Survey: how to tell true from fake AGN?*

Cortesi A., Merrifield M. R., Coccato L., Arnaboldi M., Gerhard O., Bamford S., Napolitano N. R., Romanowsky A. J., Douglas N. G., Kuijken K., Capaccioli M., Freeman K. C., Saha K., Chies-Santos A. L., 2013. MNRAS, **432**, 1010. *Planetary Nebula Spectrograph survey of S0 galaxy kinematics - II. Clues to the origins of S0 galaxies*.

Couch W. J., Newell E. B., 1984. ApJS, **56**, 143. *Distant clusters of galaxies. I - Uniform photometry of 14 rich clusters*.

Couch W. J., Sharples R. M., 1987. MNRAS, **229**, 423. *A spectroscopic study of three rich galaxy clusters at Z = 0.31*.

Couch W. J., Ellis R. S., Sharples R. M., Smail I., 1994. ApJ, **430**, 121. *Morphological studies of the galaxy populations in distant 'Butcher-Oemler' clusters with HST. 1: AC 114 AT Z = 0.31 and Abell 370 at Z = 0.37*.

Couch W. J., Barger A. J., Smail I., Ellis R. S., Sharples R. M., 1998. *ApJ*, **497**, 188. *Morphological Studies of the Galaxy Populations in Distant "Butcher-Oemler" Clusters with the Hubble Space Telescope. II. AC 103, AC 118, and AC 114 at Z = 0.31*.

Couch W. J., Balogh M. L., Bower R. G., Smail I., Glazebrook K., Taylor M., 2001. ApJ, **549**, 820. *A Low Global Star Formation Rate in the Rich Galaxy Cluster AC 114 at z=0.32*.

Crowl H. H., Kenney J. D. P., 2008. AJ, **136**, 1623. *The Stellar Populations of Stripped Spiral Galaxies in the Virgo Cluster*.

Desai V., Dalcanton J. J., Aragón-Salamanca A., Jablonka P., Poggianti B., Gogarten S. M., Simard L., Milvang-Jensen B., Rudnick G., Zaritsky D., Clowe D., Halliday C., Pelló R., Saglia R., White S., 2007. ApJ, **660**, 1151. *The Morphological Content of 10 EDisCS Clusters at 0.5 < z < 0.8*.

Dressler A., Gunn J. E., 1983. ApJ, **270**, 7. *Spectroscopy of galaxies in distant clusters. II - The population of the 3C 295 cluster*.

Dressler A., Oemler, Jr. A., Butcher H. R., Gunn J. E., 1994. ApJ, **430**, 107. *The morphology of distant cluster galaxies. 1: HST observations of CL 0939+4713*.

Dressler A., Oemler, Jr. A., Couch W. J., Smail I., Ellis R. S., Barger A., Butcher H., Poggianti B. M., Sharples R. M., 1997. ApJ, **490**, 577. *Evolution since z = 0.5 of the Morphology-Density Relation for Clusters of Galaxies*.

Dressler A., Smail I., Poggianti B. M., Butcher H., Couch W. J., Ellis R. S., Oemler, Jr. A., 1999. ApJS, **122**, 51. *A Spectroscopic Catalog of 10 Distant Rich Clusters of Galaxies*.

Dressler A., 1980. ApJ, **236**, 351. *Galaxy morphology in rich clusters - Implications for the formation and evolution of galaxies*.

Driver S. P., Popescu C. C., Tuffs R. J., Liske J., Graham A. W., Allen P. D., de Propris R., 2007. MNRAS, **379**, 1022. *The Millennium Galaxy Catalogue: the B-band attenuation of bulge and disc light and the implied cosmic dust and stellar mass densities*.

Eliche-Moral M. C., González-García A. C., Aguerri J. A. L., Gallego J., Zamorano J., Balcells M., Prieto M., 2012. AA, **547**, A48. *Evolution along the sequence of S0 Hubble types induced by dry minor mergers. I. Global bulge-to-disk structural relations*.

Eliche-Moral M. C., González-García A. C., Aguerri J. A. L., Gallego J., Zamorano J., Balcells M., Prieto M., 2013. AA, **552**, A67. *Evolution along the sequence of S0 Hubble types induced by dry minor mergers. II. Bulge-disk coupling in the photometric relations through merger-induced internal secular evolution*.

Elmegreen D. M., Elmegreen B. G., Kaufman M., Sheth K., Struck C., Thomasson M., Brinks E., 2006. *ApJ*, **642**, 158. *Spitzer Space Telescope IRAC and MIPS Observations of the Interacting Galaxies IC 2163 and NGC 2207: Clumpy Emission*.

Erwin P., Saglia R. P., Fabricius M., Thomas J., Nowak N., Rusli S., Bender R., Vega Beltrán J. C., Beckman J. E., 2015. MNRAS, **446**, 4039. *Composite bulges: the coexistence of classical bulges and discy pseudo-bulges in S0 and spiral galaxies*.

Fan X., Carilli C. L., Keating B., 2006. ARAA, **44**, 415. *Observational Constraints on Cosmic Reionization*.

Fasano G., Poggianti B. M., Couch W. J., Bettoni D., Kjærgaard P., Moles M., 2000. ApJ, **542**, 673. *The Evolution of the Galactic Morphological Types in Clusters*.

Fioc M., Rocca-Volmerange B., 1997. AA, **326**, 950. *PEGASE: a UV to NIR spectral evolution model of galaxies. Application to the calibration of bright galaxy counts.*

Fisher D., Franx M., Illingworth G., 1996. ApJ, **459**, 110. *Line Strengths and Line-Strength Gradients in S0 Galaxies*.

Font A. S., Bower R. G., McCarthy I. G., Benson A. J., Frenk C. S., Helly J. C., Lacey C. G., Baugh C. M., Cole S., 2008. *MNRAS*, **389**, 1619. *The colours of satellite galaxies in groups and clusters*.

Foreman-Mackey D., Hogg D. W., Lang D., Goodman J., 2013. PASP, **125**, 306. *emcee: The MCMC Hammer*.

Franx M., 1993. ApJ, **407**, L5. *Kinematics of an 'E + A' galaxy in Abell 665 AT Z = 0.18*.

Gallazzi A., Bell E. F., Wolf C., Gray M. E., Papovich C., Barden M., Peng C. Y., Meisenheimer K., Heymans C., van Kampen E., Gilmour R., Balogh M., McIntosh D. H., Bacon D., Barazza F. D., Böhm A., Caldwell J. A. R., Häußler B., Jahnke K., Jogee S., Lane K., Robaina A. R., Sanchez S. F., Taylor A., Wisotzki L., Zheng X., 2009. ApJ, **690**, 1883. *Obscured Star Formation in Intermediate-Density Environments: A Spitzer Study of the Abell 901/902 Supercluster*.

Gallego J., Zamorano J., Rego M., Vitores A. G., 1997. ApJ, **475**, 502. *Spectroscopic Properties and Luminosity Distribution of the Universidad Complutense de Madrid Survey Galaxies*.

Geach J. E., Smail I., Moran S. M., Treu T., Ellis R. S., 2009. ApJ, **691**, 783. *The Nature of Dusty Starburst Galaxies in a Rich Cluster at z = 0.4: The Progenitors of Lenticulars?*

Gilmour R., Gray M. E., Almaini O., Best P., Wolf C., Meisenheimer K., Papovich C., Bell E., 2007. MNRAS, **380**, 1467. *Environmental dependence of active galactic nuclei activity in the supercluster A901/2*.

Gómez P. L., Nichol R. C., Miller C. J., Balogh M. L., Goto T., Zabludoff A. I., Romer A. K., Bernardi M., Sheth R., Hopkins A. M., Castander F. J., Connolly A. J., Schneider D. P., Brinkmann J., Lamb D. Q., SubbaRao M., York D. G., 2003. ApJ, **584**, 210. *Galaxy Star Formation as a Function of Environment in the Early Data Release of the Sloan Digital Sky Survey*.

González J. J., Cepa J., González-Serrano J. I., Sánchez-Portal M., 2010. *CAMCS*, **5**, 65. *Ensemble samplers with affine invariance*.

González J. J., Cepa J., González-Serrano J. I., Sánchez-Portal M., 2014. MNRAS, **443**, 3289. *General formulation for the calibration and characterization of narrow-gap etalons: the OSIRIS/GTC tunable filters case*.

Goto T., 2005. MNRAS, **357**, 937. *266 E+A galaxies selected from the Sloan Digital Sky Survey Data Release 2: the origin of E+A galaxies*.

Graham A. W., Driver S. P., 2005. *PASA*, **22**, 118. *A Concise Reference to (Projected) Sérsic $R^{1/n}$ Quantities, Including Concentration, Profile Slopes, Petrosian Indices, and Kron Magnitudes*.

Gray M. E., Wolf C., Barden M., Peng C. Y., Häußler B., Bell E. F., McIntosh D. H., Guo Y., Caldwell J. A. R., Bacon D., Balogh M., Barazza F. D., Böhm A., Heymans C., Jahnke K., Jogee S., van Kampen E., Lane K., Meisenheimer K., Sánchez S. F., Taylor A., Wisotzki L., Zheng X., Green D. A., Beswick R. J., Saikia D. J., Gilmour R., Johnson B. D., Papovich C., 2009. MNRAS, **393**, 1275. *STAGES: the Space Telescope A901/2 Galaxy Evolution Survey*.

Gunawardhana M. L. P., Hopkins A. M., Bland-Hawthorn J., Brough S., Sharp R., Loveday J., Taylor E., Jones D. H., Lara-López M. A., Bauer A. E., Colless M., Owers M., Baldry I. K., López-Sánchez A. R., Foster C., Bamford S., Brown M. J. I., Driver S. P., Drinkwater M. J., Liske J., Meyer M., Norberg P., Robotham A. S. G., Ching J. H. Y., Cluver M. E., Croom S., Kelvin L., Prescott M., Steele O., Thomas D., Wang L., 2013. MNRAS, **433**, 2764. *Galaxy And Mass Assembly: evolution of the Hα luminosity function and star formation rate density up to z < 0.35*.

Gunn J. E., Gott, III J. R., 1972. ApJ, **176**, 1. *On the Infall of Matter Into Clusters of Galaxies and Some Effects on Their Evolution*.

Häußler B., Bamford S. P., Vika M., Rojas A. L., Barden M., Kelvin L. S., Alpaslan M., Robotham A. S. G., Driver S. P., Baldry I. K., Brough S., Hopkins A. M., Liske J., Nichol R. C., Popescu C. C., Tuffs R. J., 2013. MNRAS, **430**, 330. *MegaMorph - multiwavelength measurement of galaxy structure: complete Sérsic profile information from modern surveys*.

Heckman T. M., 1980. AA, **87**, 142. *An optical and radio survey of the nuclei of bright galaxies - Stellar populations and normal H II regions*.

Henriksen M., Byrd G., 1996. ApJ, **459**, 82. *Tidal Triggering of Star Formation by the Galaxy Cluster Potential*.

Hippelein H., Maier C., Meisenheimer K., Wolf C., Fried J. W., von Kuhlmann B., Kümmel M., Phleps S., Röser H.-J., 2003. AA, **402**, 65. *Star forming rates between z = 0.25 and z = 1.2 from the CADIS emission line survey*.

Hopkins P. F., Somerville R. S., Cox T. J., Hernquist L., Jogee S., Kereš D., Ma C.-P., Robertson B., Stewart K., 2009. *MNRAS*, **397**, 802. *The effects of gas on morphological transformation in mergers: implications for bulge and disc demographics*.

Hoyos C., Aragón-Salamanca A., Gray M. E., Maltby D. T., Bell E. F., Barazza F. D., Böhm A., Häußler B., Jahnke K., Jogee S., Lane K. P., McIntosh D. H., Wolf C., 2012. MNRAS, **419**, 2703. *A new automatic method to identify galaxy mergers - I. Description and application to the Space Telescope A901/902 Galaxy Evolution Survey*.

Icke V., 1985. AA, **144**, 115. *Distant encounters between disk galaxies and the origin of S 0 spirals*.

Izzo C., Kornweibel N., McKay D., Palsa R., Peron M., Taylor M., 2004. *The Messenger*, **117**, 33. *Gasgano and ESO VIMOS Pipeline released*.

Jaffé Y. L., Aragón-Salamanca A., Kuntschner H., Bamford S., Hoyos C., De Lucia G., Halliday C., Milvang-Jensen B., Poggianti B., Rudnick G., Saglia R. P., Sanchez-Blazquez P., Zaritsky D., 2011. MNRAS, **417**, 1996. *The effect of the environment on the gas kinematics and the structure of distant galaxies*.

Jaffé Y. L., Poggianti B. M., Verheijen M. A. W., Deshev B. Z., van Gorkom J. H., 2012. *ApJL*, **756**, L28. *Gas Reservoirs and Star Formation in a Forming Galaxy Cluster at zbsime0.2*.

Johnston E. J., Aragón-Salamanca A., Merrifield M. R., Bedregal A. G., 2012. MNRAS, **422**, 2590. *Spectroscopic bulge-disc decomposition: a new method to study the evolution of lenticular galaxies*.

Johnston E. J., Aragon-Salamanca A., Merrifield M. R., Bedregal A. G., 2013a. *ArXiv Astrophysics, preprint (arXiv:13092206). Clues to the Formation of Lenticular Galaxies Using Spectroscopic Bulge-Disk Decomposition*.

Johnston E. J., Merrifield M. R., Aragón-Salamanca A., Cappellari M., 2013b. MNRAS, **428**, 1296. *Disentangling the stellar populations in the counter-rotating disc galaxy NGC 4550*.

Kapferer W., Sluka C., Schindler S., Ferrari C., Ziegler B., 2009. AA, **499**, 87. *The effect of ram pressure on the star formation, mass distribution and morphology of galaxies*.

Kauffmann G., Heckman T. M., Tremonti C., Brinchmann J., Charlot S., White S. D. M., Ridgway S. E., Brinkmann J., Fukugita M., Hall P. B., Ivezić Ž., Richards G. T., Schneider D. P., 2003a. MNRAS, **346**, 1055. *The host galaxies of active galactic nuclei*.

Kauffmann G., Heckman T. M., White S. D. M., Charlot S., Tremonti C., Brinchmann J., Bruzual G., Peng E. W., Seibert M., Bernardi M., Blanton M., Brinkmann J., Castander F., Csábai I., Fukugita M., Ivezic Z., Munn J. A., Nichol R. C., Padmanabhan N., Thakar A. R., Weinberg D. H., York D., 2003b. MNRAS, **341**, 33. *Stellar masses and star formation histories for 10^5 galaxies from the Sloan Digital Sky Survey*.

Kauffmann G., White S. D. M., Heckman T. M., Ménard B., Brinchmann J., Charlot S., Tremonti C., Brinkmann J., 2004. MNRAS, **353**, 713. *The environmental dependence of the relations between stellar mass, structure, star formation and nuclear activity in galaxies*.

Keel W. C., Kennicutt, Jr. R. C., Hummel E., van der Hulst J. M., 1985. *AJ*, **90**, 708. *The effects of interactions on spiral galaxies. I - Nuclear activity and star formation*.

Kennicutt, Jr. R. C., Roettiger K. A., Keel W. C., van der Hulst J. M., Hummel E., 1987. *AJ*, **93**, 1011. *The effects of interactions on spiral galaxies. II - Disk star-formation rates*.

Kennicutt, Jr. R. C., 1992. ApJ, **388**, 310. *The integrated spectra of nearby galaxies - General properties and emission-line spectra*.

Kennicutt, Jr. R. C., 1998. ARAA, **36**, 189. *Star Formation in Galaxies Along the Hubble Sequence*.

Kewley L. J., Dopita M. A., Sutherland R. S., Heisler C. A., Trevena J., 2001. ApJ, **556**, 121. *Theoretical Modeling of Starburst Galaxies*.

Kodama T., Balogh M. L., Smail I., Bower R. G., Nakata F., 2004. MNRAS, **354**, 1103. *A panoramic Hα imaging survey of the z= 0.4 cluster Cl0024.0+1652 with Subaru*.

Koopmann R. A., Kenney J. D. P., 2004a. ApJ, **613**, 851. *Massive Star Formation Rates and Radial Distributions from Hα Imaging of 84 Virgo Cluster and Isolated Spiral Galaxies*.

Koopmann R. A., Kenney J. D. P., 2004b. ApJ, **613**, 866. *Hα Morphologies and Environmental Effects in Virgo Cluster Spiral Galaxies*.

Koopmann R. A., Kenney J. D. P., Young J., 2001. ApJS, **135**, 125. *An Atlas of Hα and R Images and Radial Profiles of 63 Bright Virgo Cluster Spiral Galaxies*.

Kroupa P., 2001. MNRAS, **322**, 231. *On the variation of the initial mass function*.

Lackner C. N., Gunn J. E., 2012. MNRAS, **421**, 2277. *Astrophysically motivated bulge-disc decompositions of Sloan Digital Sky Survey galaxies*.

Lackner C. N., Gunn J. E., 2013. MNRAS, **428**, 2141. *The effect of environment on discs and bulges*.

Lane K. P., Gray M. E., Aragón-Salamanca A., Wolf C., Meisenheimer K., 2007. MNRAS, **378**, 716. *Galaxy morphologies and environment in the Abell 901/902 supercluster from COMBO-17*.

Larson R. B., Tinsley B. M., Caldwell C. N., 1980. ApJ, **237**, 692. *The evolution of disk galaxies and the origin of S0 galaxies*.

Le Borgne D., Rocca-Volmerange B., Prugniel P., Lançon A., Fioc M., Soubiran C., 2004. AA, **425**, 881. *Evolutionary synthesis of galaxies at high spectral resolution with the code PEGASE-HR. Metallicity and age tracers*.

Lemze D., Broadhurst T., Rephaeli Y., Barkana R., Umetsu K., 2009. ApJ, **701**, 1336. *Dynamical Study of A1689 from Wide-Field VLT/VIMOS Spectroscopy: Mass Profile, Concentration Parameter, and Velocity Anisotropy*.

Madau P., Ferguson H. C., Dickinson M. E., Giavalisco M., Steidel C. C., Fruchter A., 1996. MNRAS, **283**, 1388. *High-redshift galaxies in the Hubble Deep Field: colour selection and star formation history to z˜4*.

Maltby D. T., Aragón-Salamanca A., Gray M. E., Barden M., Häußler B., Wolf C., Peng C. Y., Jahnke K., McIntosh D. H., Böhm A., van Kampen E., 2010. MNRAS, **402**, 282. *The environmental dependence of the stellar-mass-size relation in STAGES galaxies*.

Maltby D. T., Gray M. E., Aragón-Salamanca A., Wolf C., Bell E. F., Jogee S., Häußler B., Barazza F. D., Böhm A., Jahnke K., 2012. MNRAS, **419**, 669. *The environmental dependence of the structure of outer galactic discs in STAGES spiral galaxies*.

Margoniner V. E., de Carvalho R. R., Gal R. R., Djorgovski S. G., 2001. ApJ, **548**, L143. *The Butcher-Oemler Effect in 295 Clusters: Strong Redshift Evolution and Cluster Richness Dependence*.

Martini P., Kelson D. D., Mulchaey J. S., Trager S. C., 2002. ApJ, **576**, L109. *An Unexpectedly High Fraction of Active Galactic Nuclei in Red Cluster Galaxies*.

Martini P., Kelson D. D., Kim E., Mulchaey J. S., Athey A. A., 2006. ApJ, **644**, 116. *Spectroscopic Confirmation of a Large Population of Active Galactic Nuclei in Clusters of Galaxies*.

Masters K. L., Nichol R. C., Hoyle B., Lintott C., Bamford S. P., Edmondson E. M., Fortson L., Keel W. C., Schawinski K., Smith A. M., Thomas D., 2011. MNRAS, **411**, 2026. *Galaxy Zoo: bars in disc galaxies*.

Masters K. L., Nichol R. C., Haynes M. P., Keel W. C., Lintott C., Simmons B., Skibba R., Bamford S., Giovanelli R., Schawinski K., 2012. MNRAS, **424**, 2180. *Galaxy Zoo and ALFALFA: atomic gas and the regulation of star formation in barred disc galaxies*.

Méndez-Abreu J., Sánchez Almeida J., Muñoz-Tuñón C., Rodríguez-Espinosa J. M., Aguerri J. A. L., Rosa González D., Mayya Y. D., Vega O., Terlevich R., Terlevich E., Bertone E., Rodríguez-Merino L. H., 2011. PASP, **123**, 1107. *Wavelength Calibration for OSIRIS/GTC Tunable Filters*.

Mihos J. C., Hernquist L., 1994. ApJ, **425**, L13. *Triggering of starbursts in galaxies by minor mergers*.

Mihos J. C., Hernquist L., 1996. ApJ, **464**, 641. *Gasdynamics and Starbursts in Major Mergers*.

Miller C. J., Nichol R. C., Gómez P. L., Hopkins A. M., Bernardi M., 2003. ApJ, **597**, 142. *The Environment of Active Galactic Nuclei in the Sloan Digital Sky Survey*.

Moore B., Katz N., Lake G., Dressler A., Oemler A., 1996. Nature, **379**, 613. *Galaxy harassment and the evolution of clusters of galaxies*.

Moore B., Lake G., Quinn T., Stadel J., 1999. MNRAS, **304**, 465. *On the survival and destruction of spiral galaxies in clusters*.

Moore B., Lake G., Katz N., 1998. ApJ, **495**, 139. *Morphological Transformation from Galaxy Harassment*.

Moran S. M., Ellis R. S., Treu T., Smith G. P., Rich R. M., Smail I., 2007. ApJ, **671**, 1503. *A Wide-Field Survey of Two z ˜ 0.5 Galaxy Clusters: Identifying the Physical Processes Responsible for the Observed Transformation of Spirals into S0s*.

Morgan W. W., 1961. *Proceedings of the National Academy of Science*, **47**, 905. *The Classification of Clusters of Galaxies*.

Moss C., Whittle M., 2000. MNRAS, **317**, 667. *An Hα survey of eight Abell clusters: the dependence of tidally induced star formation on cluster density*.

Naab T., Burkert A., Hernquist L., 1999. ApJ, **523**, L133. *On the Formation of Boxy and Disky Elliptical Galaxies*.

Newton R. D. A., Kay S. T., 2013. MNRAS, **434**, 3606. *A study of AGN and supernova feedback in simulations of isolated and merging disc galaxies*.

Nipoti C., Binney J., 2007. *MNRAS*, **382**, 1481. *The role of thermal evaporation in galaxy formation*.

Noguchi M., Ishibashi S., 1986. MNRAS, **219**, 305. *Simulations of close encounter between galaxies - Behaviour of interstellar gas clouds and enhancement of star formation rate*.

Norton S. A., Gebhardt K., Zabludoff A. I., Zaritsky D., 2001. ApJ, **557**, 150. *The Spatial Distribution and Kinematics of Stellar Populations in E+A Galaxies*.

Nulsen P. E. J., 1982. MNRAS, **198**, 1007. *Transport processes and the stripping of cluster galaxies*.

Osterbrock D. E., 1989. *Astrophysics of gaseous nebulae and active galactic nuclei*, University Science Books.

Ownsworth J. R., Conselice C. J., Mortlock A., Hartley W. G., Almaini O., Duncan K., Mundy C. J., 2014. MNRAS, **445**, 2198. *Minor versus major mergers: the stellar mass growth of massive galaxies from z = 3 using number density selection techniques*.

Papovich C., Finkelstein S. L., Ferguson H. C., Lotz J. M., Giavalisco M., 2011. MNRAS, **412**, 1123. *The rising star formation histories of distant galaxies and implications for gas accretion with time*.

Pasquini L., Avila G., Blecha A., Cacciari C., Cayatte V., Colless M., Damiani F., de Propris R., Dekker H., di Marcantonio P., Farrell T., Gillingham P., Guinouard I., Hammer F., Kaufer A., Hill V., Marteaud M., Modigliani A., Mulas G., North P., Popovic D., Rossetti E., Royer F., Santin P., Schmutzer R., Simond G., Vola P., Waller L., Zoccali M., 2002. *The Messenger*, **110**, 1. *Installation and commissioning of FLAMES, the VLT Multifibre Facility*.

Peebles P. J. E., 1982. ApJ, **263**, L1. *Large-scale background temperature and mass fluctuations due to scale-invariant primeval perturbations*.

Peng Y.-j., Lilly S. J., Kovač K., Bolzonella M., Pozzetti L., Renzini A., Zamorani G., Ilbert O., Knobel C., Iovino A., Maier C., Cucciati O., Tasca L., Carollo C. M., Silverman J., Kampczyk P., de Ravel L., Sanders D., Scoville N., Contini T., Mainieri V., Scodeggio M., Kneib J.-P., Le Fèvre O., Bardelli S., Bongiorno A., Caputi K., Coppa G., de la Torre S., Franzetti P., Garilli B., Lamareille F., Le Borgne J.-F., Le Brun V., Mignoli M., Perez Montero E., Pello R., Ricciardelli E., Tanaka M., Tresse L., Vergani D., Welikala N., Zucca E., Oesch P., Abbas U., Barnes L., Bordoloi R., Bottini D., Cappi A., Cassata P., Cimatti A., Fumana M., Hasinger G., Koekemoer A., Leauthaud A., Maccagni D., Marinoni C., McCracken H., Memeo P., Meneux B., Nair P., Porciani C., Presotto V., Scaramella R., 2010. ApJ, **721**, 193. *Mass and Environment as Drivers of Galaxy Evolution in SDSS and zCOSMOS and the Origin of the Schechter Function*.

Peng Y.-j., Lilly S. J., Renzini A., Carollo M., 2012. ApJ, **757**, 4. *Mass and Environment as Drivers of Galaxy Evolution. II. The Quenching of Satellite Galaxies as the Origin of Environmental Effects*.

Perlmutter S., Aldering G., Goldhaber G., Knop R. A., Nugent P., Castro P. G., Deustua S., Fabbro S., Goobar A., Groom D. E., Hook I. M., Kim A. G., Kim M. Y., Lee J. C., Nunes N. J., Pain R., Pennypacker C. R., Quimby R., Lidman C., Ellis R. S., Irwin M., McMahon R. G., Ruiz-Lapuente P., Walton N., Schaefer B., Boyle B. J., Filippenko A. V., Matheson T., Fruchter A. S., Panagia N., Newberg H. J. M., Couch W. J., Project T. S. C., 1999. ApJ, **517**, 565. *Measurements of Ω and Λ from 42 High-Redshift Supernovae*.

Poggianti B. M., Smail I., Dressler A., Couch W. J., Barger A. J., Butcher H., Ellis R. S., Oemler, Jr. A., 1999. ApJ, **518**, 576. *The Star Formation Histories of Galaxies in Distant Clusters*.

Poggianti B. M., Desai V., Finn R., Bamford S., De Lucia G., Varela J., Aragón-Salamanca A., Halliday C., Noll S., Saglia R., Zaritsky D., Best P., Clowe D., Milvang-Jensen B., Jablonka P., Pelló R., Rudnick G., Simard L., von der Linden A., White S., 2008. ApJ, **684**, 888. *The Relation between Star Formation, Morphology, and Local Density in High-Redshift Clusters and Groups*.

Poggianti B. M., Aragón-Salamanca A., Zaritsky D., De Lucia G., Milvang-Jensen B., Desai V., Jablonka P., Halliday C., Rudnick G., Varela J., Bamford S., Best P., Clowe D., Noll S., Saglia R., Pelló R., Simard L., von der Linden A., White S., 2009. ApJ, **693**, 112. *The Environments of Starburst and Post-Starburst Galaxies at z = 0.4-0.8*.

Poggianti B. M., 2004. *Clusters of Galaxies: Probes of Cosmological Structure and Galaxy Evolution. Modeling Stellar Populations in Cluster Galaxies*.

Popesso P., Biviano A., 2006. AA, **460**, L23. *The AGN fraction-velocity dispersion relation in clusters of galaxies*.

Pracy M. B., Couch W. J., Blake C., Bekki K., Harrison C., Colless M., Kuntschner H., de Propris R., 2005. MNRAS, **359**, 1421. *Spatially resolved spectroscopy of the E+A galaxies in the z= 0.32 cluster AC 114*.

Pracy M. B., Kuntschner H., Couch W. J., Blake C., Bekki K., Briggs F., 2009. MNRAS, **396**, 1349. *The kinematics and spatial distribution of stellar populations in E+A galaxies*.

Pracy M. B., Owers M. S., Couch W. J., Kuntschner H., Bekki K., Briggs F., Lah P., Zwaan M., 2012. MNRAS, **420**, 2232. *Stellar population gradients in the cores of nearby field E+A galaxies*.

Pracy M. B., Croom S., Sadler E., Couch W. J., Kuntschner H., Bekki K., Owers M. S., Zwaan M., Turner J., Bergmann M., 2013. *MNRAS*, **432**, 3131. *Stellar population gradients and spatially resolved kinematics in luminous post-starburst galaxies*.

Prugniel P., Soubiran C., Koleva M., Le Borgne D., 2007. *ArXiv Astrophysics, preprint (arXiv:0703658). New release of the ELODIE library: Version 3.1*.

Quilis V., Moore B., Bower R., 2000. *Science*, **288**, 1617. *Gone with the Wind: The Origin of S0 Galaxies in Clusters*.

Rees M. J., Ostriker J. P., 1977. MNRAS, **179**, 541. *Cooling, dynamics and fragmentation of massive gas clouds - Clues to the masses and radii of galaxies and clusters*.

Riess A. G., Filippenko A. V., Challis P., Clocchiatti A., Diercks A., Garnavich P. M., Gilliland R. L., Hogan C. J., Jha S., Kirshner R. P., Leibundgut B., Phillips M. M., Reiss D., Schmidt B. P., Schommer R. A., Smith R. C., Spyromilio J., Stubbs C., Suntzeff N. B., Tonry J., 1998. AJ, **116**, 1009. *Observational Evidence from Supernovae for an Accelerating Universe and a Cosmological Constant*.

Rose J. A., Gaba A. E., Caldwell N., Chaboyer B., 2001. AJ, **121**, 793. *Starbursts versus Truncated Star Formation in Nearby Clusters of Galaxies*.

Rose J. A., Robertson P., Miner J., Levy L., 2010. AJ, **139**, 765. *Star Formation in Partially Gas-Depleted Spiral Galaxies*.

Rubin V. C., Ford W. K. J., Thonnard N., 1980. ApJ, **238**, 471. *Rotational properties of 21 SC galaxies with a large range of luminosities and radii, from NGC 4605 /R = 4kpc/ to UGC 2885 /R = 122 kpc/.*

Sánchez S. F., Kennicutt R. C., Gil de Paz A., van de Ven G., Vílchez J. M., Wisotzki L., Walcher C. J., Mast D., Aguerri J. A. L., Albiol-Pérez S., Alonso-Herrero A., Alves J., Bakos J., Bartáková T., Bland-Hawthorn J., Boselli A., Bomans D. J., Castillo-Morales A., Cortijo-Ferrero C., de Lorenzo-Cáceres A., Del Olmo A., Dettmar R.-J., Díaz A., Ellis S., Falcón-Barroso J., Flores H., Gallazzi A., García-Lorenzo B., González Delgado R., Gruel N., Haines T., Hao C., Husemann B., Iglésias-Páramo J., Jahnke K., Johnson B., Jungwiert B., Kalinova V., Kehrig C., Kupko D., López-Sánchez Á. R., Lyubenova M., Marino R. A., Mármol-Queraltó E., Márquez I., Masegosa J., Meidt S., Mendez-Abreu J., Monreal-Ibero A., Montijo C., Mourão A. M., Palacios-Navarro G., Papaderos P., Pasquali A., Peletier R., Pérez E., Pérez I., Quirrenbach A., Relaño M., Rosales-Ortega F. F., Roth M. M., Ruiz-Lara T., Sánchez-Blázquez P., Sengupta C., Singh R., Stanishev V., Trager S. C., Vazdekis A., Viironen K., Wild V., Zibetti S., Ziegler B., 2012. AA, **538**, A8. *CALIFA, the Calar Alto Legacy Integral Field Area survey. I. Survey presentation*.

Saunders W., Rowan-Robinson M., Lawrence A., Efstathiou G., Kaiser N., Ellis R. S., Frenk C. S., 1990. MNRAS, **242**, 318. *The 60-micron and far-infrared luminosity functions of IRAS galaxies*.

Schechter P., 1976. ApJ, **203**, 297. *An analytic expression for the luminosity function for galaxies.*

Schmidt B. P., Suntzeff N. B., Phillips M. M., Schommer R. A., Clocchiatti A., Kirshner R. P., Garnavich P., Challis P., Leibundgut B., Spyromilio J., Riess A. G., Filippenko A. V., Hamuy M., Smith R. C., Hogan C., Stubbs C., Diercks A., Reiss D., Gilliland R., Tonry J., Maza J., Dressler A., Walsh J., Ciardullo R., 1998. ApJ, **507**, 46. *The High-Z Supernova Search: Measuring Cosmic Deceleration and Global Curvature of the Universe Using Type IA Supernovae*.

Shioya Y., Bekki K., Couch W. J., De Propris R., 2002. ApJ, **565**, 223. *Spectrophotometric Evolution of Spiral Galaxies with Truncated Star Formation: An Evolutionary Link between Spirals and S0s in Distant Clusters*.

Simard L., Mendel J. T., Patton D. R., Ellison S. L., McConnachie A. W., 2011. ApJS, **196**, 11. *A Catalog of Bulge+disk Decompositions and Updated Photometry for 1.12 Million Galaxies in the Sloan Digital Sky Survey*.

Sobral D., Best P. N., Geach J. E., Smail I., Kurk J., Cirasuolo M., Casali M., Ivison R. J., Coppin K., Dalton G. B., 2009. MNRAS, **398**, 75. *HiZELS: a high-redshift survey of Hα emitters - II. The nature of star-forming galaxies at z = 0.84*.

Sobral D., Best P. N., Smail I., Geach J. E., Cirasuolo M., Garn T., Dalton G. B., 2011. MNRAS, **411**, 675. *The dependence of star formation activity on environment and stellar mass at z < 1 from the HiZELS-Hα survey*.

Sokal A. D., 1996. *Nuclear Physics B Proceedings Supplements*, **47**, 172. *Monte Carlo methods for the self-avoiding walk*.

Stasińska G., Cid Fernandes R., Mateus A., Sodré L., Asari N. V., 2006. MNRAS, **371**, 972. *Semi-empirical analysis of Sloan Digital Sky Survey galaxies - III. How to distinguish AGN hosts*.

Stasińska G., Costa Duarte M. V., Vale Asari N., Cid Fernandes R., Sodré L., 2015. *ArXiv e-prints*. *Retired galaxies: not to be forgotten in the quest of the star formation – AGN connection*.

Strateva I., Ivezić Ž., Knapp G. R., Narayanan V. K., Strauss M. A., Gunn J. E., Lupton R. H., Schlegel D., Bahcall N. A., Brinkmann J., Brunner R. J., Budavári T., Csabai I., Castander F. J., Doi M., Fukugita M., Győry Z., Hamabe M., Hennessy G., Ichikawa T., Kunszt P. Z., Lamb D. Q., McKay T. A., Okamura S., Racusin J., Sekiguchi M., Schneider D. P., Shimasaku K., York D., 2001. AJ, **122**, 1861. *Color Separation of Galaxy Types in the Sloan Digital Sky Survey Imaging Data*.

Swinbank A. M., Balogh M. L., Bower R. G., Zabludoff A. I., Lucey J. R., McGee S. L., Miller C. J., Nichol R. C., 2012. MNRAS, **420**, 672. *From star-forming spirals to passive spheroids: integral field spectroscopy of E+A galaxies*.

Teyssier R., Chapon D., Bournaud F., 2010. *ApJL*, **720**, L149. *The Driving Mechanism of Starbursts in Galaxy Mergers*.

Toomre A., Toomre J., 1972. ApJ, **178**, 623. *Galactic Bridges and Tails*.

Toomre A., 1977. *Mergers and Some Consequences*, In: *Evolution of Galaxies and Stellar Populations*, 401, eds Tinsley B. M., Larson, D. Campbell R. B. G.

Tran K.-V. H., Franx M., Illingworth G., Kelson D. D., van Dokkum P., 2003. ApJ, **599**, 865. *The Nature of E+A Galaxies in Intermediate-Redshift Clusters*.

van den Bergh S., 1976. ApJ, **206**, 883. *A new classification system for galaxies*.

van Dokkum P. G., Whitaker K. E., Brammer G., Franx M., Kriek M., Labbé I., Marchesini D., Quadri R., Bezanson R., Illingworth G. D., Muzzin A., Rudnick G., Tal T., Wake D., 2010. ApJ, **709**, 1018. *The Growth of Massive Galaxies Since z = 2*.

Verdugo M., Ziegler B. L., Gerken B., 2008. AA, **486**, 9. *The galaxy populations from the centers to the infall regions in z 0.25 clusters*.

Villar V., Gallego J., Pérez-González P. G., Pascual S., Noeske K., Koo D. C., Barro G., Zamorano J., 2008. ApJ, **677**, 169. *The Hα-based Star Formation Rate Density of the Universe at z = 0.84*.

Vogt N. P., Haynes M. P., Giovanelli R., Herter T., 2004a. *AJ*, **127**, 3300. *M/L, Hα Rotation Curves, and H I Gas Measurements for 329 Nearby Cluster and Field Spirals. II. Evidence for Galaxy Infall*.

Vogt N. P., Haynes M. P., Giovanelli R., Herter T., 2004b. AJ, **127**, 3325. *M/L, Hα Rotation Curves, and H I Gas Measurements for 329 Nearby Cluster and Field Spirals. III. Evolution in Fundamental Galaxy Parameters*.

Vulcani B., Poggianti B. M., Finn R. A., Rudnick G., Desai V., Bamford S., 2010. ApJ, **710**, L1. *Comparing the Relation Between Star Formation and Galaxy Mass in Different Environments*.

Whitaker K. E., van Dokkum P. G., Brammer G., Franx M., 2012. ApJ, **754**, L29. *The Star Formation Mass Sequence Out to z = 2.5*.

Wilman D. J., Oemler, Jr. A., Mulchaey J. S., McGee S. L., Balogh M. L., Bower R. G., 2009. ApJ, **692**, 298. *Morphological Composition of z ˜ 0.4 Groups: The Site of S0 Formation*.

Wolf C., Meisenheimer K., Rix H.-W., Borch A., Dye S., Kleinheinrich M., 2003. AA, **401**, 73. *The COMBO-17 survey: Evolution of the galaxy luminosity function from 25 000 galaxies with 0.2 < z < 1.2*.

Wolf C., Meisenheimer K., Kleinheinrich M., Borch A., Dye S., Gray M., Wisotzki L., Bell E. F., Rix H.-W., Cimatti A., Hasinger G., Szokoly G., 2004. AA, **421**, 913. *A catalogue of the Chandra Deep Field South with multi-colour classification and photometric redshifts from COMBO-17*.

Wolf C., Aragón-Salamanca A., Balogh M., Barden M., Bell E. F., Gray M. E., Peng C. Y., Bacon D., Barazza F. D., Böhm A., Caldwell J. A. R., Gallazzi A., Häußler B., Heymans C., Jahnke K., Jogee S., van Kampen E., Lane K., McIntosh D. H., Meisenheimer K., Papovich C., Sánchez S. F., Taylor A., Wisotzki L., Zheng X., 2009. *MNRAS*, **393**, 1302. *The STAGES view of red spirals and dusty red galaxies: mass-dependent quenching of star formation in cluster infall*.

Wolf C., Gray M. E., Meisenheimer K., 2005. AA, **443**, 435. *Red-sequence galaxies with young stars and dust: the cluster Abell 901/902 seen with COMBO-17*.

Worthey G., Ottaviani D. L., 1997. ApJS, **111**, 377. *Hγ and Hδ Absorption Features in Stars and Stellar Populations*.

Yamauchi C., Yagi M., Goto T., 2008. MNRAS, **390**, 383. *E+A and companion galaxies - I. A catalogue and statistics*.

Yan R., Blanton M. R., 2012. ApJ, **747**, 61. *The Nature of LINER-like Emission in Red Galaxies*.

Yang Y., Zabludoff A. I., Zaritsky D., Mihos J. C., 2008. *ApJ*, **688**, 945. *The Detailed Evolution of E+A Galaxies into Early Types*.

Zabludoff A. I., Zaritsky D., Lin H., Tucker D., Hashimoto Y., Shectman S. A., Oemler A., Kirshner R. P., 1996. ApJ, **466**, 104. *The Environment of "E+A" Galaxies*.

Zwicky F., 1933. *Helvetica Physica Acta*, **6**, 110. *Die Rotverschiebung von extragalaktischen Nebeln*.